TECHNISCHE UNIVERSITÄT WIEN
Vienna University of Technology

DISSERTATION

Pulsed Laser Deposition of Functional Oxides with Atomic Scale Control

Ausgeführt zum Zwecke der Erlangung des akademischen Grades
eines Doktors der technischen Wissenschaften unter der Leitung von

Univ.Prof. Dr.Techn. Ulrike Diebold
und
Dr. Michele Riva

Institute für Angewandte Physics E134

eingereicht an der Technischen Universität Wien
Fakultät für Physik

von

Giada Franceschi

01529932

Lambrechtgasse 3/7
1040 Wien

Wien, September 2020

Abstract

Metal oxides show a wide range of physicochemical properties, and play a major role in emerging and developing technologies. In all applications, surfaces are critically important: Devices are often driven by reactions and by interactions occurring at the materials' surfaces. One well-suited approach to explore and exploit the manifold of properties of metal oxides, and to model their interaction with the environment, is to work with single-crystalline samples in ultra-high vacuum (UHV). This surface science approach provides tight control over sample composition, environment, and surface structures, thus meeting the needs of computational modeling, which, in turn, can offer interpretation and guidance to experimental work.

Bulk-like epitaxial thin films are a sound alternative to single crystals, especially when these are impure, too small, too expensive, or simply not available. Such ideal films can in principle be realized by various deposition techniques, among others pulsed laser deposition (PLD). However, numerous works from the literature testify to the challenges intrinsic to controlling the growth of metal oxide films by PLD: Films with rough morphologies, pronounced nonstoichiometry, and unexpected properties are produced more often than desired. This is largely because many growth parameters, *e.g.*, the laser energy density, the oxygen background pressure, and the substrate temperature, have direct consequences on the film thickness, composition, crystallinity, morphology, and all the related properties. Moreover, non-idealities become more pronounced as the film thickness increases, making it hard to realize bulk-like samples of a few tens of nanometers. Multicomponent oxides are most severely affected, since their different cations suffer, *e.g.*, from preferential ablation at the target, preferential scattering with the background gas, and preferential sticking at the substrate. The challenges in producing ideal, bulk-like oxide films are exacerbated by the difficulties in reproducing PLD parameters in different setups: Every PLD chamber is designed uniquely, and the relevant parameters can be measured in various ways. As a result, tools are needed to identify and tune the relevant growth parameters and achieve the desired film properties.

This Thesis collects various studies on metal-oxide films, which have been produced and characterized with a combined PLD and surface science approach. In all cases, the

aim was to produce single-crystalline films with fully characterized surfaces, suited to address the fundamentals of the surface reactions of interest. Surface science tools, most prominently scanning tunneling microscopy (STM), were used to explore the fundamentals behind the strongly parameter-dependent growth of $In_2O_3(111)$—a transparent conductive oxide used in various catalytic and gas-sensing applications—and of $SrTiO_3(110)$ and $La_{1-x}Sr_xMnO_3(110)$, both perovskite oxides used as catalysts in solid-oxide fuel cells. In the case of In_2O_3, it was found that the oxygen stoichiometry of the deposited species, affected by the deposition conditions, strongly influences the surface diffusivity and, as a result, the film morphology. On the other hand, the studies on $SrTiO_3$ and $La_{1-x}Sr_xMnO_3$, both characterized by composition-related surface reconstructions, have demonstrated that nonstoichiometries introduced under non-optimal growth conditions tend to accumulate at the films' surfaces, forcing a change in the surface atomic structure. These changes are the potential cause for undesired morphology alterations, and may be a more general trait of perovskite oxides. It is shown how the newly developed relations between nonstoichiometry, surface morphology, and surface structure can be used to optimize film growth, and obtain stoichiometric, bulk-like, atomically flat films.

A variety of surface science techniques has been used to thoroughly characterize the surface atomic details of the optimized films, with emphasis on $La_{1-x}Sr_xMnO_3(110)$: Its surface reconstructions are presented here for the first time, and organized in a two-dimensional experimental surface phase diagram as a function of the oxygen chemical potential and the cation composition. The same tools have been used to characterize the surfaces of the more easily grown $TiO_2(001)$ anatase and Ti-doped $Fe_2O_3(1\bar{1}02)$, both interesting for their potential as catalysts for photoelectrochemical water splitting. In the case of Ti-doped $Fe_2O_3(1\bar{1}02)$ and $La_{1-x}Sr_xMnO_3(110)$, the experimental surface characterization has been complemented by *ab-initio* theoretical calculations performed by collaborators.

The importance of building model systems in the form of well-characterized single-crystalline surfaces to investigate given chemical reactions is exemplified by the studies on the oxygen incorporation on $SrTiO_3(110)$ and $La_{1-x}Sr_xMnO_3(110)$ surfaces. Oxygen incorporation is a key process in solid-oxide fuel cells, but little is known on the exact mechanisms driving it. Using such well-defined model systems has enabled to shed light on the process, at the same time highlighting the critical role of surface atomic coordination and arrangement.

Kurzfassung

Metalloxide weisen eine extrem weite Bandbreite an physikalisch-chemischen Eigenschaften auf und spielen daher bei der Entwicklung neuer Technologien eine oft tragende Rolle. Die Oberflächen dieser Materialien sind bei jenen Anwendungen von entscheidender Bedeutung, die auf chemischen Reaktionen oder anderen Oberflächenprozessen aufbauen. Für die grundlegende Erforschung und etwaige Nutzung solcher Prozesse bietet die Oberflächenphysik einen vielversprechenden Ansatz: einkristalline Proben und Experimente im Ultrahochvakuum (UHV) erlauben die Untersuchung der Eigenschaften von Metalloxiden und die exakte Modellierung der Wechselwirkung mit ihrer Umgebung. Da bei diesem Ansatz eine akkurate Kontrolle sowohl der Zusammensetzung und Struktur der Probenoberfläche als auch ihrer Umgebung vorliegt, eignen sich solche Experimente besonders gut für die enge Wechselwirkung mit theoretischer Modellierung. Dies führt nicht nur zu wesentlichen Einsichten, sondern kann auch die Interpretation von experimentellen Resultaten erleichtern und beim Design geeigneter Experimente helfen.

Wenn die erforderlichen Einkristalle oft zu klein, zu teuer oder ganz einfach nicht verfügbar sind, sind epitaktisch gewachsene Schichten eine gute Alternative. Für die Synthese komplexer epitaktischer Oxidschichten hat sich in den letzten Jahren die gepulste Laserabscheidung (Pulsed Laser Deposition, PLD) als Standardmethode herauskristallisiert. Zahlreiche Arbeiten aus der Literatur weisen jedoch auf die Herausforderungen hin, die der Kontrolle des Wachstums von Metalloxidfilmen durch PLD innewohnen: oft entstehen Filme mit hoher Rauigkeit, ausgeprägter Nichtstöchiometrie oder anderen unerwünschten Eigenschaften. Dies liegt hauptsächlich daran, dass viele Wachstumsparameter, z. b. die Laserenergiedichte, der Sauerstoffpartialdruck oder die Substrattemperatur, direkte und starke Auswirkungen auf die Filmdicke, Zusammensetzung, Kristallinität, Morphologie und alle damit verbundenen Eigenschaften haben. Darüber hinaus werden solche Nichtidealitäten mit Schichtdicke zunehmender ausgeprägter. Dies erschwert es oft, Dünnschichtproben mit einer Stärke von einigen zehn Nanometern zu realisieren, was aber notwendig ist, um ihre Eigenschaften an die von Volumseinkristallen anzugleichen. Vielkomponentige Oxide sind davon am stärksten betroffen, da ihre unterschiedlichen Kationen eine bevorzugte Ablation am Target, eine bevorzugte Streuung mit dem Hintergrundgas oder eine bevorzugte Abscheidung am Substrat erleiden können. Die Herausforderungen für die Herstellung idealer, volumenartiger Oxidfilme werden noch durch eine weitere Schwierigkeit verschärft, nämlich der

Reproduzierbarkeit von PLD-Parametern in unterschiedlichen experimentelle Aufbauten: Fast jede PLD Kammer ist anders ausgelegt, und die relevanten Parameter können auf verschiedene Arten gemessen werden. Daher werden Untersuchungsmethoden benötigt, die es ermöglichen, die relevanten Wachstumsparameter zu identifizieren und genau einzustellen um somit die gewünschten Schichteigenschaften zu erzielen.

Diese Arbeit beschreibt eingehende Studien zu Metalloxidfilmen, die mit einem kombinierten PLD- und oberflächenwissenschaftlichen Ansatz hergestellt und charakterisiert wurden. In den betrachteten Fällen bestand das Ziel jeweils darin, einkristalline Filme mit vollständig charakterisierten Oberflächen zu synthetisieren, die sich in weiterer Folge für grundlegende oberflächenphysikalische und -chemische Untersuchungen eignen.

Oberflächenwissenschaftliche Analysemethoden, insbesondere die Rastertunnelmikroskopie (Scanning Tunneling Microscopy—STM), wurden verwendet, um die Ursachen für das stark parameterabhängige Wachstum von In_2O_3 (111) zu untersuchen—einem transparenten leitfähigen Oxid, das in der Katalyse und Gassensorik zum Einsatz kommt—sowie von $SrTiO_3$(110) und $La_{1-x}Sr_xMnO_3$(110), beides Perowskitmaterialien, die als Katalysatoren in Festoxidbrennstoffzellen verwendet werden. Im Fall von In_2O_3 wurde festgestellt, dass die durch die Wachstumsbedingungen beeinflusste Sauerstoffstöchiometrie der abgeschiedenen Spezies die Oberflächendiffusion und damit die Schichtmorphologie stark beeinflusst. Sowohl $SrTiO_3$ als auch $La_{1-x}Sr_xMnO_3$ zeichnen sich durch eine Vielzahl von Oberflächenrekonstruktionen aus, welche wiederum direkt von der chemischen Zusammensetzung abhängen. Für beide Systeme zeigte sich, dass sich die unter suboptimalen Wachstumsbedingungen eingeführten Nichtstöchiometrien an den Oberflächen der Schichten akkumulieren und es somit zu einer änderung der Oberflächenstruktur kommt. Diese Veränderungen stellten sich als die Ursache für die Ausformung unerwünschter Schichtmorphologien heraus; es wird vermutet dass dies allgemein für Perowskitoxide gilt. Es wird gezeigt, wie die in dieser Arbeit hergeleiteten Beziehungen zwischen Nichtstöchiometrie, Oberflächenmorphologie und Oberflächenstruktur verwendet werden können, um das Filmwachstum zu optimieren und somit stöchiometrische, volumsartige und atomar flache Filme zu erzielen.

Eine Vielzahl komplementärer oberflächensensitiver Methoden wurde verwendet, um die atomare Oberflächendetails der optimierten Filme eingehend zu charakterisieren. Der Schwerpunkt lag hier auf $La_{1-x}Sr_xMnO_3$(110): Die Oberflächenrekonstruktionen dieses Materials wurden hier zum ersten Mal beschrieben und in zwei Gruppen kategorisiert. Ein experimentelles Oberflächenphasendiagramm, zweidimensional als Funktion des chemischen Potentials von Sauerstoff und der Kationenzusammensetzung, wurde erstellt. Derselbe Ansatz wurde verwendet, um die Oberflächen des leichter zu zie-

henden TiO_2(001)-Anatas und von Ti-dotiertem $Fe_2O_3(1\bar{1}02)$ zu charakterisieren. Diese beiden Systeme sind als Katalysatoren für die fotoelektrochemische Wasserspaltung interessant. Im Fall von Ti-dotiertem $Fe_2O_3(1\bar{1}02)$ und $La_{1-x}Sr_xMnO_3(110)$ wurden die experimentellen Messergebnisse durch—von Kollegen durchgeführte—*ab-initio* Computermodellierungen ergänzt.

Die Bedeutung der Synthese und Untersuchung von Modellsystemen in Form wohlcharakterisierter einkristalliner Oberflächen zum Verständnis chemischer Reaktionen wurde durch Versuche zum Sauerstoffeinbau auf den Oberflächen von $SrTiO_3(110)$ und $La_{1-x}Sr_xMnO_3(110)$ veranschaulicht. Obwohl dieser Einbau von Sauerstoff als Schlüsselprozess in Festoxid-Brennstoffzellen betrachtet wird, sind die genauen Mechanismen, welche diesem zu Grunde liegen, nur wenig bekannt. Die Verwendung von wohldefinierten Modellsystemen hat es ermöglicht, diesen Prozess genauer zu beleuchten und zugleich die entscheidende Rolle der Konfiguration und Koordination von Oberflächenatomen hervorzuheben.

Contents

List of Tables

List of Figures

List of acronyms

Exp. methods	UHV	Ultra-High Vacuum
	PLD	Pulsed Laser Deposition
	UV	Ultra-Violet
	TEM	Transmission Electron Microscopy
	XRD	X-Ray Diffraction
	RBS	Rutherford Backscattering Spectrometry
	RHEED	Reflection High-Energy Electron Diffraction
	LIF	Laser-Induced Fluorescence
	STM	Scanning Tunneling Microscopy
	AFM	Atomic Force Microscopy
	LEED	Low Energy Electron Diffraction
	XPS	X-Ray Photoelectron Spectroscopy
	LEIS	Low-Energy Ion Scattering
	QCM	Quartz-Crystal Microbalance
	MBE	Molecular Beam Epitaxy
	IR	Infra-Red
	ICP-MS	Inductively Coupled-Plasma–Mass Spectrometry
	TPD	Temperature-Programmed Desorption
	ToF-SIMS	Time-of-Flight Secondary-Ion Mass Spectrometry
Theor. methods	DFT	Density Functional Theory
	VASP	Vienna Ab-initio Simulation Package
	FPMD	First-Principles Molecular Dynamics

Materials	TMO	Transition Metal Oxide
	YSZ	Yttrium-Stabilized Zirconia
	LSMO	$La_{1-x}Sr_xMnO_3$, lanthanum–strontium manganite
	ITO	Tin-doped In_2O_3
Other	RT	Room Temperature
	PEC	PhotoElectroChemical
	p_{O_2}	Oxygen pressure
	μ_O	Oxygen chemical potential
	V_O	Oxygen vacancy
	ML	Monolayer
	APDB	AntiPhase Domain Boundary
	SOFC	Solid-Oxide Fuel Cell

1. Introduction

Metal oxides, their surfaces, and the promises of PLD

Metal oxides are a rightly popular class of materials. Not only are they ubiquitous in everyday life,[1] they also show a staggering range of tunable physicochemical properties, both, in their bulk, and at their surfaces and interfaces. It is an understatement that some of the most interesting electronic, magnetic, optical, and catalytic properties are found in this class of materials.[2] The class of transition metal oxides (TMOs), largely explored within this Thesis, is particularly intriguing: TMOs can be metallic, insulating, (anti)ferro/paramagnetic, ferroelectric, piezoelectric, high-temperature superconductors, multiferroic, topological insulators, catalytically active or completely inert, and they can exhibit colossal magnetoresistance and metal-to-insulator transitions depending on their exact stoichiometry and/or the environmental conditions. Such properties are being used in a diverse range of integrated technologies, in heterogeneous catalysis, and clean-energy production.[3–6]

The surface properties of metal oxides are crucial for most applications: It is at surfaces that the most relevant reactions, processes, and interactions that largely drive applications take place. The so-called surface science approach is well-suited to model these surface processes. It relies on single-crystalline materials with well-defined physical properties and atomically controlled surfaces, which are explored in ultra-high vacuum (UHV). Surface science studies over the last decades have shown that the atomic-scale properties of surfaces can differ greatly from those of the bulk. Because of the symmetries broken by the surface,[7] surface atoms typically rearrange in so-called surface reconstructions, which are characterized by specific arrangement, coordination, electronic and/or magnetic structure of the surface atoms. Metal oxides tend to exhibit a variety of complex surface reconstructions, which may be affected by both, the cation, and the oxygen composition. Additionally, metal oxides tend to show point defects (*e.g.*, oxygen vacancies or cation interstitials) whose concentration depends strongly on the preparation conditions.[8] The specific details of the surface reconstructions and of point defects influences greatly surface processes.[9–11] Hence, the precise control over the sur-

face properties offered by surface science is of extreme value for modeling surface processes reliably.

While surface science relies on single-crystalline samples, these are not always available, and they can be otherwise impure, too small, insulating, or too expensive. In such cases, bulk-like epitaxial thin films offer a sound alternative. Pulsed laser deposition (PLD) stands out among the available deposition techniques capable of producing these films. In PLD, a ultra-violet (UV) laser focused down to a high energy density 'vaporizes' a small portion of a target. The ablated material, containing a variety of atomic, molecular, and excited species, travels through a background gas (O_2, for oxides) in the form of a plasma plume, and finally condenses on a heated substrate. Under optimal conditions and appropriate lattice matching, the deposited species follow the crystalline template of the substrate: Epitaxial films are grown. PLD has key advantages for the growth of controlled oxide films. Provided that a target is available, arbitrarily complex, multi-element materials can be grown; an array of deposition parameters can be used to tune the physicochemical properties of the films; it provides a shot-to-shot (sub-monolayer) control over deposition; thanks to its high instantaneous fluxes, kinetically limited 2D growth is favored even for those systems that would grow in a 3D fashion at close-to-equilibrium conditions. These factors, in principle, allow complex materials to be grown in the form of single-crystalline films with atomically controlled surfaces that are suited for surface science investigations.

Oxide PLD in the literature

The many advantages of PLD have attracted interest from various research fields besides surface science. Remarkably, PLD has been employed to realize atomically controlled thin-film heterostructures of complex, multi-element metal oxides. These studies have been motivated by the exotic properties that can arise by coupling strongly correlated materials at atomically precise interfaces,[6,12–14] and by the ever-growing demand of downscaling devices. Numerous properties unseen in bulk oxides have been discovered at oxide interfaces fabricated by PLD—among others, novel electronic,[15–21] magnetic,[13,22–25] ferroic,[26,27], and ionic properties.[28] Transmission electron microscopy (TEM) images[13] have testified to the remarkable quality of some of these heterostructures, which is becoming comparable to that of semiconductor superlattices.

The atomic-scale control achieved in the works discussed above is more the exception than the rule in the vast community of oxide PLD. Most commonly, oxide PLD focuses on the optimization of technologically relevant processes, by using films with thicknesses of a few tens of nanometers and ill-defined morphologies. Often, the PLD parameters are modified until the desired outputs are achieved, generally following a trial-and-error

approach. This approach is taken to the extreme by combinatorial methods, typically applied to multi-element materials with doping-dependent phase diagrams. By fabricating so-called composition spreads,[29] *i.e.*, oxide films of continuously varying composition, these methods yield high-throughput exploration[30] of composition-dependent material properties. To this end, one can either alternate between two targets with doping levels at the opposite ends, or exploit the dependence of the film's properties on the PLD parameters that is discussed below. Among others, composition spreads of Mott insulators,[29] magneto-electric composites,[31] dielectrics for microwave applications,[32] and ferroelectrics[33] have been fabricated. These approaches are best suited to quickly provide composition–property maps, and push new technologies in the right direction. They do not focus on understanding the physics of the PLD processes, or achieving the degree of perfection needed for fundamental investigations.

The importance of the PLD parameters

Extending the degree of control that is now mastered for ultra-thin-film heterostructures to bulk-like oxide films of a few tens of nanometers would enable many fundamental, surface science studies on previously unexplored systems. As argued above, a tight control over the sample composition and of the surface atomic properties is essential for reliable computational modeling of the surface processes of interest. So far, however, the control over the PLD process and PLD parameters has been insufficient to achieve this goal. This is largely because many of the film's properties depend strongly on many deposition parameters. These parameters include, but are not limited to, the deposition geometry, the laser energy density, the oxygen background pressure, and the substrate temperature, which have been found to affect the physicochemical properties of the films through induced changes in thickness, composition, crystal structures, crystallinity, morphology, and even surface reconstructions.[34] Because all non-idealities become more pronounced with increasing thickness, bulk-like films of a few tens of nanometers are hard to realize. The challenge is greatest for multi-element oxides, whose different cations suffer from preferential ablation at the target (determined by the value of the laser fluence) and preferential scattering with the background gas.[34] However, also binary oxides, particularly their oxygen stoichiometry, can be influenced by the deposition parameters.[35] Controlling the films' properties is made even harder by the difficulties in reproducing PLD parameters in different setups: Every PLD chamber is designed uniquely, and the relevant parameters can be measured in various ways.[36]

Given the challenges listed above, it is clear that the desired bulk-like-quality oxide films can be achieved only upon establishing a precise correlation between PLD parameters and film properties. In fact, this has been already attempted by several tech-

niques. For instance, *ex-situ* techniques such as X-ray diffraction (XRD), Rutherford back-scattering (RBS), and TEM have been used to investigate the properties of the films as a function of the growth parameters, specifically their crystal structure and composition. XRD studies on the PLD reference system, the perovskite oxide $SrTiO_3$, have revealed that nonstoichiometry can be systematically introduced in the film by tuning the laser fluence, which causes detectable and correlated lattice expansions.[37–40] RBS analysis on other perovskite oxides have confirmed that there exists a very narrow window of parameters yielding stoichiometric transfer.[41] While insightful, these techniques suffer from a few limitations: In XRD, significant uncertainties exist in establishing a universal relation between nonstoichiometry and lattice expansion.[38] Both RBS and TEM are destructive. Moreover, RBS relies on appropriate modeling of the measured spectra,[42] while sample preparation in TEM can affect significantly the measured compositions.[43,44] Finally, the compositional detection limit of all these techniques is in the order of a few percent,[34] far above the needs of computational modeling.

The correlation between PLD parameters and film properties has also been sought after by a few *in-situ* techniques, which have proven useful to better control the growth itself. One prominent example is reflection high-energy electron diffraction (RHEED). Not only can RHEED spectra yield qualitative information about the crystallinity of the surface of the growing film (2D vs. 3D character).[45] Quantitative information can be drawn by monitoring the intensity of the specular RHEED reflection, particularly within the layer-by-layer growth regime—where a new layer develops only after the completion of the previous one. This growth regime allows accurate measurements of deposition rates, and lends itself to theoretical modeling, which can be used to derive diffusion barriers, step densities, and information about nucleation of the deposited material.[45,46] RHEED can also be used to monitor changes in the surface reconstruction during growth. Studies on the homoepitaxial growth of $SrTiO_3$(001) have revealed that its reconstructions can exhibit significant changes, even within the optimum growth window previously established by XRD,[47] and that such changes can be used as a sensitive measure of the film stoichiometry.[47,48]

Other *in-situ* techniques, such as ion probes,[49] mass spectrometry,[50,51] time and space resolved imaging,[52] and laser induced fluorescence (LIF),[53,54] have been used to gain fundamental insights about plume effects as a function of the growth conditions, aiming at rationalizing the best deposition conditions. This is a challenging task: The plasma plume is characterized by a complex mix of species, including neutrals, positive, and negative ions—all of which can be in either excited or ground states—plus diatomics and clusters. The composition, shape, and energetics of the plasma plume results from the interaction of its species. This is affected strongly by many PLD parameters, and will

largely determine the macroscopic properties of the film.[34] LIF studies on $SrTiO_3(001)$[55] have demonstrated the value in building fundamental knowledge on the plasma plume. By yielding a spatiotemporal mapping of the plasma constituents, LIF allows to trace the underlying dynamical and chemical processes, such as the propagation and oxidation of the most relevant plasma species, for example as a function of the oxygen background pressure. The study has been able to link the oxidation of plasma species to the stoichiometry and quality of the thin films grown, giving new inputs to modeling surface growth.

All the techniques presented above can provide valuable information to correlate film properties and PLD parameters. However, they all lack a crucial ability: To address the role of the surface atomic details during growth. After all, it is at the surface that the growth takes place. RHEED studies have already revealed that the surface reconstructions of the developing films evolve as a function of the nonstoichiometry introduced during growth. As already known from combined molecular beam epitaxy (MBE) and atomically resolved scanning tunneling microscopy (STM) studies on metals and binary oxides,[56] such changes in the surface atomic details can have a critical impact on the growth itself: Nucleation during the first stages of growth, diffusion properties as a function of the growth conditions, the atomic details of the surface reconstructions, and surface defects can all influence greatly the final morphology. Hence, the much-needed optimization of the PLD parameters must go hand in hand with detailed investigations of the evolution of the surface structures and morphologies during growth. Atomic-force microscopy (AFM) studies have repeatedly shown the strong influence that the PLD parameters can have on the film's morphology.[57–60] However, the influence of, and/or correlation with the atomic-scale details has not been addressed yet.

Combining PLD with surface science

As testified by the MBE studies mentioned above, scanning probe microscopies with atomic resolution such as STM are best suited to address the role of the atomic details of the surface on the growth. Nonetheless, PLD is rarely interfaced with STM, taken few exceptions.[61–64] This is partly because interfacing PLD with STM requires the whole PLD process to fulfill stringent conditions on chemical purity, and this is technically challenging. Hopefully this Thesis work shows that PLD *can* be successfully combined with atomically resolved STM, and to one's advantage. In the apparatus used within this Thesis, the PLD chamber is connected in vacuum with a full-blown surface science facility that includes STM, allowing the atomic-scale structure of films grown by PLD to be investigated without air exposure. Importantly, the STM analysis is complemented with structural and elemental studies offered by low-energy electron diffraction (LEED),

X-ray photoelectron spectroscopy (XPS) and low-energy ion scattering (LEIS) present in the same system. When combined together, these techniques offer a unique and powerful opportunity to study and establish the atomic-scale mechanisms behind oxide growth by PLD. As this Thesis shows, such studies have revealed that changes in stoichiometry, surface structures, and surface morphology in oxide films grown by PLD are correlated. These changes are informative about the effect of the growth parameters, and predictive of the film's evolution. The knowledge built with surface science is functional to tweak the PLD parameters in the right direction, and obtain high-quality metal-oxide films with the desired properties. Once these ideal films are fully characterized, they can be used as model systems to shed light on important surface processes.

1.0.1 Outline of the Thesis

This Thesis elaborates on the aspects above. Before jumping to the results, the experimental setups and techniques will be introduced in more detail in Chapter 2. This Chapter also assesses the influence of various experimental parameters on PLD growth, with emphasis on how to control them while meeting UHV surface science needs. Chapter 2 also describes a newly designed holder for a movable quartz-crystal microbalance (published in ref. 65), which can be used to precisely measure cation doses deposited in PLD from oxidic targets.

The Chapters to follow, to be shortly introduced, focus on the growth and the atomic-scale surface characterization of a variety of oxide films. In many instances, aims were to produce single-crystalline films as a replacement for bulk single crystals, and to establish a model for their surface structures with support from density functional theory (DFT). The final goal, realized for some of the systems, was to use the films as model systems to investigate technologically relevant processes and reactions at a fundamental level. Along the way, the Thesis addresses the dependence of the films' properties (mainly their composition, morphology, and surface structures) on the PLD parameters and on the evolving properties of the films themselves, and shows how STM can be used to exactly measure these changes and tweak the PLD parameters in the right direction. Because each oxide material has unique properties and areas of application, a short introduction about the system and the study is presented at the beginning of each Chapter. In many cases, it is also outlined whether and how members of the TU Wien surface science group and/or external collaborators have used the films for their individual lines of research. The final Chapter 11 complements the studies on oxide growth by PLD, addressing the crucial role of the oxygen chemical potential on oxide surface diffusion and film morphology, based on collected results from a few systems presented in this Thesis.

With each Chapter, the level of complexity is gradually built. The first Chapters 3–5 deal with the 'simple' class of binary oxides, generally less sensitive to the PLD parameters than multicomponent ones.[34] Chapter 3 starts simplest, showing how the growth of high-quality anatase TiO_2 films on $SrTiO_3(001)$ single crystals was reproduced, using already optimized growth parameters.

Next, Chapter 4 addresses the growth of Ti-doped hematite (Fe_2O_3) films with $(1\bar{1}02)$ orientation. It discusses how dopants can be introduced and tuned finely during an otherwise-trivial growth experiment, and showcases the prowess of combining PLD with surface science to build a reliable model system for fundamental investigations. These results have been published in ref. 66.

Chapter 5 focuses on the growth of In_2O_3. Despite In_2O_3 being a binary oxide, like the previous ones, and despite the good lattice match of the unit cell of In_2O_3 with the substrate used [(111)-oriented yttria-stabilized zirconia (YSZ)], achieving films of single-crystalline quality proved not to be as easy. The reason lies in the (strong) effect that the growth conditions have on the oxygen stoichiometry and diffusion of the surface indium species. The results, published in ref. 67, show that under no conditions can atomically flat films be achieved, unless two different sets of parameters yielding, respectively, kinetically limited and close-to-equilibrium growth are combined in the same growth recipe.

If the case of In_2O_3 already shows the potentially dramatic effect of the growth parameters on the surface morphology of oxide films, Chapter 6 does nothing but reinforcing the message. Focused on $SrTiO_3$, it kicks off a cascade of Chapters on perovskite oxides (for their relevance in this Thesis and elsewhere, the structural family of perovskite oxides is briefly introduced in Chapter 6). The deceivingly trivial homoepitaxial growth of $SrTiO_3(110)$ is discussed, which showcases the intrinsic challenges in achieving ideal film stoichiometries and morphologies in complex multicomponent materials. The results, published in ref. 68, demonstrate that changes in the film composition and in the surface morphology are correlated, the link being the atomic details of the surface itself, or, more specifically, its sticking properties. One key message is that atomically flat films can only be achieved if a correlation between growth parameters and changes in the surface structures is established, such that the surface structures are controlled at each stage of the growth. Chapter 7 shows a newly developed method to do so, which has been published in ref. 69. By looking at the surface structures with STM, and by correlating their change to a change in composition from the known surface phase diagram of $SrTiO_3(110)$, it is possible to deduce tiny (below 0.1%) nonstoichiometries introduced during growth, and adjust the growth parameters accordingly. It is argued that with this method, complex oxide materials can be reproducibly prepared with exceptionally small

cation concentrations.

The knowledge and the methods built up for the 'simple' case of $SrTiO_3$(110) homoepitaxy were then applied to a more complex perovskite oxide: $La_{1-x}Sr_xMnO_3$, or LSMO. Chapters 8 and 9 reveal the many commonalities between (110)-oriented LSMO and $SrTiO_3$. Also LSMO(110) displays various composition-related surface reconstructions, and these appear with different growth parameters and affect the growth. Chapter 8 presents a systematic investigation of the surface reconstructions, which are summarized in a quantitative surface phase diagram as a function of both, the cation composition, and the oxygen chemical potential, μ_O. Built on this knowledge are the growth studies presented in Chapter 9, which investigate the correlation between nonstoichiometry, surface morphology, and atomic-scale structure of LSMO films grown on $SrTiO_3$(110), the goal being to produce stoichiometric and atomically flat films. These are obtained by applying the STM-based method developed for $SrTiO_3$(110) in Chapter 7. These results are collected in ref. 70 and other manuscripts in preparation.

Optimizing the growth parameters for, and characterizing the surfaces of, LSMO films has not been only functional to showcase the role of the PLD parameters on the growth of complex perovskite oxides. Bulk-like LSMO films with single-crystalline, well-characterized surfaces are the perfect system to gain a fundamental understanding of technologically relevant reactions occurring at LSMO surfaces. Chapter 10 addresses one such reaction, *i.e.*, the incorporation of oxygen at the LSMO surface, in the context of better understanding the functioning, and optimizing the operation, of solid-oxide fuel cells. Before approaching the problem on LSMO, we have focused on its less complex (and more established) relative, $SrTiO_3$, investigating both Nb-doped and undoped single-crystals with exactly controlled surface terminations (these works are published in ref. 71, and are being prepared for submission, respectively). In all cases, it is shown that the details of the surface reconstructions matter, and, to one's surprise, they matter even more than commonly accepted factors such as the availability of oxygen vacancies or electrons.

The full list of publications (both published and in preparation) that have arisen from this Thesis is reported at the end of the Thesis.

2. Experimental methods

This technical Chapter describes the setups, techniques, procedures, and experimental details that underlie the experiments presented in this Thesis. First, the UHV apparatus that has hosted most experiments is introduced. Figure 2.1 shows that it is composed by two main parts that are connected in UHV: The so-called SPECS setup (from the company name, SPECS GmbH), with a plethora of surface science techniques that were used to prepared and characterize the samples, and the PLD chamber, mainly used to grow the films. These two parts are the focus of Sections 2.1 and 2.2, respectively. Section 2.3 gives then an overview of the most notable PLD parameters, highlighting some technical aspects that enable to interface PLD with surface science. Section 2.4 provides details about sample mounting and how insulating samples were contacted, while Section 2.5 presents a newly developed design for a movable holder for a quartz-crystal microbalance (QCM), which enables precise measurements of PLD growth rates without breaking vacuum. The final Section 2.6 briefly describes the *ex-situ* techniques that have been employed to characterize the films.

2.1 Surface analysis setup

The SPECS setup is a surface science UHV apparatus composed from two interconnected chambers: The preparation chamber, to clean the samples (via sputtering and annealing) and tune the surface composition (by molecular beam epitaxy, MBE), and the analysis chamber, used to characterize samples. The base pressure in the chambers after bake out is below 5×10^{-11} mbar. Both chambers are equipped with residual gas analysis (quadrupole mass-spectrometer RGA SRS100), and electron beam annealing (up to 1 000 °C, with 900 V, 15 mA), with a pyrometer (Impac IGA5) to monitor the sample temperature.

Samples are introduced into the preparation system through a loadlock, and are cleaned through cycles of Ar^+ sputtering and annealing. Annealing can be performed in O_2, via leak valves for gas dosing (up to 10^{-4} mbar). Sr and Ti metal evaporators are

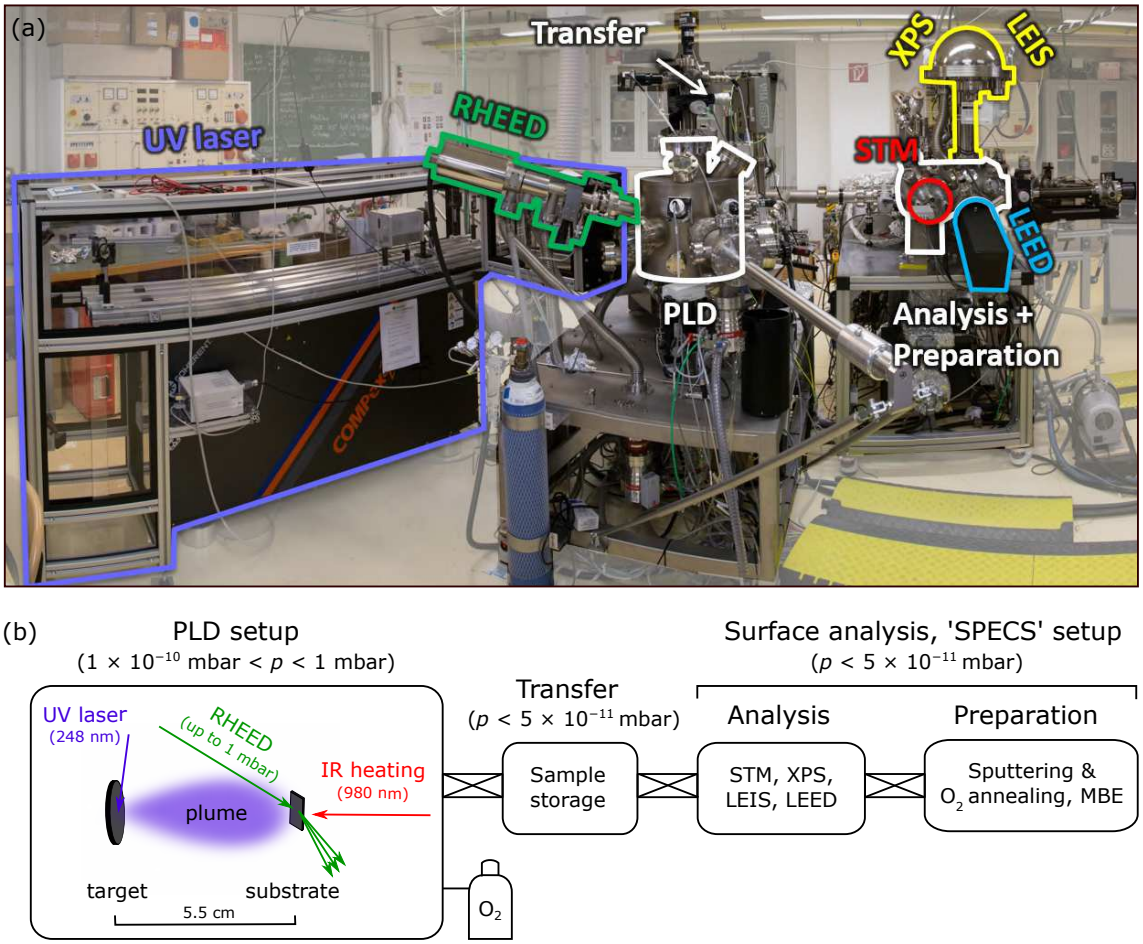

Figure 2.1. (a) Photograph of the experimental setup, composed of a PLD facility connected in vacuum via a transfer chamber to a surface science facility, comprising an analysis and a preparation chamber. (b) Schematic view of the experimental setup, highlighting the sample preparation and analysis techniques.

used to tune the surface reconstructions of $SrTiO_3$ substrates (details in Chapter 6). Ti metal is deposited from an electron-beam evaporator (EFM 3, FOCUS GmbH), while Sr metal is deposited from a low temperature effusion cell at 420 °C (LTC-40-10-284-WK-SHM, CreaTec Fischer & Co. GmbH). In all cases, material evaporated in UHV expands from the source and condenses on the substrate, held at RT. The flux is calibrated via a home-built QCM mounted on a linear feedthrough, positioned in close proximity of the sample, and operated at elevated temperature (90–100 °C).

The analysis chamber is equipped with LEED from Omicron (SpectaLEED), LEIS from SPECS (IQE 12/38 ion source with Wien filter, scattering angle 132°), STM (SPECS Aarhus 150 STM, operated at RT and in constant current mode), and XPS. The XPS setup consists of an X-ray source (Omicron DAR400) with dual anode (Mg an Al), producing Kα lines at, respectively, 1253.60 eV and 1486.61 eV for Mg and Al (300 W, 15 kV, sample current ≈120 nA), and a SPECS Phoibos 100 hemispherical analyzer (HSA) with 5-channel detector. Details about the LEIS and XPS settings are reported in Appendix A.

2.2 PLD setup

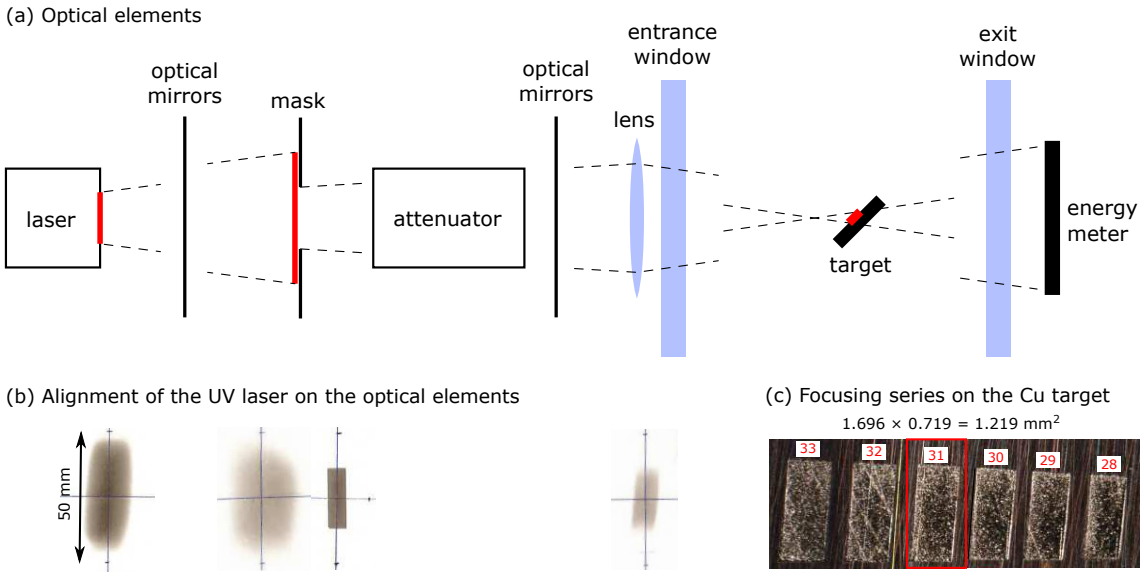

Figure 2.2. (a) Sketch of the optical elements of the UV laser system, including a series of optical mirrors, a lens for focusing on the target, a mask to cut the inhomogeneous part of the beam, and a programmable attenuator to change the pulse energy. An energy meter is placed outside of the exit window, to measure the pulse energy. (b) UV laser spots as imprinted on thermal paper placed in front of the optical elements. The spots are always centered with respect to the corresponding optical element. The mask lets through the central (and homogeneous) part of the beam. (c) Focusing series performed on the Cu target in vacuum: Each spot corresponds to a different lens position (reported on top of the spots). The lens position was set to the one giving the most uniform and regular spot (highlighted by the red rectangle), whose dimensions are reported on top.

The PLD system, combined with reflection high-energy electron diffraction (RHEED) analysis, is from Twente Solid State Technology B.V., and it is mainly controlled by a software from TSST B.V. on a PC, combining all input and output signals, and operational features such as growth recipes and signal logging.

A sketch of the UV laser system is reported in Fig. 2.2(a). The UV laser light [Coherent COMPexPro 205F, wavelength 248 nm (KrF excimer laser), pulse duration 20–50 ns, pulse-to-pulse standard deviation of the beam energy better than 0.6%] bounces through a series of optical mirrors and is focused onto the targets through a lens. An attenuator module (Coherent MicroLas) allows to set the beam energy. The energy density on the target is set by measuring the energy of the UV beam in front of the exit window of the PLD chamber (outside of vacuum, with a Coherent EnergyMax USB meter), taking into account the attenuation of the UV light by the lens and the entrance window (both situated before the targets), and of the exit window (the total attenuation by the lens, entrance and exit window amounts to ≈23.6% when no material is deposited on the windows). A mask placed before the attenuator, and in the central part of the beam, cuts its inhomogeneous part and creates a top-hat beam profile. The distance of the mask

to the focusing lens determines the demagnification of the UV beam (factor of ∼10). Up to five targets can be mounted on the detachable target carousel, and the target-to-substrate distance is fixed to ≈55 mm. The targets can be automatically scanned in the laser beam, such that their full area is ablated.

An infra-red (IR) laser is used to heat the samples. It shines directly onto the back of the sample through a hole in the sample plate. Gases (O_2, Ar, N_2) can be introduced into the PLD chamber through a gas line. The accessible and regulated pressure range extends from low 10^{-6} mbar up to 5 mbar. Mass flow controllers (Brooks instruments) allow for pressure regulation (upstream control, at p < 0.1 mbar). Filters (Swagelok) protect the mass flow controllers from small particles (minimum 500 nm diameter). Gas purifiers (SaesGetters) deliver gases with the following nominal purity: < 100 ppt for H_2O and CO_2, < 1 ppt for volatile acids, organics, and refractory compounds, < 5 ppt for volatile basis.

RHEED was used for real-time monitoring of thin film growth. In case of layer-by-layer growth, real time RHEED oscillations allow one to determine the amount of deposited material, as one oscillation corresponds to the deposition of one monolayer. A differentially pumped TorrRHEED gun allows to study RHEED oscillations in up to 1 mbar O_2 pressure. RHEED oscillations are measured by tracking the intensity of the specular RHEED spot with a kSA400 acquisition system (camera integration time 16 ms). Prior to each deposition, the intensity of the specular spot is maximized by adjusting the tilt of the substrate with respect to the incident RHEED beam. This procedure results in the in-phase condition of diffraction, where beams from neighboring terraces constructively interfere, and the modulation of the specular RHEED spot is dominated by the scattering of electrons by surface steps, *i.e.*, its intensity relates to the step density within the coherence length of the electron beam. The resulting RHEED geometry is in the order of 0.6° grazing incidence of the electron beam. It is worth mentioning that the RHEED gun is surrounded by a home-designed μ-metal housing, to screen external magnetic fields, which would modify electron trajectories.

The PLD chamber is connected in UHV to the analysis system via a transfer chamber, which also hosts a sample storage system. The transfer between the PLD and the analysis chamber is very rapid—about 30 s—and allows to analyze freshly grown samples, which are always kept in a controlled environment. The PLD and the transfer chamber base pressures were respectively below 1×10^{-10} mbar and 5×10^{-11} mbar after bake-out. It should be mentioned that the base pressure of the deposition chamber after repeated growth in up to 1 mbar O_2 background pressure rises to about 1×10^{-9} mbar, with H_2, H_2O, O_2, and CO_2 being the main components of the residual gas.

In October 2018, the vessel of the PLD chamber was replaced with a home-designed

μ-metal chamber, to better screen electromagnetic fields that disturb the RHEED measurements, and to implement a few improvements (details in Appendix C).

2.3 PLD parameters and procedures

As alluded to in Chapter 1, the instantaneous deposition by PLD is controlled by many parameters. Some of these are the background pressure and composition, UV laser pulse duration and beam divergence, ablation area on the target, target-to-substrate distance and alignment, substrate temperature, ablation target and preablation. Each of these can affect the growth mode, the composition, and the morphology of the films. The picture gets further complicated because of the intrinsic challenges in reproducing PLD parameters in different setups: Every PLD chamber is designed uniquely, and the relevant parameters can be measured in various ways. Nevertheless, this Thesis shows that once the relevant parameters are identified, they can be tuned precisely to achieve the desired film properties, even down to the atomic scale. The following Sections present a detailed overview of the parameters that play an important role in PLD. Emphasis is put on how to control them while trying to interface pulsed laser deposition of oxide films with UHV surface science needs.

2.3.1 Background gas

By tuning the value of the pressure of the background gas introduced in the PLD chamber during the growth, one can moderate the energy of the ablated species via scattering events[72] and tweak the film composition.[73] The following (simplistic) model depicts correctly qualitative trends of the film composition with the oxygen pressure:[41,52,74] At sufficiently low pressures, the ablated material is transferred congruently to the substrate, because the mean free path of the plasma species is larger than the target-to-substrate distance. In some intermediate range of pressures, the ejected species interact differently with the background gas molecules depending on their mass: Lighter species are scattered more than heavier ones, with non-trivial interactions between the ionized species in the plasma plume. Within this intermediate regime, the film will be enriched with the heavier species as the pressure increases.[41] At very high pressures, in the so-called shock-wave regime, all species are slowed down equally and kept confined, and are transferred congruently from target to substrate. Notice that these three pressure regimes cannot be identified with the value of the oxygen pressure alone, as the target-to-substrate distance (D) can also affect the transfer of material from target to substrate.[58] For the deposition of LSMO films within our apparatus (D = 55 mm), the

low-, intermediate, and high-pressure regimes are found at $p_{O_2} \leq 5 \times 10^{-3}$ mbar, $5 \times 10^{-3} \leq p_{O_2} \leq 0.2$ mbar, and above 0.2 mbar, respectively (more details in Chapter 9).

For oxides, O_2 is used as the background gas. This helps to achieve the correct oxygen stoichiometry in the film, by compensating the preferential sputtering of surface oxygen atoms from the energetic impinging cations.[72] Chapters 5 and 9 will show how the oxygen background pressure affects the growth of In_2O_3 and LSMO films, respectively. In the case of In_2O_3, the value of the oxygen pressure determines the oxidation state (hence the diffusivity) of the indium species that land and diffuse on the growing film. For a multicomponent oxide such as LSMO, the oxygen background pressures affects not only the oxygen, but also the cation stoichiometry. It will be shown how the film morphology is affected in both cases.

2.3.2 Laser pulse properties

The properties of the laser pulses (duration, beam divergence, pulse energy and energy density, pulse-to-pulse standard error, absorption at the target surface, repetition rate) are crucial for PLD. To achieve an efficient ablation of the target, the nonequilibrium excitation of the ablated volume must occur at temperatures well above the ones required for evaporation. This generally requires the laser pulse to be short in duration (100 fs–100 ns), high in energy density (0.5–20 J/cm^2), and highly absorbed by the target material. The apparatus used within this Thesis allows for pulse durations and energy densities in the ranges of 20–50 ns and 1.0–4.0 J/cm^2, respectively.

Laser fluence

The laser energy density, or laser fluence, is an especially critical parameter for multielement compounds: One element or another in the compound may be ablated preferentially depending on the value of the laser fluence, yielding a film correspondingly enriched in one component. Chapters 6 and 7 will show that stoichiometric transfer of a multicomponent oxide such as $SrTiO_3$ is only achieved upon finely tuning the laser fluence (together with the other parameters discussed in this Section). This effect is not present for binary oxides: Their composition is largely unaffected by the value of the laser fluence. Besides influencing the composition of the film via preferential ablation, the laser fluence also determines the amount of material deposited per pulse, and the energy of the ablated species.[34] Both effects may influence the growth, but they have not been investigated systematically within this Thesis.

The laser fluence on the target is determined by the pulse energy and by the ablation spot area on the target. The pulse energy can be adjusted in two ways: (i) changing

the discharge voltage of the laser, which causes a change in beam divergence and pulse duration, in turn leading to a change in the effective fluence at the target (for the same measured fluence); (ii) passing the beam through a programmable attenuator [as in this Thesis, see Fig. 2.2(a)]. The second option has the advantage of changing the pulse energy without affecting beam divergence and pulse duration.

The pulse energy on the target is measured with an energy meter, which accounts for the optical losses that the laser encounters on its path from the meter to the target. Within this Thesis, the pulse energy was measured in correspondence of a quartz window placed after the target [exit window, in Fig. 2.2(a)], so that the optical losses consist of the transmittivity of the exit window. It is not desirable to measure the pulse energy at the entrance window [before the target, see Fig. 2.2(a)], unless a shutter protects it during the deposition experiments: If a shutter is not present, the entrance window gets covered with deposits in an unpredictable way, and the optical losses cannot be accounted for correctly (notice that, instead, the transmittivity of the exit window is constant over time, because too far away from the plasma plume).

Since the laser fluence is given by pulse energy divided by the ablation spot area, the latter should be well known and controlled. Uniform and focused spots of known area are essential for reproducible experiments. Section 2.3.3 details how the UV laser spot was aligned and focused. The spot area is measured by directing the UV laser onto a polished, polycrystalline Cu target held in the target carousel and placed at the same focal distance of the other ablation targets. The spot size is measured outside vacuum via an optical microscope (a proper grid is used to set the right scale), and then evaluated via the software ImageJ.[75] This approach is UHV friendly as opposed to the wide-spread spot-size determination that involves firing the UV laser on a sheet of thermal paper mounted in the chamber at the target position.

It is worth mentioning that the UV laser ages over time, both causing a progressive decrease of the maximum pulse energy, and a higher pulse-to-pulse standard deviation. After roughly two weeks of almost every day use, the pulse-to-pulse standard deviation rised from ≈0.30% to above 0.60% of the average pulse energy. The material transfer is affected: For example, for $SrTiO_3$, an aged UV laser gas results in a Sr-richer growth (refer to Chapter 6 for further details). For this reason, the laser gas was always exchanged after two weeks of use.

Laser repetition rate

The laser repetition rate can affect the growth mode, the morphology, and even the composition of the films. For example, it was shown that the laser repetition rate can change the growth mode of $SrTiO_3$(110) from layer by layer to step flow,[76] and that $SrRuO_3$

thin films can show large Ru deficiencies with higher repetition rates, probably due to the preferential formation of volatile RuO_4.[77] In most experiments described within this Thesis, the laser repetition rate was set to 1 Hz. The influence of this parameter was not addressed systematically.

2.3.3 Alignment and spot-focusing

The relative alignment between target, substrate, IR heating laser beam, UV laser, and exit window of the PLD chamber is critical to the reproducibility of the growth experiments. Both the substrate and the target were aligned with the IR heating laser beam by using a visible pilot laser collinear with the IR. After aligning the laser optics, the UV laser was centered on the target itself.

Alignment of the laser optics

To obtain the most uniform UV laser spot on the target, as a first step of the alignment one needs to center the beam with each optical component and make sure that the mask lets through the most uniform part. Since the UV laser used within this Thesis is not provided with a pilot laser, the alignment is done by hand. To do so, all components are roughly aligned by using a sheet of white paper. A fine alignment component by component is then performed with thermal paper: At each step, a squared piece of thermal paper is carefully centered with the optical element. Based on the position of the spot, the orientation of the previous mirror is finely adjusted to center the spot with the center of the optical element. In Fig. 2.2(b), a few of these spots are shown. It can be seen that the mask cuts the central (and most homogeneous) part of the beam, and that the laser spots are always centered with the optical elements.

Notice that the optics should be reasonably clean, because any particles lying on them will be burnt by the UV laser, thus reducing the reflectivity (transmittivity, for the lens) in a non-controllable way. For this reason, all the optics have been cleaned every year with a special lens cleaning tissue and pure isopropanol, and then dried by using CO_2, taking care of minimizing halos.

Alignment and focusing of the UV laser on the target

The UV laser is aligned with the center of the ablation target by directing it on the very ductile Cu target, which is held in the target carousel at the same focal distance as all targets. Examples of imprints left on the Cu target are shown in Fig. 2.2(c). To achieve the optimal alignment, the positions of the last mirror and of the lens are adjusted until

the imprinted feature is centered with the center of the Cu target (as seen from outside from a window port).

Once the beam is centered with all the optics, centered on the target and passing through the chamber to the exit window without any unexpected losses, it is optimally focused onto the target, to get the best possible spot in terms of uniformity, sharpness and shape. The Cu target is used once again for this purpose. The lens is moved 1 mm at a time, and, at each step, the laser is shot onto the target. The resulting focusing series is reported in Fig. 2.2(c). The movement of the lens corresponds to a change of the relative position of the target with respect to the focal distance of the lens itself. The optimal lens position is found by bringing the Cu target out of the vacuum, and analyzing the spots with an optical microscope. The optimal spot is the smallest, sharpest and most uniform, namely the spot labelled with 31 mm (position of the lens) in Fig. 2.2. To re-use the Cu target, it is polished with SiC paper and sonicated in aceton and isopropanol. It is then used for the fine alignment in accordance to the new position of the lens.

Importantly, whenever inserting a target in the vacuum through the carousel, care was taken that the distance between the surface of the target and the center of the carousel was unchanged, to make sure that the alignment of all the elements involved in the PLD process was not affected. As a further check, it was always made sure before the growth that the UV laser was still centered with the last area that was scanned. In stoichiometry-sensitive experiments, further care was taken towards small misalignments possibly changing the effective ablated area: After growth, one laser pulse was shot on a fresh surface on the used target, to measure the spot area outside vacuum, and to compute the effective fluence used in the specific experiment.

2.3.4 Substrate preparation

Another key factor to the successful growth of high-quality films is the substrate. Not only the lattice parameter of the substrate should nicely match the one of the growing film, as to avoid building unwanted stress in the film. Also the flatness of the surface, its purity, and even the atomic-scale details of the surface reconstruction matter to the film properties. Chapters 6–9 discuss in detail the effects of the surface reconstruction on the composition and morphology of $SrTiO_3$(110) and LSMO(110) films.

In most cases, prior to UHV preparation, the substrates were cleaned *ex situ* to remove residuals from the polishing remains. This step often consisted in sonicating the as-received samples in warm (≈60 °C) neutral detergent (3% Extran® MA02, hereafter simply referred to as Extran) and ultrapure deionized water (milli-Q®), sometimes followed by boiling in ultrapure water to dissolve calcium oxide contaminations. All glass-

ware used to clean the samples was previously boiled in 20% HNO_3 and thoroughly rinsed in ultrapure water. After these steps, UHV preparation followed. To limit any effect of the details of the substrate surface, the substrates' surface was always prepared in the same way for each set of experiments. STM (or atomic force microscopy, AFM, for insulating substrates), LEED, and XPS were consistently used to ensure that the surface was atomically flat, clean, and with the desired surface reconstruction (details about the specific substrate preparation recipes are given in the individual Sections).

2.3.5 Substrate temperature

The substrate temperature during growth is another key parameter. Put simply, high temperatures translate in high diffusion of the landing species, which can find their energetically favorable configuration. In the best-case scenario, the growth mode is step flow or layer by layer, and the surfaces grow flat and well ordered. However, if the thermodynamically stable configuration is three-dimensional islands (this is the case of In_2O_3, see Chapter 5), high temperatures will favour this trend. Notably, the value of the temperature determines the oxygen chemical potential, which can affect drastically the diffusion of the deposited species, and hence, the surface morphology (details in Chapter 11). Finally, high temperatures cause selective segregation of species with low surface energy, potentially inducing composition gradients across the film, or excess cation segregation to the film's surface. As a result, a fine tuning of the substrate temperature is often needed to achieve the desired film properties.

To heat the substrates, an IR laser was shined directly on their back, as allowed by the mounting on plates with a through hole. The direct heating ensures a very uniform temperature distribution on the sample (within 5 °C). The sample mounting avoids any glue that would degas while heating the sample, and relies instead on clips that are spot-welded to the sample holder (Section 2.4.1). The temperature is measured with a pyrometer with an emissivity always set to 0.94, which was found to be optimal for epi-polished $SrTiO_3$ single crystals. It is worth mentioning that the IR laser spot is about 1 cm in diameter, so that also the plate is partially directly heated by the laser. To avoid introducing contamination from the heated plate onto the sample, a high-temperature- and high-p_{O_2}-resistant alloy was used for the plate, namely Nicrofer® 6025HT (also known as Alloy 602 CA).

2.3.6 Ablation targets

As a minimum requirement, the ablation target should possess a high optical absorption coefficient at the selected laser wavelength. Additionally, the target should fulfill a few

requirements regarding its density, homogeneity, composition, and purity: All these factors can impact the film properties. Note that different target materials can have different laser absorption properties and, as a consequence, different ablation rates.

High density and homogeneity. High density and homogeneity are required to avoid removal of big clusters from the target during ablation. These can land as droplets on the substrate, hindering the crystallization of a high-quality epitaxial films. Moreover, porous targets can incorporate contaminants when taken out of vacuum: When using an In_2O_3 target with 65% of the ideal density, a tendency was observed to incorporate water and hydrocarbons upon air exposure, and this seemed to influence the growth and the film morphology (Chapter 5).

Composition. The composition of the target is less crucial than its density. As already anticipated, the composition of the film is affected by a multitude of factors, including, but not limited to, the background pressure and the laser fluence. This means that the stoichiometry of the film can be adjusted by acting on the growth parameters, independent on the stoichiometry of the target (which, however, should not be grossly off). Note, however, that the composition of multicomponent targets may be affected after prolonged growth: A redistribution of the elements in the upper layers caused, *e.g.*, by different melting/vaporization points, was seen to cause a change in a target composition from $La_{0.64}Ca_{0.35}Co_{0.95}O_{2.95}$ to $La_{0.72}Ca_{0.28}Co_{0.99}O_{2.7}$.[78] These changes might be critical for experiments aiming at controlling stoichiometries with high precision. One can overcome the problem (*i.e.*, recover the initial composition) by mechanically polishing the target's surface.[34]

Purity. The purity of the target ultimately determines the purity of the film. This is of special concern for STM applications, where a contamination on the order of 1% in the film will result in a 1% coverage of unwanted species at the surface or in ≈10 atomic impurities in a 10×10 nm^2 STM image. Such impurities could easily alter the geometric and electronic properties of the surface under scrutiny. For this reason, ablation targets of the highest purity available were used within this Thesis (at least 99.99%).

Because of their high density and purity, homogeneous distribution of components, and known stoichiometry, single crystals are preferred target materials. If single crystals are not easily obtained, sintered pellets with the highest possible density and purity can be used instead. Within this Thesis, an array of different targets obtained both from single crystals and polycrystalline pellets were used, some of which were home-produced from commercial, high-purity powders, as detailed in the following. They are summarized in Table 2.1.

Synthesizing polycrystalline targets

The following Section details the synthesis procedure for home-made polycrystalline targets starting from commercial powders. In all cases, the powder was isostatically pressed in an oil press at 400 MPa at room temperature (RT) in a cylindrical silicone mold of appropriate dimensions (to avoid the oil getting in contact with the pellet, the mold was protected with three sealed layers of nitrile gloves). The pellet was then sintered in an alumina tube furnace at appropriate conditions. During the sintering, the pellet was always put in a platinum crucible, covered in unpressed powder, and protected by a Pt lid.

- **$La_{0.8}Sr_{0.2}MnO_3$**. Appropriate amounts of lanthanum oxide (99.999%, from Sigma-Aldrich), strontium carbonate (99.995%, Sigma-Aldrich), and manganese(II) acetate tetrahydrate (99.999%, Alfa Aesar) were thoroughly mixed in an agate mortar. The obtained powder was pyrolyzed in a Pt crucible with a bunsen burner, yielding a brownish, dark foam. This was then ground to a fine powder in the agate mortar, and further calcined for 1 h at 1 000 °C in air. X-ray diffraction (XRD) revealed the resulting product to be phase pure LSMO-perovskite. The powder was then pressed (dimensions of the silicone mold: 16 mm inner diameter, 6 mm height, walls thickness 2 mm; 4.3 g of powder used). To maximize the target's density, the pressing was repeated three times, each time re-grinding the pellet in the agate mortar and fitting more powder in the mold. The pressed pellet was sintered for 1 h at 1450 °C, (ramp rates of 3 °C/h), and in oxygen atmosphere (air liquide, 99.995% pure). After sintering, the target surface was ground with SiC paper and n-Octane; the non-polar n-Octane was used instead of water or ethanol to limit the effects connected to interaction with water. The target was also sonicated in the solvent for a couple of minutes in order to get rid of loose particles, then dried in air at 150 °C for 30 minutes, to let the solvent evaporate.

  The final product was compact, shiny, and with 94.1% of the ideal density. The best-matching XRD spectrum was $La_{0.8}Sr_{0.2}MnO_3$. A slight A-site deficiency—$(La_{0.73}Sr_{0.27})_{0.77}MnO_3$—was measured by laser-induced inductively coupled mass spectroscopy (ICP-MS), which also revealed a purity of 99.996%, more than one order of magnitude better than the best commercially available products, and only minimally worse than the precursors. After these characterizations, the target was mounted on the target holder, cleaned by sonication in n-Octane, dried in air for 30 minutes at 150 °C, and then inserted into the system.

- **MnO**. 3.2 g of MnO powder (99.99% purity, Alfa Aesar) were isostatically pressed (dimensions of the silicone mold: 16 mm inner diameter, 6 mm height, wall thick-

ness 2 mm), and then sintered for 2 h at 1 250 °C in an N_2:Ar = 24:76 mixture. The sintering parameters were decided according to the phase diagram of manganese oxide, aiming to form only one phase (MnO) during the process. If more than one phase is formed during sintering, the different unit cell dimensions of the different phases might cause cracking of the target. XRD then revealed the phase to be 95% MnO, plus 5% Mn_3O_4. The density was 87.9% of the theoretical density of MnO. The target was polished with SiC paper and ultrapure water before mounting.

- **1 at.% Ti:Fe_2O_3**. To produce a target with a Fe:Ti atom ratio of 99:1, Fe_2O_3 and TiO_2 powders (99.995% purity, Alfa Aesar) were carefully weighted, mixed, and ground in an agate mortar. The powder was pressed (same mold dimensions as for the LSMO target), and then sintered for 6 h at 1 200 °C and 1 bar of flowing O_2 (5 °C/min ramp rates). To achieve a flat surface, the skewed target was cut with a diamond wire saw and polished with SiC paper and ultrapure water.

Mounting targets

All targets (both polycrystalline and single crystals) were mounted on their holders by means of a UHV-compatible epoxy, and cured for 2 h in air at 150 °C. After mounting, the targets were cleaned through sonication with appropriate solvents. The targets were inserted into the vacuum system via a carousel. Each target was carefully positioned to have always the same distance between the target's surface and the center of the carousel.

Target preablation

Preablating the target's surface before growth is crucial to remove unwanted adsorbants and residues from grinding. The targets were always preablated by passing on the same area at least 10 times. For the preablation, the same pressure and fluence were used as later for film growth, since it was reported that different conditions may alter the composition and morphology of the target's surface,[79] in turn affecting the ablation process. Note that, to avoid unwanted deposition, the pristine substrate was kept in a separate chamber during preablation.[76]

Table 2.1. Summary of the PLD targets used within this Thesis. The table summarizes whether the targets are poly- or single-crystalline, their supplier, and how they have been used within this Thesis.

Targets	Details	Use
Cu	Polycr., home-made from an O-free Cu gasket of an all-metal angle valve	Alignment, spot focusing
TiO_2	Single cr. (various shapes), supplier unknown; Fe contamination seen in XPS removed by annealing at 800 °C in flowing O_2 for two days, followed by removal of the segregated Fe through mechanical polishing	Anatase/$SrTiO_3$(001); Ti:Fe_2O_3/$Fe_2O_3(1\bar{1}02)$; tune $SrTiO_3$(110) surfaces
In_2O_3	Polycr., China Rare Metal Co., Ltd. 65% ideal density	In_2O_3/YSZ(111), In_2O_3/YTO(111)
Fe_3O_4	Single cr. (various shapes), supplier unknown	Ti:Fe_2O_3/$Fe_2O_3(1\bar{1}02)$
1 at.% Ti:Fe_2O_3	Polycr., home-made	Ti:Fe_2O_3/$Fe_2O_3(1\bar{1}02)$
0.5 wt.% Nb:$SrTiO_3$	Single cr., SurfaceNet GmbH	$SrTiO_3$/$SrTiO_3$(110)
u:$SrTiO_3$	Single cr., SurfaceNet GmbH	$SrTiO_3$/$SrTiO_3$(110)
$La_{0.8}Sr_{0.2}MnO_3$	Polycr., home-made	LSMO/$SrTiO_3$(110)
La_2O_3	Polycr., China Rare Metal Co., Ltd. Strongly hygroscopic, always stored in UHV	Tune LSMO(110) surfaces
MnO	Polycr., home-made	Tune LSMO(110) surfaces

2.3.7 Deposition procedure

A typical deposition procedure followed these steps:

1. Start the laser and monitor its laser energy. Wait until the laser energy is stable over the time span required for the growth. Set the laser fluence.

2. Check the alignment of the UV laser by shooting in the center of the last scanned area.

3. Preablate the target at the growth conditions, assuming a given spot size (the real fluence is computed *a posteriori* by measuring the real spot size). In stoichiometry-sensitive experiments (Chapters 6–9), pristine targets are used: After each depo-

sition, a single laser pulse is shot on the target, its area measured (to compute the real fluence used during the previous growth), then the target is polished, cleaned, dried, and put back in.

4. Insert the substrate, align it, set the desired pressure and heat it (with a typical ramp rate of 60 °C/min).

5. Acquire a RHEED pattern of the pristine substrate, and align the RHEED beam with the substrate to follow the growth in real time.

6. Reset the laser fluence to the desired value.

7. Start the deposition while recording the variations of the RHEED intensity.

8. Post-anneal the substrate and cool it down. Acquire the RHEED pattern, and transfer it to the analysis chamber.

9. Every once in a while, check if the transmittivity of the PLD system has changed because of deposits on the windows, by measuring the energy of the UV laser before the entrance window and after the exit window. Appendix B describes how to clean windows covered in PLD deposits.

2.4 Sample mounting and contacting

2.4.1 Sample mounting

The experimental setup and the brittleness of some of the single-crystalline samples pose strict requirements on the sample mounting. In all the cases described in this Thesis, samples were mounted to their plates by spot-welding customized clips.

Nicrofer® for sample plate and clips

As mentioned above, Nicrofer® is an ideal material choice for clips and plates when working with high temperatures and high pressures, and was the most commonly used material during this Thesis. It is an alloy mainly consisting of nickel, chromium, and iron, which was tested to be stable at 1 000 °C up to 50 mbar O_2-[76] However, it has the disadvantage of losing its spring force on the sample over repeated annealing cycles. For this reason, samples periodically become loose, and must be re-mounted and re-cleaned. Ta and/or Mo maintain their spring force over repeated treatments better than Nicrofer®, but are only suited for UHV-compatible conditions (volatile oxides are formed

that contaminate the sample at high pressures/temperatures). Nicrofer® parts were always cleaned by boiling them in 20% HNO_3, followed by thorough rinsing in ultrapure water.

Mounting strategies

The sample plates are machined with a pocket to fit the sample, and have a through hole for direct heating with an electron beam or with the IR laser. The clips are fabricated from 0.25 mm-thick Nicrofer® foil (their typical width is 0.7 mm). Their mounting should fulfill several requirements: (i) Appropriate to hold the sample to the plate, to minimize sample vibrations (detrimental for STM), while avoiding to crack the sample during annealing; (ii) maintaining reasonably unaltered spring force after repeated annealing cycles at elevated temperature; (iii) complying with the constraints of the STM setup: Total height of plate and clips less than 2.1 mm in height, fit within the area enclosed by the red line in Fig. 2.3; (iv) not obstructing the RHEED beam (running parallel to the ear of the sample plate).

Figure 2.3 shows different clip designs that comply with the requirements above. In the design of Fig. 2.3(a), two M-shaped clips are spot-welded to the sample plate on opposing sides of the sample. The clips are shaped to achieve flat ends and three contact points [see panel (a_1)]. Note that when put on a sample, which slighlty protrudes from the plate, one side of the clip is lifted [see red dots in panel (a_2)]. When both ends of the clip are spot-welded to the sample plate, the contact point in the middle (black arrow) exerts force on the sample.

The design of Fig. 2.3(b) is similar to the one in panel (a), but the force on the sample is here exerted by a spacer (black arrow), made by three Nicrofer® stripes spot-welded together (for a standard plate pocket, *i.e.*, sample protruding 0.25 mm from the sample plate, the optimal thickness is given by two stripes of 0.17 mm thickness, and one of 0.25 mm). The spacer is spot-welded on a stripe that will form the clip. After filing down the rough edges of the spacer, the stripe is shaped by using a home-designed mold into a bridge-like shape, and adjusted to look like in panel (b_1). Note that the clips should always lie within the red curve (space allowed by the STM setup). This mounting, compared to that in Fig. 2.3(a), has the advantage of sustaining more annealing cycles without loosing its spring force. However, samples are more at risk of cracking during the first annealing cycle. This mounting was used for most of the experiments discussed in this Thesis.

If STM is not performed in the SPECS chamber, the constraint over the clip height is relaxed, and the mounting shown in Fig. 2.3(c) is used instead, where two clips hold the sample from the sides. This design has the advantage of allowing a simple mount-

ing and re-mounting of the sample (handy if the sample is analyzed in different setups which require different mountings). This design was used for the In_2O_3 films discussed in Chapter 5. If STM measurements are not planned in the short term, the samples are loosely mounted to the plate with two Nicrofer clips at two opposite corners of the sample.

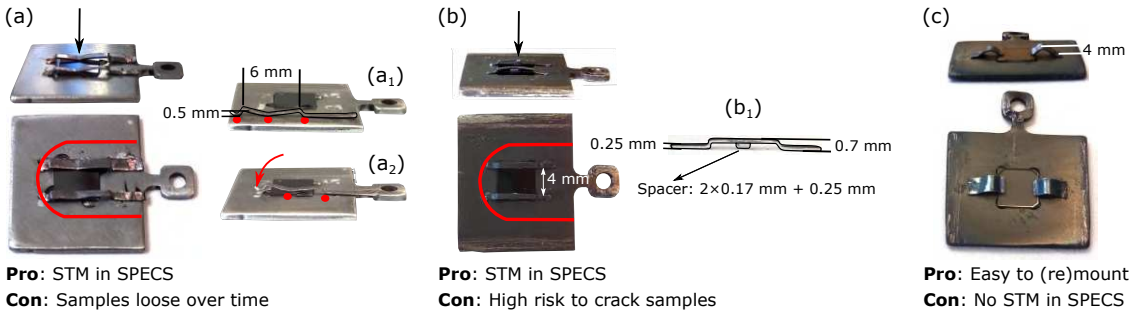

Figure 2.3. UHV types of sample mounting used within this Thesis. In all cases, hand-made clips tightly hold the sample to the sample plate, and comply with the constraints posed by the system.

2.4.2 Pt contacts for insulating and/or transparent substrates

Often it happens that a substrate with an ideal lattice match for heteroepitaxy is insulating: Then solutions must be found to measure the film with STM. An easy one is to mount the substrate with metallic clips on the plate. The clips will be covered in the conductive film during growth, and thus provide a path for the electrons to be transported from the film to the plate. However, this approach requires a *very* thick film to bridge the gap between the 'overhanging' bottom edges of the clips and the film, and it is not optimal if the sample needs to be remounted several times: Repeated remounting tends to damage the film, with eventual loss of contact. Another possibility is to connect the film and the plate *after* the growth, *e.g.*, by a clip spot-welded on one end to the plate, and bent so that it gently touches the film's surface. However, this approach has a main disadvantage: it requires to take the film outside vacuum. Moreover, it is not optimal if the samples needs to be remounted several times.

To overcome these issues, one can used the approach sketched in Fig. 2.4. It has been used for contacting In_2O_3 films on YSZ(111) (Chapter 5), as well as Ti-doped Fe_2O_3 films on undoped $Fe_2O_3(1\bar{1}02)$ substrates (Chapter 4.1.1). In essence, Pt electrodes are deposited on the edges of the front surface of the insulating substrate, as well as on its sides and back; this way, the film is contacted to the plate via the front electrodes, in turn contacted to the back and side ones (see Fig. 2.4). Besides being UHV compatible,

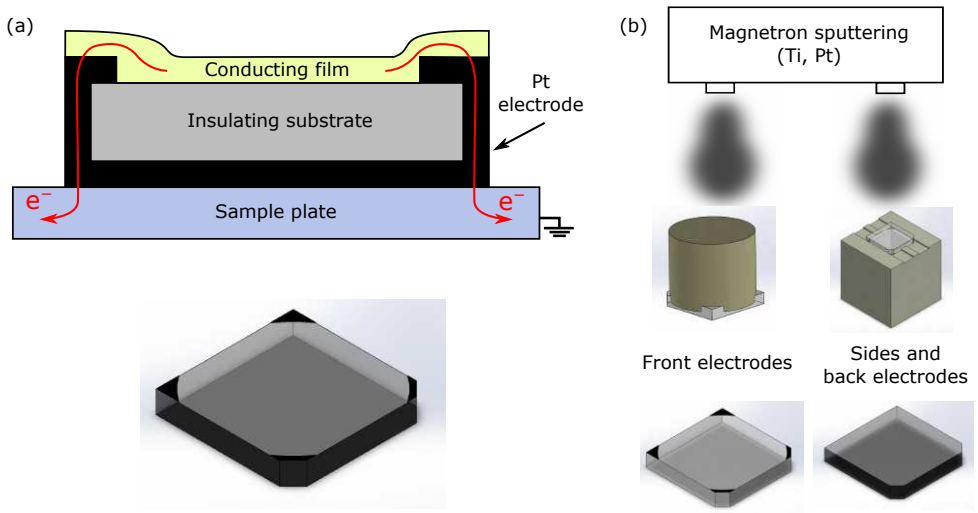

Figure 2.4. Pt electrodes for electrical contact of insulating substrates and absorption of the IR laser. (a) Sketch of the solution used for realizing electrical contact between the film and the sample plate when the substrate is insulating. Metallic (Pt) electrodes are deposited on the edges of the front surface of the substrate, as well as on its sides and on its back. This offers a path for the electrons from the film to the sample plate. The back electrode absorbs the IR laser during annealing. (b) Two masks from PEEK are used to deposit the front electrodes, and the side and back electrodes by magnetron sputtering. Renderings by Jakob Hofinger.[80]

this solution sustains repeated sample re-mountings. For substrates that are transparent to the IR laser (*e.g.*, YSZ), the presence of the back electrode serves another important purpose: It acts as an absorbing layer for the IR laser (recall that the samples are hit directly by the IR laser through the hole in the sample plate). Without the absorbing layer, the IR laser would simply pass through the substrate.

The electrodes were deposited by magnetron sputtering in Ar atmosphere at the Institute of Chemical Technologies and Analytics of the TU Wien. Home-designed and -machined PEEK masks have been used to deposit the electrodes while avoiding contaminating to the surface (dimensional 2D drawings are found in Appendix D). The sample was sandwiched between the 'front side' and the 'back side' masks. The electrodes were deposited on each side by flipping the sandwich in between. To remove the Pt, the masks were cleaned with aqua regia, and then sonicated in Extran (2 × 30 min) and ultrapure water (10 min). Note that Pt electrodes directly deposited on well-polished surfaces do not survive sonication treatments (partial exfoliation). Using thin Ti interlayers promotes sticking and stability of the Pt electrodes over time. A 10 nm/100 nm/10 nm/100 nm Ti/Pt/Ti/Pt layer was found to be stable over repeated sonication treatments.

Typically, substrates are cleaned before depositing the electrodes with two sonication cycles in Extran (15 min, rinsing in ultrapure water in between) plus 10 min sonication in ultrapure water. They undergo the same treatment after the electrodes are deposited, and before mounting. This yields mesoscopically clean surfaces, as seen in AFM (not

shown).

2.5 Precise doses in PLD: Movable holder for a quartz-crystal microbalance

This Section presents a recently developed solution for accurately measuring PLD growth rates, namely a movable holder for a quartz-crystal microbalance, or QCM. The work has been published in ref. 65.

This project has been pushed by a consistent need to accurately measure film thicknesses and growth rates. Previous to implementing the soon-to-be-described QCM device, film thicknesses were measured *post mortem* by profilometry. This is only one of many techniques suited for the purpose, besides cross-sectional transmission electron microscopy (TEM), optical and diffraction measurements, and Rutherford backscattering (RBS). These methods are generally accurate, but entail one main disadvantage: they require to break vacuum. This makes them time-consuming (they often require to grow sacrificial films), and not suited for sensitive or hygroscopic materials. For these reasons, measuring growth rates in vacuum is desirable. However, fewer methods exist to measure PLD growth rates in vacuum. RHEED is a favorite, but only possible when the growth mode is layer by layer (in that case, one RHEED oscillation corresponds to the deposition of one atomic layer). For other types of growth modes, alternative methods are needed.

The QCM is a potentially good candidate to accurately measure PLD growth rates in vacuum. QCMs are shear-mode resonators in which acoustic waves propagate perpendicular to the surface of a single crystal (usually quartz) that is cut along a well-defined direction and machined to a distinct geometry. A change in the mass of the crystal as small as 10^{-16} kg,[81] induced, *e.g.*, by the deposition of a thin film, produces a correlated and measurable change of its resonance frequency, from which growth rates can be derived.[82–84] Because they are highly accurate, easily implemented, and cheap, commercial QCM sensors have been widely used for monitoring film growth realized by various vacuum deposition techniques, including molecular beam epitaxy, atomic-layer deposition, chemical vapor deposition, and magnetron sputtering.[85–88]

QCM sensors have also been applied to PLD, albeit with some crucial limitations. Because the impinging particles in PLD are highly energetic, they can produce thermal drifts due to local changes in temperature, and surface stress due to sputter-induced defects and ion implantation. The high sensitivity of the QCM to thermal drifts and surface stress makes real-time measurements of the resonance frequency not reliable.

Moreover, QCM sensors are typically solidly fixed to the PLD apparatus, often off to one side of the substrate. This implies few disadvantages. Due to the highly directed flux of the plume towards the substrate, the growth rate on the QCM is typically smaller than that of the substrate.[89] While the difference can be in principle quantified with appropriate modeling of the deposition geometry and of the angular flux distribution of the ablation plume, in practice this is not straightforward. Additionally, the strong spatial and angular gradients of the flux composition, and their dependence on the background pressure and on the laser fluence, as argued within this Thesis, can lead to the deposition of films on the QCM crystal whose composition differs from those deposited onto the substrates. Finally, unless protected by a shutter, QCM crystals mounted in this fashion are constantly exposed to the ablated particles, regardless of whether a measurement of the deposited amounts is planned or not. Due to the finite lifetime of the crystals, this makes frequent replacements necessary.

The home-designed movable holder for a QCM that is presented in the following overcomes the aforementioned drawbacks, and has the additional advantage that it can be easily implemented without modifying the existing UHV system. The holder is compatible with standard transfer arms and provides easy insertion and transfer in UHV. It allows to place the QCM at the same position as the substrate during deposition, while its frequency is measured before and after growth in a connected UHV chamber. The operation of the device is demonstrated for Fe_2O_3 (hematite) deposition on an AT-cut, 6 MHz quartz crystal: The derived growth rates match nicely those obtained from the RHEED oscillations observed during the homoepitaxial growth of $Fe_2O_3(1\bar{1}02)$ films at identical conditions.

2.5.1 Design and implementation

The used quartz crystals are 6 MHz AT-cut plano-convex crystals from Sycon Instruments with 13.95 mm outer diameter and Au electrodes. The front electrode (≈13 mm diameter) covers the largest part of the quartz surface, while a double-anchor-shaped electrode is used for the rear side of the crystal (fully coated in a central circle of ≈6.3 mm). The resonance frequency of the QCM was measured before and after growth with a PREVAC TM-14 QCM oscillator.

Figure 2.5 shows an exploded view of the holder of the QCM crystal (complete dimensional drawings are found in ref. 65). It is composed of two stainless steel, flag-style sample plates (4 and 10, in Fig. 2.5) in a double-decker geometry (4.15 mm clearance). Both plates are compatible with standard UHV manipulators, and serve two purposes: (i) holding the crystal while maximizing the exposed area to the incoming flux and min-

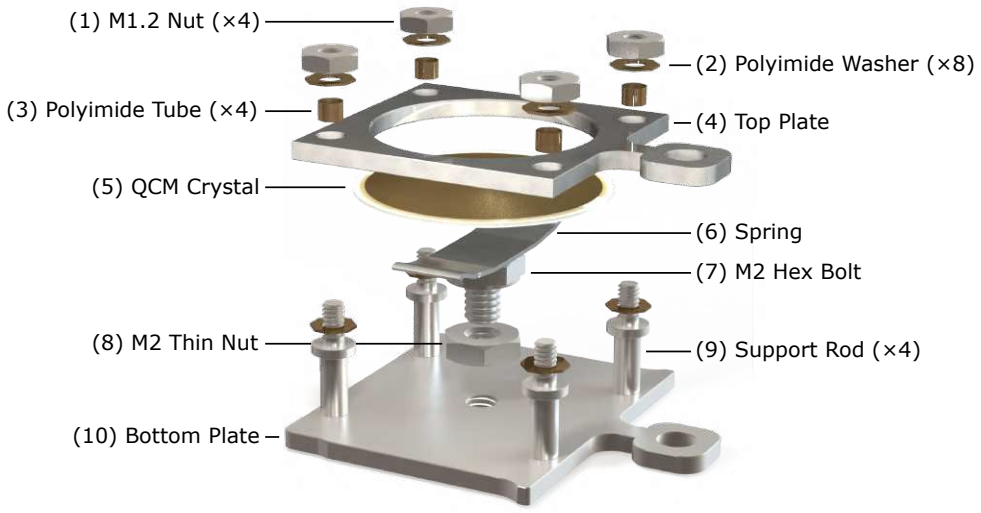

Figure 2.5. Exploded view of the movable QCM holder. Two flag-style, modified sample plates (4 and 10) in a double-decker arrangement mechanically support the QCM crystal (5) via an adjustable-spring system (6, 7, 8). Four specially shaped rods (9), spot-welded to the bottom plate (10) and fastened (1) to the top plate (4) provide mechanical stability to the holder and allow to position the crystal precisely. The plates are electrically insulated from one another via polyimide spacers (2, 3), and provide separate electrical contact to the crystal electrodes. Parts 1, 4, and 6–10 are made from AISI-316 stainless steel. See ref. 65 for the dimensional drawing of all parts. Reprinted from ref. 65.

imizing stress on the crystal, which can affect its resonance frequency;[87] (ii) providing the needed electrical contacts to the circuitry that measures the resonance frequency of the crystal.

The through-hole with 12 mm diameter in the top plate (4, in Fig. 2.5) leaves the whole active area of the crystal free. The crystal is gently pushed against the top plate by an adjustable stainless-steel spring (0.25 mm thickness; 6, in Fig. 2.5), spot-welded onto a short M2 bolt (7, 3.8 mm total length), which is screwed to the bottom plate. The bottom surface of the top plate is mirror-polished with 2400 grit (8 μm-diameter particles) SiC abrasive paper to minimize localized stress on the crystal, while the spring (6) is shaped so that electrical and mechanical contact with the crystal occurs in a symmetric fashion and as close to the edges as allowed by the double-anchor shape of the rear electrode. Four stainless steel rods (9, in Fig. 2.5) not exerting any radial stress on the crystal (clearance < 50 μm) allow its precise centering during assembling, and thus limit the chance of imposing unevenly distributed radial stress. The same rods provide the mechanical connection between the two plates: They are inserted in closely fitting receptacles machined in the bottom plate, and spot-welded in position; an M1.2 thread cut on the opposite side of the rods is used for fastening the top plate. The rods and their positions are designed to leave ample clearance (> 2.9 mm on each side) for insertion of the bottom plate in standard manipulator receptacles. To reduce mechanical stress on the crystal, only the bottom plate (not in mechanical contact with the crystal) is used during

transfers across vacuum. In addition, the width of the top plate is reduced (14.5 mm, as compared to the usual width of 18 mm for this type of sample plates), so as to prevent inadvertently inserting it into a manipulator receptacle. At the same time, this allows storage of the holder in standard multi-slot sample carousels or racks in UHV.

To measure the resonance frequency of the QCM crystal, one electrode must be set to ground while the other one is driven by the QCM oscillator. This requires that the two electrodes are electrically insulated with respect to each other. The electrical contacts in the design can be inferred from Fig. 2.5. The top and bottom electrodes of the crystal are electrically connected to the top (direct contact) and bottom plates (via the spring; 6 in Fig. 2.5), respectively. Insulation between the top and bottom plates (top and bottom electrodes of the crystal) is achieved with polyimide (Kapton®) washers cut from a 0.15 mm-thick foil and polyimide tubes (1.44 mm inner diameter, 25 μm wall thickness). The washers (2 in Fig. 2.5) are placed between the collar of the support rods and the top plate, and between the top plate and the fastening nuts (2, and 1 in Fig. 2.5, respectively); the polyimide tubes (3, in Fig. 2.5) are inserted in the clearance holes of the top plate to prevent electrical contact between the threads of the support rods and the plate itself.

The resonance frequency of the QCM crystal can be measured in any stage present in the UHV system that meets the two essential requirements of (i) being able to host the QCM holder and (ii) providing appropriate electrical contacts with small enough parasitic series impedance. For instance, one can place the QCM holder into a manipulator with a sample slot electrically insulated from ground, and use a transfer arm, a wobble stick, or some grounded object present in the chamber for contacting the upper plate of the holder.

In the context of this work, the QCM holder has been placed in the sample manipulator of the preparation chamber (Fig. 2.1). There, the bottom plate of the QCM is hosted in an electrically insulated sample receptacle that can be connected to the oscillator via an external feedthrough. The top plate is grounded by gently touching its 'handle' with a Cu block mounted on a bellowed linear manipulator. Care was taken in reproducibly establishing a well-defined electrical contact with the two plates of the holder, since variability in contact impedances causes the measured resonance frequency to scatter accordingly. To obtain reproducible frequency measurements, it was ensured that a small ($< 3\ \Omega$) and reproducible resistance could be measured between the bottom plate of the holder and the electrical feedthrough contact used to drive the crystal. (Touching or clamping the top plate with a magnetically coupled transfer rod is not ideal for the ground connection, even if the transfer rod has steel ball bearings; the resistance across these bearings is too large ($\approx 1\ \mathrm{k}\Omega$) and poorly reproducible, probably because of oxidized surfaces.)

All the parts of the holder, with exception of the quartz crystal, were cleaned prior to assembling by sonication in Extran (2 × 30 min) and ultrapure water (15 min), followed by boiling in diluted HNO_3. After insertion in the UHV system, the holder and crystal were outgassed for 30 min at 100–200 °C until recovery of the pressure. This removes adsorbed water and yields more stable resonance frequency measurements.

PLD growth on the QCM

The resonance frequency of the crystal was measured before and after film deposition in PLD. Since several deposition parameters affect the stoichiometry and the amount of material landing on the substrate (as discussed in the following Sections), the deposition on the QCM must be performed at the same conditions as during film growth. Some critical parameters are the background pressure, the laser fluence, and the relative alignment of target and substrate. The needed O_2 pressure and laser fluence were set, and the QCM was placed in the usual substrate position (*i.e.*, same distance between target and the quartz surface, and same relative alignment between QCM, UV laser and targets), as allowed by the movable design of the QCM holder and its compatibility with UHV manipulators. Moreover, the surface of the target was preablated before deposition following the standard recipe (at the growth conditions, by scanning the target in the UV laser beam, so as to hit each spot of the ablation area at least ten times, while keeping the QCM in a separate chamber).

Quantification of growth rates

To derive the mass of material deposited on the QCM based on the shifts of its resonance frequency, one can use different approximations.[83,90] These approximations depend on the amount of material deposited and on its elastic properties.[83] When the material deposited is sufficiently rigid, and the total frequency shift of the QCM Δf_{tot} is smaller than 3–4% of the original frequency, f_{q}, of the new crystal, the mass deposited on the active surface area A is well described by[83,90]

$$\frac{\Delta m}{A} = -\frac{N_{\mathrm{q}}\rho_{\mathrm{q}}}{f_{\mathrm{q}}f_{\mathrm{c}}}\Delta f, \tag{2.1}$$

where ρ_{q} and N_{q} are the mass density and the shear-mode frequency constant of the quartz crystal, respectively ($N_{\mathrm{q}} = \nu_{\mathrm{q}}/2$, where ν_{q} is the shear-wave phase velocity), and $f_{\mathrm{c}} = f_{\mathrm{q}}+\Delta f$ is the resonance frequency after deposition. The mass deposited per unit active area is easily derived using known values for ρ_{q} and N_{q} (for AT-cut crystals, $\rho_{\mathrm{q}} = 2.648$ g/cm^3 and $N_{\mathrm{q}} = 1.668 \times 10^5$ Hz cm, respectively).[83] It should be noted that Eq. (2.1)

does not take into account possible effects of stress buildup in the quartz crystal during deposition. These contribute to a change of resonance frequency of the crystal that, to a first approximation, depends linearly on the thickness of the deposited film.[91] For film growth, these changes are typically of the order of a few percent of the mass contributions in Eq. (2.1), or less, and can be included as a possible source of error when estimating growth rates. The relation $e_{(r,S)} = -K\delta S\rho_q/\rho_f$ was used for estimating the relative error $e_{(r,S)}$ due to stress buildup on $\Delta m/A$, where $K = K^{AT} = -2.75 \times 10^{-7}$ cm^2/N for AT-cut quartz,[91] $\delta S = 1 \times 10^5$ N/cm^2 (this large stress value is used to include a worst-case scenario error estimate),[91] and ρ_f is the mass density of the material deposited. For example, for the growth of hematite (Fe_2O_3, $\rho_f = 5.254$ g/cm^3), stress build up in the film can lead to a maximum relative error $e_{(r,S)} \approx 1.4\%$. Additional corrections to Eq. (2.1) due to the plano-convex geometry and the presence of the electrodes are expected to be comparable or smaller than the pessimistic estimated of $e_{(r,S)}$, and were not considered.[90,92,93] In the case of large mass loads, Eq. (2.1) should be replaced by the more exact relations that include the acoustic impedance of the deposited material.[83,90]

2.5.2 Performance evaluation: Hematite (Fe_2O_3) deposition

At moderate temperatures (below 750 °C), hematite grows layer by layer with clear RHEED oscillations (see Chapter 4), which makes this an ideal system to test the accuracy of the QCM device. To this end, the procedure was as follows:

(a) Derive the mass growth rate of Fe_2O_3 by depositing on the QCM.

(b) Derive thickness growth rates of $Fe_2O_3(1\bar{1}02)$ homoepitaxial films deposited at the same conditions from the period of the corresponding RHEED oscillations.

(c) Convert thickness growth rates from (b) to mass growth rates via the available structural model for the $Fe_2O_3(1\bar{1}02)$ system. These can be compared to the values measured in (a) with the QCM.

(a) Fe_2O_3 mass growth rates derived by the QCM

To obtain mass growth rates of Fe_2O_3 grown on the QCM, Fe_2O_3 was incrementally deposited in the PLD chamber by firing a well-defined number of laser pulses on a single-crystalline Fe_3O_4 target (0.2 mbar O_2, 2.0 J/cm^2, 5 Hz), while keeping the QCM holder at RT. At these growth conditions, the thermodynamic stability phase diagrams of iron

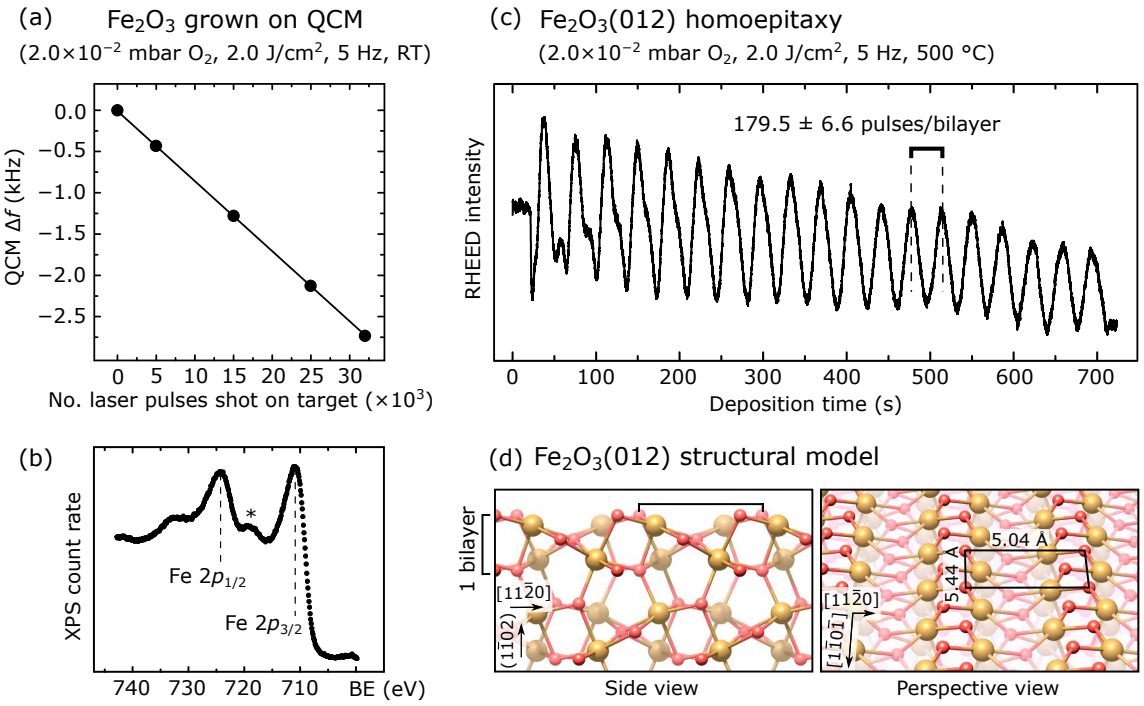

Figure 2.6. Performance evaluation of the QCM device. (a) Resonance frequency of the QCM crystal as a function of the number of laser pulses shot on the iron oxide target (RT, 2×10^{-2} mbar O_2, 5 Hz, 2.0 J/cm^2). The decrease is linear. (b) Fe 2*p* XPS peak on the film of panel (a). The presence of a pronounced satellite peak at 719 eV (indicated by the star), and the position of the Fe $2p_{3/2}$ and Fe $2p_{1/2}$ are characteristic of the Fe_2O_3 hematite phase. Since the front surface of the quartz crystal (*i.e.*, the top plate in Fig. 2.5) was not grounded during XPS measurements, the binding energy axis in Fig. 2.6(c) has been shifted such that the O 1*s* peak position corresponds to the one measured on a reference α-Fe_2O_3 single crystal. (c) RHEED oscillations observed during the homoepitaxial growth of $Fe_2O_3(1\bar{1}02)$ (500 °C, 2.0×10^{-2} mbar O_2, 5 Hz, 2.0 J/cm^2). Each oscillation corresponds to the deposition of a 'bilayer' of $Fe_2O_3(1\bar{1}02)$ [see the structural model in panel (d), adapted from ref. 66, which consists of 4 Fe atoms and 6 O atoms per unit cell [black rectangle in the perspective view of panel (d)], or 194.0 ng/cm^2. Reprinted from ref. 65.

oxides predict the formation of Fe_2O_3.[94] The shape of the Fe 2*p* XPS peak measured on the film grown on the QCM confirms that indeed Fe_2O_3 is formed rather than Fe_3O_4 [Fig. 2.6(b)]: Both the positions of Fe $2p_{1/2}$, Fe $2p_{3/2}$, and the presence of the pronounced shake-up satellite in between them [labeled by a star in Fig. 2.6(c)] are consistent with Fe^{3+}-containing compounds and prior measurements of α-Fe_2O_3.[95,96]

The QCM resonance frequency was measured after each deposition step as described in Section 2.5.1. Figure 2.6(a) shows that the QCM resonance frequency decreases linearly with the number of laser pulses, *i.e.*, with the amount of material deposited per unit active area, as expected from Eq. (2.1). The frequency shifts in Fig. 2.6(a) correspond to the average of at least three repeated measurements performed after each deposition step. Error bars were determined as the half width of the 95% confidence intervals calculated with a two-tailed Student's *t*-distribution from the standard error of the mean of these measurements. They are smaller than the symbol sizes in Fig. 2.6(a), and amount to at most ± 20 Hz (largest standard error of the mean of approximately 5 Hz). These

variations in the measured frequency are significantly smaller than the frequency shift in the kilohertz range caused by the deposition of a few nanometers of material.

From a linear fit of the data in Fig. 2.6(a), one derives a shift in the QCM resonance frequency per pulse of -0.084 ± 0.002 Hz/pulse (the uncertainty corresponds to the 95% confidence interval of the slope). With Eq. (2.1), this value can be converted into a mass growth rate $\Delta m/A = 1.06 \pm 0.03$ ng/cm^2 per pulse. Notice the high sensitivity of the QCM measurements to the deposited masses, which is obtained by depositing thick films on the crystal, such that the small error bars on the single frequency shift measurements can be neglected.

(b) $Fe_2O_3(1\bar{1}02)$ thickness growth rates derived from RHEED oscillations

Figure 2.6(c) shows the RHEED oscillations observed during the homoepitaxial growth of an $Fe_2O_3(1\bar{1}02)$ film at 500 °C. One can exclude any dependence of the growth rates on the deposition temperature: RHEED oscillations with statistically equivalent periodicity (as inferred from Fourier analysis) were observed at deposition temperatures ranging from RT to 600 °C. Notice that during the deposition of the first layers, the oscillations display a double peak that gets damped as the growth proceeds. This shoulder, whose origin is unknown at the present stage, is more prominent at lower temperatures. Nonetheless, its presence never alters the overall periodicity of the oscillations.

(c) Comparison of growth rates

From profilometry measurement on thicker $Fe_2O_3(1\bar{1}02)$ homoepitaxial films, it was derived that each RHEED oscillation, or 179.5 ± 6.6 laser pulses, corresponds to the deposition of one O–Fe–O–Fe–O bilayer [see the structural model in Fig. 2.6(d)].[66,96] Notice that growth of subunits of the bilayer would make the surface polar, and therefore unstable. Each bilayer consists of 4 Fe atoms and 6 O atoms per (1×1) unit cell [black rectangle in the perspective view of Fig. 2.6(d)], and therefore has an areal mass density of 194.0 ng/cm^2. Knowing the number of pulses needed to complete one bilayer, one can then derive a mass growth rate of 1.08 ± 0.04 ng/cm^2 per pulse. This value matches the mass growth rate of 1.06 ± 0.02 ng/cm^2 per pulse derived by growing Fe_2O_3 on the QCM at the same conditions.

2.5.3 Uses and potential improvements

Deriving thickness growth rates

The most common use of the QCM, *i.e.*, deriving thickness growth rates, is viable in principle, albeit with some precautions. The translation from mass to thickness growth rates requires the correct value of the mass density of the deposited film, which might be hard to pinpoint, especially for oxide compounds that can exhibit a variety of bulk structures. One cannot assume a priori values of densities tabulated in the literature, even if the composition of the film is known (*e.g.*, by XPS), since RT deposition on the polycrystalline surface of the QCM may or may not yield the expected bulk structures and densities. Independent measurements of the densities are required. Even so, when densities are measured *ex situ*, their value might be affected by inclusion of, *e.g.*, water. These considerations hold true for any QCM device.

Deriving rates of metal cations deposited from binary oxide targets

Another useful quantity that can be extracted from the mass growth rates of binary oxides grown by PLD is the corresponding deposition rate of metal cations. Obtaining rates of metal cations deposited from a binary oxide compound is particularly useful in the context of better understanding the surface properties of multicomponent oxide materials: As argued in Chapters 6–8, multicomponent oxides like $SrTiO_3$ and LSMO tend to exhibit a series of composition-related surface reconstructions. Establishing quantitative cation differences between these reconstructions is the first necessary step to build theoretical models of these surfaces. The QCM is the most suited method for this task. Techniques like XPS, X-ray reflectivity, XRD, and RBS are not sensitive enough, while RHEED intensity oscillations (if observed for the given system) will in general be affected by the specific surface reconstruction, as argued in Chapter 6. The one sensitive-enough technique, STM (if even available in the growth apparatus), entails one main disadvantage: While the amount deposited could be inferred from the coverage of adatoms or 2D islands deposited on a well-defined substrate, an exact quantification of the amounts of cations relies on a precise atomic-scale understanding of the underlying substrate, the adsorption sites of the deposits, and the structure of 2D islands. With the QCM design presented here, one can determine growth rates of single cations with an accuracy of fractions of an atomic layer per pulse.

Note that the composition of the binary oxide of interest may not be always known a priori, like for TiO_2 or Fe_2O_3, but may change according to the deposition conditions (take for example manganese oxide, which exists in stable forms as MnO, Mn_2O_3, Mn_3O_4,

and MnO_2). To derive the deposition rate of metallic cations in this case, the film composition needs to be measured first. The movable QCM is ideal for this task: XPS (or any other chemically sensitive technique available in the setup) can be performed on the thick film deposited on the crystal without breaking vacuum. This is not only practical, but also necessary for sensitive or hygroscopic materials whose composition might be affected by exposure to air. Chapter 8 shows how the QCM has been used to determine Mn doses needed to switch between the surface reconstructions of LSMO(110).

Improvements

So far, emphasis was laid on the use of the QCM holder for PLD. However, since the holder can be moved and stored as a standard sample in most UHV systems, it can equally be used for other deposition techniques, as well as for vacuum systems using other types of sample holders (the sample plates of the QCM holder, currently flag-style, can be modified to fit the transfer arms of the specific setup). Possible other improvements of the design include the use of SC-cut crystals, which are stress-compensated and therefore more stable than AT-cut ones, albeit more expensive.[84] Another possibility to improve the reliability of frequency measurements would be to control the crystal temperature during measurement, in order to reach an extremum of the Δf vs. T curve, where the resonance frequency is less sensitive to temperature fluctuations; this typically occurs between 70–100 °C and 150–200 °C for AT- and SC-cut crystals, respectively.[84,87] Furthermore, small modifications of the UHV setup to provide a dedicated stage where mechanical and electrical contacts to the two plates are obtained in a more reproducible fashion can limit possible effects of spurious impedances in the measurement circuit. For example, rather than using an external linear manipulator, one can introduce an additional electrically insulated connection on the stage where the frequency is measured, such that insertion of the QCM holder into the measurement setup automatically provides solid electrical contact to both electrodes of the QCM crystal. These improvements have the potential of reducing the uncertainty on single frequency measurements, and could thus allow the detection of smaller doses deposited on the QCM.

Finally, to allow deposition at elevated temperatures that are common in PLD (around and above 600 °C), $GaPO_4$ crystals could be used.[97] Using the same temperature during the growth on the QCM as on the substrates will compensate for possible temperature-dependent sticking/re-evaporation effects. In this case, modifications in the design for withstanding the high temperatures and oxidizing environment would be limited to the materials employed: ceramic insulating parts instead of polyimide, and a high-temperature-compatible and oxidation-resistant material, such as Nicrofer® (or even Pt for extreme cases), instead of stainless steel. In this case, some optimization of the ther-

mal transport between the crystal and the plates/spring might be required to ensure a uniform temperature distribution across the crystal surface. However, the overall design and procedures would stay unchanged: Since the resonance frequency is measured before and after growth at close to RT, there is no need to optimize for temperature-induced stress during frequency measurements, nor to employ expensive crystals with small temperature coefficients at the elevated growth temperatures.

2.5.4 Conclusions

This Chapter has presented the design, and discussed the benefits, of a movable holder for a QCM sensor which enables precise measurements of PLD growth rates without breaking vacuum. Its compatibility with standard UHV transfer arms allows for easy transfer across UHV chambers and makes for simple implementation into existing vacuum setups. Growth rates are determined from changes in the resonance frequency of the QCM upon deposition. The frequency is measured before and after growth in a different position than for deposition, where electrical contact to the crystal holder (in addition to the ground contact of the other electrode) can be established. If needed, the composition of the film grown on the movable QCM can be measured without breaking vacuum (in the context of this work, by XPS).

The correct functioning of the device was showcased for the deposition of hematite Fe_2O_3 films. The QCM frequency decreases linearly with the number of laser pulses shot on the growth target, and the rates are in perfect agreement with those derived from the period of the RHEED oscillations of homoepitaxial $Fe_2O_3(1\bar{1}02)$ films grown at identical conditions. The QCM device also provides accurate quantification of growth rates of cations deposited from binary oxidic targets by PLD, which can be used to quantitatively tune the surface composition of multicomponent oxide materials.

2.6 *Ex-situ* techniques

AFM

Atomic force microscopy was used to check the mesoscale morphology of both substrates and films, by using an Agilent 5500 ambient AFM in intermittent contact mode with Si tips on Si cantilevers, both in air and in dry Ar atmosphere.

XRD

X-ray diffraction was used to inspect the crystallographic bulk properties of the grown films, and to determine the phase of powders and sintered targets. The experiments were performed at the TU Wien X-ray Center (PANalytical Empyrean; Cu Kα_1 radiation obtained with a 2-pass Ge(220) hybrid monochromator; a GaliPIX3D area detector with 0.02 rad Soller slits was used to measure reciprocal-space maps). XRD data were analyzed with the xrayutilities Python library.[98] Both the acquisition of the experimental data and their analysis was performed by Michele Riva. For this reason, this Thesis does not enter in the details of the XRD data presented.

ICP-MS

Inductively coupled plasma mass spectrometry was used to measure the stoichiometry and estimate the purity of several samples, including powders, sintered targets, and PLD-grown films. Experiments were performed in collaboration with the group of Prof. Andreas Limbeck, at the Institute of Chemical Technologies and Analytics, TU Wien.

Both laser-ablation and solution-based ICP analyses were carried out. Laser-ablation ICP is used directly on solid samples: a laser beam is focused on the sample surface and ablates material from it. The ablated species are then transported to the secondary excitation source of the ICP-MS instrument, for ionization of the sampled mass through a plasma torch. The excited ions in the plasma torch are subsequently introduced into a mass spectrometer detector for both elemental and isotropic analysis. One advantage is that the sample does not need any preparation. Moreover, the solid target can be pre-ablated roughly up to hundreds of nanometers thickness per shot, so that superficial contaminants can be removed, and reliable bulk analysis can be performed.

Solution-based ICP is suited for powders, but can also be used for solid samples (removing sacrificial layers from the samples). For each measurement, ≈0.1 g of powder was dissolved in concentrated HCl, and heated the solution for 1 h at 80 °C. The solution was then diluted with water until an HCl concentration of 1% was achieved (maximum value permitted for the mass spectrometer analyses). The sample preparation was replicated a few times to achieve reliable statistics. Note that solution-based ICP is more accurate than laser-ablation ICP in quantifying components, since higher uncertainty exists in the possible incongruent ablation of some of the chemical constituents in the latter case. On the other hand, particular care should be taken while extracting a sample for solution-based ICP: There is the risk of contaminating the sampled material, *e.g.*, with the scraping tool.

RBS

Rutherford back-scattering experiments were performed by René Heller at the Institute of Ion Beam Physics and Materials Research at the Helmholtz-Zentrum Dresden-Rossendorf e.V. for determining the stoichiometry of PLD-grown LSMO films (Section 9.5). All measurements were performed using a 1.7 MeV He ion beam directed under normal incidence onto the sample. The detector was mounted under a backscattering angle of 170°. Detector resolution was determined in advance to be 17 keV. The total acquired charge was 10–20 μC and its actual value was determined by fitting the bulk signal for each spectrum. The simulation code SIMNRA was used for determining areal densities and layer compositions.

3. TiO_2 anatase films on $SrTiO_3(001)$

3.1 Introduction

With this Chapter, focused on TiO_2, starts a series that addresses the growth and the characterization of the simplest class of oxide materials—the binary oxides. In some ways, TiO_2 can be viewed as the simplest among the simple. For one, TiO_2 is the most investigated single-crystalline system in the surface science of metal oxides.[99] Secondly, the growth community has already paid great attention to the growth of single-crystalline TiO_2 films. And yet, those are exactly the reasons why the attempt to reproduce the growth of TiO_2 (anatase) films is appropriately placed here, as the first result of this Thesis. In its humbleness, it shows the potential of PLD to realize high-quality oxide films, and of STM to ensure that their atomic-scale properties are those that one seeks after.

The widespread scientific interest in TiO_2 comes from its many and diverse applications. To name some, photocatalysis, gas sensing, self-cleaning surfaces, water purification, heterogeneous catalysis, coatings, pigments, cosmetics, and bone implants.[99] Part of the success of TiO_2, besides it having ideal physicochemical properties for many key processes, lies in its long-term stability, non-toxicity, and cost-effectiveness. TiO_2 exists in three polymorphs: rutile, anatase, and brookite, all made up of differently arranged distorted TiO_6 octahedra. The crystal structure, as well as the shape and the size of the nanoparticles, defines the area of application: Each crystalline modification has different physicochemical properties, such as density, refractive index, and photochemical reactivity.[100] For example, the anatase polymorph, the focus of this Chapter, and whose tetragonal unit cell is shown in Fig. 3.1(c), tends to show much higher photocatalytic activity than both rutile and brookite.[100–102] However, the photocatalytic activity does not only depend on the structural phase of TiO_2. It is also strongly affected by the crystallite size, orientation, specific surface areas, impurity levels, oxygen stoichiometry, pore structure, and, of course, the atomic details of the active surfaces.[99,101,103,104] To

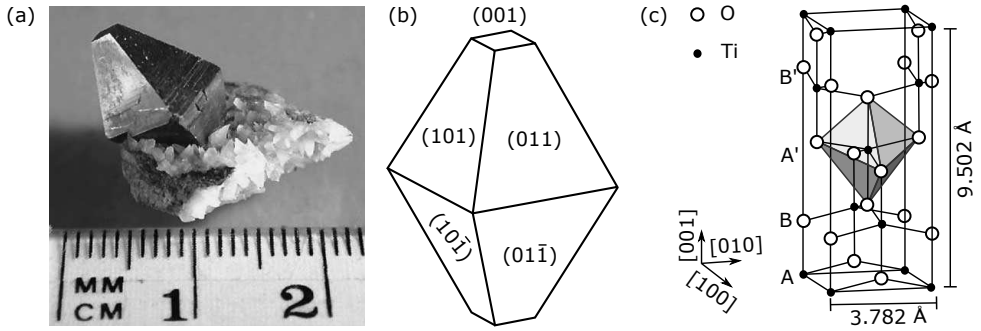

Figure 3.1. (a) Natural anatase TiO_2 single crystal, reprinted from ref. 99. (b) Calculated Wulff shape of an anatase TiO_2 crystal, adapted from ref. 105. (c) Bulk unit cell of anatase, containing four TiO_2 units. Corner-sharing, slightly distorted octahedra such as the one highlighted in gray form (001) planes; they connect with their edges to the plane of octahedra below. Adapted from ref. 105.

gain a fundamental understanding of the relevant processes occurring, *e.g.*, during photocatalysis, the more reliable approach is using well-defined model systems, in the form of single crystals or single-crystalline films with controlled surface orientation, termination, amount of defects, etc. Only with such ideal model systems can all the factors possibly participating in the reactions be disentangled.

On anatase, such well-defined studies have faced a roadblock for a while: Anatase is a metastable phase, and sufficiently large and pure single crystals have been hard to obtain up until recently. Meanwhile, scientists have worked around the issue by growing epitaxial anatase films on suitable substrates by a variety of techniques, including MBE, chemical vapor deposition, and PLD.[104,106–110] Considerable attention has been given to the (001) orientation, the second most stable facet of anatase [following the (101), see Wulff shape in Fig. 3.1(b)]. It was shown that this facet is more reactive than other majority surfaces exposed in anatase nanoparticles.[111] In UHV, the (001) surface is stabilized by a (4×1) reconstruction (see below), which dramatically reduces its reactivity.[112] However, it was predicted that the reconstruction should be lifted in liquid.[113,114] During this Thesis, (001)-oriented films have been grown to test these theoretical predictions experimentally, by taking advantage of an apparatus that allows dosing ultrapure liquid water to UHV-prepared samples without air exposure.[115]

$SrTiO_3(001)$ and $LaAlO_3(001)$ have been successfully used as substrates for the growth of (001)-oriented anatase, yielding high-quality films with atomically flat surfaces.[35,106,107,116,117] This is not too surprising for $LaAlO_3(001)$, having an almost perfect lattice match with anatase, *i.e.*, 0.2%. It was shown that the growth of anatase on $LaAlO_3(001)$ occurs in a layer-by-layer fashion, and works over a wide range of oxygen chemical potentials. On the other hand, the mismatch with $SrTiO_3(001)$ is significantly worse, namely –3.1%. It was argued[106] that this tensile strain is minimized by means of Sr interdiffusion during the first stages of growth, which enables the growth of a pseudomorphic

defective Sr_xTiO_{2+y} film matched with the substrate. After a critical thickness is overcome, unstrained anatase islands nucleate on this pseudomorphic films, and eventually merge to produce a continuous film. The resulting surface is atomically flat in STM [see Fig. 3.2(a)], and exhibits mutually orthogonal domains with (4×1) periodicity predicted by theory,[112] as seen in the LEED pattern of Fig. 3.2(c) [Fig. 3.2(b) shows the close-up STM image of one of such domains]. Similar results have been reproduced on multiple occasions.[107,109,116]

The following Sections discuss the successful attempt at reproducing high-quality anatase films grown on $SrTiO_3(001)$. Most of the results presented have been collected during the Project Work of Sebastian Moser.

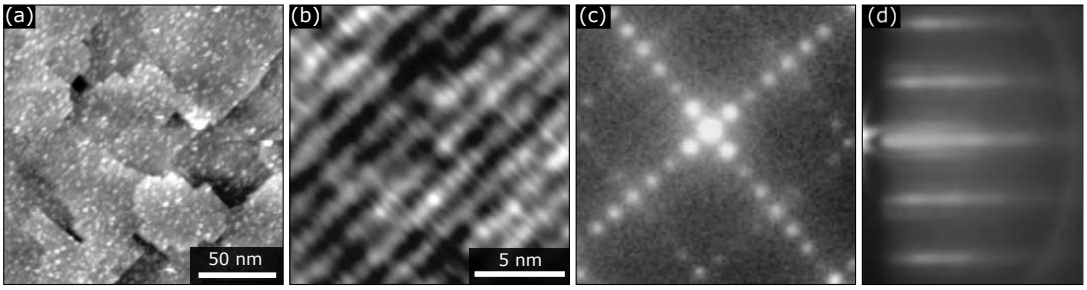

Figure 3.2. TiO_2 anatase film grown by PLD on $SrTiO_3(001)$ from the literature (adapted with permission from ref. 106). (a, b) STM images, (c) LEED and (d) RHEED patterns. The data reproduce the theoretically predicted (4×1) periodicity. The LEED pattern (c) shows that two mutually orthogonal domains are present at the surface. One such domain is visible in the STM image in panel (b).

3.2 Results

3.2.1 Substrate: $SrTiO_3(001)$

The single-crystalline $SrTiO_3(001)$ substrates were purchased from CrysTec GmbH and they were specified as 0.5 wt.% Nb_2O_5 doping, dimensions of $5 \times 5 \times 0.5$ mm^3, and miscut $< 0.3°$. As shown in Fig. 3.3(a), the unit cell of $SrTiO_3$ is cubic, with a Ti atom in the center octahedrally coordinated to oxygen atoms, and Sr atoms sitting at the corners. For small miscuts like in this case, the (001) orientation exhibits alternating SrO and TiO_2 terraces, as seen from Fig. 3.3(b). To avoid preferential sticking effects during growth, $SrTiO_3(001)$ substrates are commonly prepared to exclusively exhibit the TiO_2 termination.[118,119] For the same purpose, a recipe inspired from ref. 119 was used, consisting in:

- Sonication in 3% Extran (2×30 min), and ultrapure water (30 min), to remove residues from the mechanical polishing. As seen from Fig. 3.3(c), the surface appears clean after this treatment, but with jagged steps.

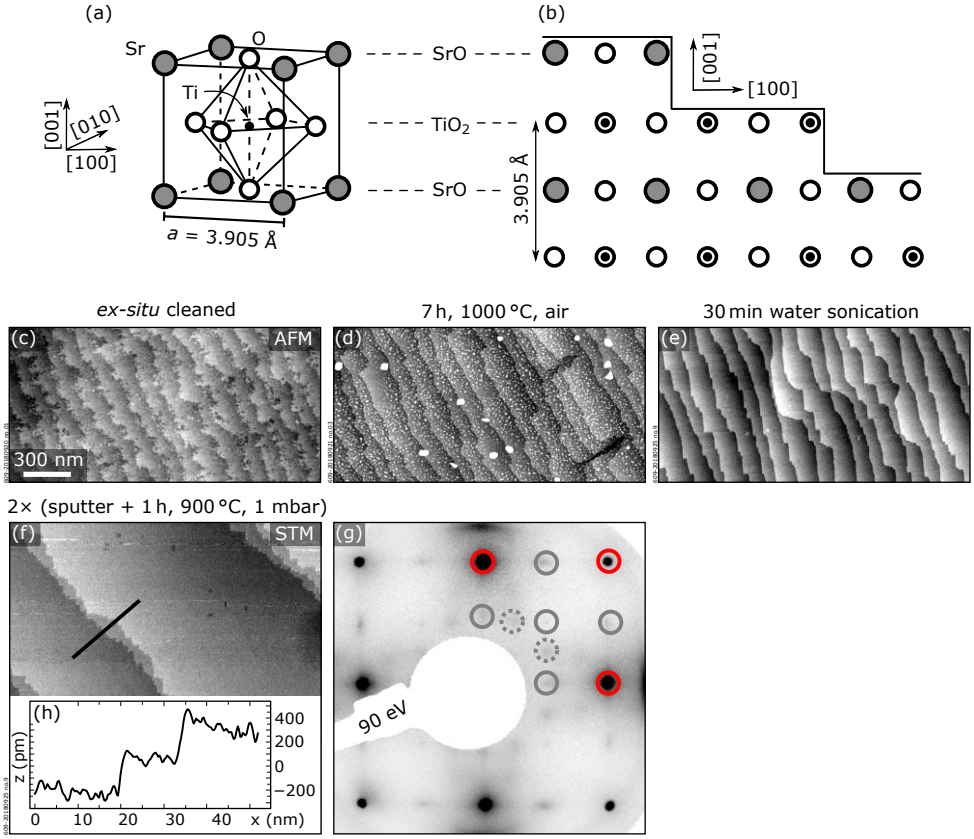

Figure 3.3. Preparation of $SrTiO_3(001)$ substrates. (a, b): Bulk-truncated models for the (001) surface of $SrTiO_3$. (c–e) 2×2 µm^2 AFM images of the $SrTiO_3(001)$ surface documenting the *ex-situ* cleaning procedure. (f) 500×280 nm^2 STM image of the UHV-clean $SrTiO_3(001)$ surface. (g) Corresponding LEED pattern; the bulk truncated, (2×2), and $c(4 \times 2)$ spots are highlighted in red, solid gray, and dashed gray, respectively.

- Annealing in air at 1000 °C for 7 h. As it appears from Fig. 3.3(d), the steps are smoother, but 3D clusters with diameter of 20–50 nm and height 3.0–5.5 nm appear, as well as smaller islands dispersed on the terrace (diameter 1–10 nm, height < 1 nm). These have been previously assigned to the segregation of excess Sr from the bulk, forming SrO_x or $Sr(OH)_x$ agglomerates at the surface.[120]

- Sonication in ultrapure water for 15 min, to dilute SrO from the surface and achieve a Ti-terminated surface [Fig. 3.3(e)]. The surface appears clean, with straight steps separated by ≈4 Å, *i.e.*, the interlayer distance between TiO_2 planes [Fig. 3.3(b)].

Notice that this recipe does not make use of buffered hydrofluoric acid, which is often employed for the same purpose, but inevitably induces undesired F contaminations.[118] After the treatment outlined above, the sample was mounted as detailed in Section 2.4.1, and inserted in the UHV system. After annealing for 1 h at 700 °C and 7×10^{-6} mbar O_2, XPS revealed that the surface was free from typical contaminants coming from the *ex-situ* treatments (C, K, Na, Ca, not shown). As seen from Fig. 3.3(f), the surface appeared

atomically flat in STM, with terraces separated by monoatomic steps of ≈4 Å height. The corresponding LEED pattern in Fig. 3.3(g) shows a (1 × 1) periodicity, plus faint (2 × 2) and $c(4 \times 2)$ structures, consistent with previous reports on $SrTiO_3(001)$.[121,122] The substrate preparation was deemed successful.

3.2.2 Film growth and characterization

For the anatase growth on the freshly prepared substrate, the growth parameters were chosen based on previous works from Radovic *et al.*,[106] specifically: 650 °C, 7×10^{-6} mbar O_2, 1.5 J/cm^2, 1 Hz. 10 min post-annealing at the same conditions followed the growth. Two films of ≈50 and ≈100 nm thickness were successfully grown with this recipe. Figure 3.4 summarizes the results on the thinner one. Real-time RHEED monitoring of the specular spot [Fig. 3.4(a)] shows a rapidly decaying signal with a small shoulder, followed by a progressive recovery of the intensity. The absence of RHEED oscillations was already reported in the literature,[110] and it is consistent with a Stranski-Krastanov growth mode.[106,107] The progressive increase of the RHEED intensity could be consistent with the merging of 3D islands generated after the wetting layer.

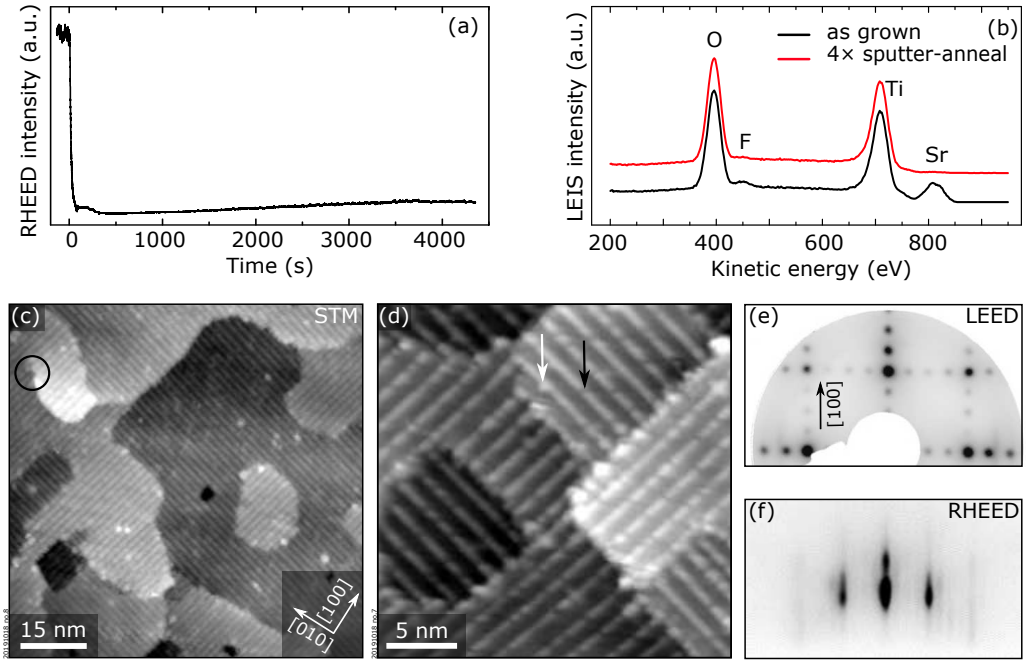

Figure 3.4. UHV characterization of an anatase $TiO_2(001)$ film of ≈ 50 nm thickness. (a) Real-time monitoring of RHEED intensity. (b) LEIS spectra after growth (black) and after four sputtering-annealing cycles (red), showing the removal of segregated Sr. (c, d) 80 × 80 nm^2 and 25 × 25 nm^2 STM images of the sputtered surface, showing the characteristic mutually orthogonal domains with (4 × 1) periodicity. Typical dark and bright defects are indicated by black and white arrows, respectively. (f, g) Corresponding LEED and RHEED patterns.

XPS surveys (not shown) reveal no other peak than of O and Ti, except for a small

Sr signal. The intensity of this Sr peak increases with the thickness of the anatase film (not shown), suggesting that Sr segregates from the $SrTiO_3$ substrate during growth, as already reported by other growth studies performed at similar temperatures.[109,116,123] LEIS [Fig. 3.4(b)] confirms the presence of Sr at the surface after growth (the small F signal observed in the LEIS spectra derives from a known contamination introduced by the mass-spectrometer). A few sputtering–annealing cycles (same annealing conditions as for the growth) are effective in removing the excess Sr, as seen in Fig. 3.4(b). This confirms that Sr segregates to the surface during growth.

The STM images of the resulting Sr-free surface in Figs. 3.4(c, d) reveal an atomically flat morphology with a few screw dislocations, one of which is indicated by the black circle in panel (c). Consistent with the literature, mutually orthogonal domains with a (4×1) periodicity are visible. This is seen also in the LEED pattern of Fig. 3.4(e), which exhibits both (4×1) and (1×4) periodicities. The surface exhibits numerous atomic defects, seen as dark and bright spots on the bright rows of the (4×1) reconstruction [indicated by the dark and white arrows in Fig. 3.4(d), respectively]. They have been assigned to TiO_2 vacancies and to intercalated Ti^{+3}, respectively, and it was shown that their amount depends on the annealing conditions[104] (the quantification of these defects was beyond the scope of the planned experiments). The surface of the as-grown film exhibits numerous bright clusters (not shown), likely associated to segregated Sr. These clusters are removed with the sputtering treatments discussed above. For completeness, the RHEED pattern of the surface in Fig. 3.4(f) is reported, also displaying a (4×1) periodicity. Similar results were obtained by growing a film twice as thick with same parameters on top of the previous one (not shown). Thicker films commonly show sharper LEED/RHEED features, indicating an improved crystallographic order.

3.3 Summary

The epitaxial growth of TiO_2 anatase films on $SrTiO_3(001)$ was successfully reproduced. The substrates were cleaned *ex situ* and prepared to exhibit the TiO_2-terminated surface with a F-free recipe inspired by ref. 119. The anatase films were grown at 650 °C and 7×10^{-6} mbar O_2, following the recipe from ref. 106. Small amounts of Sr were found to segregate during growth, but the excess Sr at the surface could be successfully removed with a few sputtering–annealing cycles. The resulting surface is atomically flat, exhibiting the already reported mutually orthogonal domains with a (4×1) periodicity.

These films have been used by Jan Balajka to test the interaction of the (4×1)-reconstructed (001) surface of TiO_2 anatase with ultra-pure liquid water, within the apparatus described in ref. 115. Preliminary results have shown that the (4×1) recon-

struction is retained upon immersion in liquid water, in agreement with ref. 124, and at odds with predictions from theoretical works.[113,114]

4. Ti-doped α-$Fe_2O_3(1\bar{1}02)$ films

4.1 Introduction

This Chapter deals with another notable binary oxide: α-Fe_2O_3, or hematite, the most stable iron oxide at ambient conditions (see the phase diagram of iron oxides in Fig. 4.1). The study presented here testifies to the strength of the combined PLD–surface science approach to produce well-defined model systems for fundamental investigations. Aiming to better understand the photoelectrochemical (PEC) water splitting taking place at Ti-doped hematite surfaces, high-quality Ti-doped hematite films of $(1\bar{1}02)$ orientation were produced and characterized. By alternating between an iron oxide and a titanium oxide target during the growth, the doping level of the film could be tuned at will and with high accuracy, always retaining single-crystal-like quality. The surface atomic-scale changes induced by Ti dopants were observed and quantified by STM, and, with support from DFT, modeled. As argued later, the tunable and well-defined model system that has been built offers reliable routes to shed light on the fundamental processes governing PEC water splitting at hematite surfaces.

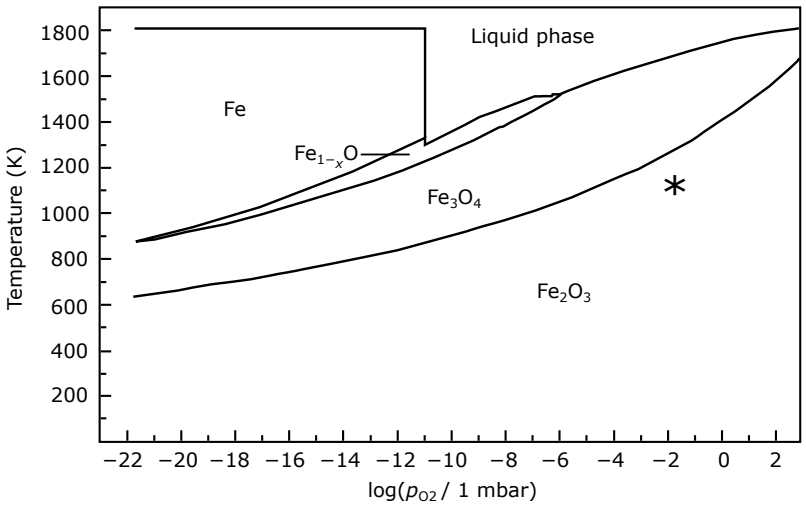

Figure 4.1. Phase diagram of iron oxides. The asterisk indicates the growth parameters chosen for the hematite films. Adapted with permission from ref. 94.

Before presenting and discussing the results, a brief summary is given of the properties and the applications of α-Fe_2O_3 (Section 4.1.1). Section 4.1.2 addresses the promises and the challenges connected to the use of Ti-doped α-Fe_2O_3 for hydrogen production via PEC water splitting, stressing the benefits of having a well-defined and tunable system to model the relevant processes.

4.1.1 α-Fe_2O_3

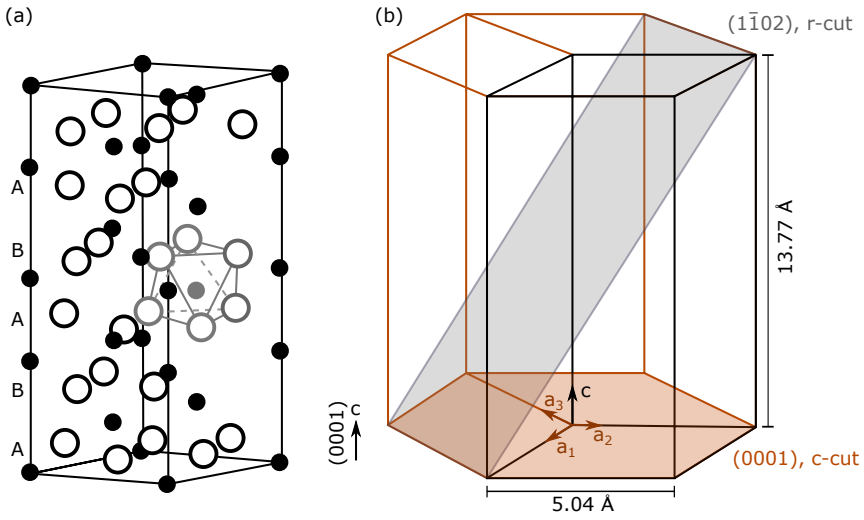

Figure 4.2. (a) Bulk unit cell of α-Fe_2O_3 (b) Schematics showing the orientation of the $(1\bar{1}02)$ plane (gray) within the hexagonal unit cell of α-Fe_2O_3 (black).

α-Fe_2O_3 is a transition metal oxide. It crystallizes in the corundum structure shown in Fig. 4.2, with O anions (empty circles) forming a hexagonal close-packed sublattice with ABAB stacking, and Fe^{3+} cations (full dots) occupying two-thirds of the octahedral interstitials and forming two sublayers [one distorted octahedron is shown in gray in Fig. 4.2(a)].[125]

Besides being stable at ambient conditions, α-Fe_2O_3 is ubiquitous and not toxic. These qualities, plus the specific physicochemical properties, have boosted technological and scientific interest in α-Fe_2O_3 spanning many fields, including hydrogen production via PEC water splitting (the main motivation for the studies presented in this Chapter), as well as energy storage,[126,127] gas sensing,[128] catalysis (particularly relevant is the production of styrene[129]), waste-water treatments,[130] and geochemistry.[131] In all these applications, reactions occur at the surface of hematite, and the desire is often to improve their activity and/or selectivity. This is a dream challenge for surface scientists: If available, one can use a well-defined model system suited for atomic-scale investigation to unveil the role of specific surface stoichiometries, structural properties, defects, environmental conditions, etc. on a given reaction, and has a chance of optimizing it.

However, this line of research has been hampered by some technical challenges: The available natural hematite single crystals often contain ill-defined amounts of impurities that segregate to the surface upon annealing, while STM is hindered by the 1.9–2.2 eV bandgap of the material.[132] Sputtering–annealing cycles may be effective to remove contaminations and/or achieving sufficient conductivity for STM,[96] but, as shown later, this treatment modifies the surface morphology unreliably. A viable strategy to obtain conductive, highly crystalline surfaces that are suited for STM investigations is to grow *doped* epitaxial films: For small enough doping levels, the effect of the dopants can be deemed negligible, or at least known and controlled. Such films would be ideal systems to study the basics of a plethora of phenomena with STM. At the same time, as argued in just a moment, doped films with tunable doping level can be of direct interest for fields like PEC water splitting.

4.1.2 Ti-doped α-Fe_2O_3 for PEC water splitting

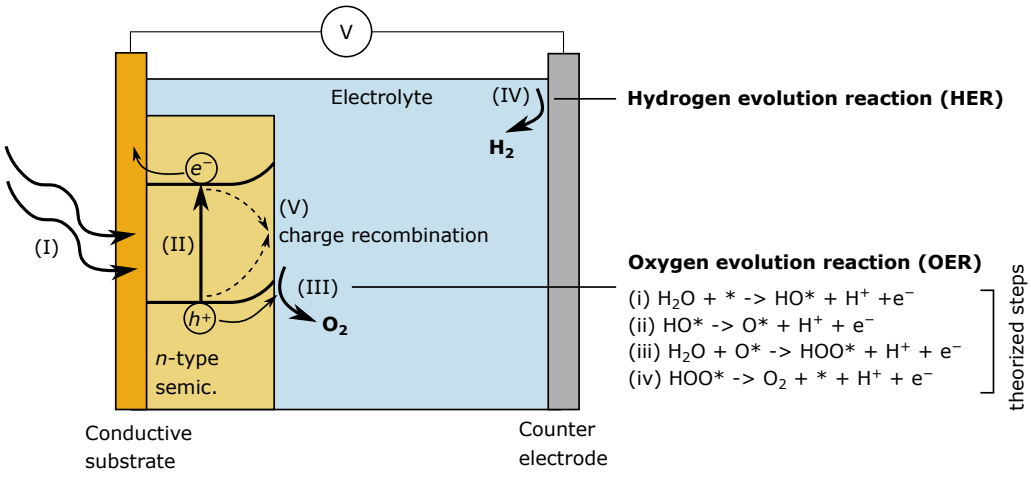

Figure 4.3. Sketch of a photoelectrochemical cell. Light is absorbed at a semiconductor anode (I), producing electron–hole pairs (II). These charges either trigger redox reactions (III, IV) at the surfaces of the electrodes, or recombine at the anode (V).

Since its discovery roughly half a century ago,[133] PEC water splitting has become a well-attended field of research in its own right.[134] The reason for the high interest is that PEC water splitting is a sustainable, cost-effective, and eco-friendly way to produce hydrogen, holding promise for the development and mass-distribution of hydrogen-based energy technologies.

The basic principle of PEC is simple: Solar energy is used to split water into molecular oxygen and hydrogen, which can be then harvested and used in energy applications. Figure 4.3 shows the sketch of a PEC cell. Light is absorbed at a semiconductor material supported by a conductive substrate, which acts as the working anode (I) (the next Sec-

tion discusses why hematite is an ideal anode material); if the photon energy is larger than the band-gap of the anode, electron–hole pairs form (II). Holes migrate towards the anode/electrolyte interface and trigger the oxygen evolution reaction (OER), *i.e.*, production of molecular oxygen from water, or water oxidation (III). Electrons travel to the counter electrode and enable the production of hydrogen by reducing water (hydrogen evolution reaction, HER) (IV). Note that a fraction of the electron–hole pairs recombines in the bulk and at the surface of the anode, thus not contributing to fuel generation (V). Since the OER reaction (III) is one bottleneck of the overall PEC performance, many efforts have been put in understanding the detailed mechanisms of this reaction, mostly on a theoretical ground. Commonly accepted theoretical models assume the reaction to take place via subsequent elementary steps of proton-coupled electron transfers[135] (see Fig. 4.3; the star stands for the reactive site or for absorption at the reactive site). However, these processes have not been isolated experimentally. Identifying the reactive sites involved at each stage of the OER reaction with controlled experiments is a necessary step to optimize the OER reaction and the overall PEC performance.

The anode material affects OER performances greatly. Ideal qualities are band energetics that allow efficient harvest of visible light, high charge mobility and long charge carrier diffusion length to limit charge recombination, and optimal catalytic activity for OER. Welcomed bonuses are (electro- and photoelectro-)chemical stability in the electrolyte, sustainability, cost-viability, and environmental friendliness of the material.[134] α-Fe_2O_3 (for simplicity of notation, the α will be dropped from now on) is a promising anode candidate because it theoretically enables a solar-to-hydrogen efficiency of 15%, as well as for its high stability, non-toxicity, abundance, and low-cost.[134,136] However, at present, hematite anodes for PEC have only seen the light of research laboratories. The poor kinetics for water oxidation, fast charge recombination, and low conductivity[134,136] hamper the photoelectrochemical performance, and hinder commercial use.

To enhance the PEC performance of Fe_2O_3 anodes, both nanostructuring and incorporation of foreign cations (most commonly, Ti) have proven effective.[137] The mechanisms through which nanostructuring the anode improves the performance are rather clear: First, there is an increased surface area that can participate to the OER. Moreover, the typical diameter of the crystallites is comparable to the hole diffusion length, so that most of the photogenerated holes can reach a surface before recombination. On the other hand, the correlation between increased PEC activity and introduction of Ti dopants in Fe_2O_3 is less straightforward to pinpoint. In fact, many properties of hematite can affect the OER and are possibly doping-dependent. These include the electrical conductivity in the bulk and at the surface,[138] the surface crystallographic orientation and its morphology,[137,139–141] its atomic-scale structure[71,137,142] and the surface states that are

involved in the relevant processes.[143] Understanding the influence of Ti doping on the OER process requires to disentangle these properties. However, this is tricky for most of the commonly synthesized Ti-doped hematite electrodes, which are characterized by complex, nanostructured morphologies that are not easily controlled nor modeled.[136,137] Moreover, both their morphology and their photoelectrochemical activity are affected by the doping level, *e.g.*, as a result of passivation of grain boundaries by the dopants.[139] To date, the question of the correlation between OER activity of Fe_2O_3 photoanodes and Ti doping remains open.

Restating a mantra of this Thesis, single-crystalline samples (*e.g.*, in the form of epitaxial films) may offer a solution, providing routes to establish the correlation between Ti doping and increased OER activity of Fe_2O_3 photoanodes. Their atomically defined surfaces could enable to precisely investigate and model how Ti impurities affect the atomic-scale details of the surface, in turn allowing to disentangle contributions due to structural, morphological, electronic, and crystallographic effects.[137,142,144] Producing such well defined films is the first necessary step in this direction. In fact, single-crystalline epitaxial films of Ti-doped hematite (Ti:Fe_2O_3) with the (0001) orientation have been successfully grown by oxygen-assisted MBE.[144,145] However, there has been no investigation on the influence of Ti on the atomic-scale details of the (0001) surface of these Ti-doped films, nor on the OER. The lack of atomic-scale investigations is possibly in part due to the controversy over the atomic-scale model of the (0001) termination of Fe_2O_3.[142,146] The less investigated $(1\bar{1}02)$ termination (or r-cut) of hematite [see Fig. 4.2(b)] is a more sound model system in this respect. Recently, combined surface science and DFT studies[96,147] have unveiled two relatively simple surface terminations intrinsic to this facet that are stable under UHV conditions: The stoichiometric, bulk-truncated (1×1) (Fig. 4.4), and the reduced (2×1) surfaces.[148] Both surface structures can be reproducibly prepared by standard sputtering–annealing cycles at appropriate oxygen chemical potentials. Their reliable experimental realization and the availability of confirmed, atomic-scale models make them ideal model systems to investigate how Ti impurities affect hematite surfaces and their OER activity. In fact, this Chapter shows that the small amounts of Ti dopants introduced (below 3 at.%) cause only a minor modification of these surfaces.

Note also that doping this system with Ti should enhance its conductivity,[138,139] a bonus for STM. As mentioned before, contaminant-free, undoped $Fe_2O_3(1\bar{1}02)$ single crystals are not conductive enough for STM, unless their bulk is reduced by repeated (60–100) sputtering–annealing cycles to introduce oxygen vacancies.[96] This treatment roughens the surface, though, complicating STM measurements and the interpretation of reactivity studies. Increasing the conductivity with Ti doping would cut the need

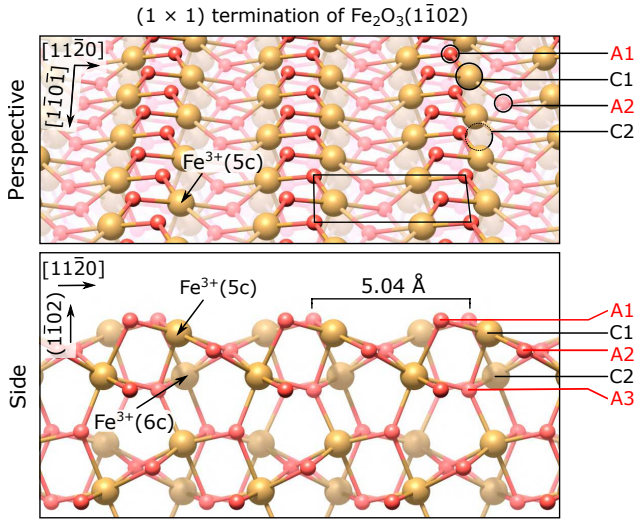

Figure 4.4. α-$Fe_2O_3(1\bar{1}02)$ surface. Perspective (top row), and corresponding side views (bottom row, looking along the $[1\bar{1}01]$ direction) of the (1×1) terminations of $Fe_2O_3(1\bar{1}02)$, as calculated in ref. 96. The direction perpendicular to the surface is labeled as $(1\bar{1}02)$ in round brackets because there is no integer-index vector corresponding to that direction for the $(1\bar{1}02)$ plane. The (1×1) structure is characterized by zigzag rows of oxygen and iron atoms and has a unit mesh measuring 5.04×5.44 Å^2. The coordination of Fe cations is indicated in brackets, and the first anion and cation layers are indicated. Adapted from ref. 66.

for harsh sputtering treatments, thus facilitating and stimulating more surface science studies on this promising system.

The Sections to follow discuss the growth of epitaxial Ti-doped $Fe_2O_3(1\bar{1}02)$ films and their surface characterization and modeling. Most of the results presented have been published in ref. 66. The focus is set on the (1×1) surface of Fig. 4.4, addressing how it is modified locally by the presence of Ti, from both an STM and a DFT point of view. Based on the established well-defined model system, the Chapter moves on to present an envisioned experimental strategy to investigate OER in the future. Section 4.7 shortly outlines in which other contexts have the films been employed, while Section 4.9 shows the successful attempt at growing a Ti-doped hematite film with (0001) orientation, using the same parameters and procedures as for the $(1\bar{1}02)$ orientation.

4.2 Methods

Growth parameters. All Ti-doped $Fe_2O_3(1\bar{1}02)$ films discussed in this Thesis were grown by PLD by alternating deposition from TiO_2 and Fe_3O_4 single-crystalline targets. The deposition parameters were always set to 2.0 J/cm^2 laser fluence, 5 Hz, O_2 pressure of 2×10^{-2} mbar, substrate temperatures of 850 °C, and ramp rate of 60 °C/min. The substrate temperature was ramped down to RT right after growth (no post-annealing). More details about the rationale behind the choice of the growth parameters are given

in Section 4.3.1.

Note that the strategy used here to introduce the desired doping in the hematite films is based on alternating growth from TiO_2 and iron-oxide targets. Another possibility is to grow from a single, Ti-doped hematite target. While alternating between targets yields high flexibility in tuning the doping level, it requires a careful calibration of the deposited amounts: As seen throughout this Thesis, sticking effects (Chapter 6), the oxygen chemical potential (Chapters 5 and 9) and the laser fluence (Chapter 6) can all affect the deposition process. Section 4.8.1 discusses how the doping levels have been determined.

The doping levels of the films discussed here have been measured to be (0.77 ± 0.06) at.% and (3.09 ± 0.24) at.%, such that 0.77 at.% doping corresponds to x = 0.0077 in the commonly used $(Fe_{1-x})_2Ti_xO_3$ notation. For simplicity of notation, these doping levels are henceforth referred to as 0.8 at.% and 3.1 at.%, or simply 'low' and 'high'. The doping levels of 0.8 at.% and 3.1 at.% were achieved by running an automated growth recipe consisting of 120 cycles in which one (or three, for 3.1 at.%) laser pulses were shot on the TiO_2 target, followed by 500 (375) laser pulse(s) shot on the Fe_3O_4 target. The low-doped films [120 cycles of (500 + 1) laser pulses] are of (91.5 ± 7.4) nm thickness, as evaluated from stylus profilometer measurements (not shown). Alternation between the targets was allowed by an automated recipe which repeatedly switched targets, scanned the desired target, and shot a defined number of pulses before stopping the scanning, and switch targets again. Note that the reduced magnetite (Fe_3O_4) was used as a target because it was available at the moment of the experiment; the oxygen stoichiometry of the film (desirably Fe_2O_3, in this case) is anyway dictated by the growth conditions, rather than the oxygen stoichiometry of the target.

A few ultra-low-doped films (below 0.03 at.%) have also been grown by alternating deposition from the same Fe_3O_4 single crystal and a home-synthesized 1 at.% Ti-doped hematite target (details about this target are given in Section 2.3.6; the recipe consisted in alternating 9 pulses on the 1 at.% Ti-doped Fe_2O_3 target with 300 pulses on the Fe_3O_4 target at 850 °C, 2×10^{-2} mbar O_2, 2 J/cm^2, 5 Hz; the estimated 0.03 at.% doping assumes that ablation of the 1 at.% Ti:Fe_2O_3 and Fe_3O_4 is comparable). This small doping level is sufficient to achieve enough conductivity for STM, while the sample's properties can be still essentially regarded as those of the undoped ones (there is no indication of Ti at the surface).

Substrate: $Fe_2O_3(1\bar{1}02)$. $Fe_2O_3(1\bar{1}02)$ single crystals were used as substrates (SurfaceNet GmbH, $5 \times 5 \times 0.5$ mm^3, one-side polished, $< 0.3°$ miscut). Depending on

the availability at the time of the experiments, either as-received crystals or crystals previously used by colleagues in the group for UHV experiments have been used as substrates. The as-received crystals were cleaned *ex situ* by sonicating in heated 3% Extran (2×30 min) and ultrapure water (10 min), in order to remove contamination resulting from polishing. To overcome the insulating nature of the substrates, and ensure electrical contact of the conductive film to the sample plate, appropriate Pt electrodes were deposited on the substrates, as discussed in Section 2.4.2. Because Fe_2O_3 absorbs the IR radiation better than Pt, Pt deposition on the back of the sample was limited to a 0.5 mm-wide frame at the edge of the sample, rather than on the whole surface of the back. The substrates were then mounted as discussed in Section 2.4.1, and inserted in UHV.

UHV preparation of the surface followed. To grow high-quality epitaxial films, this preparation must yield atomically flat surfaces. In this respect, a crystal with an UHV history is problematic: To achieve sufficient conductivity for STM, undoped Fe_2O_3 single crystals typically undergo repeated (60–100) sputtering–annealing cycles in UHV,[96] which results in severely roughened surfaces, as seen from Fig. 4.5(a): 2–4 nm-deep pits surrounded by 2–4 nm-high rims are ubiquitous. It was found that ideal morphologies can be recovered by annealing for 1 h at 900 °C and 1 mbar O_2 [Fig. 4.5(b)], or after a couple of sputtering–annealing cycles performed at the same conditions [Fig. 4.5(c)]. Besides yielding atomically flat morphologies like the one of Fig. 4.5(c), this treatment also removes surface contaminants, as seen from XPS (not shown): Neither typical contaminants coming from the *ex-situ* treatments (C, K, Ca, Na), nor foreign metals commonly present in hematite natural crystals (*e.g.*, Mn, Cr) were observed in the survey spectra acquired with 50 eV pass energy (neither at normal nor at grazing exit). Prior to each growth experiment, two sputtering–annealing cycles were always performed at these conditions, both for fresh crystals and for those with an UHV history.

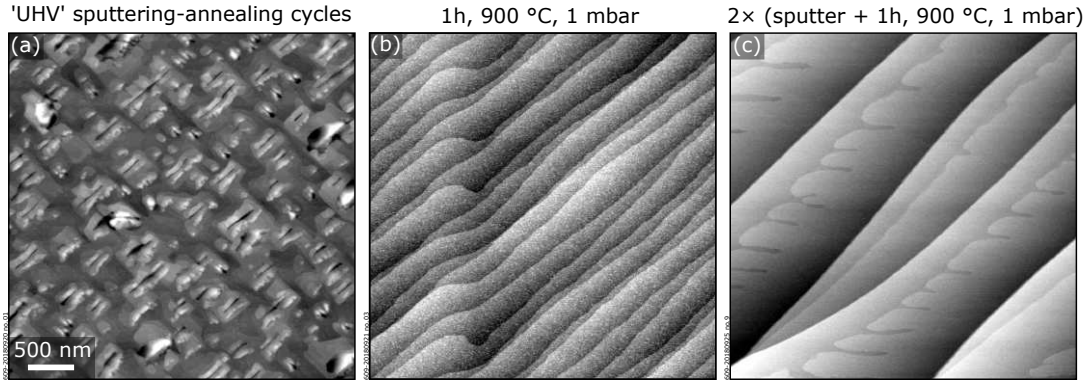

Figure 4.5. UHV preparation of the substrates, undoped $Fe_2O_3(1\bar{1}02)$ single crystals. 3×3 μm^2 AFM images after (a) repeated sputtering–annealing cycles in UHV aiming to make the sample conductive for STM; (b) after annealing for 1 h at 900 °C and 1 mbar O_2; (c) after two cycles of sputtering plus annealing at 900 °C and 1 mbar O_2.

Evaluation of the trench coverages. The coverages (θ) of the Ti-induced trenches (see Fig. 4.7 below) were evaluated with the processing software ImageJ.[75] They correspond to the fractional amount (in monolayers) of missing Fe atoms in the topmost cation layer. The trench coverages reported were obtained by averaging the values measured on at least ten atomically resolved 50×50 nm^2 STM images acquired at different spots on the sample. To evaluate the number of missing Fe atoms at the surface, a skeletonized mask selecting only the lattice position of surface Fe atoms was overlaid to the image (this mask was created from the maxima of the Fourier-filtered image). A threshold function was then applied to the area of the image under the mask to count the ratio of pixels of a trench with respect to the number of total pixels selected by the mask. Regions in proximity ($\approx$2 nm) of steps were discarded from the analysis. Error bars of the coverages represent 90% confidence intervals calculated with a two-tailed Student's t-distribution from the standard error of the mean that was obtained by statistical evaluation of several STM images. Error bars of derived quantities are calculated assuming statistical independence of the quantities involved.

Computational details. DFT calculations were performed by Florian Kraushofer and Matthias Meier. They employed the Vienna ab-initio simulation package (VASP)[149,150] with the projector augmented wave method[151,152] describing the electron-ion interactions. The Perdew, Burke, and Ernzerhof[153] exchange–correlation functional was employed together with a Hubbard U (U_{eff} = 4.0 eV, consistent with previous works)[96,154] to treat the highly correlated Fe 3d electrons.[155] The value U_{eff} = 4.0 eV was shown to best reproduce the experimental values of the bandgap and the Fe–Fe distances in the bulk of Fe_2O_3.[156] The same U_{eff} was used for the Ti dopant ions so as not to artificially bias the 3d electron occupations among different transition metal cations.[157] For the best structures, calculations were also repeated with U_{eff} = 5.0 eV for Ti^{4+} as derived from experiments and first-principle calculations,[157–159] with no significant changes in the relative stabilities of the structures. The plane-wave basis-set cut-off energy was set to 450 eV. Asymmetric slabs consisting of 20 atomic layers (*i.e.*, four O–Fe–O–Fe–O units, $\approx$13 Å slab thickness) were constructed based on the previously optimized bulk structure. A vacuum gap of 16 Å was used to separate periodic images of the slab along the direction normal to the surface.[96] Supercell sizes for testing Ti dopant positions ranged from (2×1) to (4×4), depending on the defects considered. A γ-centered **k**-mesh of $4 \times 8 \times 1$ was used for the (2×1) cells and adjusted according to supercell size, down to $2 \times 2 \times 1$ for the (4×4) slabs. All surface models were relaxed until the residual forces acting on ions were smaller than 0.02 eV/Å. The reference energy of a free

oxygen molecule in the triplet state in a $10 \times 11 \times 12$ Å^3 cell was calculated with the same functional and potential as for the Fe_2O_3 slabs. The chemical potential of oxygen was referenced to half of the energy of one oxygen molecule $1/2(E_{O_2})$; in the following, this quantity is named $\mu_O{}^{DFT}$. Notice that this definition does not account for entropic contributions, as is common in *ab-initio* thermodynamics.[156,160]

4.3 Experimental results

4.3.1 Choosing the growth parameters

Three main parameters were optimized to achieve the desired high-quality films: The O_2 background pressure, the substrate temperature, and the doping level. They were chosen to comply with three main (intertwined) constraints: (i) stabilize the oxidized hematite phase; (ii) achieve sufficient diffusion during growth to yield well-ordered, single-crystalline films; (iii) ensure a dilute, uniform distribution of Ti dopants within the film. The laser fluence and the laser repetition frequency were kept the same for all experiments, at 2.0 J/cm^2 and 5 Hz, respectively.

Stabilize the hematite phase and achieve high crystallinity

The hematite phase was always stabilized by choosing appropriate combinations of temperature and pressure, in line with the stability phase diagram of iron oxides shown in Fig. 4.1 from ref. 94, showing that changes in temperature are always linked to changes in pressure. Temperatures enforcing a step-flow regime were aimed for, to achieve the highest possible crystallinity. The threshold temperature for growth in step-flow mode was established by growing homoepitaxial films of Fe_2O_3 at different temperatures (each time at sufficiently oxidizing background pressure), while monitoring the real-time intensity of the RHEED specular spot. RHEED oscillations consistent with a layer-by-layer growth were observed below 750 °C, while no oscillations were observed above 800 °C, a possible sign of step-flow growth. Interestingly, the rates of deposition during the layer-by-layer regime (as inferred from the periodicity of the corresponding RHEED oscillations) is identical from room temperature to 600 °C, suggesting that re-evaporation effects are negligible. This fact has been important for the proof of principle of the movable QCM holder presented in Section 2.5.

Diffusion of Ti with the substrate temperature

Next it was tested whether these high temperatures yield the desired uniform doping profile across the bulk of the film. An even distribution of dopants in the film is necessary for effectively contacting it to the Pt electrodes that was deposited on the pristine substrate (see Section 2.4.2).

In principle, high temperatures should favor the diffusion of the dopants, but their behavior is not known a priori: Irreversible migration toward the bulk of the Fe_2O_3 substrate or severe segregation to the surface could take place. While it has been reported both experimentally and computationally[138,145] that Ti atoms substitute Fe cations in the bulk of doped films in a random fashion, it has been also observed that Ti tends to accumulate at the hematite surface.[139] To test the behavior of the dopants with the substrate temperature, a fixed amount of Ti was deposited in PLD: 10 laser pulses at RT, and 2×10^{-2} mbar O_2 on a UHV-prepared, undoped $Fe_2O_3(1\bar{1}02)$ single crystal. Subsequently the sample was annealed for 15 min at increasingly higher temperatures. The deposited amount was chosen to be small enough to avoid the formation of ill-defined, Ti-rich areas, but sufficiently large to allow detection of changes in the XPS Ti 2*p* signal [Section 4.8.1 shows that 10 laser pulses correspond to 0.32 ML, where 1 ML corresponds to the number of Fe atoms in one cation layer per (1×1) surface unit cell of $Fe_2O_3(1\bar{1}02)$, or 7.3×10^{14} at./cm^2]. To ensure deposition of consistent amounts of material in all experiments, the pressure during deposition was kept constant. To recover the pristine sample, the sample was re-prepared by annealing for 30 min at 1 000 °C, 0.2 mbar O_2 before each deposition/annealing experiment.

The corresponding XPS Ti 2*p* spectra are shown in Fig. 4.6(a), while their intensity, normalized to the intensity of the peak after room-temperature deposition, is plotted

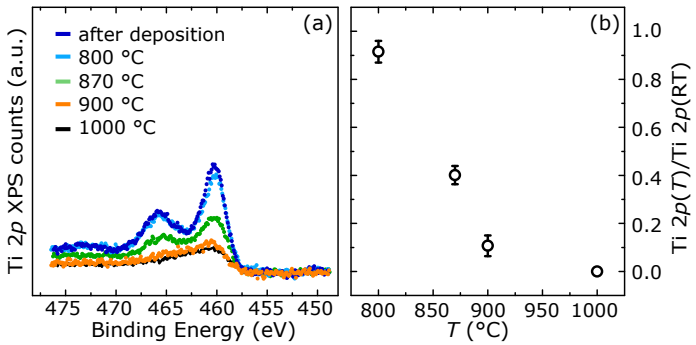

Figure 4.6. Effect of substrate temperature on the diffusion of Ti dopants. (a) XPS Ti 2*p* spectra measured on a UHV-prepared, undoped $Fe_2O_3(1\bar{1}02)$ single crystal after depositing 0.32 ML Ti at RT and annealing for 15 min at 2×10^{-2} mbar O_2 and the temperatures indicated (the sample was re-prepared each time). Increasing temperatures cause Ti diffusion to the bulk until the pristine sample is recovered at 1 000 °C. (b) Intensity of peaks from panel (a), normalized to the intensity measured after each corresponding deposition at RT. Reprinted from ref. 66.

against the annealing temperature in Fig. 4.6(b). The intensity of the Ti 2*p* peaks was evaluated in CasaXPS by normalizing their area to the one of the corresponding O 1*s* peak, and subtracting the normalized intensity of the O 1*s* satellite superimposed to this feature that originates from the Kβ line of the Al X-ray source. The intensity and line-shape of the O 1*s* satellite had been previously measured on a reference, undoped $Fe_2O_3(1\bar{1}02)$ sample. All XPS peak areas were evaluated after subtracting a Shirley-type background. The small change observed upon annealing at 800 °C suggests that the dopant diffusion is largely inhibited at this temperature. On the other hand, 870 °C and 900 °C produce a 60% and a 90% decrease in the XPS signal, respectively, while at 1 000 °C the Ti signal is completely lost. These results are in qualitative agreement with literature data on iron self-diffusion in bulk hematite single crystals[161–163] (while no data exist for bulk diffusivity of Ti dopants in hematite, one can expect diffusion coefficients for Ti of the same order of magnitude as for Fe): In 15 min, Fe cations are predicted to travel only 0.1—0.3 nm at 800 °C while they can cover longer distances at higher temperatures (0.7—3 nm at 900 °C, and 4—24 nm at 1 000 °C), consistent with the observed decrease of the XPS intensity.

850 °C was chosen as the growth temperature, because it allows fast dopant diffusion while avoiding complete irreversible diffusion into the bulk of the substrate. Moreover, this temperature enforces a step-flow growth mode (see previous Section). *Post-mortem* tests performed on films grown at 850 °C, 2×10^{-2} mbar O_2 support this choice: First and foremost, the samples can be measured in STM at RT (U_{sample} = +2 V, I_t = 0.2 nA) after a single sputtering–annealing cycle, as opposed to undoped single crystals that typically require reduction of the bulk via tens of cycles.[96] Moreover, the amount of Ti-induced defects (see next Sections) stays roughly unchanged upon performing several consecutive sputtering–annealing cycles, suggesting a reasonably uniform distribution of the dopants within the films. Post-annealing of the films was avoided to prevent excessive diffusion of the Ti dopants in the bulk.

4.3.2 UHV-prepared films

Figure 4.7 compares how different bulk doping levels (0.8 at.% and 3.1 at.%) affect the surfaces of UHV-prepared Ti:$Fe_2O_3(1\bar{1}02)$ films. After growth, the films' surfaces were prepared following the procedures for single-crystalline, undoped $Fe_2O_3(1\bar{1}02)$ samples.[96] One can either prepare a (2×1) structure under reducing conditions (Ar^+ sputtering plus UHV annealing at 600 °C), or a stoichiometric, bulk-terminated (1×1) structure (Fig. 4.4) under slightly oxidizing conditions (Ar^+ sputtering plus annealing at $> 1 \times 10^{-6}$ mbar O_2, 550 °C). Due to their strongly insulating nature, hematite surfaces of undoped crys-

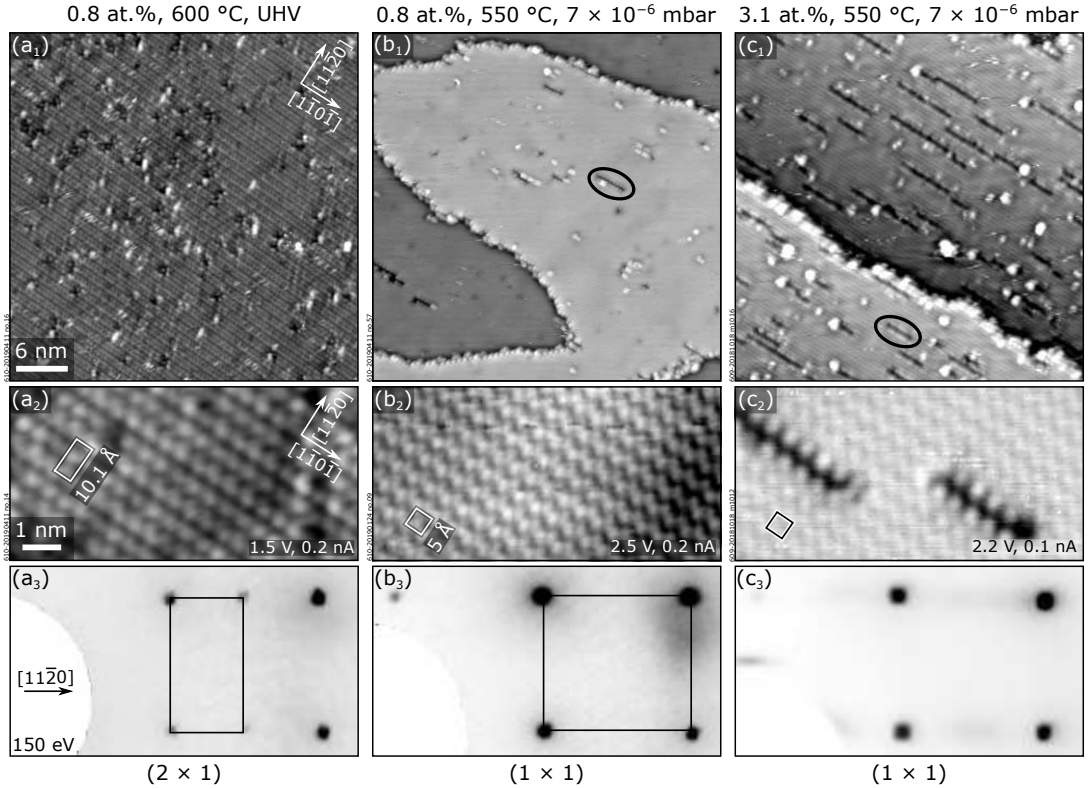

Figure 4.7. UHV-prepared surfaces of differently doped Ti:$Fe_2O_3(1\bar{1}02)$ films. (a_1, b_1, c_1): 40 × 40 nm^2 STM images; (a_2, b_2, c_2) 9 × 4.5 nm^2 STM images; (a_3, b_3, c_3): corresponding LEED patterns. Left and middle columns: (2 × 1) and (1 × 1) terminations, respectively, obtained on the 0.8 at.% Ti-doped films with standard sputtering–annealing cycles [anneal 20 min at 600 °C, UHV for the (2 × 1), and 20 min at 550 °C, 7 × 10^{-6} mbar O_2 for the (1 × 1); the corresponding experimental oxygen chemical potentials μ_O^{exp} are calculated as −1.95 eV and −1.55 eV]. Except for the dark rows, the surfaces are very similar to those found on undoped single crystals. Right column: Defective (1 × 1) surface obtained on a 3.1 at.%-doped film after preparation at slightly oxidizing conditions (550 °C, 7 × 10^{-6} mbar O_2); a mostly (1 × 1) surface is obtained, with additional dark rows along the $[1\bar{1}0\bar{1}]$ direction. The (1 × 1) periodicity is seen in the close-up STM (c_2); faint streaks corresponding to an (n × 1) periodicity are observed in LEED (c_3). Preparing the 3.1 at.%-doped film at reducing conditions results in a (2 × 1) reconstruction comparable to the one shown in the left column (not shown). Reprinted from ref. 66.

tals can only be imaged in STM after sufficient reduction of the bulk, commonly achieved with several (60–100) sputtering–annealing cycles.[96] Remarkably, both Ti-doped films are conductive in STM at U_{sample} = 2 V, I_t = 0.1 nA at RT after a single sputtering–annealing cycle. Figures 4.7(a_1–c_1) show the mesoscale appearance of their surfaces after two sputtering–annealing cycles. The 50–200 nm wide, atomically flat terraces are separated by monoatomic steps of ≈3.5 Å height. The surface quality of these Ti-doped films is significantly higher than that of the severely roughened surfaces typical of undoped crystals following the harsh sputtering treatments [Fig. 4.5(a)].

The low-doped film reproduced both the (1 × 1) and the (2 × 1) surface structures known from undoped samples, as seen from the close-up STM images [Figs. 4.7(a_2, b_2)] and the LEED patterns [Figs. 4.7(a_3, b_3)]. The (2 × 1) surface [Fig. 4.7(a)] shows paired

rows of bright protrusions running along the $[1\bar{1}0\bar{1}]$ direction with a 10.1 Å periodicity along the $[11\bar{2}0]$ direction, in agreement with STM images obtained on undoped samples.[96] The (1×1) surface [Fig. 4.7(b)] is also in line with previous experimental reports, with zigzag lines of bright protrusions (Fe atoms) along the $[1\bar{1}0\bar{1}]$ direction, separated by ≈5.0 Å in the $[11\bar{2}0]$ direction [compare also with the structural model of Fig. 4.4(b)]. Note that there is no evidence for Ti impurities at the (2×1) surface (the observed defects are also typical for undoped single crystals). On the (1×1) surface, however, some new features are present in the form of dark rows oriented along the $[1\bar{1}0\bar{1}]$ direction, as highlighted by the black oval in Fig. 4.7(b_1). Below it is argued that these defects are induced by the presence of subsurface Ti, and that they form when a zigzag row of surface Fe atoms is missing. From an STM evaluation of the coverage of dark lines, one can obtain the amount of Fe atoms missing at the surface (details in Section 4.2); on the (1×1) surface of the 0.8 at.% film in Fig. 4.7(b_1), (2.08 ± 0.39)% surface Fe sites are missing.

On films with a four-times larger doping level, the same (2×1) reconstruction apparently unmodified by Ti can be prepared as for the 0.8 at.% film (not shown). However, some changes are observed when the surface is exposed to oxidizing conditions to achieve the (1×1) termination: While the mesoscale morphology is atomically flat [Fig. 4.7(c_1)], more dark rows along the $[1\bar{1}0\bar{1}]$ direction appear, suggesting a correlation between dark rows and Ti doping. Apart from the dark rows the surface still resembles the (1×1) termination. The (1×1) periodicity is observed in the LEED pattern in Fig. 4.7(c_3) (together with a faint, streaky intensity in between the integer-order spots), and the typical zigzag lines are seen in the close-up STM images of Fig. 4.7(c_2). A statistical evaluation reveals that the coverage of dark rows now corresponds to (18.4 ± 1.1)% of surface Fe sites.

Note that the properties of the UHV-prepared films are somewhat different from the as-grown films: As shown in Section 4.8.3, the conditions employed during growth result in a partial Ti segregation at the surface, and in ill-defined, poorly ordered, Ti-rich phases. By removing the excess Ti with Ar^+ sputtering, one can instead investigate the effect of minor doping levels on well-controlled hematite surfaces. After this first cycle, the amount of Ti at the surface remains unchanged even after tens of sputtering cycles at standard, UHV-compatible preparation conditions. This is seen in XPS (no change in the Ti 2*p* intensity), and in STM (coverage of dark rows at the surface), indicating a uniform doping level throughout the film. However, a small increase of the Ti content was observed at the surface after hundreds of cycles. This is attributed to the smaller sputter yield for Ti than Fe (0.7 and 1.7, respectively), and to the fact that Ti atoms sit in

the subsurface (see Section 4.4).

Effect of post-growth Ti deposition on trench coverages

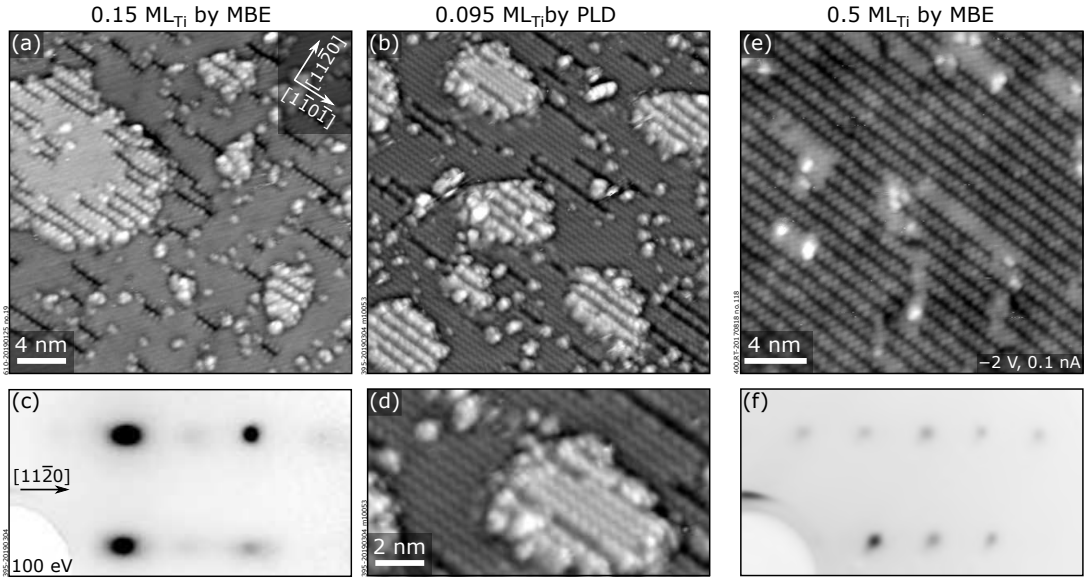

Figure 4.8. Deposition of sub-monolayer amounts of TiO_2 on $Fe_2O_3(1\bar{1}02)$. (a, b) 28 × 28 nm^2 STM images showing the effect of sub-monolayer deposition of Ti on (a) a (1 × 1)-terminated 0.8 at.% Ti:$Fe_2O_3(1\bar{1}02)$ film such as in Fig. 4.7(b), and (b) on an undoped $Fe_2O_3(1\bar{1}02)$ substrate. Similar results are achieved both by PLD [(a) 0.095 ML Ti, 550 °C, 2 × 10^{-2} mbar O_2, 2 J/cm^2], and by MBE [(b) 0.15 ML Ti, 500 °C, 5 × 10^{-6} mbar O_2]. On the terraces, dark rows along the $[1\bar{1}0\bar{1}]$ direction appear without significant alteration of the remaining (1 × 1)-structured areas. Additionally, small and irregular islands are formed. (c) LEED pattern corresponding to the surface in panel (b): An additional half-integer faint periodicity corresponds to the closest separation between the dark rows. (d) 14.6 × 8 nm^2 STM image showing that the small islands appearing on the surface after deposition display the same (1 × 1) periodicity as the underlying terrace. (e) 22 × 22 nm^2 STM image of a $Fe_2O_3(1\bar{1}02)$ surface after deposition of 0.5 ML Ti by MBE. The trenches cover 50% of the surface. (f) LEED pattern of the surface in panel (e), showing a (2 × 1) periodicity. Adapted from ref. 66.

To confirm that the dark rows are indeed associated with the Ti dopants, submonolayer amounts of Ti were deposited by PLD (followed by O_2 annealing) on the surface of Fig. 4.7(b), *i.e.*, on an almost defect-free (1 × 1) surface. Ti was also deposited by MBE on an undoped $Fe_2O_3(1\bar{1}02)$-(1 × 1) sample. The results for depositions around 0.1 ML are shown in the left and center columns of Fig. 4.8. Both depositions, by PLD and MBE, result in the formation of dark rows at the surface, confirming their correlation to Ti. Additionally, small and irregular islands are formed; they exhibit the same (1 × 1) surface structure as the underlying terrace [Fig. 4.8(d)]. In areas with a large number of dark rows, neighboring lines assemble to form an (n × 1) periodicity, with a local minimum spacing of n = 2 lattice units along the $[11\bar{2}0]$ direction. This preferential local arrangement is also reflected in the LEED pattern of Fig. 4.8(c): in between the main (1 × 1) spots, a faint horizontal streak characteristic of an (n × 1) periodicity

is visible, with enhanced intensity in the region of half-integer spots. The similarity between PLD and MBE deposition allows one to exclude that the dark rows are caused by sputter-induced damage from energetic species ablated in PLD. Notice that the nominal amounts of Ti deposited by MBE for these experiments (calibrated by a QCM) match those derived from the coverage of trenches measured in STM.

By depositing larger amounts of Ti, the number of the dark rows increases, until saturation coverage is reached for deposition of $\geq$ 0.5 ML Ti, when the trenches cover 50% of the surface [Figs. 4.8(e, f)]. The resulting structure, discussed in more detail later, is imaged as zigzag lines with a (2 × 1) ordering.

Effect of $\mu_O{}^{exp}$ on trench coverages

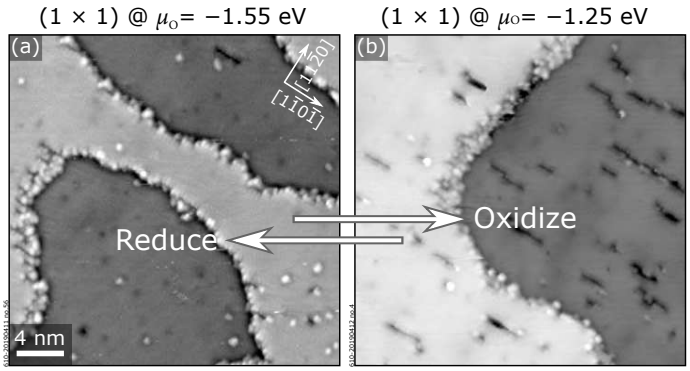

Figure 4.9. Effect of μ_O on Ti-induced defects. The density of dark rows on the surface of a 0.8 at.% Ti:$Fe_2O_3(1\bar{1}02)$-(1 × 1) film increases upon annealing at more oxidizing conditions: (a) annealing at 550 °C, 7 × 10^{-6} mbar O_2, corresponding to $\mu_O{}^{exp}$ = −1.55 eV; (b) annealing at 550 °C, 3 × 10^{-2} mbar O_2, corresponding to $\mu_O{}^{exp}$ = −1.25 eV. STM images are 40 × 40 nm^2 in size, and were acquired at U_{sample} = +2 V, I_t = 0.2 nA. Reprinted from ref. 66.

The coverage of dark rows at the (1 × 1) surface can be controlled by varying the bulk doping, as seen in Figs. 4.7(b, c), and by depositing sub-monolayer amounts of Ti after growth (Fig. 4.8). For the low-doped film, a dependence of the coverage of dark rows on the oxygen chemical potential $\mu_O{}^{exp}$ used during annealing was also observed (Fig. 4.9). The almost pristine (1 × 1) surface of the 0.8 at.% doped films in Fig. 4.9(a) exposes more dark rows after annealing at higher μ_O [Fig. 4.9(b)]. Specifically, the initial (2.08 ± 0.39)% coverage of dark rows, observed at 550 °C, 7 × 10^{-6} mbar ($\mu_O{}^{exp}$ = −1.55 eV), changes to (4.57 ± 1.40)% after 10 min at 550 °C, 3 × 10^{-2} mbar ($\mu_O{}^{exp}$ = −1.25 eV). The coverage of dark rows does not change upon further annealing at the same conditions: A coverage of (4.03 ± 0.47)% was measured after 40 min. Furthermore, the process is fully reversible: The initial coverage of dark rows is recovered by annealing again for 20 min at 550 °C, 7 × 10^{-6} mbar. Intriguingly, this phenomenon was not observed on the high-doped films: There, the coverage of dark rows is preserved at 550 °C at all O_2 pressures

between 7×10^{-9} mbar ($\mu_O{}^{exp}$ = −1.79 eV) and 3×10^{-2} mbar ($\mu_O{}^{exp}$ = −1.25 eV).

4.4 Theoretical results

4.4.1 Preferred sites for Ti substitution

Florian Kraushofer and Matthias Meier performed DFT calculations to find a structural model for the Ti-correlated dark lines that appear on the (1 × 1) surface of the Ti:$Fe_2O_3(1\bar{1}02)$ films. Different Ti concentrations were tested based on the model for the (1 × 1) surface in Fig. 4.4. Since previous works have demonstrated that dilute Ti impurities substitute Fe,[138,145] the first test was only Ti substitution without introducing additional defects. In a (2 × 2) supercell, a single, isolated Ti atom was placed in five different positions, one in each of the first five cation layers (for this set of calculations, asymmetric slabs with 30 atomic layers were used). The corresponding energy gains were compared to the energy gain of one Ti ion substituting Fe in a (2 × 2 × 3) bulk supercell [containing the same number of O, Fe and Ti ions as the (2 × 2) surface slabs, *i.e.*, the same distance between Ti atoms in the replicas; the supercell volume was fixed]. The results are shown in black in Fig. 4.10(a). Substituting one Fe atom for Ti in layers deeper than C3 is comparable to substitution in the bulk, while for layers C1, C2 and C3 there is an energy gain. Substitution in layer C2 shows the strongest energy gain (0.29 eV gain compared to substitution in the bulk, and 0.23 eV, and 0.19 eV compared to layers C1 and C3, respectively).

The calculations showed that introducing one Ti dopant always results in the formation of an electron polaron. The polaron localizes at an Fe cation, which acquires a charge state of 2+. For Ti substitution in layers C1, C2, and C3, the polaron preferentially localizes on an Fe atom in the topmost cation layer C1. Ti substitution in layers C4 and C5 causes the polaron to localize in layers C3 and C6, respectively. To address how the interaction between the dopant and the polaron affects the formation energies of Fig. 4.10(a), the same structures were calculated with one electron artificially removed from the cell, in practice removing the polaron and its interaction with the dopant.[164] This compares the substitutional energies for Ti dopants without the influence of the polaron. The energy gain with respect to substitution in the C5 layer are plotted in red in Fig. 4.10(a) (Ti substitution in layer C5 was used as reference in this case as this layer is sufficiently far from the surface to be considered bulk-like; since the dopants have the same distances in all slabs, this choice allows one to neglect charge corrections[165] other than the jellium automatically included in the VASP code). Also in this case, the C2 layer is preferred over neighboring ones, but the energy differences are less pronounced than

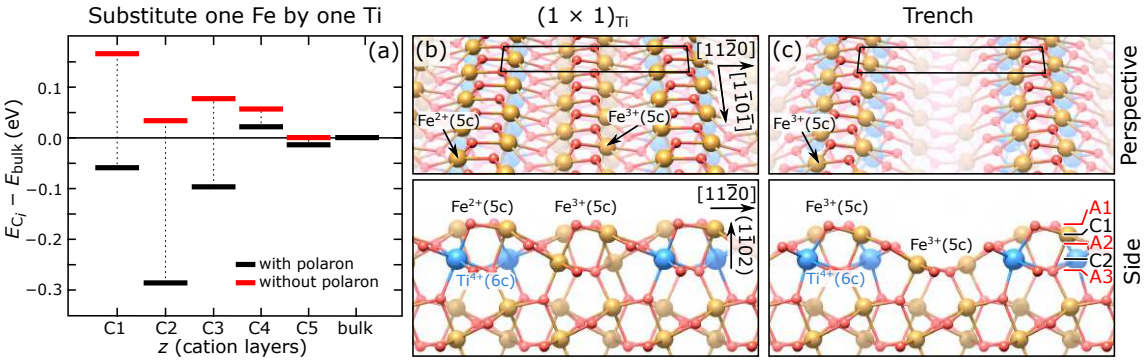

Figure 4.10. (a) Black: Calculated formation energies for substituting one Fe atom by one Ti atom in a given layer in a (2 × 2) supercell of the $Fe_2O_3(1\bar{1}02)$-(1 × 1) surface, relative to the formation energy for substitution in the bulk. For the calculation shown in black (polaron not artificially removed), the reference configuration is a bulk structure with a unit cell containing the same number of atoms as the slabs with Ti in different (sub-)surface layers. Red: Calculated formation energies for the same systems, but with one electron artificially removed, such that the polaron is not present. In this case, Ti substitution in layer C5 was used as reference. (b, c) Calculated surface structures for 2 Ti atoms per (2 × 1) unit cell. Ti is accumulated in layer C2, and preferentially orders in zigzag rows along the $[1\bar{1}0\bar{1}]$ direction. (b) $(1 \times 1)_{Ti}$ structure, stable at reducing conditions: The structure of undoped (1 × 1) is retained, and surface Fe atoms above Ti have a charge state of 2+. (c) (2 × 1) trench structure, stable at oxidizing conditions: An equal number of Fe and O atoms is removed from the surface, allowing every remaining surface Fe to maintain a 3+ charge state. Atoms are labeled according to their coordination to oxygen. Adapted from ref. 66.

when the polaron is present. Moreover, substitution of isolated Ti atoms in layer C5 appears slightly more favorable than in layers closer to the surface when the polaron is removed. Therefore, most of the energy difference between C2 and the deeper layers is attributed to the dopant–polaron interaction.

4.4.2 Ti-induced surface modifications

It was also considered how two (or more) Ti atoms interact and thus preferentially arrange in the system. Rather than staying isolated, two Ti atoms in a (2 × 2) surface slab pair in the C2 layer along the $[1\bar{1}0\bar{1}]$ direction such that they share an O bonding partner in the A3 layer. This results in an energy gain of 0.08 eV, or 0.04 eV per Ti. The best arrangement for two Ti atoms per (2 × 1) supercell (twice the amount of Ti) is shown in Fig. 4.10(b) and Fig. 4.11(b), and labeled in the following as $(1 \times 1)_{Ti}$. It is the most favorable arrangement of surface Ti, with 0.08 eV energy gain per Ti atom relative to isolated Ti in a C2 site, if one allows only cation substitutions without further modifying the composition. It consists of an infinite zigzag chain of Ti atoms in the C2 layer running along the $[1\bar{1}0\bar{1}]$ direction, in which each Ti shares both of its O bonding partners in layer A3 with a neighboring Ti. The top layer appears as a structurally unmodified (1 × 1). The calculated spin magnetic moments suggest that the surface Fe atoms directly above the Ti rows take on an Fe^{2+} charge state (3.5 μ_B), while all other Fe atoms remain Fe^{3+}

($4\ \mu_B$).[166] Further increasing the Ti concentration and substituting every Fe atom in layer C2 by Ti does not cause extra energy gain nor energy cost.

When modifications in the composition are allowed, another structure is more favorable than the $(1 \times 1)_{Ti}$ surface at some values of ${\mu_O}^{DFT}$. This is shown in Fig. 4.10(c) and Fig. 4.11(c). It is named trench reconstruction. The trenches are formed in the surface layers as a result of removing two Fe and two O atoms per (2×1) unit cell from the C1 and A1 layers, respectively. Because of this modification, the remaining surface Fe returns to a 3+ charge state, while Ti remains 4+ [see Fig. 4.10(c)]. Note that the concentration of Ti discussed here, *i.e.*, two atoms per (2×1) unit cell all over the surface, is well above what is experimentally achieved with the doped films. For smaller concentrations, the trench spacing along $[11\bar{2}0]$ can be expanded [see for example Fig. 4.11(d)] and/or short trench structures can be constructed by breaking the periodicity along $[1\bar{1}0\bar{1}]$. Figures 4.11(e–g) show a few examples [an additional oxygen atom per unit cell is missing in the structures of panels (f) and (g)].

Figure 4.11(a) shows the 'formation energies' of the reconstructions described above as a function of ${\mu_O}^{DFT}$, normalized to the supercell area and to the number of Ti atoms. As detailed in ref. 66, it plots the normalized differences $\Delta\phi$ in the grand potentials of each structure and its reference, taken as a surface with the same amount of Ti doping in the subsurface, but without trenches. Overall, DFT predicts the Ti-induced trench defects to be stable over a wide range of oxygen chemical potentials. The infinite trenches [black and gray lines, perspective views in Figs. 4.11(c, d)] are more stable than the (1×1)-terminated surface [red line, perspective view in Fig. 4.11(b)] when ${\mu_O}^{DFT} \geq -2.3$ eV.

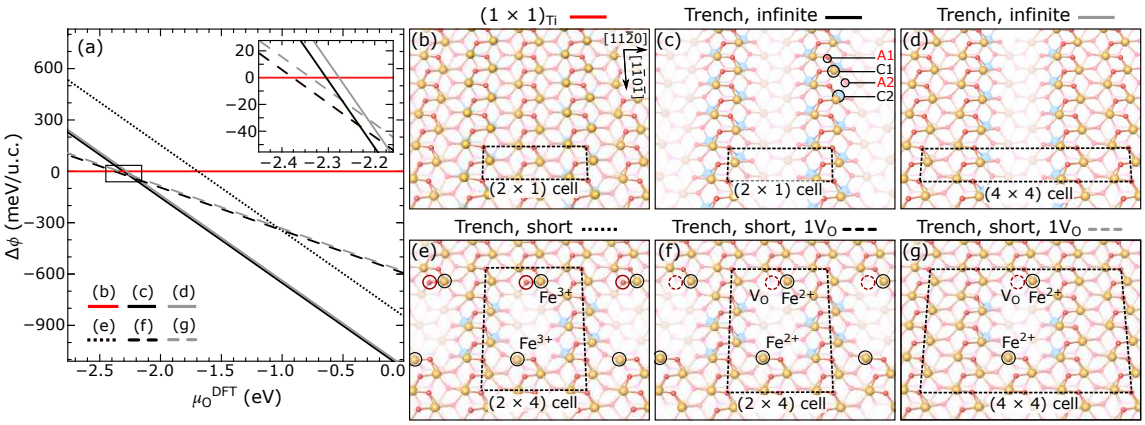

Figure 4.11. Surface phase diagram and structures of Ti:$Fe_2O_3(1\bar{1}02)$ as a function of ${\mu_O}^{DFT}$. (a) Formation energies per Ti atom and (1×1) unit cell of trench structures with different spacings, relative to surfaces with the same amount of Ti doping in the subsurface, but without trenches, *i.e.*, a combination of undoped (1×1) and the $(1 \times 1)_{Ti}$ structure in panel (b). The inset shows the region around ${\mu_O}^{DFT} = -2.3$ eV in greater detail. (c, d) Perspective views of trenches indefinitely extended along the $[1\bar{1}0\bar{1}]$ direction, with a periodicity of two and four unit cells along the $[11\bar{2}0]$ direction, respectively; (e–g) short trenches with and without one additional oxygen vacancy (V_O) per supercell. The dimensions of the supercells are indicated in the panels. Reprinted from ref. 66.

The spacing between the trenches does not play a major role: the black and gray lines are degenerate within the accuracy of DFT. Similarly, it was observed that the spacing between the trenches along $[11\bar{2}0]$ is irrelevant for the short trenches. Figure 4.11(a) plots the formation energy for the short trench of Fig. 4.11(e) (dotted line). It can be seen that shortening the trench along $[1\bar{1}0\bar{1}]$ results in a significant energy cost, likely associated with the reduction of the coordination for atoms at the trench edges. The short trenches can compete with the infinite ones when one oxygen atom is removed from the trench edge [see Figs. 4.11(f, g), and the corresponding dashed lines in the phase diagram]: In the $\mu_O{}^{DFT}$ region between −2.4 and −2.3 eV, the short trenches with one additional oxygen vacancy are slightly preferred. This is because removing equal amounts of Fe and O from the surface layers to form a trench leaves one O atom at one end of the trench 2-fold coordinated [red circle in Fig. 4.11(e)]. Removing this weakly bound O atom results in an overall slightly more reduced stoichiometry, with the excess charge localizing on the neighboring Fe atom to form one Fe^{2+} at each end of the trench defect [Figs. 4.11(f, g)]. One can eliminate this polaron by removing two additional FeO units at trench edges of this structure (not shown). The formation energy of this structure is degenerate with the one of Fig. 4.11(e), and, thus, unfavorable (not shown).

4.4.3 Experimental vs. simulated STM images

Figure 4.12 shows high resolution STM images of the trench defects imaging filled and empty states, together with the superimposed STM simulations from the models of the Ti-induced defect. The top row shows an isolated trench defect, while the bottom row shows the full coverage (0.5 ML) of trenches. The isolated trench defect appears as a dark line in both the simulated and the experimental filled-state images [negative sample bias, Fig. 4.12(b), where oxygen appears bright],[96] reproducing the missing zigzag row of oxygen in the topmost layer [Fig. 4.10(a)]. The match between theory and experiment is further supported by comparing experimental and simulated empty-state images [positive sample bias, Fig. 4.12(c)]: At these conditions, the STM tip images the unsaturated dangling bonds of Fe, which are slightly tilted away from their topmost O neighbors.[96] In the presence of a trench, two Fe zigzag rows are replaced by a dark area lined by isolated point features on both sides. This relates to the missing iron atoms in the topmost layer [Fig. 4.10(a)]. The isolated points are the remains of the two zigzag rows affected by the removal of Fe cations.

Good agreement also exists between the experimental and the simulated images of the full coverage of trenches (bottom row), which was obtained by depositing 0.5 ML of Ti at RT on an undoped $Fe_2O_3(1\bar{1}02)$-(1×1) surface, followed by 20 min annealing in

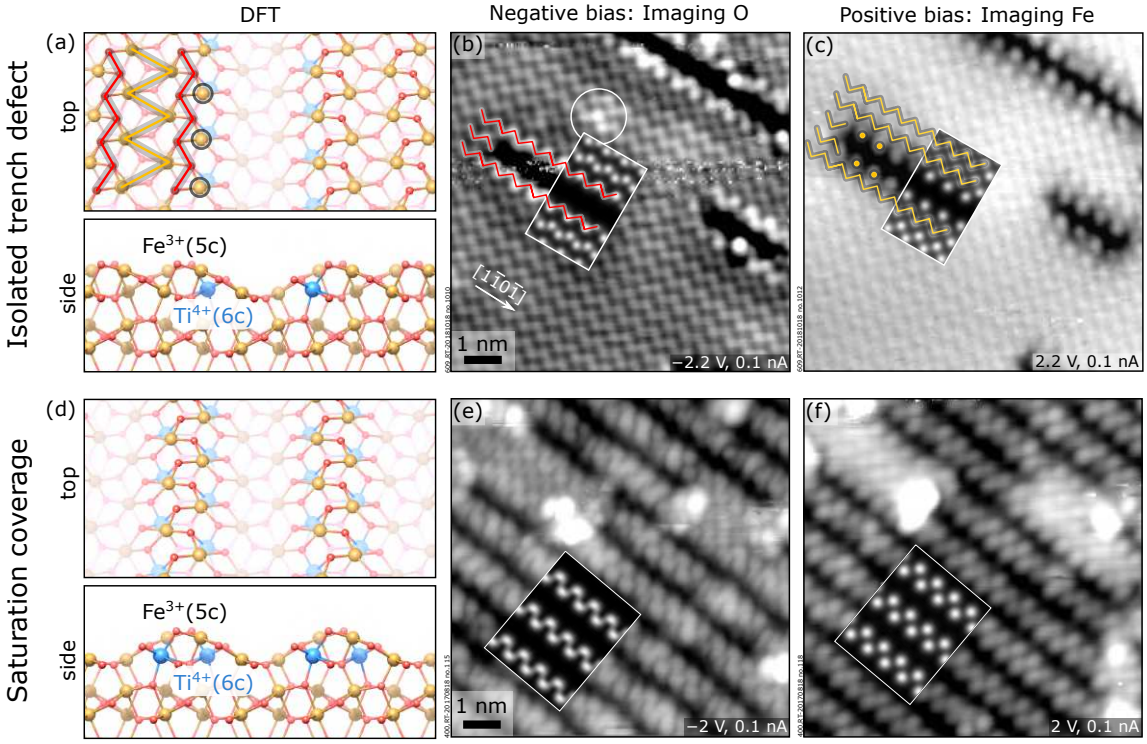

Figure 4.12. DFT models and experimental and simulated STM images of the Ti-modified (1 × 1) surface, at both negative and positive sample biases. The top and the bottom row refer to isolated trenches and saturation coverage of trenches, respectively. Top row: At negative sample bias, the surface reconstruction appears as a missing zigzag row of O atoms in the surface layer along the $[1\bar{1}0\bar{1}]$ direction. At positive sample bias, two rows of iron are missing from the top layer, and are imaged as a dark area surrounded on both sides by isolated point features. Bottom row: At negative sample bias, every other zigzag row is missing due to the (2 × 1) trenches. At positive sample bias, half of every zigzag is missing, and every zigzag line imaged on the (2 × 1) structure consists of the remaining halves of two (1 × 1) zigzag lines. The STM simulations were performed at constant height (3 Å above the surface) on a (6 × 1) supercell, with U_{sample} = −2 V and +2 V in (b, e) and (c, f), respectively. Adapted from ref. 66.

UHV at 600 °C, plus depositing another 0.5 ML Ti at room temperature followed by 30 min annealing at 1×10^{-6} mbar O_2 and 550 °C. Comparable results were obtained after deposition of only 0.5 ML Ti followed by annealing at the same conditions. At negative sample bias, every other zigzag row is missing due to the (2 × 1) trenches. At positive sample bias, half of every zigzag is missing, and every zigzag line imaged on the (2 × 1) structure consists of the remaining halves of two (1 × 1) zigzag lines. This essentially corresponds to the rows of single protrusions lining the edges of a trench for isolated trench defects [see Fig. 4.12(d)], paired with the same features in the neighboring trench. It is worth noting that, based on the structural model, 0.5 ML Ti should be sufficient to saturate the trench structure with a (2 × 1) periodicity; however, there is no sign of excess Ti in the STM images in Fig. 4.12 (obtained by depositing more than 0.5 ML, see above), suggesting that additional Ti substitution in the subsurface does not cause further changes to the surface structure at these coverages (bulk diffusion of Ti should be inhibited at the temperature used in this preparation, see Section 4.3.1).

Modulation in the apparent height of the surface atoms.

It is worth noting that, below the saturation coverage of trenches, the local corrugation of the surface is not uniform, see Fig. 4.13: some atoms within the structurally unmodified (1×1) areas appear with different contrast. A modulation in the apparent height of the surface atoms is also visible in Fig. 4.7(b_2). As discussed in detail in ref. 66, the long-range modulation in the apparent height of the surface is due to the Ti-induced modification of the density of states for surface Fe and O atoms far away from the trench itself.

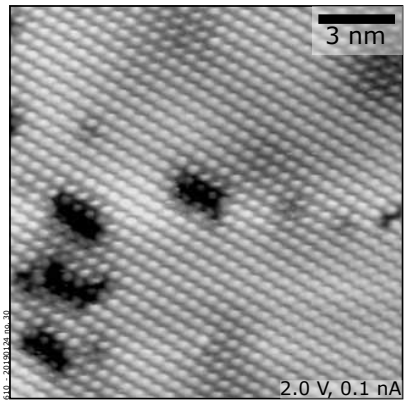

Figure 4.13. Modulation in the apparent height of the surface atoms of Ti:$Fe_2O_3(1\bar{1}02)$ films. The STM image is 15×15 nm^2.

4.5 Discussion

Consistent with previous studies on $Fe_2O_3(0001)$,[138,145] this work shows that Ti dopants in low concentration (below 3.1 at.%) do not tend to agglomerate to form titania phases in $Fe_2O_3(1\bar{1}02)$. On the contrary, the (2×1) surface of slightly reduced, undoped single crystals is fully preserved, while the stoichiometric (1×1) surface is only slightly modified by Ti substituting Fe (leading to dark lines along the $[1\bar{1}0\bar{1}]$ direction). The following discussion will focus on the (1×1) surface and the observed Ti-induced modifications.

DFT suggests that Ti preferentially occupies the first subsurface layer [layer C2 in Fig. 4.10(a)], independent of the Ti concentration or $\mu_O{}^{DFT}$. This allows Ti to maintain a sixfold coordination to oxygen, and a charge state of 4+ [Figs. 4.10(b, c)]. Based on the results of Fig. 4.10(a), one can attribute the preference for the C2 layer over deeper layers to the attractive interaction of the Ti-induced electron polaron (preferentially localizing on an iron in layer C1) with a neighboring Ti. Purely structural effects seem to play a minor role, as the energy differences between layer C2 and deeper layers are only 0.02–0.04 eV when the polaron is removed. The preference for the C2 layer over the immediate surface layer C1 is likely due to the different oxygen affinities of the cations:

Ti has higher oxygen affinity than Fe, and will therefore maximize its coordination with O atoms. This is possible if Ti occupies the subsurface layer C2, while it would be fivefold coordinated if it replaced Fe in layer C1.

4.5.1 Structural model of Ti-induced trenches

Among the structures with subsurface Ti, presented in Fig. 4.10 and Fig. 4.11, the best model for the dark lines observed on the (1×1) surface of the UHV-prepared films [Figs. 4.7(b, c)] is the Ti-induced trench structure, shown as infinitely long trenches in Fig. 4.10(c), and Figs. 4.11(c, d), and as short trenches in Figs. 4.11(e–g). This structure is characterized by missing rows of surface Fe and O and substitutional Ti in the subsurface. The charge of the two missing $Fe^{3+}O^{2-}$ units per unit cell length is compensated by replacing two subsurface Fe^{3+} atoms with Ti^{4+}.

Several facts support this assignment. (i) First, the high resolution STM images of the dark lines are in excellent agreement with the STM simulations of the trench structure (Fig. 4.12). (ii) Moreover, deposition of Ti on a pristine (1×1) surface not only causes the formation of dark lines, but also of hematite islands, as seen in Fig. 4.8. The hematite islands likely consist of oxygen from the gas phase and Fe atoms displaced by both, the substitutional Ti and the formation of the trenches. (iii) Finally, the predictions of the theoretical phase diagram of Fig. 4.11 are qualitatively confirmed experimentally. On the 3.1 at.%-doped film, long, at times bunched, trenches were observed that are well modeled by the infinite trench structures of Figs. 4.11(c, d). These are predicted to be preferred at all experimentally accessible values of oxygen chemical potential at 550 °C (this temperature was chosen because Ti diffusion is largely inhibited[161–163], see Section 4.3.1): At the lower limit of O_2 partial pressure of $\approx 1 \times 10^{-13}$ mbar, and at 550 °C, $\mu_O{}^{exp} = -2.19$ eV, which is higher than the theoretical threshold for trench formation of $\mu_O{}^{DFT} = -2.3$ eV. (In practice, since equilibrium at these low partial pressures will not be reached in a reasonable time, the smallest experimentally accessible value of $\mu_O{}^{exp}$ is even larger.) Consistently, the coverage of the dark lines on the 3.1 at.%-doped film does not change upon annealing over the accessible range of oxygen chemical potentials. ($\mu_O{}^{exp}$ was varied from −1.80 eV to −1.25 eV by annealing at 550 °C for 20 min at O_2 pressures ranging from 7×10^{-9} mbar to 3×10^{-2} mbar). On the low-doped film (0.8 at.%), the defects are shorter and sparser because of the smaller doping level, and their coverage decreases when annealing at $\mu_O{}^{exp} \leq -1.6$ eV (Fig. 4.9). This transition is interpreted as the evolution to the defect-free $(1 \times 1)_{Ti}$ surface from the trench structure. Note that the content of Ti in layer C2 stays unchanged, as suggested by the saturation of the coverage of line defects after a few minutes of annealing (Fig. 4.9), and the fact that at

the annealing temperature of 550 °C bulk diffusion of Ti is inhibited (see Section 4.3.1). Hence, the transition essentially consists of filling up the trenches by Fe and O. Fe atoms likely come from steps, as Fe diffusion in the bulk is inhibited at 550 °C,[161–163] while O is taken from the sample or from the gas phase. This behavior is qualitatively in line with the prediction of DFT that the $(1 \times 1)_{Ti}$ surface can be stabilized upon crossing a certain threshold of ${\mu_O}^{DFT}$ [see inset of Fig. 4.11(a), ${\mu_O}^{DFT} \leq -2.4$ eV]. For the smaller doping level, one should avoid making quantitative comparisons between theory and experiments, because (i) the smallest concentration of dopants achievable with DFT with acceptable computational effort is significantly larger than the experimental one; (ii) kinetic limitations that are not considered and could limit the agglomeration of short trenches into longer ones; (iii) entropic contributions (including, *e.g.*, mixing terms) that are also not taken into account in the DFT results and could affect the relative formation energies in non-trivial ways.

While for both, infinite and short trenches, a 2× periodicity in the $[11\bar{2}0]$ direction is predicted to be degenerate with a 4× periodicity, experiments may suggest a preference for the 2×, especially in the vicinity of steps. In fact, a local (2×1) periodicity is observed when sufficiently large amounts of Ti (around 0.1–0.2 ML) are deposited on an $Fe_2O_3(1\bar{1}02)$-(1×1) surface followed by oxygen annealing [see, for example, some of the islands in Figs. 4.8(a, b)]. The full coverage of (2×1)-periodic dark lines can be obtained for Ti coverages around and above 0.5 ML [Figs. 4.8(e, f)]. The good agreement between the experimental and simulated STM images at the saturation coverage (bottom row of Figs. 4.12) further supports the assignment of the trench structure model for the observed defects.

4.5.2 An experimental route for mechanistic insights into the photocatalysis of Ti-doped hematite

As anticipated in Section 4.1.2, during photocatalytic reactions, charge carriers generated by absorbed light are transferred to adsorbed molecules that react at the surface. The overall reactivity of the photocatalyst is determined by the combination of several factors. Firstly, the efficiency of light absorption and charge migration to the surface, which are influenced by the bulk electronic structure and conductivity (*e.g.*, critical factors are recombination centers or charge traps in the bulk). Secondly, the local electronic structure of the surface, which establishes how efficiently charge carriers are exchanged between the reactants and the catalyst.[136] Finally, the specific arrangement and the coordination of the topmost atoms, defining which sites are available and preferred for adsorption, dissociation, and reaction.[71,124,167–170] Although the specific reaction pathways

are defined by the electronic and geometric details of the surface, their role is often overlooked. This is partly because photoelectrochemical current–voltage measurements—commonly used to quantify the overall efficiency of a photocatalyst—lack the ability of isolating these factors. When dopants are introduced in the system and cause an increase in its photocatalytic activity, it is even harder to pinpoint the exact cause, as the foreign elements will affect all the above ingredients.

The Ti:$Fe_2O_3(1\bar{1}02)$ system should be suited to address these effects one by one. The Ti dopants introduce excess electron carriers in the bulk, which affect the electrical conductivity. Ti also modifies the local surface electronic structure: The distribution of states is altered far from the trench, and, in its proximity, a new in-gap state appears close to the valence band maximum (see ref. 66). These may modify the adsorption energy of molecules, the localization of charge carriers, and the effectiveness of charge transfer to adsorbates. Finally, the Ti-induced modification in the surface atomic structure (trenches) makes new atoms available as possible reaction sites [Fe in layer C2, O in layer A3, not accessible on the undoped $Fe_2O_3(1\bar{1}02)$-(1×1) surface], and changes the local coordination of others (the O atoms in layer A2 at the trench edge become 3-fold coordinated). All these effects are expected to influence reactions.

In the following, an experimental route is proposed to disentangle the role of the efficiency of charge transport in the bulk, and of surface electronic and atomic structure on the photocatalytic activity of the model system presented here. To this end, for each factor suitable descriptors are identified that can be quantified experimentally. The first descriptor is the coverage of trenches, θ, which is used to describe the effect of Ti on the surface atomic structure. θ is expressed as the fraction of surface unit cells composing trenches, can be measured by STM or other scanning probe techniques. The second descriptor is the near-surface concentration of the dopants (in the following, 'surface doping'), which is used for quantifying the Ti-induced changes on the surface electronic structure. This quantity affects both, the local density of states of Fe and O atoms potentially available as reaction sites, and the availability of electrons directly accessible to adsorbed molecules. Consistent with the definition of the bulk doping in atomic percent, one can define a surface doping as $c^{s}_{Ti} = n_{Ti}/(n_{Ti} + n_{Fe})$, where n_{Ti} and n_{Fe} are the total numbers of Ti and Fe cations in layers C1 and C2. At oxidizing conditions, all available subsurface Ti atoms produce trenches with coverage θ. It can be derived that the surface doping equals $c^{s}_{Ti} = \theta/(2 - \theta)$ at these conditions (see Section 4.8.2). Hence, the surface doping levels of the 0.8 at.%- and 3.1 at.%-doped films correspond to (2.06 ± 0.24)% and (10.1 ± 0.7)%, respectively (as derived from the corresponding θ values, see Section 4.3.2). The ratio between these surface doping levels is 4.93 ± 0.67, close to the ratio of the bulk doping levels of the two films. Note also that the surface doping levels

Table 4.1. Dependence of intrinsic properties of Ti:$Fe_2O_3(1\bar{1}02)$ model surfaces on some experimental parameters. A change in (i) oxygen chemical potential, (ii) amount of post-growth-deposited Ti, or (iii) bulk doping produces discernible effects on the coverage of trenches, the surface doping, and the bulk conductivity.

Experimental parameter	Trench coverage	Surf. Doping	Bulk cond.
Oxygen chemical potential, μ_O	$f(\mu_O)$	—	—
Ti amount after growth, θ_{Ti}*	θ_{Ti}	$\theta_{Ti}/(2-\theta_{Ti})$	—
Bulk doping, c^b_{Ti}	6 c^b_{Ti}*	$3c^b_{Ti}/(1-3c^b_{Ti})$	$f(c^b_{Ti})$

* At large enough Ti amounts and/or μ_O.

are approximately three times larger than the nominal bulk doping levels. This is likely due to the strong preference for Ti to occupy the C2 layer over the neighboring ones, so that C2 acts as a 'potential well' [Fig. 4.10(a)], attracting some Ti atoms from deeper layers. Finally, the third descriptor is the bulk conductivity, used as a measure of the efficiency of charge separation.[137] Table 4.1 summarizes how these descriptors (columns) are affected by three independent experimental 'handles' (rows), *i.e.*, the oxygen chemical potential, the amount of Ti deposited after growth, and the bulk doping.

Oxygen chemical potential. As discussed above, μ_O can influence the coverage of trenches at the surface. However, the surface doping is not affected, because the amount of both subsurface Ti and surface Fe stays unchanged when trenches are formed (recall that bulk diffusion of both Ti and Fe is inhibited at the temperatures used). In the range of temperatures and oxygen pressures employed, the bulk conductivity is also not affected.[171]

Amount of Ti deposited after growth. Deposition of controlled amounts of Ti by PLD or MBE affects the coverage of trenches θ and the surface doping, but not the bulk conductivity. θ can be expressed as a function of the amount of Ti deposited in monolayers, θ_{Ti}. 0.5 ML of Ti, *i.e.*, one Ti atom per (1×1) unit cell, or two Ti atoms per (2×1) unit cell, correspond to the highest trench coverage of 50% [Fig. 4.10(b), Fig. 4.11(c)], *i.e.*, 2 Fe atoms missing per (2×1) unit cell, or θ = 0.5 ML. Hence, $\theta = \theta_{Ti}$ (up to the 0.5 ML saturation coverage of trenches). The surface doping changes according to its relation with θ.

Bulk doping. A change in the bulk doping, *i.e.*, the concentration of Ti dopants in the bulk, c^b_{Ti}, tunes the bulk conductivity and the coverage of trenches θ: the STM evaluations reveal that θ is ≈6 times larger than the bulk doping (for low Ti concentrations, this is valid at oxidizing conditions only). The change in θ translates in a modification of the surface doping.

To gain insights in the role of dopants on reactivity, one would normally prepare

several samples with different values of bulk doping (c^{b}_{Ti}), and evaluate how the reactivity changes with c^{b}_{Ti}. Most often, however, this dependence will be a combination of the three relations in the last row of Table 4.1, as a result of the entanglement of the factors in the top row of Table 4.1. With the two additional 'handles' identified here (θ_{Ti} and μ_O), one can modify the coverage of trenches and/or surface doping of the samples by either depositing Ti after growth or using μ_O. The contributions of trenches and surface doping can then be isolated by comparing the experimental dependences of the reactivity on θ_{Ti} and μ_O with the relations in Table 4.1. After the critical factors are identified, further atomic-scale investigations, supported by theoretical calculations based on the structural models established here, can be used to shed light on the reaction pathways and mechanisms of interest.

4.6 Conclusions

The work on the single-crystalline Ti-doped α-$Fe_2O_3(1\bar{1}02)$ films presented in this Chapter testifies to the prowess of combining PLD growth with atomic-scale characterization to build reliable model systems for investigating surface reactions at a fundamental level. When grown under optimized conditions, the films display atomically flat surfaces and uniform doping distribution. For doping levels below 3 at.%, the native surface reconstructions of undoped Fe_2O_3 are largely preserved, except for local trench defects that are induced by the Ti dopants, which were modeled by DFT. The detailed characterization and tunability of this system provides the means to model OER processes occurring at Ti-doped hematite surfaces and improve PEC performances.

4.7 Applications of the Ti-doped $Fe_2O_3(1\bar{1}02)$ films

As mentioned before, well-defined films with sufficiently low levels of doping can be essentially regarded as undoped samples, but with the added bonuses of enough conductivity for STM and LEED, absence of impurities, and atomically flat morphologies. Such films, together with films with purposively higher doping, have been used within the following projects, most of which are currently undergoing:

- Performing fundamental investigations on the role of single metal atoms on the catalytic activity of Fe_2O_3. For this task, ultra-low-doped films (below 0.03 at.%) films have been employed. This value of doping provides the needed conductivity

for STM without substantially affecting the electronic properties of the sample, and minimizes the amount of Ti-induced defects at the surface. Nikolaus Resch has deposited sub-monolayer amounts of Rh on these films, aiming to stabilize single Rh atoms (interesting for catalytic applications), and has investigated their thermal stability.

- Validating the DFT models of the (1×1) and of the (2×1) surfaces by performing LEED-IV measurements (collaboration with Lutz Hammer from Friedrich-Alexander Universität in Erlangen, Germany).

- Investigating the effect of doping on polaron conductivity in hematite by non-contact q+ AFM (collaboration of Martin Setvin with Jesús Redondo from the Institute of Physics of the Czech Academy of Sciences, Prague, Czech Republic).

- Investigating the interaction of the $(1\bar{1}02)$ surface of Fe_2O_3 with electrolytes of varying acidity dosed under UHV-compatible conditions, within the liquid-drop apparatus described in ref. 115 (Florian Kraushofer).

4.8 Complementary results

4.8.1 Evaluation of the bulk doping

As mentioned before, the bulk doping level in Ti:$Fe_2O_3(1\bar{1}02)$ films grown by PLD from two different targets cannot be trivially determined by the ratio of laser pulses shot on the iron-oxide and on the titania targets, as different absorption of the UV laser, sticking effects, as well as the specific values of the oxygen chemical potential and the laser fluence, can affect the distinct species differently. To determine the doping level in the films, the amounts of Fe and Ti deposited per pulse were separately evaluated. This information was then translated to the relative number of shots on the two targets needed for a specific doping level. Another approach would have been to use the movable QCM holder described in Chapter 2, but this was not yet developed at the time of these experiments.

The technique of choice for quantifying these sub-monolayer amounts was STM. While XPS could in principle be used for the same purpose, it is more demanding, as it requires (i) modeling the dopant distribution, (ii) knowing the relative sensitivity factors for Fe and Ti, and (iii) ensuring that photoelectron diffraction effects on the single-crystalline samples do not alter the Ti and Fe intensities. A reliable evaluation of the Ti amount deposited per pulse requires to precisely measure amounts around 0.1 ML.

If larger amounts are deposited at once (around 1 ML), Ti-rich phases form, which can complicate the quantification.

Amount of Ti deposited per pulse. Since conductive samples are required to perform STM, a 'low-doped' film with an almost perfect (1×1) termination was used as substrate, as per Figs. 4.7(b_1, b_2). To ensure that the same amount of ablated material was reaching the substrate, Ti was deposited at the same laser fluence and O_2 pressure (2.0 J/cm^2, 2×10^{-2} mbar) as during growth. However, a lower sample temperature (550 °C) was used to avoid segregation/interdiffusion of Ti. While the lower temperature might lead to a slight overestimation of the amount deposited due to a possibly larger sticking at 550 °C vs. 850 °C, the very low vapor pressure of Ti species (for Ti metal: 4×10^{-12} mbar at 850 °C, and 5×10^{-20} mbar at 550 °C; possibly even lower for Ti-O species), suggests that re-evaporation can be neglected. The amount of Ti deposited per pulse was quantified by evaluating the coverage of dark rows that thereby developed, using the estimated number of Ti atoms per unit cell that yield the dark rows, as inferred from the DFT results. The reference is the trench structure with (2×1) periodicity [Fig. 4.12(d)], which is characterized by 50% coverage of dark rows, and corresponds to one Ti atom per (1×1) surface unit cell, *i.e.*, 0.5 ML Ti. As a baseline, the coverage of dark rows was first evaluated on the pristine sample that was annealed for one minute at the same conditions later used for the deposition. This reference number was subtracted from subsequent evaluations. The same experiment was repeated by depositing first one pulse of TiO_2, then three pulses, each time re-preparing the sample in between and keeping the annealing time within one minute. The two experiments gave consistent results, and showed that a single laser pulse corresponds to the deposition of 3.2×10^{-2} Ti atoms per (1×1) surface unit cell, or $T_{\mathrm{Ti}} = 3.2 \times 10^{-2}$ ML.

Amount of Fe deposited per pulse. Since the growth mode is step flow, it is not possible to evaluate the amount of Fe deposited per pulse from the RHEED oscillations typically present in layer-by-layer mode. The thickness of a Ti-doped film grown with a known number of pulses was measured with a stylus profilometer. It was found that 60 000 Fe pulses with 120 intervening Ti pulses, deposited at 850 °C, 2×10^{-2} mbar O_2, 2.0 J/cm^2, correspond to a thickness of (91.5 ± 7.4) nm, or $T_{\mathrm{tot}} = (497 \pm 40)$ ML (given an interlayer spacing of 0.368 nm/bilayer, and that one bilayer of hematite contains four cations per unit cell, or 2 ML). One can then derive the amount of Fe atoms deposited per pulse as $T_{\mathrm{Fe}} = (T_{\mathrm{tot}} - 120T_{\mathrm{Ti}})/60\,000 = (8.22 \pm 0.67) \times 10^{-3}$ ML.

Estimation of the doping level. With the evaluation of the amount of Ti and Fe deposited per pulse in units of monolayer, and knowing the relative number of pulses shot on the two targets during growth, one can estimate the doping level. The low-doped film has a 1:500 ratio of laser pulses on the TiO_2:Fe_3O_4 targets; hence, the doping level can

be evaluated as $(1 \times T_{\mathrm{Ti}})/(1 \times T_{\mathrm{Ti}} + 500 \times T_{\mathrm{Fe}}) = (0.77 \pm 0.06)$ at.%. The high-doped film, with a four-fold higher ratio (3:375), has then a (3.09 $\pm$ 0.24) at.% doping level. To simplify the reading, these doping levels are referred to as 0.8 at.% and 3.1 at.%, respectively. One should mention that part of the deposited Ti segregating during growth is removed by the UHV treatments, especially for the 3.1 at.%-doped film [see Fig. 4.14(f)]. As a result, the true doping level of the bulk will likely be marginally smaller than 3.1 at.%. However, quantifying of the amount of Ti removed by these treatments from XPS data is not trivial because the distribution of dopants at the surface of the as-grown film is unknown.

4.8.2 Relation between surface doping, trench coverage, and Ti coverage

Consistent with the established definition of bulk doping in atomic percent, Section 4.5.2 has defined a 'surface' doping as $c^{\mathrm{s}}_{\mathrm{Ti}} = n_{\mathrm{Ti}}/(n_{\mathrm{Ti}} + n_{\mathrm{Fe}})$, where n_{Ti} and n_{Fe} are the numbers of Ti and Fe cations in layers C1 and C2. In light of the DFT models of the trench structures, one can relate the coverage of trenches θ measured by STM and the surface doping defined above. In this section, this relation is derived explicitly.

As shown in Section 4.4.2, a trench is formed as a result of the substitution of 2 Fe atoms in layer C2 by 2 Ti atoms in a (2 $\times$ 1) cell, and the simultaneous removal of 2 additional Fe atoms from layer C1 in the same cell (refer to the structural models in Fig. 4.11). θ is measured as the fraction of Fe atoms removed from layer C1 when a trench is formed: 2 Fe atoms removed from the C1 layer in a (2 $\times$ 1) cell (that contains four atoms), corresponds to a 50% coverage of trenches [*i.e.*, the structure in Fig. 4.11(c)], or θ = 0.5 ML.

Consider now that each cation layer in a (1 $\times$ 1) cell of undoped $Fe_2O_3(1\bar{1}02)$ contains two atoms. Doping an ($l \times m$) cell with k Ti atoms result in (i) replacement of k Fe atoms in layer C2 (out of the $2lm$ originally present), and (ii) removal of k Fe atoms from layer C1 (out of the $2lm$ originally present). Thus, the coverage of trenches amounts in this case to $\theta = k/2lm$, while the doping is

$$c^{\mathrm{s}}_{\mathrm{Ti}} = \frac{n_{\mathrm{Ti}}}{n_{\mathrm{Ti}} + n_{\mathrm{Fe}}} = \frac{k}{k + 2(2lm - k)} = \frac{k/2lm}{2 - k/2lm)} = \frac{\theta}{2 - \theta}.$$

Following the definition of monolayer, the coverage of Ti is, instead, the fraction of cations in layer C2 replaced by Ti, *i.e.*, $\theta_{\mathrm{Ti}} = k/2lm = \theta$.

4.8.3 As-grown films

The growth conditions (850 °C, 2×10^{-2} mbar O_2) result in partial segregation of Ti to the surface. This is most evident from the XPS results in Fig. 4.14(f) that show the evolution of the Ti 2*p* peak of a 3.1 at.% film as a function of its thickness. The increase is not linear, suggesting that only part of the Ti segregates to the surface.

The surface of the as-grown films, both 0.8 at.% and 3.1 at.% (of 62 nm and 92 nm thickness, respectively) appear morphologically flat in the STM and AFM images shown in Figs. 4.14(a, d), respectively. Large parts of the surface of the 0.8 at.% film exhibit the well-known (1×1) structure of $Fe_2O_3(1\bar{1}02)$,[96] with dark rows identified as characteristic Ti-induced features. However, sparse, irregular patches with no evident periodicity co-exist with these well-ordered regions [yellow arrow in Fig. 4.14(a)]. These patches feature roughly half the apparent height of a single step of the hematite surface (≈1.8 Å, to be compared with 3.68 Å for one O–Fe–O–Fe–O repeat unit). The disordered nature of these areas hinders fundamental studies at an atomic level. For this reason, the surface was reprepared by Ar^+ sputtering plus UHV-compatible O_2 annealing (550 °C, 7×10^{-6} mbar). The resulting surface, shown in Fig. 4.14(b), is an almost perfect $Fe_2O_3(1\bar{1}02)$-(1×1).

The surface of the as-grown 3.1 at.% film was not measured in STM right after growth. The *ex-situ* AFM image in Fig. 4.14(d) reveals the presence of round-shaped, 10–40 nm-wide features, never observed on UHV-treated hematite surfaces. Both the unusual appearance of the surface and the 6.2-fold higher XPS Ti 2*p* signal with respect to the 0.8 at.%-doped film [values extracted from the spectra in Figs. 4.14(c, f)] suggest that a new, Ti-rich phase formed at the surface. The Ti XPS increases more than in proportion to the doping level. A possible explanation is that this new phase, once nucleated, catches deposited Ti and floats up during growth. It is likely that the formation of the Ti-rich phase is related to the rather high O_2 pressures used (PLD growth was performed at 2×10^{-2} mbar), while it is not favorable under more reducing conditions. This may be related to the fact that substitutional Ti^{4+} in the Fe_2O_3 lattice leads to Fe^{2+}, while higher oxygen chemical potentials favor Fe^{3+}, which can coexist with Ti^{4+} only in a different crystal lattice such as in Fe_2TiO_5 (pseudobrookite). As per the low-doped film, this higher bulk doping was investigated on a UHV-prepared surface rather than on the as-grown film. After two sputtering–annealing cycles, the Ti 2*p* spectra saturate to the one shown in Fig. 4.14(f) with red symbols. In STM, the surfaces appear as in Fig. 4.14(e), *i.e.*, a $Fe_2O_3(1\bar{1}02)$ modified by Ti-induced line defects. These results show that, despite the accumulation of Ti in the near-surface region that is caused by Ti segregation during growth, one can recover well-defined hematite surfaces that are only slightly modified

by the presence of Ti.

4.9 Growth of (0001)-oriented Ti-doped Fe_2O_3 films

The same recipe used to grow a 0.8 at.%-doped film on the $(1\bar{1}02)$ termination of hematite [120× (1 pulse on TiO_2 target + 500 pulses on Fe_3O_4 target) at 850 °C, 2×10^{-2} mbar O_2, 2 J/cm^2, 5 Hz] was applied to grow a Ti-doped homoepitaxial film with (0001) orientation. The collected results on the as-grown (0001) film are comparable to the $(1\bar{1}02)$ termination: the sample is conductive in LEED [above 40 eV, as for the $(1\bar{1}02)$ oriented

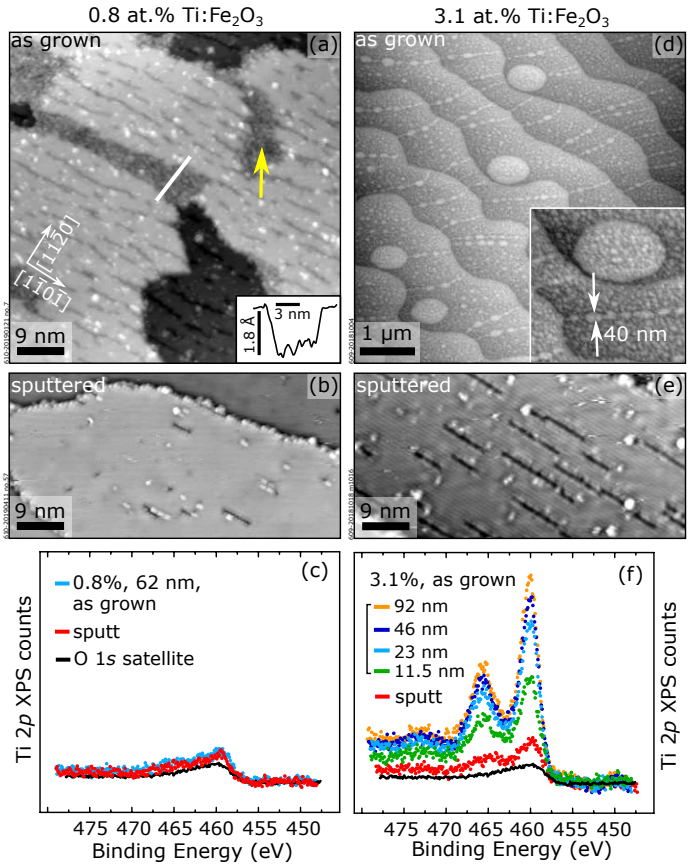

Figure 4.14. Ti segregation during the growth of Ti:$Fe_2O_3(1\bar{1}02)$ films. (a) and (b) STM images of a 0.8 at.% Ti-doped film of 62 nm thickness right after growth, and after UHV preparation, respectively. After growth, disordered areas, presumably Ti-rich phases [yellow arrow in panel (a), line profile of the white line in the inset] coexist with (1 × 1) areas with dark rows. (b) After one sputtering–annealing cycle, a mostly (1 × 1) surface is recovered. (c) The corresponding XPS Ti 2*p* signals are only slightly above the detection limit, thus it is difficult to determine whether the surface Ti concentration decreases with sputtering. (d) 6 × 6 µm^2 AFM image of a 3.1 at.% Ti-doped film of 92 nm thickness after growth, showing bright, circular features on the terraces. (e) After sputtering, the surface displays a (1 × 1) periodicity with dark rows in STM. (f) XPS of the as-grown film shows significant Ti enrichment, which increases with thickness, but is efficiently removed by sputtering. Reprinted from ref. 66.

samples], a small Ti signal is visible in XPS (not shown), and the surface morphology appears atomically flat in *ex-situ* AFM (Fig. 4.15).

It was not investigated systematically how Ti modifies the atomic-scale details of the surface, mostly because the structure of the undoped $Fe_2O_3(0001)$ is still under debate. STM and LEED-IV experiments are planned on the doped (conductive) films to unveil details about the surface structure and Ti-induced atomic-scale modifications.

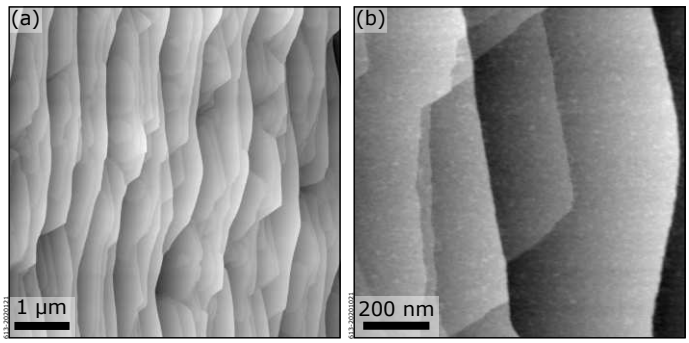

Figure 4.15. Morphology of a Ti:$Fe_2O_3(0001)$ film grown at the same conditions as per the 0.8 at.%-doped $(1\bar{1}02)$ films [120× (1 laser pulse on the TiO_2 target plus 500 pulses on the Fe_3O_4 target) at 850 °C, 2×10^{-2} mbar O_2, 2 J/cm^2, 5 Hz]. (a, b) 6×6 µm^2 and 1×1 µm^2 AFM images, respectively.

5. In_2O_3 films on YSZ(111)

5.1 Introduction

This Chapter addresses the growth of another binary oxide, In_2O_3, which was grown on (111)-oriented yttria-stabilized zirconia (YSZ). The focus is not as much as in the previous Chapter on establishing the atomic-scale properties of the film: In this case, single crystals do exist, and atomic-scale models for their surfaces have been established already. One practical reason to grow the thin-film counterpart is because the available single crystals are small, in fact too small for any surface science technique but local scanning probe microscopies. Growing films with bulk-like properties on sufficiently large substrates opens up exciting possibilities involving a multitude of area-averaging techniques. However, this is not necessarily trivial. In fact, the case of In_2O_3 discussed here shows that not all binary oxides, 'simple' to grow only by assumption, behave as expected: Growing atomically smooth In_2O_3(111) films proves to be challenging, if not impossible at any given set of deposition parameters.

The Chapter presents a systematic investigation of the dependence of the morphology of In_2O_3 films on the growth parameters. Such knowledge was used to develop a recipe that combines two growth regimes and yields films with the longed-for atomically smooth morphologies. Meanwhile, the role of the substrate on the first stages of growth is also highlighted: it is shown that the matching of the unit cells of the substrate and the growing material can induce the formation of antiphase domain boundaries that propagate through the growing film.

Before illustrating and discussing the results (most of which have been collected during the Master Thesis work of Jakob Hofinger, and published in ref. 67), an introduction is given about In_2O_3 and the existing literature on both the atomic details of its (111) surface and the growth of (111)-oriented thin films (Sections 5.1.1 and 5.1.2). The experimental methods are presented in Section 5.2, which also gives a short overview on the preparation of the YSZ(111) substrates. Section 5.6 summarizes the set of experiments where the films have been employed.

5.1.1 $In_2O_3(111)$

In_2O_3 is a post-transition metal oxide and crystallizes in the bixbyite structure [see Fig. 5.1(a)]. It belongs to the class of transparent conductive oxides,[172] being transparent in the visible regime[173] while possessing a high electrical conductivity.[174] These properties are shared with tin-doped In_2O_3 (referred to as indium-tin oxide, or ITO), which, together with the undoped material, is widely employed in various technological applications such as optoelectronics,[175–177] gas sensing,[178–180] and catalysis for reverse water–gas shift reactions.[181,182] Adding to its potential, In_2O_3 has recently shown promises for catalytic reactions such as hydrogenation of CO_2 to methanol,[183,184] and semi-hydrogenation of acetylene to ethylene.[185]

As it so often happens, in all applications where In_2O_3 is used, the relevant physical processes occur at the surfaces of the material, so that the device functionality is tightly bound to the surface properties of In_2O_3. The (111) termination is particularly relevant, as it is characterized by the lowest surface energy [see the the Wulff construction in Fig. 5.1(c)]. This facet will be predominantly exposed in In_2O_3 nanoparticles. As discussed below, single-crystalline $In_2O_3(111)$ samples have been used to model the surface properties of this termination and understand the phenomena underlying the various applications.

Figure 5.2 summarizes the STM–DFT findings on the (111) surface of In_2O_3 single crystals.[186] Panel (a) shows the appearance of the surface in STM after annealing at slightly oxidizing conditions (500 °C, 1×10^{-6} mbar O_2). It displays a threefold-symmetric array of dark, triangular depressions. The DFT model on the left side of Fig. 5.2(c) reveals that this termination is essentially a relaxed, bulk-terminated (1×1).

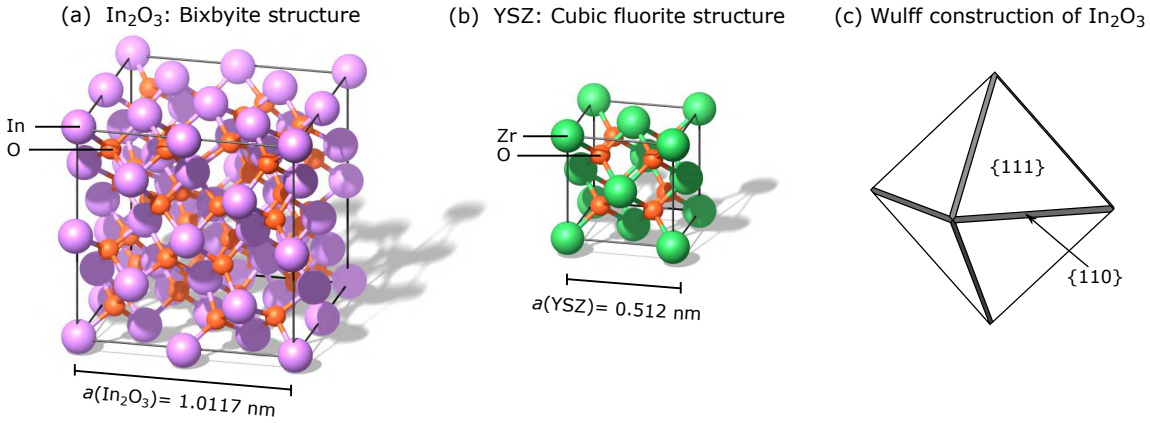

Figure 5.1. (a) Bulk unit cell of In_2O_3, which crystallizes in the bixbyite structure. The cubic unit cell contains a total of 80 atoms, with 32 atoms of In octahedrally coordinated to O, and 48 O atoms with tetrahedral coordination to In. (b) Bulk unit cell of yttria-stabilized zirconia (renderings by Michele Riva). (c) Calculated Wulff shape for an In_2O_3 single crystal, adapted with permission from ref. 172.

The unit cell, highlighted by the white rhombus both in the experimental image and in the theoretical model, contains 12 threefold-coordinated O atoms, 4 sixfold-coordinated In atoms, and 12 fivefold-coordinated In atoms; the dark triangles observed in STM are located at the position of sixfold-coordinated In (blue). After annealing at reducing conditions (500 °C, UHV), the surface appears as in Fig. 5.2(b), with bright dots sitting at the position of the dark triangles of the oxidized surface. DFT reveals that the bright dots correspond to In adatoms (see the right side of the DFT model): Opposed to other well-known oxide systems, *e.g.*, TiO_2 and CeO_2, exposing the surface of In_2O_3 to reducing conditions does not produce surface oxygen vacancies. The In-terminated surface is stable over a wide range of oxygen chemical potentials, as the low vapor pressure of metallic indium hinders the evaporation of In adatoms. At elevated temperatures the In adatoms diffuse along the surface, until they reach the lowest-energy position at the center of the dark triangles. When the surface is reoxidized, the In atoms react with oxygen and form small, stoichiometric In_2O_3 islands.

Establishing a structural model for the surface terminations of $In_2O_3(111)$ has allowed to investigate how the surface atomic details affect many key phenomena, *e.g.*, gas adsorption,[187,188] charge injection,[180] and interaction with organic molecules.[189] While

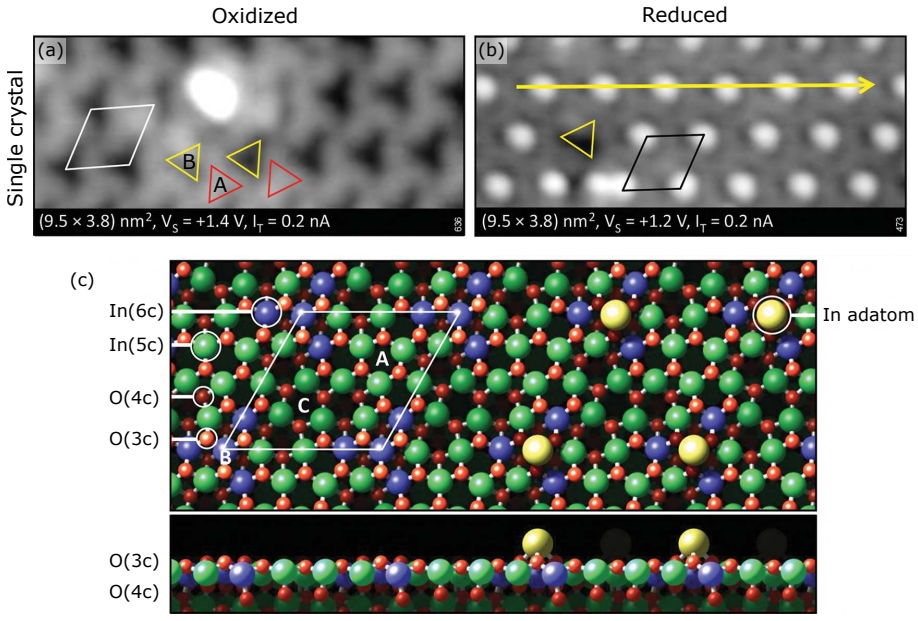

Figure 5.2. $In_2O_3(111)$ surface in STM and DFT. Depending on the annealing conditions, either an oxidized (a) or a reduced (b) structure can be obtained [500 °C, 1×10^{-6} mbar O_2 for (a), and 500 °C, UHV for (b)]. The reduced surface in panel (b) exhibits an ordered array of In adatoms (bright dots) sitting at the center of the 3-fold symmetric 'dark triangles' of the oxidized surface in panel (a). These dark triangles correspond to the positions of highly-coordinated In surface atoms. The corresponding DFT-derived model (c) shows the oxidized In_2O_3 surface, with In adatoms at the right side. Atoms are colored according to their coordination, *i.e.*, In(6c) is blue, In(5c) green, O(4c) dark red, and O(3c) bright red; In adatoms are yellow. Adapted with permission from ref. 186.

exciting, these studies were limited to local techniques such as STM and AFM, because of the small size of available single-crystals (only 1–2 mm diameter[190]). Area-averaging techniques such as temperature-programmed desorption (TPD), X-ray and ultra-violet photoelectron spectroscopies were excluded. As anticipated, to overcome the problem one can grow single-crystalline films on sufficiently large substrates (see Fig. 5.3). This could breach the fundamental knowledge on key catalytic processes occurring with superior efficiency at In_2O_3 surfaces, *e.g.*, semi-hydrogenation of acetylene to ethylene, CO_2 hydrogenation to methanol, electro-catalytic CO_2 reduction reactions in liquid solution, and photocatalytic reverse water–gas shift reactions.[183–185] In particular, such area-averaging investigations could shed light on the interaction between In_2O_3 surfaces and water, and its role for the above reactions.[191–194]

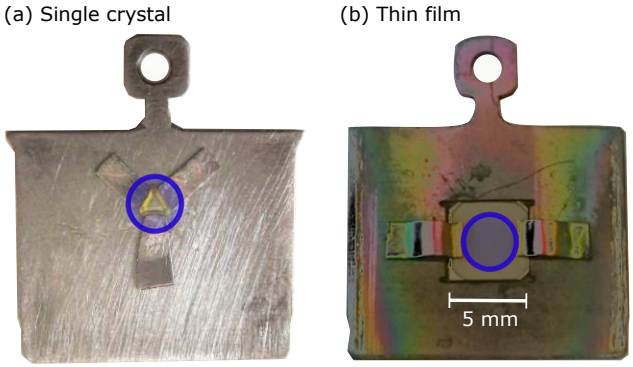

Figure 5.3. Comparison between an In_2O_3 single crystal and a In_2O_3 thin film grown within this Thesis. The small lateral dimension of the single crystal (a) inhibits the use of area-averaging techniques such as TPD (compare the dimension of the crystal with the size of the TPD spot in the available TPD setup[195] highlighted in blue). The problem is overcome with thin films (b), grown on 5×5 mm^2 substrates.

5.1.2 Epitaxial films on YSZ(111)

Epitaxial In_2O_3(111) and ITO(111) films have already been grown by both MBE and PLD, mainly using YSZ as a substrate,[57,196–198] thanks to the reasonably small lattice mismatch of 1.77% between the lattice parameter of In_2O_3 (1.0115 nm)[190] and twice the lattice parameter of YSZ (2×0.5147 nm = 1.0294 nm). In one case, the atomic-scale structure of a thin (12 nm) ITO/YSZ(111) film grown by MBE was resolved with STM (Fig. 5.4).[196] The surface reproduces the oxidized termination observed on single crystals [cf. Fig. 5.2(a)]. 10-nm-wide orientational domains attributed to the initial nucleation of the film are observed. Growing thicker films proves to be more challenging: The reports on the morphology of thick epitaxial In_2O_3(111) films are scarce, and when present, not reproducible. Growing atomically flat films at any set of parameters from the literature was not successful.

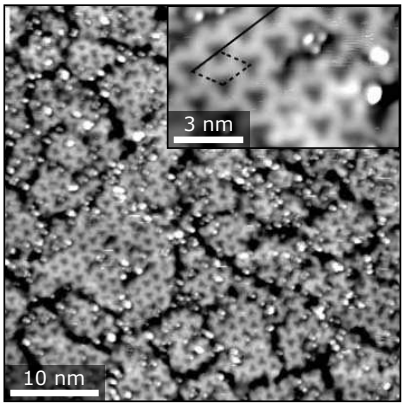

Figure 5.4. 12 nm-thick ITO/YSZ(111) film from ref. 196, grown by MBE. The film reproduces the atomic-scale details of the oxidized termination of In_2O_3(111) single crystals [cf. with Fig. 5.2(a)]. The surface is 'broken' in 10-nm-wide rotational domains.

To understand the reason, and to ultimately find a recipe to achieve the desired bulk-like films, the growth and the morphology of In_2O_3 on YSZ(111) were systematically investigated as a function of two key parameters: The oxygen background pressure and the substrate temperature. These two parameters are already known to affect the properties of In_2O_3 films. A variable amount of oxygen vacancies and/or In interstitials can form depending on the oxygen chemical potential determined by pressure and temperature, thus affecting the electrical conductivity of the film.[199–201] Also, it was reported that sufficiently reducing conditions lead to the formation of volatile In_2O species, which can cause film etching.[202]

The findings presented here are consistent with the literature: At reducing conditions, reduced species form and diffuse quickly on the surface, producing discontinuous films with large, mound-like islands. At more oxidizing conditions, oxidized species form and diffuse slower on the surface, causing small islands to dominate the morphology. To achieve ideal, flat morphologies, these two regimes are combined in a three-step growth recipe. The resulting films are ≈81% relaxed with respect to the pseudomorphic case, as judged from XRD, and exhibit the same atomic-scale surface structures as In_2O_3 single crystals (as determined by STM), while overcoming their size limitation (see Fig. 5.3). However, they are more sensitive to the preparation conditions than single crystals: When subjected to prolonged reducing treatments, they break along antiphase domain boundaries that arise from the one-on-four lattice matching of the In_2O_3 and YSZ(111) surface unit cells. The film morphology can, however, be recovered by high-temperature annealing under oxidizing conditions.

5.2 Methods

Growth parameters. The In_2O_3 films (thickness between 9 and 190 nm) were grown from a sintered target (China Rare Metal Material Co., Ltd., 65% density, $\geq$ 99.99% purity) at 2.0 J/cm^2 laser fluence, 1 Hz, with substrate temperatures varying between 700 °C and 900 °C, and O_2 pressures between 7×10^{-6} mbar and 0.2 mbar. For some experiments, a set ratio of O_2:Ar pressure was introduced in the chamber during growth, while keeping the total pressure at 0.2 mbar. After growth, all films were post-annealed for 30 min at the growth conditions.

Substrate: YSZ(111). YSZ(111) single crystals (CrysTec GmbH, $5 \times 5 \times 0.5$ mm^3, 9.5 mol% Y_2O_3-doped, one-side polished, $< 0.3°$ miscut) were used as substrates. Striving for atomically flat surface morphologies with straight, monoatomic steps, it was investigated how different preparation procedures affect the surface morphology of YSZ(111).

The *ex-situ* non-contact AFM images of Fig. 5.5 show the effect of a few different preparation procedures on as-received YSZ(111) single crystals. Sonication in Extran (2×30 min) and ultrapure water (10 min) reveals jagged steps separating monoatomic terraces [panel (a)]. The morphology improves by annealing at 1 050 °C in air for 3 h [panel (b)]. However, the irregular shape of the steps and the size of the small islands near them suggests that the diffusion of the surface species is kinetically limited. Indeed, annealing at higher temperature (1 h at 1 350 °C, inside pre-cleaned alumina crucibles, ramp rate 8 °C/min) yields the desired straight steps, separated by atomically flat terraces [panel (c)]. The exact procedure used to prepare each as-received substrate for the growth of In_2O_3 has been as follows:

- Sonication in Extran (2×30 min) and ultrapure water (10 min), as per Fig. 5.5(a). This step removes contamination from polishing residues.

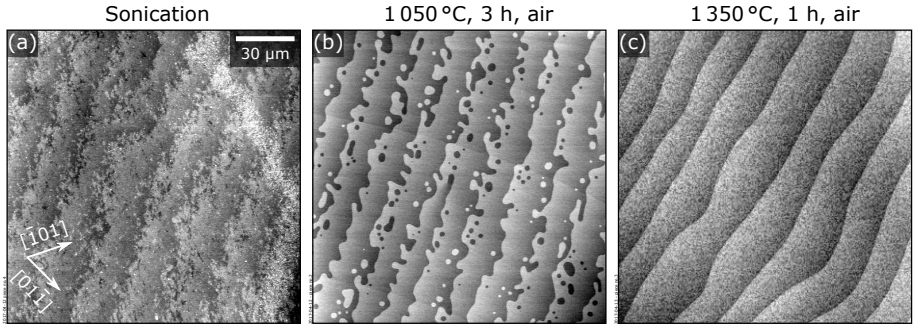

Figure 5.5. (6×6 µm^2) AFM images of YSZ(111) substrates documenting the *ex-situ* treatments. (a) 2×30 min sonication in Extran, plus 10 min sonication in ultrapure water. (b) 3 h air annealing at 1 050 °C. (c) 1 h air annealing at 1 350 °C.

- Annealing in air for 1 h at 1 350 °C, as per Fig. 5.5(c).
- Deposition of a Pt film on the back of the sample, to ensure absorbtion of the IR laser—see Section 2.4.2.
- Deposition of Pt electrodes at the corners of the front surface and at the sides of the sample, to overcome the insulating nature of YSZ (band gap of 5.7 eV[203])—see Section 2.4.2.
- Sonication in Extran (2 × 15 min) and ultrapure water (15 min). After this step, the surface quality was always checked with AFM, to ensure it was comparable to that of Fig. 5.5(c). At times, this step results in partial damaging of the Pt layer, and subsequent redeposition of Pt on the sample's surface. Additional cleaning cycles are performed until the needed surface quality is observed in AFM.
- Mounting [see Fig. 5.3(b) in Section 2.4.1], and insertion in the UHV system.
- Annealing for 20 min in UHV at 550 °C, to remove 'adventitious' carbon (judging by XPS, not shown).

In_2O_3 target. The In_2O_3 target employed for the growths is relatively porous (65% of the ideal density), and there are indications that this can affect the growth of In_2O_3 films under certain circumstances. After inserting the target in UHV, a significant degassing was always observed (pressure rise in the 10^{-7} mbar range, mainly H_2O and hydrocarbons), likely because the target acts as a 'sponge' when moved outside vacuum. If films are grown shortly after insertion of the target in UHV, the resulting film morphology is significantly worse than after prolonged use of the target in UHV: Pits of tens of nanometers thickness are observed in the first case, as opposed to the atomically flat morphologies obtained by growing at the same conditions after prolonged use of the target (or after the target is heated by the IR laser). Two factors could be responsible for these changes in the surface morphology: (i) The presence of H_2O or other contaminants incorporated in the target, which may affect the diffusion of the landing species, and thus, the surface morphology; (ii) the absorption coefficient of the target that changes after prolonged use (the target's surface becomes black), and, as a consequence, causes a change in the amount of material ablated per pulse. This in turn could change the thickness of the thin film deposited during the first step of the recipe, possibly influencing the final morphology (see Section 5.3.3). The films presented here were all grown after similar use/degassing of the target.

Film thicknesses. The thickness of the films was evaluated from the periodicity of

the first RHEED oscillations and further confirmed by stylus profilometer measurements performed on the thickest, continuous films (not shown). For disconnected films, 'equivalent' thicknesses were considered. The equivalent thickness is the thickness one would have if all material concentrated on the disconnected islands would be uniformly distributed across the film. It was evaluated from the measured coverage of islands and their average height.

XPS analysis. The Auger parameters (Fig. 5.14) were evaluated from the position of In $3d_{5/2}$ and In $M_4N_{45}N_{45}$ peaks. The peaks were fitted in CasaXPS with an asymmetric Gaussian–Lorentzian line shape after subtraction of a Shirley-type background.

Definition of oxygen chemical potential, μ_O. For calculating the oxygen chemical potential $\mu_O(T, p_{O_2}) = 1/2\,\mu_{O_2}(T, p_{O_2})$ at a given growth temperature T and oxygen partial pressure p_{O_2}, the ideal-gas expression[160] was used

$$\mu_{O_2}(T, p_{O_2}) = \mu^0_{O_2}(T) + k_B T \ln\left(\frac{p_{O_2}}{p_0}\right), \tag{5.1}$$

where k_B is Boltzmann's constant, $p_0 = 1$ bar, and T is the absolute temperature in Kelvin, while

$$\mu^0_{O_2}(T) = H_{O_2}(T, p_0) - H_{O_2}(0\,\mathrm{K}, p_0) - T\,[S_{O_2}(T, p_0) - S_{O_2}(0\,\mathrm{K}, p_0)] \tag{5.2}$$

is chosen such that $\mu_{O_2}(0\,\mathrm{K}, p_{O_2}) = 0$.[160] The enthalpy and entropy per O_2 molecule, $H_{O_2}(T, p_0)$ and $S_{O_2}(T, p_0)$ are derived from thermochemical tables.[204] The ideal-gas chemical potential is a convenient way of incorporating in one descriptor the combined contributions of growth temperature and oxygen partial pressure. Strictly speaking, μ_{O_2} determines the thermodynamic stability of In_xO_y species at equilibrium; nevertheless, as long as exchange with the gas phase is fast enough, it can be also employed for non-equilibrium processes like PLD.

5.3 Results

5.3.1 Effect of oxygen background pressure and substrate temperature

Ex-situ AFM was used to investigate the influence of the O_2 pressure and substrate temperature on the morphology of thin In_2O_3(111) films grown on identically prepared YSZ

substrates (see above). Figure 5.6 summarizes the results. Pronounced differences are observed at different sets of parameters. The effect of the O_2 pressure can be appreciated by comparing the morphologies of similarly thick films grown at 700 °C and O_2 pressures ranging from 7×10^{-6} mbar to 0.2 mbar [Figs. 5.6(a–d)]. At the lowest pressure [panel (a)], the film consists of large, triangularly shaped and well-separated three-dimensional (3D) islands (up to 30 nm high, 200- to 500-nm lateral size), with flat tops showing monoatomic terrace steps. Flat terraces separated by monoatomic steps are present between the In_2O_3 mounds. Higher pressures lead to the formation of smaller, irregular, connected 3D islands [see, *e.g.*, the line profile at the bottom of panel (d)]. The root-mean-square (rms) surface roughness measured on (1×1) μm^2 images steadily decreases with increasing pressure, from 2.7 nm, to 2 nm, an 0.7 nm, for 5×10^{-3}, 3×10^{-2}, and 0.2 mbar, respectively. The qualitative behavior of the RHEED specular-spot intensity monitored during the growth is similar at all conditions, displaying a single oscillation cycle, followed by a steady decrease of the signal (not shown). This behavior is indicative of a Stranski–Krastanov growth mode, characterized by the formation of a flat film (in this case of one layer thickness) followed by 3D island growth. Thus, the monoatomic steps observed between the islands in panel (a) are most likely YSZ steps covered by a single In_2O_3 layer.

In_2O_3 films grown in an O_2–Ar mixture [Figs. 5.6(f–h)], always with a total pressure

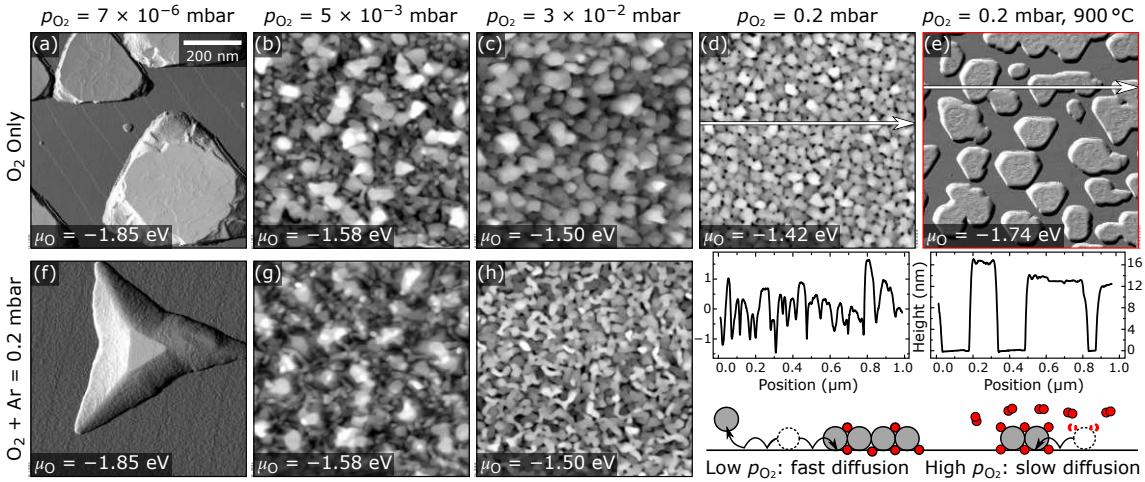

Figure 5.6. Morphology of In_2O_3 thin films: Effect of O_2 pressure and temperature. AFM images $(1 \times 1$ μm$^2)$ of In_2O_3/YSZ(111) thin films are shown in the main panels. Films grown at 700 °C in (a–d) an O_2 environment, and (f–h) an Ar–O_2 mixture, with a total pressure of 0.2 mbar, and the O_2 partial pressure p_{O_2} corresponding to the films in panels (a–c). Increasing the substrate temperature from (d) 700 °C to (e) 900 °C while keeping p_{O_2} at 0.2 mbar produces a morphology similar to that of panel (a). The changes in morphology are assigned to the differences in μ_O (reported at the bottom left of each AFM image). All films are 9 nm thick, except for the one in panel (d) that is 15 nm thick. Due to the large height of the islands in panels (a), (e), and (f), these images have been differentiated, and are shown as illuminated from the left. Line profiles extracted along the white arrows are reported in the bottom part of panels (d) and (e). Adapted from ref. 67.

of 0.2 mbar, but with p_{O_2} equal to those employed for the films in Figs. 5.6(a–c), highly resemble the films grown with O_2 only: At the lowest p_{O_2}, large, triangular, flat-topped, separated islands are observed, while, on increasing p_{O_2}, the surfaces evolve to continuous films consisting of smaller islands with steadily decreasing surface roughness. These comparisons show that, at fixed temperature, only the oxygen partial pressure is responsible for the diffusivity of the surface species: The large islands formed at low p_{O_2} can be attributed to surface energy minimization (near thermodynamic equilibrium), *i.e.*, fast surface diffusion. Instead, the smaller islands formed a high p_{O_2} are a sign of growth limited by diffusion. The total pressure in the chamber does not significantly affect the growth mechanism. The small differences in the island shapes obtained at the lowest oxygen pressure could be partly caused by the experimental difficulty in precisely controlling the oxygen flow at high Ar pressures and/or by a dependence of the relative surface energies of different In_2O_3 facets on the atmosphere: Since Ar and O_2 are introduced via the same gas line, the actual oxygen pressure employed for the O_2–Ar mixture growth of Fig. 5.6(f) might be slightly lower than for Fig. 5.6(a).

Increasing the growth temperature from 700 °C to 900 °C at 0.2 mbar O_2 results in large, flat-topped, well-separated islands, as seen from Figs. 5.6(d, e). They are up to 22 nm high and 100 to 200 nm wide, as seen from the line profile at the bottom of Fig. 5.6(e), similar to those observed when growing at 700 °C, 7×10^{-6} mbar [Fig. 5.6(a)].

For convenience, the bottom-left corner of each figure panel reports the value of the chemical potential of oxygen μ_O, which combines the effects of substrate temperature and oxygen partial pressure (see Section 5.2 for the definition of μ_O). Notice that comparable μ_Os yield remarkably similar growth morphologies.

5.3.2 Effect of film thickness

It is apparent from Fig. 5.6 that none of the In_2O_3 thin films grown with a single set of parameters (substrate temperature and p_{O_2}) displays the desired, atomically flat surface: The films consist of either large and separated mounds or small, interconnected islands that result in a relatively large rms surface roughness. Increasing the film thickness is not beneficial at any set of growth parameters. For instance, when thick films (up to 10 times thicker than the films discussed above, *i.e.*, around 80 nm) are grown at the same conditions of the thin films in Figs. 5.6(b–d), the surface undergoes a significant roughening (not shown): The pre-existing islands remain disconnected, and the surface roughness significantly increases (rms value up to 5 times larger). When, instead, thicker films are grown at close-to-equilibrium conditions (900 °C, 0.2 mbar O_2, see Fig. 5.7), the large, well-separated, flat-topped In_2O_3 islands of Fig. 5.7(a) progressively merge, growing in

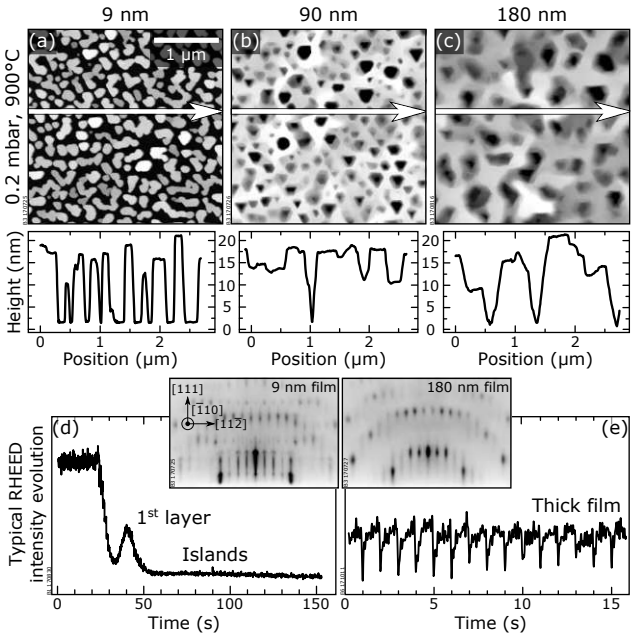

Figure 5.7. Morphology of In_2O_3 thin films: Effect of film thickness. (a–c) AFM images and associated line profiles of In_2O_3(111)/YSZ grown at 900 °C, 0.2 mbar O_2. Starting from disconnected islands (a), a progressive merging is observed (b), but the thick film retains 20 nm-deep pits (c). (d, e) Real-time monitoring of the RHEED specular spot intensity. A Stranski–Krastanov growth mode (d) is followed by step-flow (e), when the film completely wets the surface. Inset: RHEED patterns of the thin and the thick film. The initially 3D-like surface evolves towards a more 2D-like character. Reprinted from ref. 67.

both height and lateral dimension and forming a continuous film [Fig. 5.7(b)]. However, numerous pits, as deep as 20 nm, are visible on the surface, and the initial roughness is essentially preserved. Further increasing the thickness [Fig. 5.7(c)] partially helps in reducing the number of pits and delivers a surface with atomically flat regions in between the pits (measurable in STM, not shown); however, the overall surface roughness is preserved [4.2 nm rms for the film in Fig. 5.7(c) when evaluated on 6×6 µm^2 images]. The transition to a locally flatter surface is confirmed by the real-time monitoring of the RHEED specular spot: At first, a Stranski–Krastanov behavior is observed [Fig. 5.7(d)], characterized by one oscillation maximum followed by a steady decrease of the intensity. As the islands coalesce and the film wets the whole surface, the RHEED intensity exhibits a sharp decrease at each pulse of the UV laser, followed by a rapid recovery to the initial value [Fig. 5.7(e)]. This is indicative of the fast diffusion of the deposited species, which are readily incorporated at the surface of the growing film (*e.g.*, at steps). The RHEED pattern in the inset of Fig. 5.7 evolves from 3D-like to more 2D: While thin films are characterized by a regular periodicity in the direction orthogonal to the surface (left panel), pronounced Laue circles are visible on the thicker films (right panel). Despite the improved quality, the film roughness is still deemed unsatisfactory, as the high density of steps in proximity of the pits can severely affect, *e.g.*, the local electronic structure[205] or the chemistry of the material.[206]

5.3.3 Recipe to obtain atomically flat films

The difficulties in growing thick In_2O_3 films with an atomically flat surface can be surpassed with a three-step buffer-layer growth recipe (Fig. 5.8) that relies on the preparation of a closed and flat thin film before the subsequent (homoepitaxial) growth of a thick film under close-to-equilibrium conditions:

- Step 1: Growth of a 15 nm-thick film at 700 °C, 0.2 mbar O_2 (followed by a 30 min post-annealing at the growth conditions), to form a connected In_2O_3 film completely covering the substrate surface. As seen from Figs. 5.8(a_1, a_2), this film consists of small islands characterized by a pronounced 3D-like diffraction pattern in RHEED [Fig. 5.8(a_4)]. The periodicity of the (111) surface of In_2O_3 [186] appears in the LEED pattern in Fig. 5.8(a_3), in addition to faint half-integer spots that are neither observed on single crystals nor on thicker films. (The origin of these additional spots was not investigated within this Thesis.) The large size of the LEED spots is consistent with a relatively poor long-range order of the surface crystallinity.

- Step 2: Postannealing the film at 900 °C, 0.2 mbar O_2, 45 min, to flatten the film surface. The small islands merge, and the film morphology improves [Figs. 5.8(b_1, b_2)]. At the same time, shallow pits (4 nm deep) start to form. The optimal postannealing time (to sufficiently flatten the surface while limiting the number and depth of the pits) was found to be around 45 min. The sharper spots in LEED [Fig. 5.8(b_3)] and the streaky appearance of the RHEED pattern, together with the enhanced intensity along the Laue circles [Fig. 5.8(b_4)], testify to the increased crystallinity and 2D character of the surface.

- Step 3: Growth of additional 175 nm (for a total of 190 nm) on top of the annealed thin film, at 900 °C, 0.2 mbar O_2. The growth proceeds by fast surface diffusion of the deposited species and provides a closed, atomically flat film [Figs. 5.8(c_1, c_2)], with 10- to 200-nm-wide terraces separated by monoatomic steps, and just a few, shallow pits (up to 10 nm deep). The typical rms roughness of the films ranges between 0.4 and 0.6 nm (measured on 6×6 μm^2 images), *i.e.*, approximately one order of magnitude better than for films of similar thickness grown at one set of parameters (cf. Fig. 5.7). The bright and sharp spots of the LEED pattern [Fig. 5.8(c_3)] and the very pronounced Laue circles in RHEED [Fig. 5.8(c_4)] attest to the high crystalline quality of the surface.

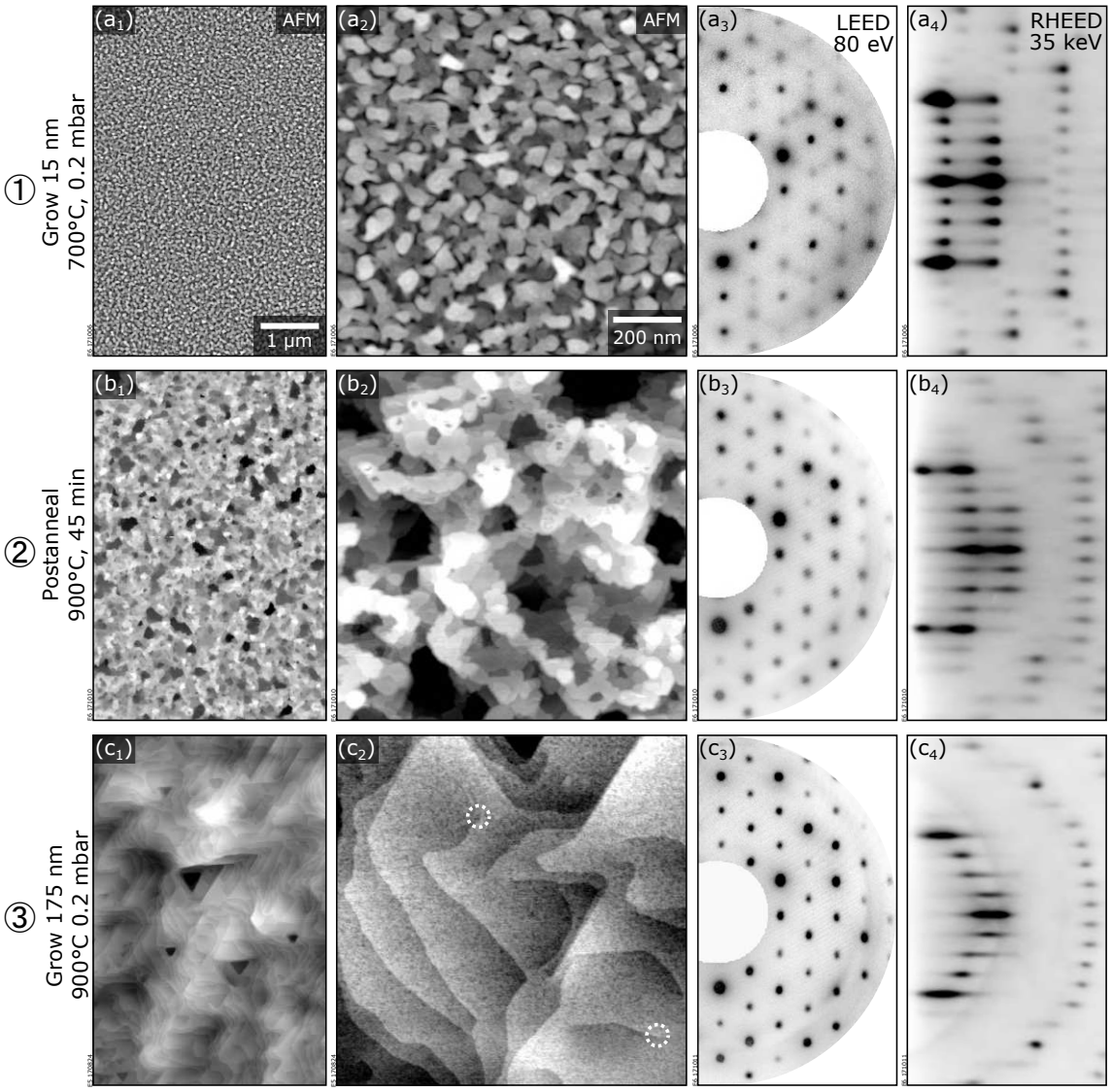

Figure 5.8. Three-step recipe to grow atomically flat In_2O_3(111)/YSZ films of 200 nm thickness. (1) A thin, closed film is grown under kinetically limited conditions [(a_1)–(a_4)]. (2) Postannealing the film at higher temperatures promotes surface flattening [(b_1)–(b_4)]. (3) A thick film is deposited on top at close-to-equilibrium conditions, such that rapid diffusion and incorporation of the deposited species occurs, yielding a well-controlled and atomically flat surface [(c_1)–(c_4)]. The sharpening of the LEED spots and the enhancement of the 2D character of the RHEED patterns from step (1) to step (3) demonstrate the improved crystallinity of the surface. Reprinted from ref. 67.

5.3.4 XRD characterization

Figure 5.9 shows XRD reciprocal-space maps acquired around symmetric 4,4,4_c and asymmetric 6,2,2_c reflexes from a ≈200 nm-thick In_2O_3 film grown with the three-step growth recipe described above. Growth along the [111] direction causes a trigonal distortion of the cubic unit cell of In_2O_3 as a result of the lattice mismatch with the YSZ substrate. Hence, a different indexing than on the cubic In_2O_3 is needed: Given a cubic, relaxed In_2O_3 unit cell, a hexagonal basis with in-plane and out-of-plane lattice param-

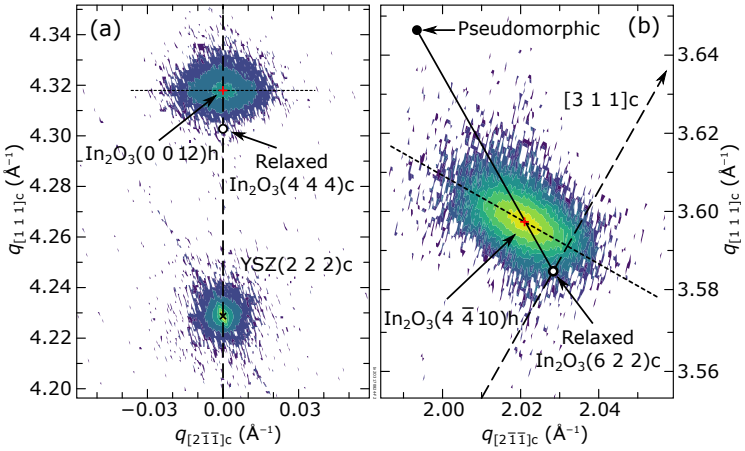

Figure 5.9. Structural properties of 200 nm-thick In_2O_3/ YSZ(111) films from XRD. Reciprocal-space maps acquired around (a) symmetric and (b) asymmetric reflexes (grazing incidence); $q_{[2\bar{1}\bar{1}]c}$ and $q_{[111]c}$ represent the in-plane and out-of-plane components of the transfer momentum, respectively, where $q = 2\pi/d$ when d is the distance between diffracting planes; "c" stands for Miller indexes of the cubic unit cell, while "h" refers to the trigonally distorted In_2O_3 lattice. In panel (a) Bragg peaks from YSZ 2,2,2$_c$ and In_2O_3 0,0,12$_h$ reflexes are visible. In panel (b) only the hexagonal In_2O_3 4,$\bar{4}$,10$_h$ reflex is accessible to the measurement, since diffraction from YSZ(311)$_c$ planes requires transmission of the incoming x-rays through the sample. The peak positions expected for cubic, relaxed In_2O_3 4,4,4$_c$ and In_2O_3 6,2,2$_c$ reflexes are indicated in panels (a) and (b), respectively. The ideal Bragg position for a fully strained, pseudomorphic In_2O_3 film, as well as the In_2O_3 relaxation line (solid) are also shown in panel (b). The dotted lines in panels (a) and (b) are perpendicular to the cubic [111] and [311] directions, respectively. Reprinted from ref. 67.

eters a=$\sqrt{2}d_{(100)c}$≈1.430 nm and $c = \sqrt{3}d_{(100)c}$≈1.752 nm, respectively, can be defined, where $d_{(100)c}$=1.0115 nm is the cubic lattice parameter of In_2O_3.[190] With this definition, the cubic 4,4,4$_c$ and 6,2,2$_c$ reflexes of relaxed In_2O_3 correspond to the hexagonal 0,0,12$_h$ and 4,$\bar{4}$,10$_h$ Bragg peaks, respectively. The ideal positions of these reflexes for cubic, relaxed In_2O_3 are indicated in Fig. 5.9 with open circles. The tensile lattice mismatch with the YSZ substrate will cause the in-plane and out-of-plane lattice parameters a and c of the In_2O_3 film to expand and contract, respectively. Indeed, the symmetric 0,0,12$_h$ film reflex is found at larger out-of-plane momentum transfers than for a cubic In_2O_3 crystal, as visible in Fig. 5.9(a), and the asymmetric 4,$\bar{4}$,10$_h$ Bragg peak in Fig. 5.9(b) is moved to smaller (larger) in-plane (out-of-plane) reciprocal space positions. It should be noted that the film is not fully pseudomorphic, since its reflexes are observed at momentum transfers between the ones expected for a fully strained, pseudomorphic In_2O_3/YSZ(111) film [black dot in Fig. 5.9(b)] and the relaxed, cubic In_2O_3. Quantitative evaluation of the lattice parameters of the film from the reciprocal space maps in Fig. 5.9 yields $a_{\text{film}} = 1.435$ nm and $c_{\text{film}} = 1.746$ nm, corresponding to residual strains $\epsilon_{\parallel} = 0.334\%$ and $\epsilon_{\perp} = -0.332\%$ along the in-plane and out-of-plane directions. The residual strain $\epsilon_{\parallel}$ is only 19% of that in a pseudomorphic film. It can be noticed that both, the symmetric, and the asymmetric film reflexes appear broadened along the direction parallel to the diffracting planes [dotted lines in Fig. 5.9]. While the broadening

of the symmetric peak could be consistent with both, a limited lateral correlation length (*i.e.*, grain size), and the presence of microscopic tilting (*i.e.*, mosaicity), the broadening direction of the asymmetric peak suggests the latter scenario. In fact, this is further supported by the presence of screw dislocations at the surface of the films [see dashed circles in the AFM image of Fig. 5.8(c_2)]. Screw dislocations form to relieve the misfit strain with the substrate, and cause a ≈0.19° microscopic tilting, as determined from the full-width at half maximum of the reflexes.

5.3.5 STM characterization

Oxidized and reduced terminations

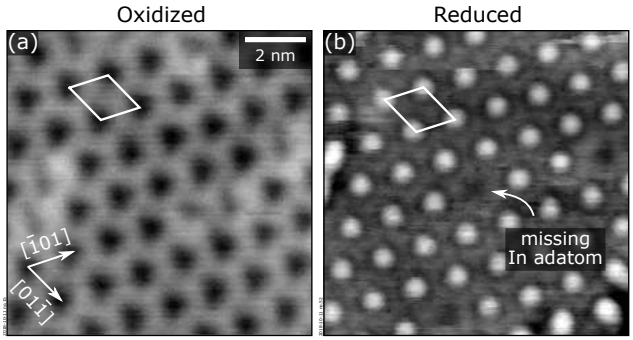

Figure 5.10. The In_2O_3(111) oxidized (a) and reduced (b) surfaces on the thin films, reproducing the same terminations observed on the surfaces of In_2O_3 single crystals[186] (see main text for preparation conditions). Unit cells are indicated by white rhombi. Reprinted from ref. 67.

The films' surfaces were further characterized with STM, to test the reproducibility of the surface morphologies observed on In_2O_3 single crystals after standard preparation procedures. The characteristic features observed on the oxidized and reduced terminations of In_2O_3(111) single crystals [Figs. 5.2(a, b)] are well reproduced on the films [Figs. 5.10(a, b)].

The oxidized termination is observed on the films right after growth or after high-pressure annealing of the film (900 °C, 0.2 mbar O_2), and when exposing the reduced surface to slightly oxidizing conditions, similarly as for single crystals ($\geq$ 20 min at 500 °C, $\geq 1 \times 10^{-6}$ mbar O_2). The reduced termination, instead, is obtained by annealing the as-grown film under reducing conditions ($\geq$ 10 min at 350–500 °C, UHV), or after standard sputtering–annealing cycles ($\geq$ 10 min, 1 keV, 2–8 $\times$ 10^{-6} mbar Ar, ≈6 μA, followed by $\geq$ 20 min annealing under reducing conditions). The areal coverage of In adatoms increases with time and temperature within this temperature range, as expected from earlier studies performed on single crystals.[186] The full coverage of In adatoms—as per Fig. 5.10(b) and Fig. 5.11(a)—can be obtained only by sputtering–annealing cycles.

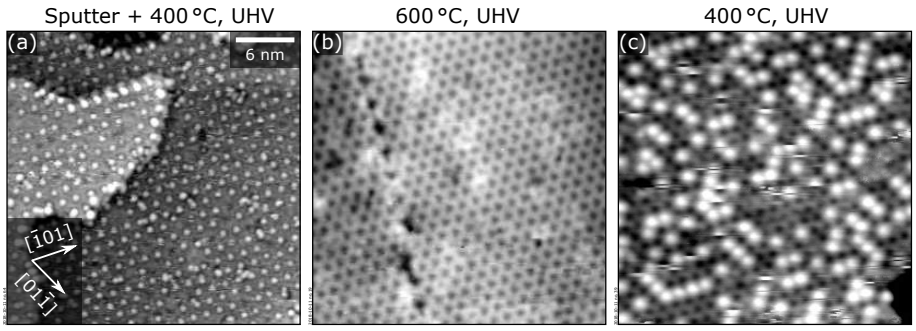

Figure 5.11. Transitions between oxidized and reduced terminations of In_2O_3(111) films, as observed in STM (the images are 30 × 30 nm^2). (a) After sputtering plus annealing at 400 °C in UHV, the surface exhibits a full coverage of In adatoms. (b) Annealing in UHV at 600 °C produces a transition to the oxidized termination. (c) Annealing back in UHV at 600 °C makes In adatoms appear again. The 'scratches' visible in panel (c) are most likely due to loosely adsorbed H_2O from the chamber background that are easily moved by the STM tip while scanning.

Interestingly, a transition to the oxidized termination was observed when annealing in UHV at temperatures higher than 500 °C [Fig. 5.11(b)]. The transition is reversible: Annealing at lower temperatures (still in UHV) produces a partial coverage of In adatoms on the surface [Fig. 5.11(c)]. This behavior is surprising, as one would expect to retain the reduced termination at more and more reducing conditions. A tentative explanation it that an increase in temperature not only makes the conditions more reducing, but also allows migration of the excess oxygen in the film or in the YSZ substrate to the surface. This excess oxygen can produce the oxidized termination even at reducing conditions. This theory could also explain why the full coverage of In adatoms cannot be achieved by annealing only, but requires additional sputtering (sputtering is preferential to oxygen, hence it helps the formation of the reduced termination). To understand whether single crystals share a similar transition with the thin films, similar annealing experiments are planned for In_2O_3 single crystals.

Antiphase domain boundaries and other surface defects

Figure 5.10 shows that the atomic-scale structure of the thin films is consistent with the one of single crystals. On a mesoscopic scale, however, some defects are seen that are not present on single crystals. These defects consist of antiphase domain boundaries (APDBs), 'trenches', and screw dislocations (occasionally, a few screw dislocations are present also on In_2O_3 single crystals).

APDBs are present on the as-grown films [white arrow in Fig. 5.12(a), close up in Fig. 5.12(d)]. From a comparison of the positions of dark triangles on the left- and right-hand sides of Fig. 5.12(d), it is clear that an in-plane shift of half a unit cell exists across the domain boundary, with localized defect sites [darker appearance in Fig. 5.12(d)] connecting the two domains. These defects are assigned to the one-on-four lattice matching

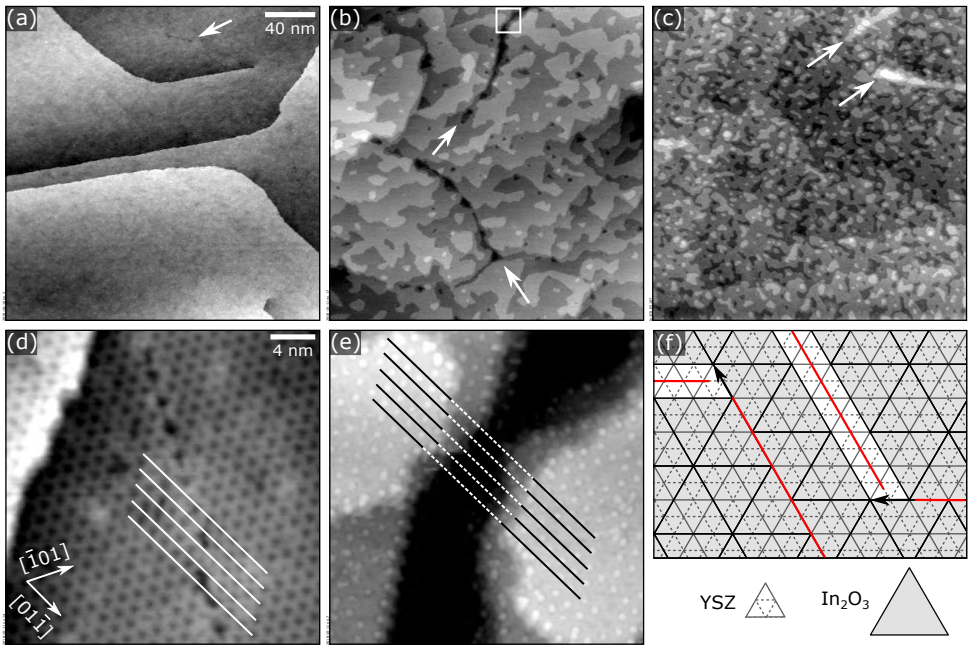

Figure 5.12. Antiphase domain boundaries. (a–e) STM images (U_{sample} = +1.8 V, I_t = 0.1–0.2 nA, top row: 250 × 250 nm^2, bottom row: 28 × 28 nm^2). (f) Superposition of YSZ and In_2O_3 unit cells: solid and dashed lines correspond to the (111) projection of bulk unit cells (black: In_2O_3, light gray: YSZ) and to the surface unit cell of YSZ(111), respectively. Shifts of multiples of a quarter of the In_2O_3(111) unit cell along one of the three $\langle 1\bar{1}0 \rangle$ high-symmetry directions are possible and lead to the formation of antiphase domain boundaries (APDBs, red lines). In panel (d), a shift of half a unit cell is observed across a domain boundary. Material is preferentially lost at these defects under reducing conditions, resulting in the formation of several-layers-deep trenches [white arrows in panel (b) and close-up in panel (e)]. The half-unit-cell shift observed on same-height terraces across the trench in panel (e) confirms that trenches originate from APDBs. Bright ridges [white arrow in panel (c)] are formed on reoxidation (60 min, 550 °C, 5 × 10^{-6} mbar) of a reduced surface with trenches. Reprinted from ref. 67.

of the surface unit cells of In_2O_3 and YSZ(111) (more details in the Discussion in Section 5.4).

After sputtering followed by mild UHV annealing at 400 °C, the surface becomes rougher and more defects appear in the form of few-layers-deep trenches. These extend along the high-symmetry directions of In_2O_3(111) [white arrow in Fig. 5.12(b), close-up in Fig. 5.12(e)]. Figure 5.12(e) highlights the presence of an in-plane shift of half a unit cell across the trench for same-height terraces. Similarly to single crystals, longer and harsher reducing treatments lead to a further roughening of the surface, with the appearance of small, triangularly shaped islands with straight step edges oriented along the three $\langle 1\bar{1}0 \rangle$ high-symmetry directions of In_2O_3(111) and the appearance of clusters of In adatoms on the surface (not shown). Moreover, the lateral size and depth of the trenches increase on harsher reducing treatments [see Fig. 5.13(a) for the AFM image of an overly reduced film], entailing a narrower window of parameters for preparing the films under reducing conditions than for single crystals. The formation of the trenches under reducing conditions is consistent with recent reports showing that deposition of

In_2O_3 under reducing conditions leads to film etching, as induced by the decomposition of In_2O_3 into volatile In_2O and oxygen species.[202]

When the reduced surface is reoxidized multiple times under UHV-compatible conditions, another type of defect appears, in the form of bright ridges, again along the high-symmetry directions of the surface [white arrows in Fig. 5.12(c), obtained after annealing at 500 °C in 5×10^{-6} mbar O_2, 60 min] and coexisting with the trenches. Annealing at the growth conditions (900 °C, 0.2 mbar O_2, $\geq$ 1 h) is effective to recover a trench/ridges free surface: Fig. 5.13 shows the transformation of a severely reduced surface to an ideal, atomically flat morphology.

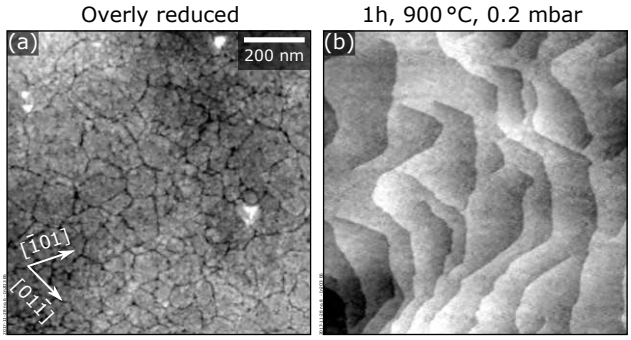

Figure 5.13. Re-oxidation of 'broken' In_2O_3(111) films. (a) Surface of an In_2O_3(111) film after tens of sputtering–annealing cycles in UHV. (b) Surface of the same film after re-oxidation. The AFM images are (1×1) μm^2.

5.4 Discussion

5.4.1 Oxygen chemical potential and film morphology

Generally, the morphology of PLD-grown films is ruled by surface diffusion and nucleation. These are influenced by several factors, including the energy of the landing particles—determined by the laser fluence and scattering of the plume species in the background gas[207,208]—the thermal energy supplied by the substrate,[76] and the specific details of the surface structure.[68] The results presented here show that the morphology of In_2O_3/YSZ(111) films, *i.e.*, the surface diffusion, is considerably affected by the oxygen chemical potential μ_O used during growth. By comparing the morphologies of thin In_2O_3 films grown with O_2 only and with an O_2–Ar mixture [cf. Figs. 5.6(a–c) and Figs. 5.6(f–h)], one can exclude that scattering of the plume species with the background gas is a primary factor for the observed differences. Indeed, Ar and O_2 have similar masses (40 and 32 u, respectively); if the kinetic energy of the incoming particles were to rule the resulting morphology, films grown in the O_2–Ar mixture, always at the same total pres-

sure of 0.2 mbar, would be all very similar and would closely resemble those grown at $p_{O_2} = p_{tot} = 0.2$ mbar [Fig. 5.6(d)].

Instead, it is here suggested that the changes in surface diffusivity with μ_O relate to a change in the nature of the mobile adspecies, *i.e.*, their oxygen stoichiometry. Their oxygen stoichiometry is in turn tied to their ability to diffuse at the surface.

A link between μ_O and the oxygen stoichiometry of indium oxide appears from both experimental and theoretical studies:[200,201,209,210] Higher electrical conductivities obtained at reducing conditions have been assigned to the formation of oxygen vacancies and indium interstitials. An XPS analysis on the films is consistent with this interpretation, as discussed below.

As expected from the small equilibrium concentration of oxygen vacancies in In_2O_3 at the employed growth conditions ($[V_O] \leq 0.003\%$ of lattice oxygen at the most reducing conditions[211]), no appreciable changes of the O 1*s*/In 3*d* intensity ratio are detected with μ_O (not shown). However, more information can be inferred by the so-called Auger parameter (Fig. 5.14). Figure 5.14(a) shows the sketch of a generic Auger process. A deep core-hole generated, *e.g.*, by photoabsorption in level C' is filled by an electron in the higher-lying level C''. The energy gained from this transition is transferred to an electron belonging to higher-lying level C''', which is emitted with kinetic energy E_{kin}. Within the frozen-orbital approximation, E_{kin} would only depend on the binding energies of the core levels involved. In reality, E_{kin} is affected by initial and final state effects originating from intra- and extra-atomic relaxations, in turn dependent on the chemical environment of the core-ionized atom. The Auger parameter, defined as the sum of the kinetic energy of the Auger electron and the binding energy of a photoelectron of the same element,[212] carries this chemical state information: It can be demonstrated that, to a good approximation, the Auger parameter shift between two chemical states is proportional to the extra-atomic relaxation or polarization energy coming from the neighbour ligands of the core-ionized atom.[213] Notice that the Auger parameter is defined by the difference of two kinetic energies (corrected by the photon energy of the X-rays). This can be accurately measured even in presence of static charging, and is thus particularly useful for insulating or semiconducting materials, whose Fermi level is not well defined with respect to the Fermi level of the spectrometer.[212]

Figure 5.14(b) plots the In($3d_{5/2}$, $M_4N_{45}N_{45}$) Auger parameter measured on several In_2O_3(111) films grown at different oxygen chemical potentials. Higher Auger parameters are measured on films grown at higher values of μ_O. Auger parameters measured in In_2O_3 compounds describe the extent to which photoinduced In core holes are screened by the O ligands and/or by conduction-band electrons, whose concentration is directly related to $[V_O]$.[212] Intuitively, this can be understood as follows: indium core-holes (pos-

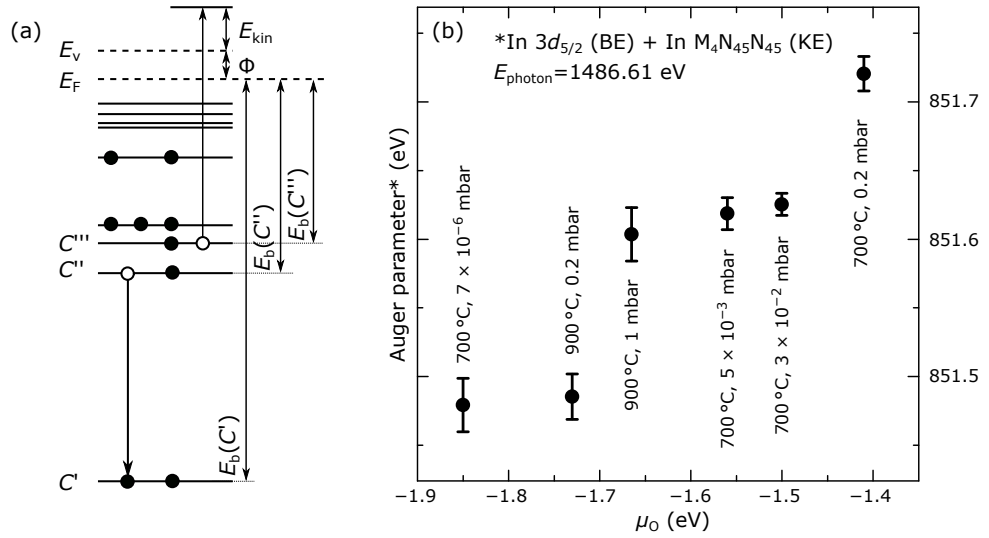

Figure 5.14. (a) Sketch of an Auger process. E_V, E_F, and ϕ stand for vacuum level, Fermi level, and system work function, respectively. In the sketch, a photogenerated core-hole in level C' is filled by an electron in the higher-lying level C''. The energy gained by the system is transferred to an electron belonging to level C''', which is emitted with kinetic energy E_{kin}. In the frozen-orbital approximation, E_{kin} would only depend on the binding energies of the core levels involved (indicated on the right-hand side of the sketch). In reality, E_{kin} is affected by initial and final state effects originating by intra- and extra-atomic relaxations which depend on the chemical environment of the core-ionized atom, and can be measured with Auger parameters. (b) Auger parameter of In_2O_3(111) films grown at different μ_Os. The Auger parameter is defined as the sum of the binding energy of In $3d_{5/2}$ photoelectrons and the kinetic energy of In $M_4N_{45}N_{45}$ Auger electrons. Its decrease with decreasing μ_O correlates with the formation of more reduced In species. Adapted from ref. 67.

itively charged) are screened by negatively charged O ligands and/or conduction band electrons. The more effective this screening, the smaller is the attraction that the outgoing Auger electron feels to the nucleus. As a consequence, this Auger electron is emitted with larger kinetic energy, and this reflects in a larger Auger parameter. Given the small oxygen nonstoichiometry of In_2O_3 at the growth conditions used, one can assume a proportional scaling of the Auger parameter with the average number of O atoms in the neighborhood of the photoionized In.[212] Hence, the smaller Auger parameter obtained at reducing conditions suggests that the concentration of oxygen vacancies in the films increases at low μ_O. This reasonably suggests that increasingly reduced species are also formed during growth at lower μ_O. Indeed, reduced species—such as In_2O suboxides—have been detected during MBE growth of In_2O_3 films at reducing conditions.[202,214] It was also observed that In_2O tends to easily re-evaporate, causing a significant decrease in the film growth rate.[202,214] A twofold decrease in the initial growth rate is also witnessed from the most oxidizing to the most reducing conditions, as judged by the number of laser pulses needed to complete the first RHEED oscillation. This strengthens the hypothesis that reduced (volatile) species are formed when growing at low μ_O.

The correlation between diffusion and desorption barriers[215] could then explain the

fast diffusion observed at low μ_O on the films: Substoichiometric, highly volatile species such as In_2O are formed at reducing conditions, and they easily diffuse on the surface. While one cannot exclude that re-evaporation of deposited material could have an influence on the island sizes, this factor alone could not explain the tenfold difference in island diameter observed when going from the most reducing to the most oxidizing conditions (Fig. 5.6). It should be mentioned that, at fixed μ_O, *i.e.*, fixed oxygen stoichiometry of the adspecies, an increase of temperature should boost the diffusivity of adsorbate species, in accordance with the thermally activated nature of the diffusion process. While a systematic study at fixed μ_O as a function of temperature was not performed, one can note that, regardless of temperature, the Auger parameter of films grown at similar μ_O follows a consistent trend (Fig. 5.14). This supports the idea that μ_O defines the stoichiometry of the diffusing species and, thus, of the film.

5.4.2 Antiphase domain boundaries and other surface defects

While the In_2O_3 films presented here reproduce the atomic-scale details of single crystals,[186] they feature some mesoscopic defects (ridges on the oxidized surface and trenches on the reduced one, as well as screw dislocations) that are not observed on synthetic single crystals, as seen in Fig. 5.12.

The presence of trenches and ridges can be ascribed to the one-on-four matching between the In_2O_3(111), as shown in Fig. 5.12(f). In fact, the lattice parameter of the projec-

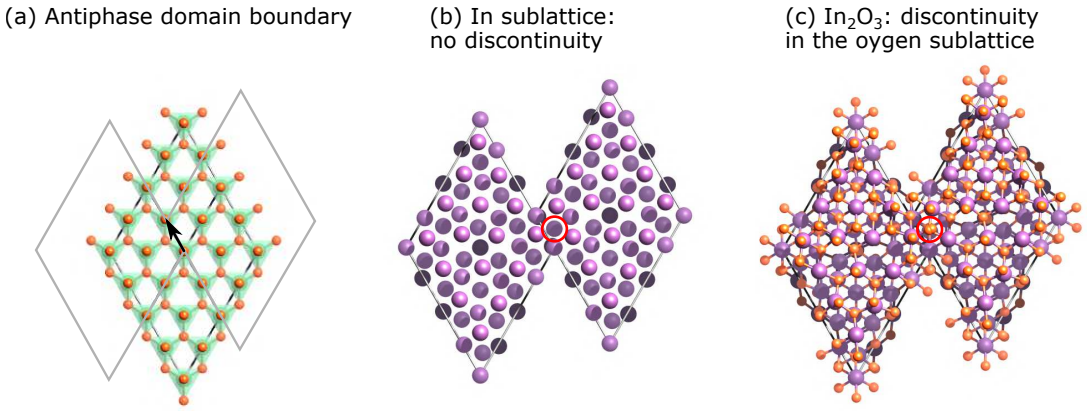

Figure 5.15. Lattice alignment at antiphase domain boundaries in In_2O_3(111). (a) YSZ(111) lattice. The purple rhombi represent two unit cells of In_2O_3 placed on the YSZ lattice as to create an antiphase domain boundary (along the white arrow). (b) In sublattice of these two In_2O_3 unit cells. The In sublattice is continuous. (c) Same unit cells as in panel (b), complemented with the oxygen sublattice. Discontinuities exist in the oxygen sublattice (see white circle) that could cause preferential material loss at these defects. Renderings by Michele Riva.

tion of the bulk unit cell of YSZ along (111)-oriented planes is two times smaller than the one of In_2O_3; however, the presence of two equivalent sites along each low-index direction within this cell effectively results in a four-to-one relation with In_2O_3(111). During the first stages of growth, In and O adatoms arrange on YSZ to match the In_2O_3 surface unit cell [shaded triangles in Fig. 5.12(f)] with the one of YSZ that is four times smaller (dashed triangles). However, in-plane shifts of multiple YSZ surface units along the high-symmetry directions may occur between neighboring In_2O_3 islands, causing the formation of antiphase domain boundaries on their coalescence [see, *e.g.*, Fig. 5.12(d)]. Similar line defects have been already observed on MBE-grown ultrathin In_2O_3 films on YSZ(111) (see Fig. 5.4). It is then at these domain boundaries that trenches form under reducing conditions, as confirmed by the in-plane shifts of the surface termination of same-height terraces across a trench [Fig. 5.12(e)].

The reason for the formation of the trenches at reducing conditions can be found by superimposing the In_2O_3 and YSZ unit cells (Fig. 5.15): While the cation lattice runs continuously across an antiphase domain boundary [panel (b)], discontinuities exist in the oxygen sublattices [panel (c)].[198] It is possible that the discontinuity in the oxygen ordering leads to a higher lattice energy for these sites, thereby causing a preferential material loss at these defects.

When the reduced film with trenches is reoxidized (at mildly oxidizing conditions), In_2O_3 can be formed, and the trenches eventually close. In addition, material accumulates locally, forming the observed bright 'ridges' [Fig. 5.12(c)]. It is plausible that material accumulates in proximity of the domain boundaries and is not able to diffuse farther (as the similar size of the islands and the ridges suggests); the local accumulation might occur because the defects are still locally reduced, *i.e.*, with an excess of In adatoms that react with the oxygen from the environment to form In_2O_3. When the films are instead annealed at sufficiently high oxygen pressures and temperature (*e.g.*, the 900 °C, 0.2 mbar used for film growth), diffusion is fast enough to create a uniform, oxidized surface, with neither ridges nor trenches (Fig. 5.13).

5.5 Conclusions and outlook

This Chapter has highlighted the strong role that the PLD parameters can have on the film morphology, even for the seemingly simple case of a binary oxide like In_2O_3. In particular, it has discussed the role of the oxygen chemical potential μ_O: It affects the surface morphology by determining the stoichiometry of the diffusing indium species, hence their diffusivity at the surface. Understanding which growth regimes take place under which conditions has been useful to develop a successful growth recipe that yields

atomically flat, almost bulk-like In_2O_3(111) films, which display the same atomic-scale surface properties as available single crystals. The role of the YSZ substrate on the quality of the film was also addressed: The non perfect one-on-four matching relation of In_2O_3 unit cell with that of YSZ causes the formation of antiphase domain boundaries that propagate through the growing film, causing it to be slightly more sensitive to reducing preparation conditions than single crystals.

To reduce the extent of the problem, it is planned to grow In_2O_3 on a different substrate, where less APDBs should be formed: yttrium titanate ($Yi_2Ti_2O_7$, YTO). Its bulk lattice constant suggests an ideal one-on-one match with In_2O_3 (mismatch of 0.0034%), although the presence of two equivalent sites of the (111) cuts effectively causes a one-on-two lattice match. Based on the experience with the YSZ substrate, one can expect the formation of APDBs also in this case. Yet, the one-on-two match of In_2O_3 with YTO offers significantly fewer options for shifts than for the one-on-four match with YSZ, such that less APDBs should form.

The APDBs formed on the films are detrimental for the UHV preparation of their surface, but they may also bring opportunities: They could be used as model systems to gain a deeper understanding of gas-sensing devices based on In_2O_3. In such devices, the conductivity of In_2O_3 changes upon absorption of given molecules according to the type and concentration of the gas. It is widely believed that the change in conductivity is largely induced by molecules that adsorb at grain boundaries, thereby exchanging electrons. The APDBs formed on the otherwise single-crystalline In_2O_3(111) films are a simpler and more controlled version of grain boundaries, and they could be used to study the atomic-scale mechanisms behind molecular adsorption and charge transfer.

5.6 Applications of the In_2O_3(111) films

The In_2O_3(111) films presented here have been used within the following projects, most of which are currently undergoing:

- Investigating the interaction between water and the (111) surface of In_2O_3. TPD, AFM, STM, and XPS experiments performed under UHV-compatible conditions have been complemented by STM and XPS investigations of the films' surfaces after exposure to water at more realistic conditions. Specifically, the films have been exposed to water vapor (31 mbar at RT) and to liquid water, in the apparatus described in ref. 115. The results, summarized in ref. 216, have revealed that molecularly adsorbed species require ambient conditions to get stabilized on the

In_2O_3(111) at RT, and propose a dense hydrogen-bond network structure together with hydroxyls that dominate the solid-liquid interface.

- Investigating and quantifying CO_2, H_2 and H_2O adsorption, dissociation, and reaction on the (111) surface of In_2O_3, by combining planar laser-induced fluorescence with near-ambient pressure XPS (collaboration with the group of Prof. Edvin Lundgren from Lund University, Sweden).

- Investigating the adsorption behavior of organic molecules including 1,4,5,8,9,11-Hexaazatriphenylenehexacarbonitrile, also known as HAT-CN, which is the current state of the hole transport layer material in organic light-emitting diodes (collaboration with Peter Jacobson from the University of Queensland, Australia).

- Investigating the adsorption behavior of several organic molecules (*e.g.*, CuPc, 6P, BDA) on In_2O_3, and their network arrangements and mobility as a function of the coverage by means of low-energy electron microscopy (collaboration with Matthias Blatnik from the Central European Institute of Technology, Brno, Czech Republic).

- Investigating the interaction of the (111) surface of In_2O_3 with electrolytes of varying acidity dosed under UHV-compatible conditions. The aim is to build a model system to study the role of In_2O_3 during the electrochemical reduction of CO_2.[217] The results collected by Francesca Mirabella within the liquid-drop apparatus described in ref. 115 have revealed that the surfaces of the In_2O_3 films show no morphology change down to pH 3.8.

6. $SrTiO_3$(110) homoepitaxy

6.1 Introduction

This is the first Chapter on an oxide material with more than one cation: The upcoming protagonist, $SrTiO_3$, has two cations. While this may not strike one as a major issue, several literature studies have proven that the fact that $SrTiO_3$ has two cations can be critical for the composition of the films and other properties, even when the films are grown homoepitaxially: Because Sr and Ti are affected uniquely by the growth parameters, non-optimal PLD growth conditions may result in significant cation nonstoichiometry,[37,218,219] extended lattice constants,[37,55,219] and even cause $SrTiO_3$ films to become ferroelectric at room temperature.[220,221] As it has been already (and it will still be) argued within this Thesis, these non-idealities are not unique to $SrTiO_3$ films, but apply to all multi-element materials grown by PLD: Most films tend to deviate significantly from the single-crystalline standard,[34] showing rough morphologies and non-stoichiometric compositions. The aim of this Chapter—through the relatively simple case of $SrTiO_3$ homoepitaxy—is to unveil the unexplored mechanisms behind surface roughening in complex oxides and the link to the introduced nonstoichiometry. Most of the results presented here have been published in ref. 68.

The Chapter focuses on the effect of one PLD parameter in particular, the laser fluence, on the homoepitaxy of (110)-oriented $SrTiO_3$ films: It will show that different laser fluences introduce different nonstoichiometries, and translate in markedly different surface morphologies. The STM investigations presented here unveil the fundamental, yet too-often-overlooked ingredient that lies behind such changes: The surface atomic structure of the growing film. Before going to the results in Section 6.3, the next Section will give an introduction about perovskite oxides, the structural family to which $SrTiO_3$ belongs. A detailed description of the surface reconstructions intrinsic to the (110) termination of $SrTiO_3$ will follow, as they will be key throughout the next two Chapters.

6.1.1 Perovskite oxides

Perovskite oxides are characterized by the ABO_3 formula, and by the same (or very similar, at least compatible) crystal structure. The ideal perovskite oxide structure, exhibited by $SrTiO_3$ and shown in Fig. 6.1, is cubic (although deviations with orthorhombic, rhombohedral, tetragonal, monoclinic, and triclinic symmetry are known[222]). The center position of the cubic unit cell is occupied by the A cation, with formal oxidation state smaller than the B cation, and mainly belonging to the rare- and alkaline-earth metal groups. The skeleton of the structure is built by corner-sharing octahedra of the B cation, a higher valence, reducible transition metal with smaller ionic radius. (In $SrTiO_3$, the A and B cations are given by Sr and Ti, respectively). Remarkably, perovskite oxides can accommodate with 100% substitution some 30 elements on the A site and over half the periodic table on the B site.[2] Because of the wide range of ions and valences that this simple structure can accommodate, the perovskites lend themselves to chemical tailoring. In turn, this opens up almost endless and exciting possibilities to control the interplay between spin, charge, orbital and lattice degrees of freedom in these materials, and achieve unique properties.[4] One example is $La_{1-x}Sr_xMnO_3$, protagonist of Chapters 8 and 9: It is obtained by the partial Sr-for-La substitution in $LaMnO_3$, and it shows doping-dependent transitions from metal to insulator and from ferro- to anti/paramagnetic. The richness of the properties of perovskite oxides can be further extended by combining them in controlled thin-film heterostructures (possible because they all share the same backbone structure): Unexplored functionalities can be achieved by coupling their degrees of freedom at well-defined interfaces.[6,12,14] Among others, novel electronic,[15–21] magnetic,[13,24,25] ferroic,[26,27] and ionic properties[28] have been explored.

The unique properties of perovskite oxides are exploited in a varied array of integrated technologies, including piezoelectric, capacitive, optoelectronic, thermistive,

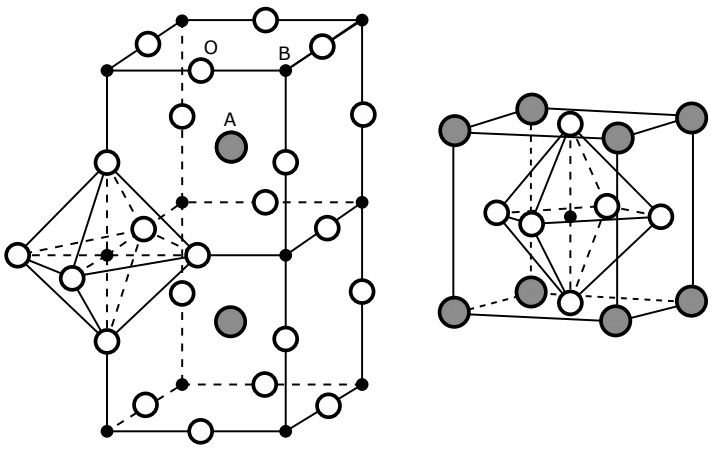

Figure 6.1. Cubic perovskite ABO_3 structure.

ferroelectric and spintronic devices, solid-state chemical sensors, electronics based on high-temperature superconductors, and high-density storage, but also in heterogeneous catalysis and clean-energy production (and the list goes on).[3–6] In all cases, the precise details of the surfaces and interfaces of the perovskite material play a key role: It is at the surface that reactions take place, and again it is at the surface that functionalities of interfacing materials are coupled. This has recently stimulated efforts for gaining a detailed (atomic-scale) understanding of perovskite oxide surfaces. In fact, some three-element perovskite oxides including $SrTiO_3$ have enjoyed detailed surface science investigations that have unveiled the particulars of their surface reconstructions.[223–231] Still, the knowledge on more complex materials is scarce, taken few exceptions,[64] partly due to the intrinsic challenges in synthesizing single-crystalline samples with well-defined surfaces. This will hopefully be at least partially clarified during the following Chapters.

$SrTiO_3$ is often defined the prototypical perovskite oxide. It exemplifies the richness of bulk, surface, and interface properties that can be accessed within a single perovskite material: Donor doping by chemical impurities,[232,233] oxygen vacancies,[232] or field effect,[233,234] can turn the same material into an insulator, a metal, or even a superconductor. Moreover, local enrichment of oxygen vacancies was found to induce confinement of electronic conductivity in the form of 2D electron gases.[235,236] These plentiful properties can be tuned in $SrTiO_3$ thin films by playing with the growth parameters. Notably, by virtue of its suitable lattice matching with a variety of other complex perovskite oxides, and because single-crystalline samples are readily available at a moderate price (a $5 \times 5 \times 0.5$ mm^2 sample costs about 30 €), $SrTiO_3$ is widely used as a substrate for epitaxial growth of films and heterostructures.

6.2 $SrTiO_3(110)$: Structure and phase diagram

As anticipated before, the homoepitaxial studies of $SrTiO_3$ presented here are made on (110)-oriented samples. This orientation is less common than the (001), which is historically chosen for perovskite oxide growth over the (110). Nonetheless, the (110) termination is more suited to addressing the role of the surface reconstruction on film growth. The (001) surface, generally prepared with wet-chemical methods, is mostly assumed to exhibit a well-defined, bulk-truncated (1×1) termination after the preparation treatments, while, in fact, such a structure has only been resolved at the atomic scale on as-cleaved crystals.[227,237] A variety of composition-related but hardly controllable surface reconstructions tend to appear otherwise.[238] On the other hand, it will be shown in a moment that the (110) surface exhibits well-known and tunable surface reconstructions, for many of which DFT models have been established. This makes it the ideal system

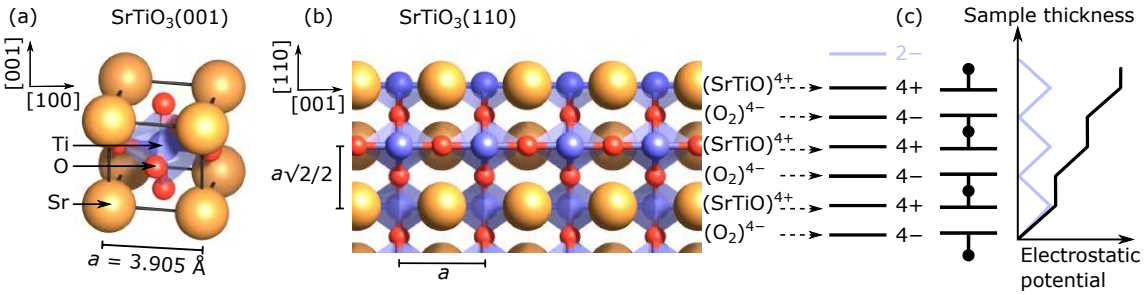

Figure 6.2. (a) $SrTiO_3$ unit cell: $SrTiO_3$ crystallizes in the cubic perovskite ABO_3 structure. (b) Bulk-truncated model of the (110) surface: Planes of opposite charge alternate along the [110] direction, leading to a diverging electrostatic potential with increasing thickness (c). The instability is compensated by introducing reconstructed layers with $-2e$ formal charge on top of a bulk-truncated $(SrTiO)^{4+}$ plane. Renderings from Michele Riva.

for atomically resolved studies.

The bulk-truncated side view of $SrTiO_3(110)$ is shown in Fig. 6.2(b). It can be seen in panel (c) that the alternation of $(SrTiO)^{4+}$ and $(O_2)^{4-}$ planes makes this termination susceptible for the polar catastrophe,[1,239,240] and intrinsically unstable in its bulk-terminated form. Compensation of the diverging electrostatic energy is accomplished by introducing reconstructed TiO_x-rich layers bearing a formal $-2e$ charge per bulk unit cell on top of a bulk-truncated $(SrTiO)^{4+}$ plane.

Figure 6.3 summarizes the reconstructions found on $SrTiO_3(110)$, as seen in STM and LEED. Because of their origin in the polarity compensation, they are exceptionally stable.[71] Each reconstruction is composed of a combination of tetrahedrally and octahedrally coordinated TiO_x units, additionally including a few Sr atoms.[230,241–243] While the TiO_x enrichment is required to compensate for the polar nature of the $SrTiO_3(110)$ surface, each of the structures in Fig. 6.3 has a slightly different composition: Structures on the left are characterized by a smaller Ti enrichment than those on the right. Each surface structure represents a thermodynamic equilibrium phase, as determined by the cation chemical potentials, and can therefore be reversibly and reproducibly prepared by tuning the near-surface stoichiometry. This is achieved by deposition of small amounts of Sr or Ti (followed by high-temperature annealing in O_2 ambient) via, *e.g.*, MBE[244] or PLD,[71] as indicated in the bottom part of Fig. 6.3 in units of monolayers (ML). In this context, 1 ML corresponds to the number of Sr (or Ti) sites in a $(SrTiO)^{4+}$ plane of $SrTiO_3(110)$, *i.e.*, 4.64×10^{14} at./cm^2.[245] More details about the cation doses needed to switch between adjacent reconstructions are given in Section 6.2.1.

Note that $SrTiO_3(110)$ is not the only complex oxide whose surface reconstructions are related by near-surface stoichiometry: Similar relations between surface reconstructions and composition were reported for $LaAlO_3(110)$,[231] $LiNbO_3(0001)$,[246] $BaTiO_3(001)$,[224] $PbTiO_3(001)$,[247] and (001)-,[238,248] and (111)-oriented[228,249,250] $SrTiO_3$. Chapter 8 will show

that a similar behavior is shared also by LSMO(110).

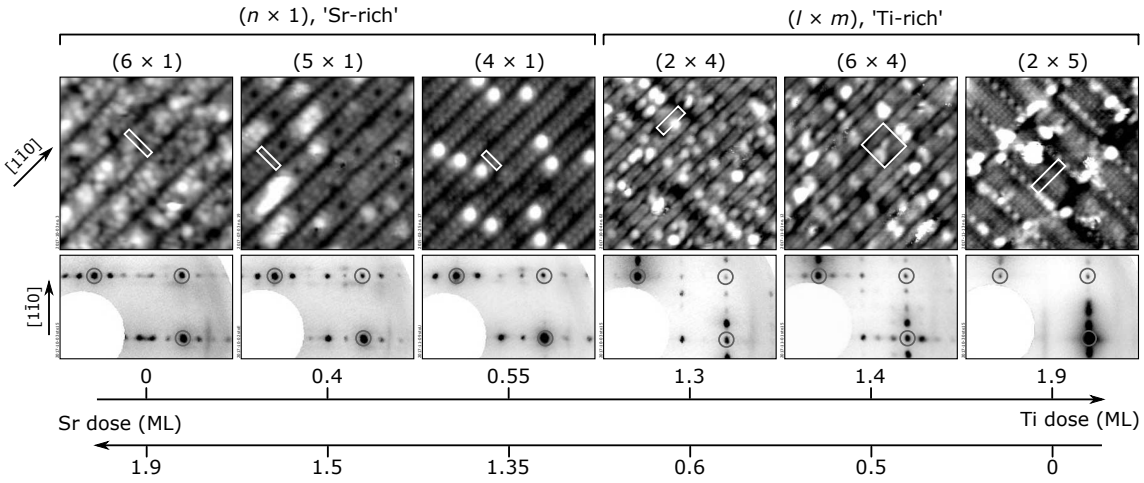

Figure 6.3. Surface phase diagram of $SrTiO_3(110)$. Selected reconstructions with different periodicities are shown as they appear in STM (top row; 12×12 nm^2 each) and LEED (bottom row; 90 eV, one quadrant shown with inverted gray scale). The reconstructed unit cells are outlined in white in each STM image. In each LEED pattern the bulk-derived diffracted beams are highlighted with grey circles. Each of the surface structures can be reversibly and reproducibly prepared by tuning the local surface stoichiometry. This can be achieved by deposition of small amounts of Sr or Ti via MBE or PLD (followed by high-temperature annealing in O_2 ambient), as indicated in the bottom part. One monolayer (ML) is the density of cation sites in a bulk-truncated $SrTiO_3(110)$ plane, *i.e.*, 4.64×10^{14} atoms/cm^2. Adapted from ref. 68.

6.2.1 The $(n \times 1)$ series

The reconstructions of the $SrTiO_3(110)$ phase diagram in Fig. 6.3 can be classified in two families: $(n \times 1)$, in the following often referred to as 'Sr-rich', and $(l \times m)$, 'Ti-rich'. Reconstructions belonging to the $(n \times 1)$ series share a similar surface structure and similar properties, and they can coexist on the surface. They all consist of a network of rings of corner-sharing TiO_4 tetrahedra residing on a bulk-like $(SrTiO)^{4+}$ plane. Figure 6.4 shows the typical STM appearance and the DFT models of the (4×1) and (5×1) reconstructions. In both cases, the unit cell is marked by white rectangles. In the (4×1) [Figs. 6.4(a, b)], rows of six-membered rings alternate with rows of ten-membered rings along the $[1\bar{1}0]$ direction. The structure of (5×1) and (6×1) can be obtained by modifying the number of members in the tetrahedra rings: In the (5×1) [see Figs. 6.4(c, d)] they are eight- and ten-membered, while there are only ten-membered rings in the (6×1) (not shown). In STM, both reconstructions appear as rows separated by dark trenches running along the $[1\bar{1}0]$ direction. Their width along the [001] direction is of 4 and 5 unit cells, for the (4×1) and for the (5×1), respectively. Bright and dark features (marked by orange and purple arrows) are present on the surface. As discussed in the following, they are linked to the presence of antiphase domain boundaries.

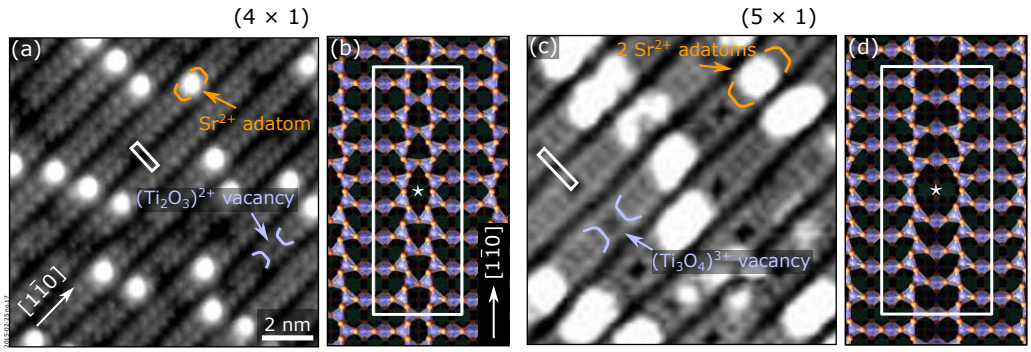

Figure 6.4. (4 × 1) and (5 × 1) reconstructions of $SrTiO_3(110)$. (a, c) 12 × 12 nm^2 STM images (typical parameters: U_{sample} = +2 V, I_t = 0.2 nA). (b, d) Top view of the DFT models of vacancy cluster antiphase domain boundaries ('W-type') on (4 × m) and (5 × l) with $m = l = 8$. Unit cells (≈1.56 × 0.55 nm^2 and ≈1.95 × 0.55 nm^2, respectively) are highlighted by white rectangles. In the STM images, Sr adatoms and Ti_2O_3 and Ti_3O_4 vacancy clusters are highlighted by orange and violet arrows, respectively. The positions of the latter are indicated by asterisks in the DFT models. Adapted from ref. 69.

Antiphase domain boundaries. Because the surface unit cells break the mirror symmetry of the bulk-truncated $SrTiO_3(110)$ surface, two types of antiphase domain boundaries form where two (4 × 1) [or (5 × 1)] mirror domains connect. They are called 'C-' and 'W-type'.[243] Figs. 6.4(c, d) show a DFT model of the structure with domain boundaries (the C-type one is in the middle of the cells): Here, the wings of the 'boomerangs' [*i.e.*, the eight- (ten-) membered rings along the [1$\bar{1}$0] direction] point away from each other (sketched in violet in the STM images). On the W-type, instead, they point towards each other (sketched in orange in the STM images).[243]

C-type boundaries are obtained by removing one $(Ti_2O_3)^{2+}$ unit on the (4 × 1), and one $(Ti_3O_4)^{3+}$ unit on the (5 × 1), respectively, on the positions indicated by the asterisks in Figs. 6.4(b, d). In both cases, this relieves strain between the $SrTiO_3(110)$ bulk-truncated surface layer and the 'ideal' reconstruction overlayer without domain boundaries.[243] In STM, these vacancy clusters appear as dark points [violet arrows in Figs. 6.4(a, c)]. On the (4 × 1), for each $(Ti_2O_3)^{2+}$ complex removed at the C-type domain boundary, a Sr^{2+} adatom is placed at the W-type domain boundary, restoring the charge balance in the surface layer.[243] These Sr adatoms are visualized as bright protrusions in STM [orange arrow in Fig. 6.4(a)]. A similar argument applies to (5 × 1): The missing charge of the $(Ti_3O_4)^{4+}$ vacancies at C-type boundaries can be compensated by introducing cationic species of equal net charge. Ref. 69 suggests that two additional Sr^{2+} atoms are anchored on the 5× lines in between two type-C domain boundaries. Indeed, STM reveals that bright protrusions appear between vacancy domain boundaries [see Fig. 6.4(c)]; also, the size of these bright protrusion is larger than those present on the (4 × 1), consistent with the hypothesis of more than one Sr^{2+} atoms sitting at the W-type domain boundary on the (5 × 1) surface.

Cation dose to move between the (4 × 1) and the (5 × 1) reconstructions. Wang and colleagues obtained the experimental doses at the bottom of Fig. 6.3 by depositing the pure metals after careful calibration of the corresponding effusion cells.[245] The authors optimized the temperature of the sources to achieve exactly stoichiometric co-deposition of Sr and Ti, as determined by RHEED. In order to exclude possible spurious effects in the determination of the absolute doses, such as, *e.g.*, incomplete sticking or re-evaporation, the work in ref. 69 compares the Sr dose required to switch the $SrTiO_3$(110) surface structure from pure (4 × 1) to pure (5 × 1), with the stoichiometry of the two surfaces as derived from DFT calculations. Establishing a precise relation between compositional changes and surface structure changes is crucial for the results to be presented in Chapter 7, showing how small nonstoichiometries introduced in PLD can be deduced by monitoring the evolution of the surface structures.

The experimental dose amounts to $(0.55 - 0.40)$ ML $= 0.15$ ML (cf. bottom axis of the phase diagram in Fig. 6.3), and corresponds to an excess (deficiency) of 0.15 Sr (Ti) atoms per (1 × 1) surface unit cell on a pure (5 × 1)-reconstructed surface. The structural models for the ideal (4 × 1) and (5 × 1) surfaces correspond to $Ti_{6/4}O_{16/4}$ and $Ti_{7/5}O_{19/5}$ surface compositions,[251] respectively, or to a $6/4 - 7/5 = 0.1$ Ti atoms deficiency per (1 × 1) surface unit cell. However, the domain boundaries that are characteristic of these surfaces (see previous Section) interact with each other, causing their average separation to be well defined [see Figs. 6.5(c, d)]. As a result of this superperiodicity, additional spots are seen in the LEED patterns [Figs. 6.5(a, b)]. Hence, these reconstructions are better described by (4 × m) and (5 × l) unit cells. The average periodicity along the $[1\bar{1}0]$ direction, corresponding to the distance between equivalent antiphase domain boundaries, was evaluated from several STM images. It amounts to $\langle m \rangle = 11 \pm 2$ and $\langle l \rangle = 9.2 \pm 2.5$ for the (4 × m) and (5 × l) structures, respectively. The difference in the $[1\bar{1}0]$ super-periodicity for the two structures is reflected in a corresponding different spacing of the split spots observed in LEED [see insets of Fig. 6.5(a, b)]. These spacings amount to $d^*_{[1\bar{1}0]}/(11.05 \pm 0.09)$ and $d^*_{[1\bar{1}0]}/(9.1 \pm 0.2)$ for the (4 × m) and (5 × l) structures, respectively, as judged by fitting Gaussian peaks to cross-sectional spot profiles ($d^*_{[1\bar{1}0]}$ is the distance between integer-order LEED spots along $[1\bar{1}0]$). Therefore, the corresponding real-space periodicities along $[1\bar{1}0]$ are $\langle m \rangle = 11.05 \pm 0.09$ and $\langle l \rangle = 9.1 \pm 0.2$, in perfect agreement with the values obtained by STM. These superperiodicities should be included in the DFT-derived structural models to properly account for the composition of the (4 × m) and (5 × l) surface structures. As a result of the missing $(Ti_2O_3)^{2+}$ unit and the additional Sr^{2+} atom (see previous Section), the composition of one (4 × m) surface unit cell is $mTi_6O_{16} + 1Sr - 1Ti_2O_3 = SrTi_{6m-2}O_{16m-3}$, corresponding to a $Sr_{1/4m}Ti_{(6m-2)/4m}O_{(16m-3)/4m}$ composition per (1×1) unit cell. Given that

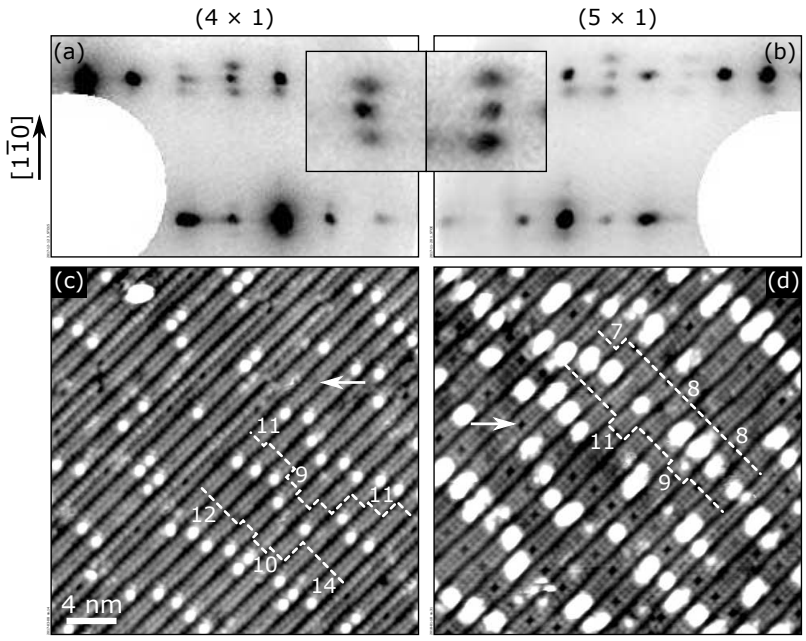

Figure 6.5. (a–d) $SrTiO_3(110)$ surfaces (mostly) $(4\times m)$- (a, c) and $(5\times l)$-reconstructed (b, d), respectively. (a, b) LEED patterns (90 eV, inverted gray scale, one quadrant shown); the insets show blowups of the $(3/4, 1)$ and $(-4/5, 1)$ spots in panels (a) and (b), respectively. The spot splitting characterizes the average periodicity $\langle m\rangle$ and $\langle l\rangle$ of $(4 \times m)$ and $(5 \times l)$, respectively. (c, d) STM images (30×30 nm^2). Dashed lines enclose a few domains on $(4 \times m)$ and $(5 \times l)$, whose sizes m and l are indicated as a multiple of the $[1\bar{1}0]$ in-plane lattice period. Adapted from ref. 68.

$\langle m\rangle = 11$, as determined by LEED and STM, the average composition of a $SrTiO_3(110)$-$(4 \times m)$ surface is then $Sr_{1/44}Ti_{64/44}O_{173/44}$ per (1×1) surface unit cell. One can derive the composition of a $(5 \times l)$ in analogy with what done for the $(4 \times m)$, and derive $l\mathrm{Ti_7O_{19}}+2\mathrm{Sr}-1\mathrm{Ti_3O_4} = \mathrm{Sr_2Ti_{7l-3}O_{19l-4}}$ per $(5 \times l)$ unit cell, or $Sr_{2/5l}Ti_{(7l-3)/5l}O_{(19l-4)/5l}$ per (1×1) unit cell, so that the average composition for the experimentally derived $\langle l\rangle = 9$ is $Sr_{2/45}Ti_{60/45}O_{167/45}$.

From the $Sr_{1/44}Ti_{64/44}O_{173/44}$ and $Sr_{2/45}Ti_{60/45}O_{167/45}$ model compositions of $(4 \times m)$ and $(5 \times l)$ reconstructions, one concludes that evolution from a $(4 \times m)$- to a $(5 \times l)$-reconstructed surface requires removal of $|60/45-64/44| = 0.121$ Ti atoms and addition of $|2/45 - 1/44| = 0.022$ Sr atoms per (1×1) unit cell. This corresponds to a net addition (removal) of 0.143 Sr (Ti) atoms: For example, when 0.143 ML Sr are deposited on a (4×1) surface, 0.022 Sr atoms per unit cell are directly incorporated in the (5×1) surface structure, while the remaining 0.121 Sr atoms form stoichiometric $SrTiO_3$ by removing 0.121 Ti atoms from the (4×1) structure. The 0.121 ML $SrTiO_3$ are then accommodated, *e.g.*, at step edges. Therefore, the net difference in stoichiometry between the two surface reconstructions (*i.e.*, 0.143 ML) should be compared with the 0.15 ML experimentally determined cation dose reported in the phase diagram of Fig. 6.3. The very good agreement between these two values (within 5%) suggests that the calibration of the experimental doses in the surface phase diagram is largely free of spurious effects

such as, *e.g.*, incomplete sticking or re-evaporation. As an immediate consequence, this also limits the relative uncertainty in the cation excess determination with the method detailed in Chapter 7 to better than 5%.

Coexistence of $(n \times 1)$ reconstructions. Because the reconstructions belonging to the $(n \times 1)$ series share similar structural properties, they tend to coexist on the same surface without phase-separating into distinct domains. If, say, the surface has a composition between the (4×1) and the (5×1) monophase surfaces, interwoven (4×1) and (5×1) lines will be simultaneously present (see Fig. 6.6). In both surfaces of panels (a) and (b), the majority of the surface is (4×1)-reconstructed, but few (5×1) lines (blue) are present. On some occasions, lines of one reconstruction can 'jump' one (or multiple) lattice units along the [001] direction, so that the lines can appear fragmented (white arrows). This mixture of reconstructions can also be seen from LEED, showing a partial overlap of (4×1) and (5×1) spots, most evident at the location indicated by the black arrow. This clear spot splitting is less visible when the coexisting $(n \times 1)$ structures have a ratio other than 50%. In these cases, the minority lines tend to have a well-defined separation along [001], and this causes a broadening of the LEED intensities.

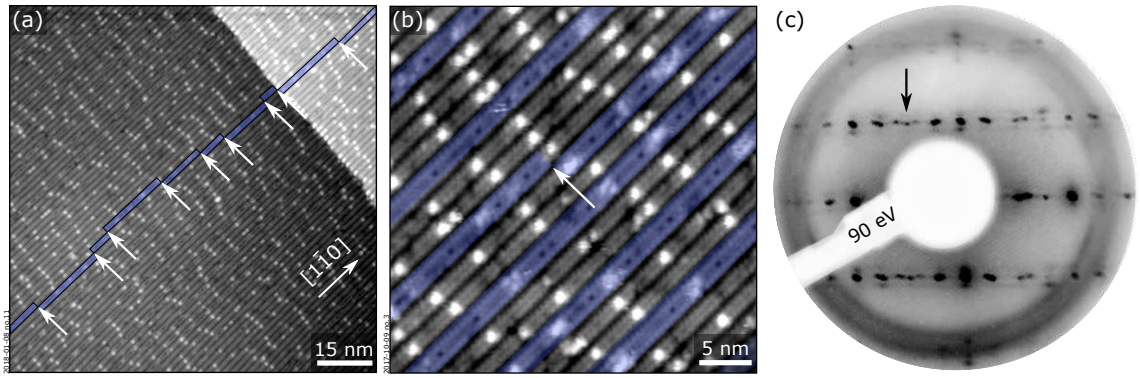

Figure 6.6. Mixed $(4\text{–}5 \times 1)$ surfaces of $SrTiO_3(110)$. (a) 100×100 nm^2 STM image of a mixed surface. One (5×1) line is highlighted in blue. It runs continuously along the $[1\bar{1}0]$ direction, albeit with jumps of one unit cell across the [001] direction (white arrows). (b) 30×30 nm^2 STM image on another mixed surface, where all (5×1) lines are highlighted in blue. The white arrow indicates the jump of one of these lines across the [001] direction. (c) LEED pattern corresponding to the image in panel (b). The superposition of (4×1) and (5×1) spots originating from the simultaneous presence of both reconstructions is indicated by the black arrow.

Stability of the $(n \times 1)$ reconstructions. Reconstructions belonging to the $(n \times 1)$ series are stable upon annealing 1 000 °C and 50 mbar O_2. They are usually prepared at 1 000 °C and 7×10^{-6} mbar O_2 (see Section 6.2.2). Notably, the $(n \times 1)$ periodicity remains visible in RHEED at these temperatures (not shown).

6.2.2 The $(l \times m)$ series

The reconstructions belonging to the $(l \times m)$ series essentially consist of a double layer of octahedrally coordinated Ti. The (2×5) reconstruction is the most investigated within this Thesis, and it will be the focus of this Section.

Figure 6.7 shows the appearance of the (2×5) reconstruction in STM [panel (a)], and the corresponding DFT model [panel (b)]. In STM, the structure appears as ≈2.8 nm-wide rows oriented along the [001] direction, composed of alternating by dark troughs and bright dots. The DFT model reveals that the reconstruction is composed by two atomic layers. The subsurface layer consists of edge- and corner sharing TiO_6 octahedra. The top layer hosts sixteen edge-sharing TiO_6 octahedra, and two TiO_5 units, in which the apical oxygen atom is missing. Finally, five-fold coordinated Sr atoms alternate with the TiO_5 units, with a two-fold periodicity along [001].[242] These Sr adatoms correspond to the bright dots visible in STM.

Cation dose to move to the (2 × 5). The Ti dose needed to obtain the (2×5) surface from the other reconstructions of the phase diagram in Fig. 6.3 was not available from the literature. In the work of ref. 69, this dose is derived by scaling the PLD-deposited TiO_2 amount necessary to move from (4×1) to (2×5) to the corresponding dose that allows switching between (5×1) and (4×1). The experimental dose needed to switch between the (5×1) and the (2×5) was then compared with the dose derived from the available DFT models, in analogy with the analysis presented in Section 6.2.1 for the relative compositions of the (4×1) and (5×1). Importantly, one should care that a '(2×5)' surface actually shows a mixture of $(2 \times 4)/(2 \times 5)$ periodicities, each with two possible structures—*i.e.*, $(2 \times k)a/b$.[242] Assuming an even mixture of the four structures, the model net stoichiometry difference between '(2×5)'- and (5×1)-reconstructed sur-

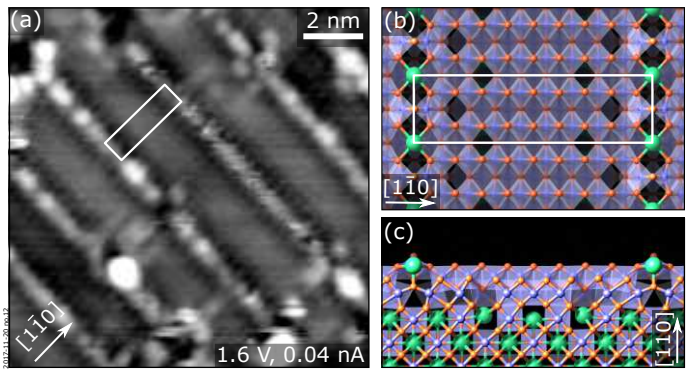

Figure 6.7. (2×5) reconstruction of $SrTiO_3(110)$. (a) (12×12) nm^2 STM image. (b) DFT model from ref. 242. The unit cell (≈0.78×2.76 nm^2) is highlithted by white rectangles. Sr, Ti, and O atoms are in green, blue, and red, respectively. Renderings by Michele Riva.

faces amounts to 1.64 ML. This number agrees, within 10%, with the 1.5 ML experimental dose reported in Fig. 6.3. The larger discrepancy obtained in this case might be due to the lack of modeling of domain boundaries on the $(2 \times k)a/b$ structures.

Stability of the $(l \times m)$ reconstructions. Apart from the (2×5), the reconstructions of the $(l \times m)$ family are stable up to $1\,000\,^{\circ}$C and 50 mbar O_2. The (2×5) is only stable up to around $600\,^{\circ}$C.

Preparation of $SrTiO_3(110)$ substrates

UHV-prepared $SrTiO_3(110)$ surfaces were used for a variety of experiments within this Thesis. As a starting point for most experiments, the surface was prepared to exhibit a mixed $(4–5 \times 1)$ structure. These include the homoepitaxy experiments described in Section 6.3), the growth of LSMO(110) (Chapters 8 and 9), and the oxygen exchange experiments described in Chapter 10. (2×5) samples were prepared for oxygen exchange experiments described in Chapter 10. The preparation procedure is detailed in the following.

Prior insertion in UHV, the $SrTiO_3(110)$ single crystals (synthetic crystals from CrysTec GmbH, Germany, 0.5 wt.% Nb_2O_5-doped, $5 \times 5 \times 0.5$ mm^3, angular miscut of <0.3°), are cleaned *ex situ*. Two cycles of sonication for 20 min in Extran and 10 min in ultrapure water are effective in removing residues from the mechanical polishing, while boiling for 10 min in ultrapure water dissolves any CaO traces originating from the polishing procedure. Each sample is then mounted on a plate with customized clips, as described in Section 2.4.1 [Fig. 2.3(b)], and inserted into the UHV system.

Figure 6.8(a) summarizes the UHV preparation. First, the sample is 'test-annealed', to proof-check the mounting: During the high-temperature annealing, the clips can reshape and may exert too much force on the sample and cause it to crack. If the sample survives the test annealing, three cycles of sputtering and annealing are performed. The now-clean surface usually exhibits a mixture of the (2×4) and (6×4) reconstructions, as seen from LEED (refer to the phase diagram in Fig. 6.3). The surface structure is adjusted to exclusively exhibit the desired reconstruction, by MBE (or PLD) deposition of Sr or Ti, with subsequent oxygen annealing. The amounts of Sr or Ti to be deposited are chosen based on the results of the LEED patterns, in accordance with the phase diagram of Fig. 6.3. For details on the calibration of the Sr and Ti doses, refer to Appendix F. A last check is performed in XPS and STM for the cleanliness of the sample. Figures 6.8(b, c) show the 500×500 nm^2 STM images of representative (4×1)- and (2×5)-reconstructed surfaces. They both exhibit hundreds of nanometers-wide terraces separated by monoatomic steps.

Note that the composition, and hence, the surface structure, of $SrTiO_3(110)$ is very sensitive to sputtering treatments, to the extent that different reconstructions macroscopically coexist on the surface if the sputtering is not uniform across the sample. This effect was observed by sputtering the surface with a fixed ion gun (not rastering over the whole sample surface): Despite the broad beam, the center of the sample becomes Ti-richer than the sides, with a related and detectable change in the surface reconstructions, which might span from the (2×4) to the (5×1) on the same sample. This preferential sputtering is likely because the process preferentially removes O atoms,[11] leaving undercoordinated cations behind. During the subsequent annealing, more Sr evaporates than Ti because of the higher vapor pressure. Manually rastering the sample in the ion beam alleviates the problem. Another effective (but time-consuming) solution is to iteratively shade the parts of the sample that are Ti richer with home-made masks, while depositing controlled amounts of TiO_2 in PLD on the rest of the surface (and checking LEED at each step). Before the experiments, it was always ensured to start from uniform samples by checking LEED in different positions.

The preparation of undoped $SrTiO_3(110)$ samples follows the same steps as for the doped ones. Additionally, after each annealing step in oxygen, the samples are further annealed for 30 min in UHV. This step introduces enough oxygen vacancies to make the sample conductive (hence measurable in LEED and STM). Note that annealing the undoped samples without any oxygen pressure after the sputtering treatment produces a persistent (2×5) reconstruction, which is not recovered even upon Sr deposition (followed by oxygen plus UHV annealing). It was not checked whether the same effect

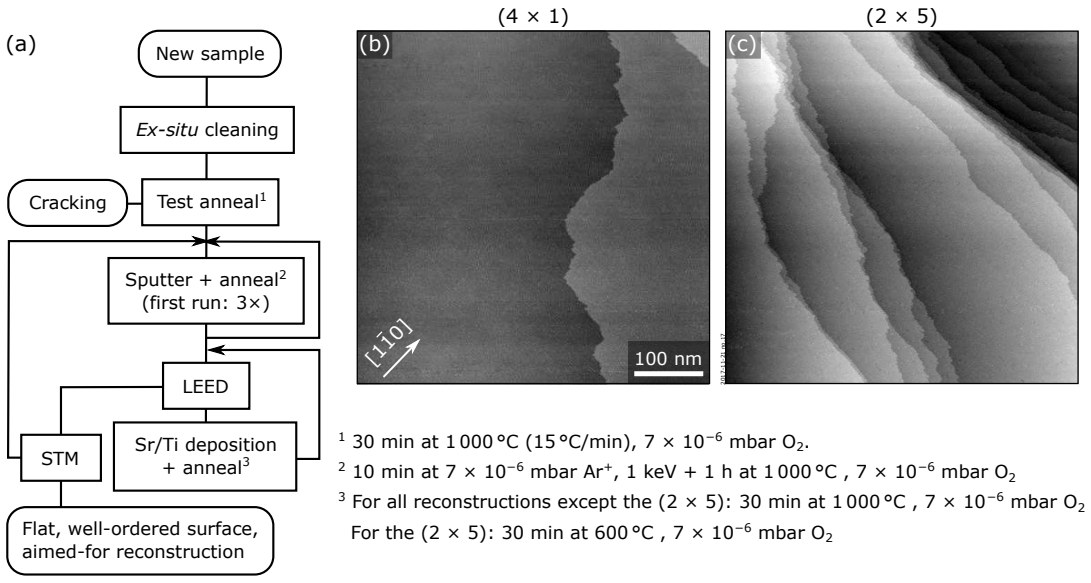

Figure 6.8. Preparation of $SrTiO_3(110)$ substrates. (a) Flow diagram for the preparation of $SrTiO_3(110)$ substrates. (b, c) 500×500 nm^2 STM images of as-prepared (4×1) and (2×5) surfaces.

occurs on the doped samples. It is possible that the Ti-rich reconstructions are retained even after deposition of Sr (followed by UHV annealing) because Sr evaporates easily when it is not sufficiently oxidized. Figure 6.9 shows that the STM images and LEED patterns of (4 × 1) and (2 × 5) reconstructions realized on undoped samples reproduce the findings on the Nb-doped counterparts.

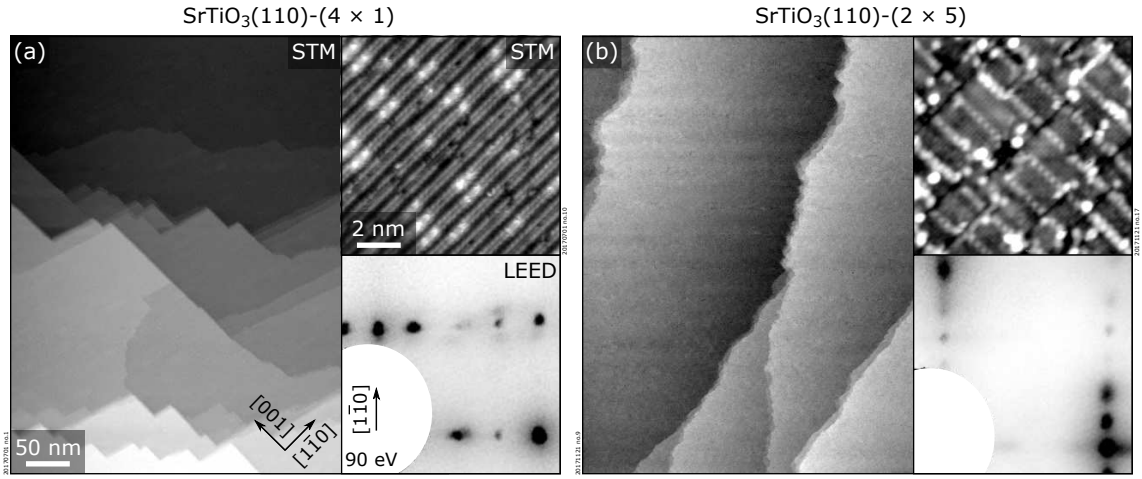

Figure 6.9. STM images and LEED patterns of the (4 × 1) (a) and (2 × 5) (b) surface reconstructions realized on nominally undoped $SrTiO_3(110)$ single-crystals. The main panels are 378 × 500 nm^2 STM images. The small-scale STM images are 20 × 20 nm^2. The surfaces reproduce the morphology and atomic scale details of the same reconstructions obtained on Nb-doped $SrTiO_3(110)$ samples.

$SrTiO_3(110)$ homoepitaxy

$SrTiO_3$ films were grown on $SrTiO_3(110)$ samples prepared as described above (both 0.5 wt.% Nb_2O_5-doped and undoped) from single crystalline $SrTiO_3$ targets (from MaTeck GmbH and CrysTec GmbH, both 0.5 wt.% Nb_2O_5-doped and undoped) at 750 °C, 7 × 10^{-6} mbar O_2, laser fluences between 1.3 and 3.9 J/cm^2, and 1 Hz repetition frequency. All films were post-annealed for 10 min at the growth conditions. Their thickness was measured by live-monitoring the intensity of the specular spot of reflected electrons from RHEED (beam along the [1$\bar{1}$0] direction). More details about the growth procedure are given in Section 2.3.7.

6.3 Understanding and optimizing $SrTiO_3(110)$ homoepitaxy

This Section addresses the link between composition changes, systematically introduced by varying the laser fluence, and morphology modifications during the homoepitaxy

of $SrTiO_3(110)$. The results presented here, published in ref. 68, show that the surface atomic structure, influenced by the nonstoichiometry introduced during growth, has a prominent role in defining the film morphology.

6.3.1 Laser fluence and film stoichiometry

Previous works on (001)-oriented $SrTiO_3$ films have shown that the value of the laser fluence can significantly impact the film composition: Below a certain threshold value the films grow Sr rich,[37,40,79] while for higher values the films were reported to grow both close to stoichiometric[79] and Ti rich.[37,40] This Section shows that the (110)-oriented films share similar trends.

The nonstoichiometry introduced in the films presented here was measured with the STM-based approach described in Chapter 7. In a nutshell, this approach revolves around the phase diagram of Fig. 6.3: If nonstoichiometries are introduced during growth, they change the composition of the bulk of the film and/or of the surface, in turn producing a change in the surface structure according to the phase diagram of Fig. 6.3. Chapter 7 demonstrates the all introduced nonstoichiometry segregates to the surface of the $SrTiO_3(110)$ films. As a result, films of different thicknesses can be compared by measuring the nonstoichiometry introduced 'per layer', obtained by dividing the measured surface stoichiometry change by the number of layers. Figure 6.10 exemplifies this: It collects the nonstoichiometry per layer of various $SrTiO_3(110)$ films (thickness between 7 and 52 layers, *i.e.*, ≈1.7–14.3 nm) that were introduced with different laser fluences. Positive (negative) values stand for Sr (Ti) enrichment. One can distinguish between two regimes, A and B. Fluences below a given threshold (2.6 J/cm^2, regime A) produce Sr enrichments, consistent with previous observations during homoepitaxial growth on $SrTiO_3(001)$.[37,40,79] Higher fluences (regime B) deliver slight Ti enrichments or almost-ideal stoichiometry, in accordance with the work of Dam *et al.*,[79] but at odds with the pronounced Ti-enrichment documented elsewhere.[37,40] Below it is argued that the deposition flux is actually (at least slightly) Ti-rich above a certain threshold, as expected from literature findings on $SrTiO_3(001)$ films,[37,40,79] but that the details of the (110) surface reconstruction and their sticking properties determine the non-ideal composition observed.

Note that the values of the threshold fluence reported in the literature are quite scattered (ranging from 0.3 J/cm^2 to 2.3 J/cm^2),[37,40,79,252] and differ somewhat from the value of 2.6 J/cm^2 obtained here (Fig. 6.10). One can think of at least three reasons: (i) As already discussed in Section 2.3, in addition to the nominal value of the laser fluence, several other factors can affect the introduced nonstoichiometries. These include O_2

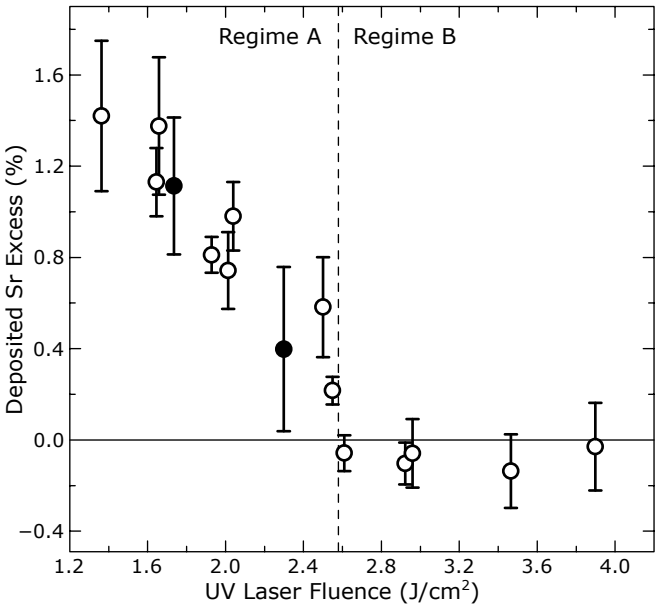

Figure 6.10. Cation nonstoichiometry per deposited layer in homoepitaxial $SrTiO_3(110)$ films as a function of the laser fluence. Open circles correspond to the homoepitaxial growth of Nb-doped $SrTiO_3$ on Nb-doped $SrTiO_3(110)$ substrates, while full symbols refer to the growth of undoped $SrTiO_3$ films on Nb-doped $SrTiO_3(110)$. The nonstoichiometries are measured with STM, by relating the change in the surface structure evolving during growth to the corresponding composition change via the phase diagram of Fig. 6.3. Below a threshold fluence (dashed vertical line), decreasing fluences result in larger and larger Sr enrichment (regime A), while higher fluences (regime B) produce slight Ti enrichment or close-to-ideal compositions. Reprinted from ref. 68.

background pressure, target-to-substrate distance and alignment, laser spot (dimension, uniformity, shape), aging of the UV laser gas ('old' KrF gas systematically results in Sr-richer films), preablation of the target (the target should be sufficiently preablated at the same conditions used during growth), choice of the ablation area (when picked too close to a previously ablated area, redeposited material from the first area can affect the results), and unreliable measurement of the laser fluence. (ii) The various designs of commercial PLD chambers and the lack of accepted methods to measure many relevant parameters can complicate the consistency of the quantitative data from laboratory to laboratory.[37,76] (iii) The specific details of the surface structures of $SrTiO_3(001)$ can affect the growth and, consequently, the introduced nonstoichiometries differently than on the $SrTiO_3(110)$ films. It is worth noting that quantitatively similar results are obtained if undoped $SrTiO_3$ films are grown on undoped $SrTiO_3(110)$ substrates (full symbols in Fig. 6.10), suggesting a minor role of the (possible) oxygen nonstoichiometry on the cation composition of the deposited films.

Interpreting trends in nonstoichiometry with the laser fluence

The trends observed in the film composition with the laser fluence find contradictory interpretations in the literature. For this reason, before going forward with the results, a parenthesis is opened here to discuss these opinions as well as the author's own understanding.

One of such interpretations relies on the preferential ablation of Ti from the target. In the work of ref. 40, fluorescence measurements reveal that, shortly after the ablation, the 'initial' plume (*i.e.*, close to the target) is stoichiometric at low fluences, and Ti-enriched at higher fluences. XPS on the ablation spots on the target reveal an excess of Sr at the target surface, possibly consistent with the preferential ablation of Ti. The authors argue that the stoichiometry of the initial plume is altered via interactions with the background gas (the growths were performed at 10^{-1} mbar), shifting the plume's stoichiometry to more Sr-rich, as the Ti ions, light plasma constituents, are depleted from the central part of the plume. As a consequence, when the almost stoichiometric initial plume observed at low fluences is depleted from Ti, Sr-rich films are obtained. Close to the threshold fluence, the nonstoichiometry of the plume is exactly compensated by the Ti losses due to scattering, yielding stoichiometric films. Finally, at high fluences, the initial plume is so strongly rich in Ti that, even after the interaction with the background gas, the films remain Ti rich. One can identify a few weak points in this interpretation. First, the same observations (Sr-rich, stoichiometric and Ti-rich films for increasing fluences) are seen also at experimental conditions where the background gas does not play a role (see ref. 37 and the present work). Furthermore, it is unlikely for the Ti to be ablated in favor of Sr, given the higher vapor pressure of Sr. The observed Sr enrichment at the target surface could be caused by Sr segregation. The observed Ti enrichment of the plume could be caused by the weak fluorescence of Sr-containing species.

The author's interpretation is at odds with the one from ref. 40 discussed above, and it is instead based on previous discussions from refs. 37,79. Sr enrichments observed at low fluences are assigned to preferential Sr ablation from the target. This is reasonable, given that Sr has a higher vapor pressure than Ti. EDX measurements showed a micrometer-deep Sr composition gradient when targets were ablated at low fluences,[79] suggesting that Sr diffuses through the laser-induced melt towards the target's surface to replenish the Sr depleted by the preferential ablation. This could explain why the Sr-rich growth can be maintained over a long period. This model can also explain the trends observed with increasing fluences: As the fluence increases, the thickness of the ablated spot becomes comparable to the diffusion length of Sr in the laser-induced melt, and the Sr diffusion cannot compensate anymore for the preferential ablation. As a result, films grown at higher fluences (still below the threshold) are less and less nonstoichiometric.

In ref. 79, the films were found stoichiometric above a certain threshold (at odds with the small Ti enrichments observed in this work and a few more recent reports showing strong Ti enrichments[37,40]). A reasonable explanation for the Ti-enrichment of the films at high fluences could be induced by a mechanism similar to that described above. The ablation is still preferential to Sr, but, as the fluence increases, the ablated area becomes deeper and deeper, and the Sr diffusion from within the target is less and less able to compensate for the Sr ablation: Ti-enriched films are grown. The observed difference in slopes of nonstoichiometries as a function of laser fluence in the two regimes (Sr rich and Ti rich) can be explained by accounting for sticking effects: They are not included in the model for the evaluation of the nonstoichiometries (see Chapter 7). The smaller slope in the Ti-rich regime could arise from a smaller sticking of TiO_x species on (2×4) areas. Moreover, one cannot exclude non-linearities in the ablation mechanisms as a function of the fluence.

In ref. 37, another effect besides preferential ablation at the target is discussed, *i.e.*, the angular distribution of the ejected Sr and Ti in the ablation plume. However, the experiments presented here are characterized by such low pressures (7×10^{-6} mbar) that the corresponding mean free path exceeds the target-substrate distance, and thus also such effects can be ruled out. Film re-sputtering can be also excluded as a possible influencing effect, because of the relatively small fluences employed, the 'large' target-to-substrate distance,[37] and because no surface roughening is observed at the atomic scale.

6.3.2 Nonstoichiometry and surface morphology

As seen from Fig. 6.10, STM can be successfully employed to evaluate the nonstoichiometry introduced during growth. At the same time, STM gifts with precious information about the corresponding changes in the surface morphology, which is addressed here. Figure 6.11 shows the surface morphology (top row) and the surface structure (bottom row) of several representative $SrTiO_3(110)$ films with different nonstoichiometries, obtained at increasing fluence from left to right. Regimes A and B (cf. Fig. 6.10) produce markedly different surface morphologies. Films belonging to regime A tend to retain flat surfaces [Figs. 6.11(a_1, b_1)], while high fluences (regime B) induce the development of few-layers-deep pits [dark in Fig. 6.11(d_1)] that get deeper, wider, and more numerous as the growth proceeds: High fluences are detrimental for the surface quality.

A closer look at the changes occurring at the atomic scale (bottom row of Fig. 6.11) is of primary importance to understand the origin of the morphological roughening, as discussed below. Note that each substrate was initially prepared to exhibit a comparable

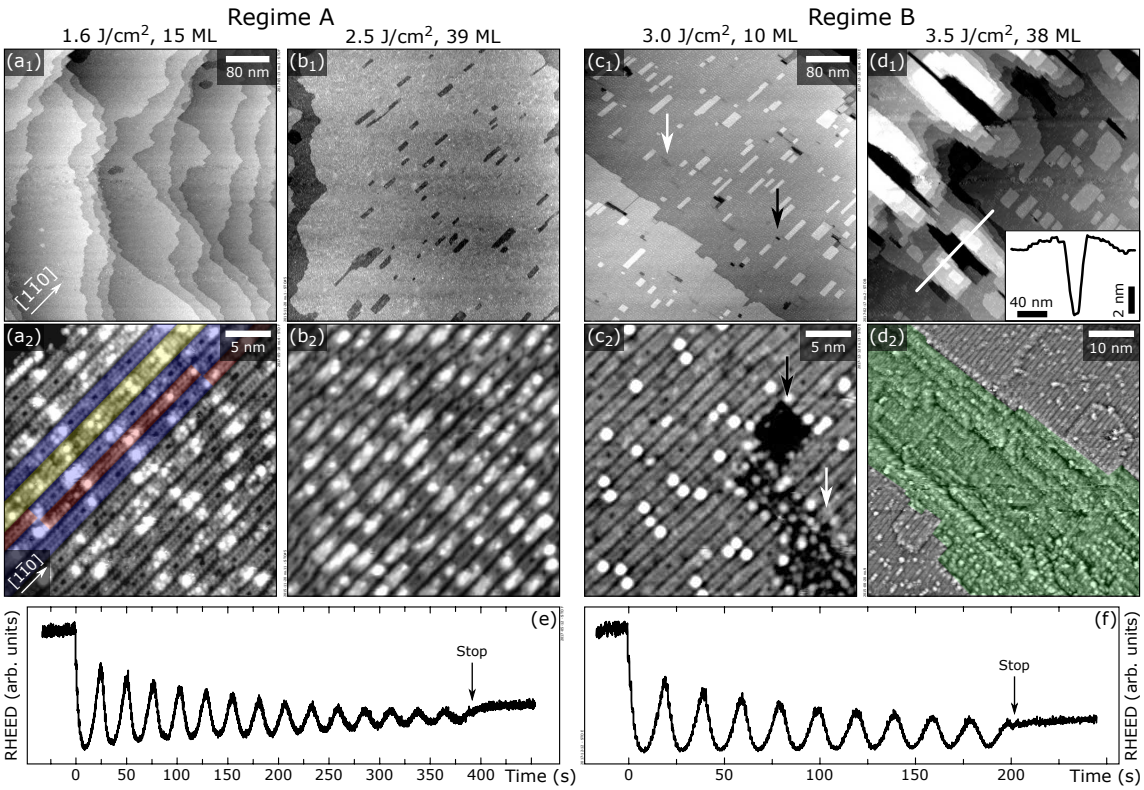

Figure 6.11. Effect of nonstoichiometric deposition conditions on the surface morphology of $SrTiO_3(110)$ films. STM images and RHEED intensity oscillations of representative, nonstoichiometric homoepitaxial $SrTiO_3(110)$ films, obtained at different laser fluences (increasing, from left to right). Sr-rich films (a_1, a_2), (b_1, b_2) exhibit atomically flat surfaces with a mixture of $(n \times 1)$ lines. In (a_2), yellow, blue, and red areas mark (6×1)-, (5×1)-, and (4×1)-reconstructed areas, respectively; in (b_2), the surface consists almost exclusively of (5×1) lines. Slight Ti enrichment (c_1, c_2) triggers the formation of small (2×4) patches (white arrows) that interrupt $(n \times 1)$ terraces. Higher fluences cause the appearance of few-layers-deep pits (d_1, d_2) that are (2×4) reconstructed. A representative pit is shown in green in the high-pass filtered image in (d_2) from a 20 layers-thick film grown at 2.55 J/cm^2. In the inset of (d_1), the STM profile of one of the pits is shown. The precursors of the pits are indicated by black arrows in (c_1, c_2). (e, f) Specular-spot RHEED intensity oscillations of films (a_1) and (c_1) showing a behavior that is representative of films grown in regimes A and B, respectively. Reprinted from ref. 68.

surface to ensure a reproducible starting point: The surface always showed a mixture of interwoven (4×1) and (5×1) lines with a well-defined ratio [between 60% and 95% (4×1) coverage]. Low-fluence (Sr-rich) films always retain a mixture of $(n \times 1)$ lines [Figs. 6.11(a_2, b_2)]. A small Sr excess [Fig. 6.11(b_2)] shifts the initially (4×1)–(5×1) surface to almost exclusively (5×1) lines; as detailed in Chapter 7, the Sr excess is quantified by determining the change in the number of (5×1) lines as a result of the growth. Larger Sr enrichments [Fig. 6.11(a_2)] drive the initial (4×1)–(5×1) surface to a mixed (5×1)–(6×1) composition [the simultaneous presence of few (4×1) lines is assigned to an imperfect equilibration of the surface]; there the same concept can be applied for the evaluation of the Sr excess.

For fluences slightly above the threshold, a new, Ti-rich (2×4) phase appears on the

(4×1)–(5×1) terraces [see the small patches appearing darker in Figs. 6.11(c_1, c_2), some of which are indicated with arrows]. The formation of this Ti-rich reconstruction is consistent with the expected Ti enrichment of the flux at these conditions. At larger fluences and/or for thicker films, pits develop on the surface [Figs. 6.11(d_1, d_2)]. Since similar pits were also observed during Ti-enriched MBE growth of $SrTiO_3(110)$,[253] one can exclude that their formation is caused by possible sputter damage induced by the higher laser fluences employed in this regime. The large depth of 22 layers of the pits in Fig. 6.11(d_1), along with their narrow width [see the pit profile in the inset of Fig. 6.11(d_1)], hindered obtaining reproducible atomic resolution at their base. Shallower pits enabled to resolve that their bottom is (2×4)-reconstructed. This is for example seen in Fig. 6.11(d_2) that displays the high-pass filtered image of a nine layers-deep pit obtained on a different film [(2×4) areas are shaded in green]. In general, LEED patterns acquired on high-fluence films (*i.e.*, with pits) consistently display a (2×4) periodicity in addition to the $(4–5 \times 1)$ periodicity associated with the $(n \times 1)$ terraces (not shown). The pit in Fig. 6.11(d_2) shows another representative feature: rims of $(n \times 1)$ islands elongated along the $[1\bar{1}0]$ direction that decorate the edge of the pit, a few layers higher than the surrounding terrace.

The quantitative evaluation of the nonstoichiometry within regime B follows the same procedure as for regime A, that is, by relating the change in the surface structure to the composition change via the phase diagram (Fig. 6.3). This means evaluating the relative number of different $(n \times 1)$ lines, as well as accounting for the new (2×4) areas. It is surprising that the stoichiometry of the films of regime B is close to the one of the corresponding substrates, and that it does not show a significant trend with fluence (Fig. 6.10). Note that one cannot exclude that systematic errors are introduced during the evaluation of the (2×4) patches and pits: The (2×4) patches are very often quite small and sparse, requiring the acquisition of sufficient statistics on a rather large scale, which, on the other hand, makes it hard to discern $(n \times 1)$ from (2×4) areas. Similar problems occur for the evaluation of the pits. As a result, it is possible that slight Ti enrichments are, in fact, introduced with increasing fluences, as the increased number of pits would suggest. Nevertheless, the difference between regimes A and B (Fig. 6.10) is striking; if a Ti excess is introduced at high fluence, it is significantly smaller than the Sr excess observed at low fluences, and with no apparent trend. Since all films exhibit comparable Sr $3d$ to Ti $2p$ intensity ratios in XPS and no statistically significant difference with respect to the $SrTiO_3$ substrates (details in Section 7.3), one can exclude that Ti atoms are implanted in the bulk during Ti-rich growth. The simplest explanation for achieving quasi-ideal stoichiometries with a Ti-rich flux is that TiO_x species stick less on the newly formed Ti-rich surfaces than SrO_x species.

Note that a qualitative analysis of the RHEED oscillations can be misleading in predicting the evolution of the film morphologies during the growth. Figures 6.11(e, f) show the RHEED oscillations of two representative Sr-rich and Ti-rich films, corresponding to the films in Fig. 6.11(a_1) and (c_1), respectively. Generally, a decrease in the intensity of maxima in the RHEED oscillations is assigned to surface roughening. However, this decrease is present in both, regime A, Sr-rich growth [Fig. 6.11(e)] and regime B [Fig. 6.11(f)], although an appreciable surface roughening only occurs in the latter case. Note that the intensity of oscillation minima of Sr-rich growths increases as the growth proceeds [Fig. 6.11(e)], while staying roughly constant in the Ti-rich regime. It is plausible that the diffraction geometry, initially optimized for the (4×1) reconstruction, is not ideal for the developing (5×1) and (6×1) phases, causing an overall decrease of the contrast in RHEED oscillations. Interestingly, this effect is markedly pronounced when moving between reconstructions belonging to the same $(n \times 1)$ family. These results send an important message: RHEED oscillations are not necessarily a reliable means to predict the development of the film morphology.

6.3.3 The role of the surface reconstruction

To understand the mechanisms behind the development of rough surfaces in the presence of the (2×4) structure [opposed to the flatness of the films exhibiting uniform $(n \times 1)$-reconstructed surfaces], the role of the surface reconstruction during the growth of $SrTiO_3(110)$ was investigated in depth. The early stages of growth were investigated at different conditions, starting from different surface reconstructions.

Submonolayer deposition of $SrTiO_3$ on a $(n \times 1)$-reconstructed surface results in a

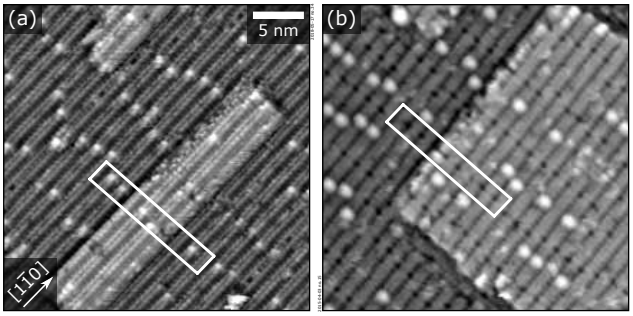

Figure 6.12. Submonolayer growth of homoepitaxial $SrTiO_3(110)$ starting from $(n \times 1)$ surfaces. Submonolayer amounts of material deposited on a (4×1)–(5×1)-reconstructed surface result in single-layer-high islands elongated along the $[1\bar{1}0]$ direction under different growth conditions: (a) four laser pulses, 6×10^{-6} mbar O_2, 750 °C, 1.7 J/cm^2; (b) one laser pulse, 3×10^{-2} mbar O_2, 850 °C, 2.0 J/cm^2. The surface reconstruction floats on top of the growing islands that retain the same (4×1)–(5×1) reconstruction as the substrate. Sr adatoms and TiO_x vacancy clusters form lines that run uninterrupted across the edges of the islands, as highlighted by the white rectangles. Reprinted from ref. 68.

morphology similar to the one shown in Fig. 6.12 over a wide range of deposition conditions (fluence between $1.3\,\mathrm{J/cm^2}$ and $3.9\,\mathrm{J/cm^2}$, pressure between 5×10^{-6} mbar and 3×10^{-2} mbar O_2, temperature between 650 °C and 850 °C). In each case, the surface is characterized by rectangular, single-layer-thick islands, elongated along the $[1\bar{1}0]$ direction. Larger islands are formed when the substrate is hotter, as surface diffusion is enhanced. The islands display the same $(n \times 1)$ reconstruction of the substrate, with the characteristic dark and bright features sitting at antiphase domain boundaries (cf. Section 6.2.1). These features run uninterrupted across the island edges, indicating that the reconstruction floats to the surface during growth. This is enabled by the intrinsic openness and flexibility of the $(n \times 1)$ structure: Its TiO_4 tetrahedra can temporarily distort and change their coordination to host additional species, thus enabling the flow of material to subsurface regions, and then easily readjust to the thermodynamically preferred structure.

When starting from a different surface reconstruction, both the island shape and their areal coverage change visibly. Figure 6.13 compares the islands formed upon submonolayer deposition at the same conditions on different surfaces: (a) monophase (4×1); (b) monophase (2×4); (c) mixed, with discrete patches either (4×1)- or (2×4)-reconstructed. The islands are rectangular on both surfaces, but oriented differently: On the (4×1) [Fig. 6.13(a)], the preferential direction is the $[1\bar{1}0]$, as in Fig. 6.12, while on the (2×4) [Fig. 6.13(b)] islands are elongated along $[001]$. The island directionality is likely caused by the structural details of the reconstructions that enforces anisotropic diffusion of the adspecies along specific crystallographic directions. The differences in the shapes of the evolving islands are also apparent on the mixed surface [Fig. 6.13(c)], where the island morphology in each patch is determined by the surface reconstruction of the pristine substrate. Similar islands (aspect ratio, directionality) as on the monophase (4×1) and (2×4) samples are formed on the (4×1) and (2×4) patches, respectively. Importantly, not only the island shapes, but also their areal coverage is markedly different on the two reconstructions. A statistical analysis reveals that the island coverage changes from 0.237 ± 0.012 to 0.144 ± 0.010 from (4×1) to (2×4), roughly corresponding to a 1.6-times smaller areal coverage on (2×4). On the mixed surface, a tendency becomes apparent to accumulate material at the interface between two reconstructions, specifically on the (4×1) side.

One can exclude that the lower coverage on the (2×4) surface is due to step flow: In Fig. 6.13(b), the island coverage close to the step (20%, small rectangle) is only slightly larger than in the middle of the terrace (14.4%, large rectangle); consequently, the lower island coverage on (2×4) areas cannot be assigned to material accumulating at step edges. The differences in island coverage can be explained instead by invoking a dif-

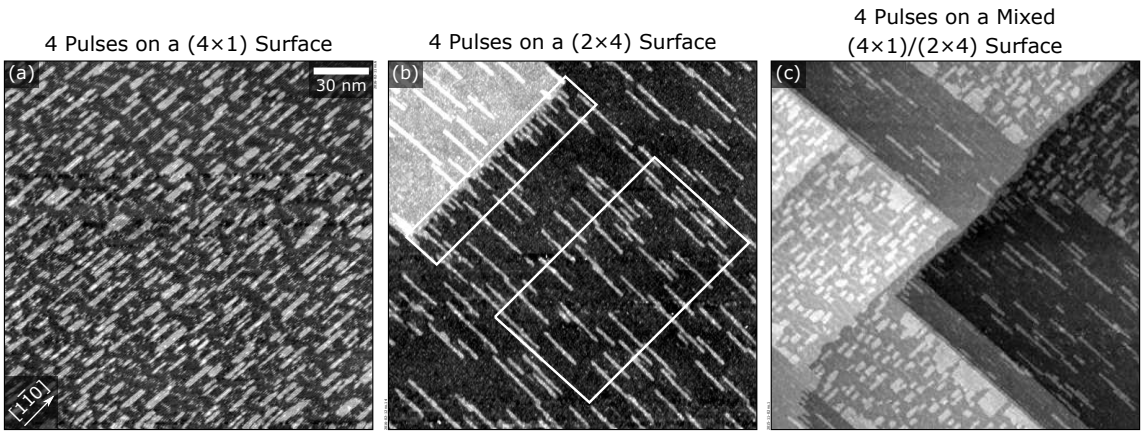

Figure 6.13. Surface-dependent sticking on $SrTiO_3(110)$. The same amount of material (4 laser pulses at 1 Hz, 5×10^{-6} mbar O_2, 650 °C, 2.55 J/cm^2) was deposited on different starting surfaces: (a) A (4×1)-reconstructed surface, (b) a (2×4)-reconstructed surface, (c) a mixed $(4 \times 1)/(2 \times 4)$ surface. Notice that (a) results in the deposition of 1.6 times more material than when starting from a (2×4)-reconstructed surface (b). Also, on the (4×1) surface of panel (a) diffusion is preferential along the $[1\bar{1}0]$ direction, whereas on the (2×4) surface in panel (b) diffusion is along the $[001]$ direction. The difference in sticking and diffusion direction is also evident when starting from a mixed $(4 \times 1)/(2 \times 4)$ surface, as shown in panel (c). In panel (b), a small (large) rectangle indicates the area close to (far from) a step, on which fractional island coverages can be evaluated. Reprinted from ref. 68.

ferent sticking on each surface reconstruction, which is related to their propensity to incorporate the incoming species. Crucial hints come from the details of the surface structures, as was unveiled by the work published in ref. 71 and illustrated in Chapter 10, which has addressed why $(n \times 1)$ structures are more effective than $(l \times m)$ structures at incorporating oxygen from the gas phase. The $(n \times 1)$ structures are open, flexible, and composed of undercoordinated TiO_4 tetrahedra, whereas the $(l \times m)$ structures are rigidly packed with fully coordinated TiO_6 octahedra. The $(n \times 1)$ surfaces incorporate more oxygen because their tetrahedra are able to temporarily distort and change their coordination to accommodate oxygen, while this process is highly unfavorable for the saturated octahedra on $(l \times m)$-reconstructed surfaces. A similar mechanism is expected to occur during the growth of $SrTiO_3$. It is less favorable for the (2×4) to change the coordination of its stiff and saturated TiO_6 octahedra to accommodate the incoming species. Consequently, a higher re-evaporation rate is expected on (2×4), which could explain the smaller island coverage measured on this reconstruction. The accumulation of material on (4×1) areas near the boundary of the two reconstructions on the mixed surface [Fig. 6.13(c)] can be explained with the same idea: Diffusing adatoms on the (4×1) find a high Ehrlich–Schwoebel barrier to traverse the boundary between the two phases, as incorporation in the (2×4) is unfavorable; they are rather 'reflected' at the interface between the two phases, while material from the (2×4) side can reach the neighboring (4×1) area, and get accommodated there. Notice that the size of the accumulated material is comparable to that of the islands on the (4×1) terraces, as expected

from the diffusion length in that area.

The above considerations allow us to explain the formation of pits in regime B (as defined in Fig. 6.10): Under (slightly) Ti-rich deposition conditions, (2×4) patches nucleate after the growth of a few layers [Figs. 6.11(c_1, c_2)], perhaps triggered by local fluctuations in the surface composition. As the growth proceeds, due to the smaller sticking on (2×4) areas, the effective growth rate in these regions is slower than on the surrounding terraces, and, in turn, pits develop. Additionally, given the small width of the pits as compared to the distance between islands formed on the (2×4) reconstruction, it is possible that the (fewer) incoming species that stick on the (2×4) patches do not nucleate islands: They could then simply diffuse toward the neighboring (4×1) terrace where they can be more easily incorporated, thus contributing to the rims of $(n \times 1)$ islands decorating the pit [Figs. 6.11(d_1, d_2)]. Species diffusing on $(n \times 1)$ terraces that find a high barrier to descend toward the pit can also contribute to the development of the rims. Since the typical size of the rims is comparable to the one of islands nucleating on the lower terraces, one concludes that the formation of these rims is to be ascribed to kinetic limitations at this temperature. To conclusively assert whether all incoming material that sticks on (2×4) areas spills out to form the rims, or if it contributes, at least partially, to the (slow) growth of the pit, one should compare the empty volume of the pit with the 'rim volume'. This quantitative evaluation is unfortunately hindered by the finite sharpness of STM tips (at best, a slope of the pit wall around 30° could be measured). As a consequence, the quantitative evaluation of the volume of pits from STM images is unreliable. What is beyond doubt is that the difference in the sticking properties between (2×4) and $(n \times 1)$ is responsible for the surface roughening observed in the $SrTiO_3(110)$ films.

6.4 Conclusions

This Chapter has shown the value of pairing PLD and STM in yet another context. Atomically resolved STM was used to correlate changes in stoichiometry, surface structures, and surface morphology in homoepitaxial $SrTiO_3(110)$ films. The analysis has revealed the ultimate origin of surface roughening in $SrTiO_3(110)$: The often-neglected surface atomic structure. It was shown that the nonstoichiometry introduced during growth with different laser fluences modifies the surface composition and the surface atomic structure of the films. Under Ti-rich conditions (high fluences), two surfaces with different sticking coefficient can develop and coexist at the surface. As the growth proceeds, pits are formed in the low-sticking areas, worsening the overall morphology. In this regime, the film stoichiometry is also affected by surface sticking, leading to a quasi-

ideal composition instead of the expected Ti enrichment. Surface roughening does not occur when the surface is uniformly reconstructed with Sr-richer structures. However, atomically flat surfaces do not necessarily stand for ideal stoichiometries (as evidenced by the Sr-rich films obtained at decreasing fluences).

One message that this Chapter aims to convey is that growing atomically flat and stoichiometric films of complex oxides is not trivial, albeit doable if one is in control of the surface reconstructions that develop during growth, and that STM can help with this. It is not unlikely that the often-reported surface roughening of other complex oxides might be similarly related to the surface atomic details as for the case of $SrTi_3(110)$ discussed here. As it will be shown, this argument is strengthened by the results presented in Chapter 9, regarding the growth of another perovskite oxide, LSMO(110).

7. Detection of small nonstoichiometries with STM

7.1 Introduction

The previous Chapter 6 has shown that the growth parameters can affect the stoichiometry, hence the surface structure, hence the surface morphology of complex multicomponent oxides like $SrTiO_3$. This Chapter presents a newly developed, STM-based method to control these properties with unprecedented accuracy.

The accurate control of the stoichiometry of oxide films (among other properties) is becoming more and more critical for fields like oxide electronics,[233,254,255] which require detection limits around or better than 0.1%.[47,245] However, the customary tools to characterize film stoichiometry do not reach this limit. These 'standard' tools include *ex-situ* X-ray fluorescence (XRF), energy dispersive X-ray (EDS) or electron energy loss spectroscopies (EELS) in a transmission electron microscope, XPS, RBS, and XRD. XRF, EDS, EELS and XPS directly measure compositions and are characterized by accuracies in quantifying the major elements of the order of a few percent.[34] RBS is capable of sensitivities as low as 0.5% on elemental ratios,[34] but relies on appropriate modeling of the measured spectra. XRD, instead, measures the film lattice parameter, which is indirectly related to the stoichiometry of the compound.[37,38,256] For example, for $SrTiO_3$, both Ti and Sr excess give rise to an expansion of the lattice parameter relative to the stoichiometric value of 3.905 Å (see Fig. 7.1).[37–39,257] XRD is therefore limited to deviations from stoichiometry that are sufficiently large to produce detectable peak shifts. Furthermore, extended defects in the lattice, such as dislocations and grain boundaries, also lead to changes in the XRD patterns,[258] to the extent that films grown by MBE exhibit smaller lattice expansions with respect to PLD- or sputter-deposited ones at comparable deviations from the optimal stoichiometry.[38] As a result, significant uncertainties exist in establishing a universal relation between nonstoichiometry and lattice expansion.

To achieve the 0.1% (or better) sensitivity demanded by developing thin-film tech-

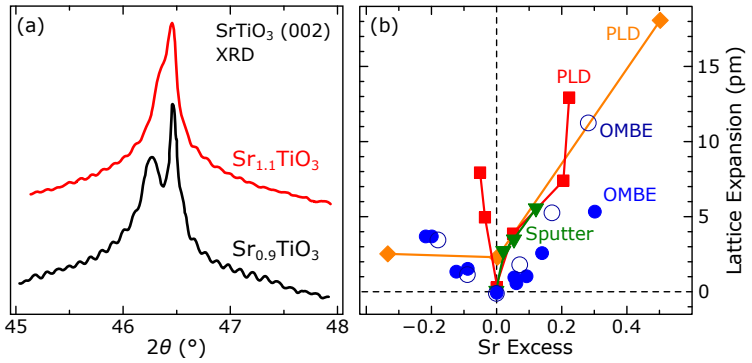

Figure 7.1. Measuring nonstoichiometry in $SrTiO_3$ with XRD. Both Ti and Sr enrichments produce lattice expansions that can be measured by XRD. (a) θ-2θ curves of OMBE-grown, nonstoichiometric homoepitaxial $SrTiO_3$(001) films of ≈100 nm thickness. (b) Lattice expansions measured on several homoepitaxial $SrTiO_3$(001) films, correlated to the corresponding cation excesses. Adapted with permission from ref. 38.

nologies, new tools are needed. One possibility is to exploit structural features that have a strong dependence on the cation composition, such as the surface atomic structure: As shown by Fig. 6.3 in Section 6.2, the surface atomic structure of $SrTiO_3$(110) has a strong dependence on the Sr/Ti ratio at the surface, which is in turn influenced by the nonstoichiometry introduced during growth. Based on this concept, RHEED was recently used to monitor changes in the surface reconstructions of $SrTiO_3$ as a sensitive measure of the film stoichiometry.[47,48] These studies have revealed that $SrTiO_3$(001) homoepitaxial films exhibit significant changes in their surface reconstructions upon varying the growth parameters, even within the optimum growth window previously established by XRD.[47] This already indicates that detecting changes in the surface structures is a more sensitive tool to optimize film stoichiometry than XRD (or other 'standard' techniques) alone.

In the work presented here, published in ref. 69, this concept has been taken forward, aiming to derive even smaller changes in the surface reconstructions (hence in the surface stoichiometry) than what can be done by RHEED: The intrinsically superior resolution of STM was exploited to detect *fractional* changes in the surface reconstruction, which allow to reach the required 0.1% detection limit. The Chapter discusses the details of the STM-based method used to this end, showcasing it for the homoepitaxial growth of $SrTiO_3$(110). Notably, for the case of oxide films in which the nonstoichiometry is largely accommodated at the surface—as it is the case for $SrTiO_3$(110)—this approach has no lower detection limit for the deposited cation excess.

After discussing how the stoichiometry of a generic film evolves during growth under nonstoichiometric conditions (Section 7.2.1), Section 7.2.2 will detail how stoichiometry changes can be derived from measured changes in the surface structure. Section 7.2.3 will finally exemplify the use of the method for the homoepitaxy of $SrTiO_3$(110).

7.2 Approach

7.2.1 Deposition of nonstoichiometric films

Figure 7.2 sketches how the stoichiometry of a generic film evolves during growth under nonstoichiometric conditions. For simplicity, it is assumed that the substrate is stoichiometric, and that the deposited flux is characterized by a constant nonstoichiometry, such that a total excess x of one of the cations is introduced during the growth of every layer. (This hypothesis is reasonably well verified if the sticking coefficients of the deposited species do not change appreciably during growth, which is plausible for sufficiently small changes in the surface structure). It is assumed that a fraction x_s of the cation excess x floats at the surface during growth. The remaining cation excess $x_\mathrm{b,f} = x - x_\mathrm{s}$ remains stationary in the deposited layer (*e.g.*, for kinetic reasons), and modifies the composition of the bulk of the film accordingly. Both x_s and $x_\mathrm{b,f}$ modify the composition of the surface. Specifically, during the growth of each atomic layer, a cation excess $x = x_\mathrm{s} + x_\mathrm{b,f}$ is introduced in the surface layer. After the growth of the first atomic layer, the surface stoichiometry changes, with respect to that of the substrate S_sub, as

$$\Delta S(1) = S(1) - S_\mathrm{sub} = x = x_\mathrm{s} + x_\mathrm{b,f}.$$

Upon growing the second layer, a cation excess $x_\mathrm{b,f}$ is left behind in the subsurface layer, while x_s is transferred to the newly deposited layer. This quantity adds to the excess x introduced directly from the deposition, so that

$$\Delta S(2) = S(2) - S_\mathrm{sub} = x_\mathrm{s} + x = 2x_\mathrm{s} + x_\mathrm{b,f}.$$

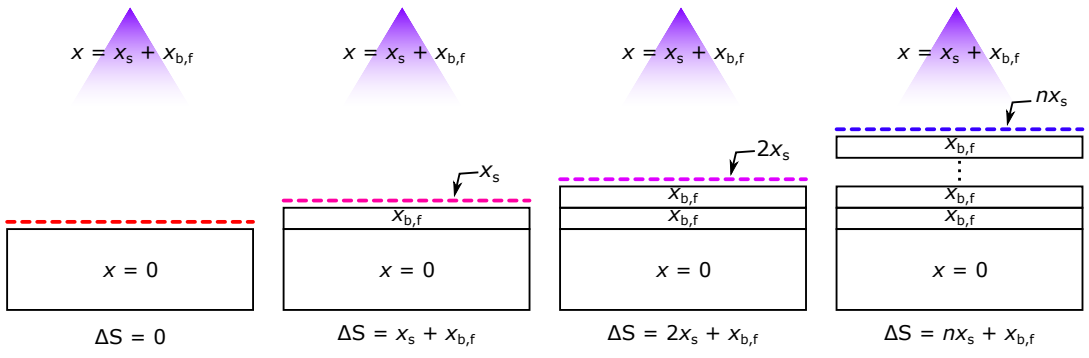

Figure 7.2. Evolution of the stoichiometry of a generic film under nonstoichiometric deposition conditions, hypothesizing a stoichiometric substrate and a constant flux nonstoichiometry. A fraction x_s of the total cation excess x floats to the surface during growth, while the remaining cation excess $x_\mathrm{b,f}$ remains stationary in the deposited layer. ΔS represents the change in surface stoichiometry as a result of film growth.

Simple iteration of this reasoning leads to the expression for the change of surface stoichiometry (with respect to that of the substrate) upon growth of n layers

$$\Delta S(n) = nx_{\mathrm{s}} + x_{\mathrm{b,f}}. \tag{7.1}$$

Eq. (7.1) essentially means that one can derive the deposited cation imbalance x based on the change of the surface stoichiometry ΔS, provided that the distribution of nonstoichiometry within the film is known. The following Sections discuss the approach to measure ΔS, showcased for the homoepitaxy of $SrTiO_3$(110).

7.2.2 How to derive ΔS?

In a nutshell, ΔS is derived from the correlated changes in the surface structure. As discussed in Section 6.2, many perovskite oxides display a variety of reconstructions that are related by near-surface stoichiometry. The change in surface composition ΔS caused by nonstoichiometric growth (Fig. 7.2) should produce a correlated change in the surface structure, which is measured with STM.

Note that there are two indispensable conditions for applying this approach: (i) A well-defined relation between changes in surface composition and changes in the surface structure must be available. This is the case for $SrTiO_3$(110) and for LSMO(110), as seen in Chapter 6 and Chapter 8, respectively; (ii) the distribution of nonstoichiometry within the film must be known. Section 7.3 shows that for the case of $SrTiO_3$(110) homoepitaxy, all nonstoichiometry segregate to the surface. In other words, the bulk grows nearly stoichiometric, or $x_{\mathrm{b,f}} = 0$ in Eq. (7.1). Hence, the measured change of the surface stoichiometry is proportional to the total excess x and to the film thickness n as

$$\Delta S(n) = nx_{\mathrm{s}} + x_{\mathrm{b,f}} = nx_{\mathrm{s}} = nx,$$

and the total excess x can be derived as

$$x = \Delta S(n)/n. \tag{7.2}$$

Let us now tackle how to use a surface phase diagram like that of Fig. 6.3 to measure surface nonstoichiometries with STM. The phase diagram of Fig. 6.3 not only yields the stoichiometry of a monophase surface with respect to the one of an arbitrarily chosen reference structure. It can also be used to define the (relative) stoichiometry of the surface of a multi-phase $SrTiO_3$(110) sample, *i.e.*, with coexisting surface reconstructions. In case such a surface is composed of $i = 1, \ldots, k$ reconstructions with fractional cov-

erages θ_i, its (relative) stoichiometry can be expressed as

$$S = \sum_{i=1}^{k} \theta_i \left(s_i - s_\mathrm{R}\right) = \left(\sum_i \theta_i s_i\right) - s_\mathrm{R}, \tag{7.3}$$

where s_i and s_R correspond to the stoichiometry of a monophase surface with reconstruction i, and the one of a chosen reference structure, respectively. These quantities correspond to the cation doses reported in the surface phase diagram of Fig. 6.3. With Eq. (7.3), one can compare the stoichiometry of any two $SrTiO_3$(110) surfaces A, B as

$$\Delta S_\mathrm{A,B} = S_\mathrm{B} - S_\mathrm{A} = \sum_i (\theta_i^\mathrm{B} - \theta_i^\mathrm{A}) s_i, \tag{7.4}$$

where the contribution of the (common) reference structure cancels out. A simplified version of Eq. (7.4) can be used when the same two reconstructions (1 and 2), at equilibrium with one another, are present on surfaces A and B (with different fractional coverages). The change in the surface stoichiometry is then

$$\Delta S_\mathrm{A,B} = \Delta\theta_1^\mathrm{B,A} \Delta s_{1,2}, \tag{7.5}$$

where $\Delta\theta_1^\mathrm{B,A} = \theta_1^\mathrm{B} - \theta_1^\mathrm{A}$ is the difference in the coverage of the first reconstruction on the two surfaces, while $\Delta s_{1,2} = s_1 - s_2$.

Note that A and B in Eqs. (7.5) and (7.4) are entirely generic surfaces. Therefore, these relations can be used to compare the surface stoichiometry of a $SrTiO_3$(110) film with respect to its corresponding substrate, as well as to compare the relative surface stoichiometry of two deposited films, or the change in the surface stoichiometry of a film as a result of post-growth treatments. Note also that Eqs. (7.5) and (7.4) describe only the stoichiometry of the very surface: Conclusions concerning the stoichiometry of the bulk underneath require to establish an appropriate relation between the stoichiometry of the surface and the one of the bulk itself. Such a relation (along with more generalized models) is derived in ref. 69.

7.2.3 Implementation: $SrTiO_3$(110) homoepitaxy

This Section exemplifies how to apply Eq. (7.5) with the homoepitaxial growth of a slightly Sr-rich $SrTiO_3$(110) film. Figure 7.3 compares the morphology and structure of an as-prepared $SrTiO_3$(110) substrate and of the corresponding homoepitaxial film of ≈15-layers thickness (≈4.2 nm). On large-area STM images [Figs. 7.3(a, b)], both substrate and film show 20–300 nm-large, atomically flat terraces, separated by single- or

multi-layer steps. The deposition was interrupted just after the completion of the fifteenth atomic layer, as seen from the *in-situ* RHEED intensity oscillations.[69] As a result, a few single-layer-high, atomically flat islands are visible on the terraces of the surface of the film in Fig. 7.3(b). Upon growth, the surface structure changes from predominantly (4×1)- to mainly (5×1)-reconstructed, as seen from the LEED patterns in Figs. 7.3(e, f). This corresponds to a change toward a more Sr-rich surface. Such a change is reflected in the atomic-scale STM images of Figs. 7.3(c, d). In Figs. 7.3(c, d) lines with (4×1) and (5×1) periodicities are highlighted for clarity in red and blue, respectively.

As compared to the qualitative picture provided by LEED, STM allows a quantitative determination of the relative coverage of the two reconstructions by directly measuring the fractional areas occupied by the two reconstructions. For example, the relative coverage of (4×1)-reconstructed areas in a sample comprising (4×1) and (5×1) reconstructions can be calculated as

$$\theta_{4\times1} = \frac{4N_{4\times1}}{4N_{4\times1} + 5N_{5\times1}},$$

where $N_{4\times1/5\times1}$ are the numbers of (4×1) and (5×1) lines in an STM image. This coverage can be directly plugged into Eq. (7.4) to derive the change of surface stoichiometry.

To gain enough statistical significance, several STM images comparable to those in Figs. 7.3(c, d) were acquired at different spots on the sample, totaling 1 000–2 000 lines (typically this corresponds to acquiring 15–30 images of 70×70 nm^2 size). With this approach, one determines that $85.4 \pm 3.5\%$ of the surface of the substrate in Fig. 7.3(c) has a (4×1) reconstruction, while $14.6 \pm 3.5\%$ is (5×1)-reconstructed. After growth of a 15.25 layers-thick film, $10.6 \pm 1.4\%$ of the surface of the sample retains the (4×1) reconstruction, while $89.4 \pm 1.4\%$ is (5×1). According to Eq. (7.4), this corresponds to a change in the surface stoichiometry upon growth $\Delta S = (11.22 \pm 0.80)\%$ ML Sr (compare formulas in Fig. 7.3 with Equations from Section 7.2.1).

Note that the applicability of the approach discussed here is granted for any experimental technique capable of accessing the structure of the material's surface, and is not restricted to scanning probe microscopies. In fact, the method boils down to the determination of the fractional coverages of each reconstruction present at the surface [Eq. (7.4)]. This can also be accomplished, for example, by quantitatively analyzing LEED or RHEED diffraction patterns. In this case, one should expect a larger $\Delta\theta_{\text{min}}$ than with STM, and, consequently, an increased detection limit for similarly thick films [Eq. (7.6)].

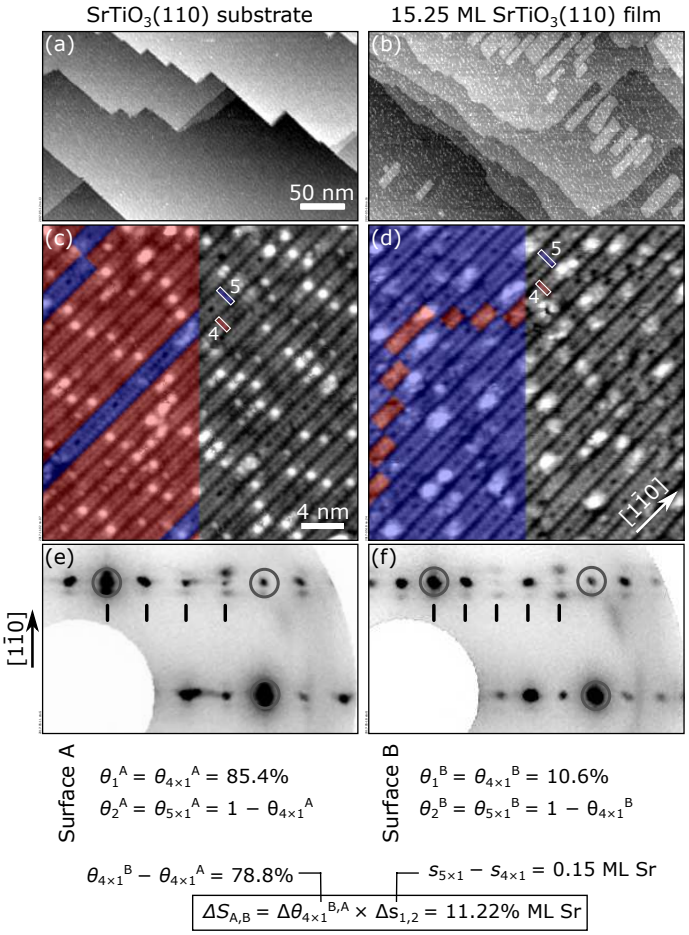

Figure 7.3. Morphology and atomic-scale structure of a 15.25 layers-thick homoepitaxial $SrTiO_3(110)$ film (laser fluence 1.9 J/cm^2). (a, b) 350 × 210 nm^2 STM images; (c, d) (30 × 30 nm^2) STM images; (e, f) LEED patterns (90 eV, inverted gray scale). In the left half of panels (c, d), lines exhibiting (4 × 1) and (5 × 1) periodicities are highlighted in red and blue, respectively, while the corresponding reconstructed unit cells are outlined in white. In panels (e, f), bulk-derived (1 × 1) diffracted beams are marked with red circles, while the periodicity of reconstruction-related spots is marked by vertical dashes. Adapted from ref. 69.

7.3 Nonstoichiometry segregation

7.3.1 Experimental evidence

It was anticipated that $SrTiO_3(110)$ accumulates all nonstoichiometries at the surface, so that Eq. (7.2) can be used to derive the excess cations introduced during growth by simply dividing the surface stoichiometry change ΔS measured with STM by the number of layers deposited. This Section demonstrates that this scenario is supported by XPS and XRD data, and by purposively designed STM-based experiments.

XPS data. The Sr 3*d*/Ti 2*p* intensity ratios of several films were referred to the ratios of the corresponding substrates, and plotted as a function of the laser fluence employed

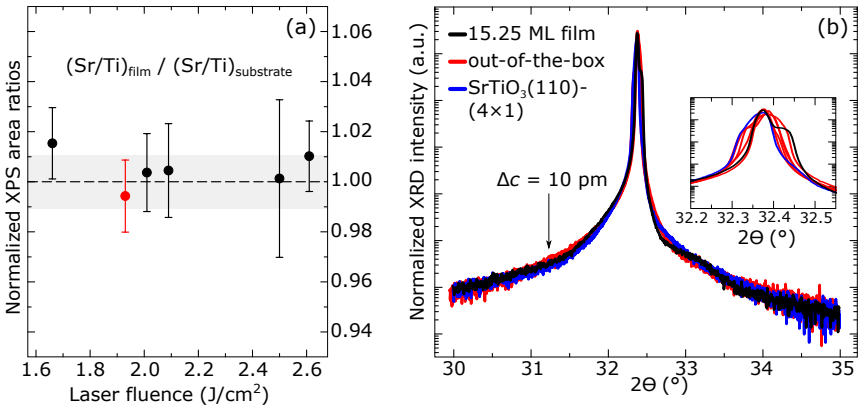

Figure 7.4. XPS (a) and XRD (b) data supporting the segregation of cation nonstoichiometry in $SrTiO_3(110)$. (a) The Sr $3d$/Ti $2p$ ratio of each film was normalized to the corresponding ratio measured on the substrate, leading to the relative intensity ratios $(Sr/Ti)_{film}/(Sr/Ti)_{substrate}$ plotted as a function of the UV laser fluence (peak intensities were evaluated from the area subtended by the peaks, after subtraction of a Shirley-type background). The data point corresponding to the film of Fig. 7.3 is red. The dashed line at $(Sr/Ti)_{film}/(Sr/Ti)_{substrate} = 1$ corresponds to films with the same composition of the corresponding substrates. (b) High-resolution XRD (Cu Kα_1) coupled symmetric scan around the (110) reflection of $SrTiO_3$. The diffractogram acquired on the film of Fig. 7.3 is displayed in black, while XRD scans measured on five out-of-the-box samples, as well as on one substrate that was prepared to show predominantly a (4×1) reconstruction, are plotted in red and blue, respectively. The vertical arrow marks the expected position of the (110) Bragg reflection from a $SrTiO_3(110)$ film whose lattice parameter is expanded by 10 pm.[259] The inset shows a blowup of the same curves in proximity of the substrate peak. The small deviation in the curves, characterized by the presence of duplicate features, is attributed to small-angle twinning of the commercial single crystal substrates. These are present on all samples, and are not related to the growth of the homoepitaxial film. Adapted from ref. 69.

to grow them [Fig. 7.4(a)]. In red is highlighted the data point corresponding to the 15 ML-thick film of Fig. 7.3, characterized by a measured surface nonstoichiometry of $\Delta S = (11.22 \pm 0.80)\%$ ML Sr. Consider now the extreme scenario in which the excess cations introduced during growth are uniformly distributed within the bulk of the film with no accumulation at the surface, such that the change in composition of the surface directly reflects the one of the bulk underneath. In this case, the Sr $3d$/Ti $2p$ intensity ratios should show a trend as a function of the laser fluence, and should differ from the intensity ratio of the corresponding substrate. In fact, the inelastic mean free paths for the photoelectrons ($\lambda_{Ti\,2p} = 2.05$ nm and $\lambda_{Sr\,3d} = 2.53$ nm[260]) are approximately half the thickness of a film of 15 ML (≈ 4.2 nm). As a result, XPS signals are dominated by film contributions, even at normal emission. [For reference, the gray band in Fig. 7.4(a) reports the change in the XPS intensity ratios when the reconstruction of the $SrTiO_3(110)$ surfaces changes from (4×1) to (5×1), as simulated with the SESSA software[261]]. The XPS data show that this hypothesized scenario, where the nonstoichiometry is uniformly distributed in the bulk of the film, does not apply. There is no appreciable change of the XPS intensity ratios as a result of the film growth: Films grown at different laser fluences (and with different surface nonstoichiometries measured in STM, cf. Fig. 6.10) fall

on the same line within the error bars. In other words, when measured in XPS, the films are indistinguishable from each other and from the substrates. From an XPS standpoint, most (if not all) nonstoichiometries are accommodated at the surface.

XRD data. *Ex-situ* high-resolution XRD was performed at the Massachusetts Institute of Technology [Fig. 7.4(b)]. Symmetric $\omega-2\Theta$ coupled scans were performed around the (110) reflection of $SrTiO_3$ with monochromatized Cu Kα_1 radiation [$\lambda = 1.540562$ Å; 2-bounce Ge(022) monochromator] employing a point detector (5° Soller slits). The black curve corresponds to the film in Fig. 7.3 with $\Delta S = (11.22 \pm 0.80)\%$ ML Sr, while the blue and the red diffractograms correspond to five out-of-the-box samples and one substrate prepared to exhibit the (4×1)–(5×1) reconstruction, respectively. Once again, consider the extreme case in which the cation excess is uniformly distributed within the bulk of the film. This would result in a seriously expanded out-of-plane lattice parameter (10–15 pm),[37] which should produce a distinguishable feature in XRD. However, the diffractogram shows only one main feature, where diffraction from the $SrTiO_3$(110) substrate occurs, and no additional features are observed at those angles at which a 10 pm expansion of the film out-of-plane lattice parameter would be expected [vertical arrow; such a shoulder is visible in the XRD data of the non-stoichiometric film of Fig. 7.1(a)].[259] Furthermore, the XRD scan on the film closely matches the diffractograms acquired on the reference samples. The small differences visible in the main substrate feature [see inset of Fig. 7.4(c)] are likely related to small-angle twinning of the commercial $SrTiO_3$(110) crystals. These are present on all samples, and are not related to the growth of the homoepitaxial film. Therefore, according to XRD, the nonstoichiometry of the bulk of the film is close to the one of the substrate.

One concludes that neither XPS nor XRD are able to distinguish between $SrTiO_3$(110) substrates and the film in Fig. 7.3, while the difference is clearly observable by STM. This is in line with the hypothesis that, during growth, the large majority of the cation nonstoichiometry is accumulated at the surface of the film, while its bulk grows nearly stoichiometric (or at least with a bulk nonstoichiometry smaller than the detection limit of XPS and XRD on $SrTiO_3$ films of ≈4 nm thickness, which it is estimated to be no less than ≈2% and ≈3%, respectively). The hypothesis is strengthened by the two following control experiments that were performed with STM.

STM control experiments no.1: Linearity of nonstoichiometry with increasing film thickness. Homoepitaxial $SrTiO_3$(110) films of varying thickness were deposited at fixed laser fluence of 1.7 J/cm^2, and measured the corresponding change in surface sto-

ichiometry via the change of the surface reconstruction (Fig. 7.5). The idea is that if *all* cation excess segregates to the surface, the measured nonstoichiometry should scale linearly with the thickness. Note that each films was grown on the same substrate, after the surface had been re-prepared to exhibit a fractional coverage of (4×1)-reconstructed areas ranging between 75% and 85% (starting from a similar surface reconstruction should limit the impact of sticking).

The results support the hypothesis. As shown by the STM images in the insets of Fig. 7.5, the surface structure of the film progressively evolves from mixed (4×1)–(5×1)-reconstructed to an essentially pure (5×1) periodicity. Correspondingly, the change in surface stoichiometry ΔS linearly increases with the thickness of the deposited film, consistently with the model in Eq. (7.1). A linear fit to the data (gray line in Fig. 7.5) allows to estimate the fractional excess of Sr atoms accommodated at the surface (x_s) and distributed in the bulk ($x_{b,f}$), as the slope and intercept of the fitting line, respectively. Specifically, it is found that a nonzero excess fraction $x_s = 0.99 \pm 0.19\%$ of Sr atoms accumulates at the surface of the growing film for each deposited layer. At the same time, there is no statistical evidence that the amount of excess Sr cations distributed in the bulk of the film ($x_{b,f} = 0.4 \pm 1.4\%$) is different from zero.

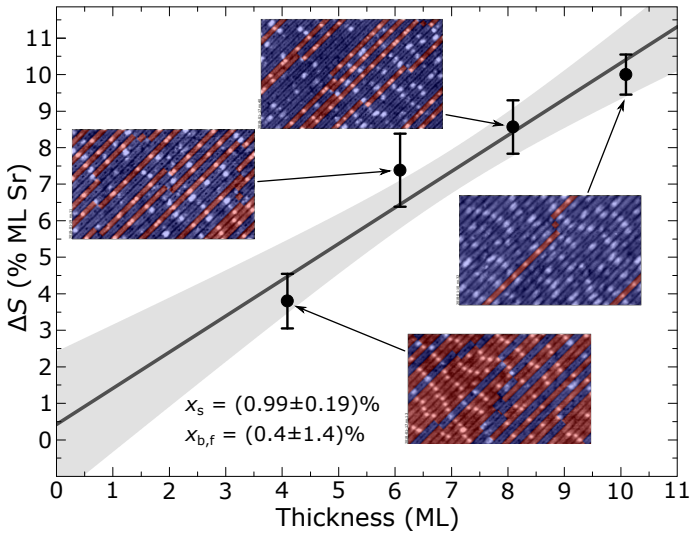

Figure 7.5. Segregation of cation nonstoichiometry in $SrTiO_3(110)$: STM evidence. Change of surface stoichiometry upon homoepitaxial growth of $SrTiO_3(110)$ films of increasing thickness (laser fluence 1.7 J/cm^2), as derived from STM data. Error bars correspond to 99% confidence intervals, as derived from the statistical evaluation of STM images. Representative STM images (50×30 nm^2) are shown as insets. (4×1)- and (5×1)-reconstructed areas are highlighted in red and blue, respectively. The gray line represents a linear fit to the data, while the shaded area corresponds to the 70% confidence band of the fit. The slope (x_s) and intercept ($x_{b,f}$) of the linear fit are reported together with their standard errors. Reprinted from ref. 69.

STM control experiment no.2: Nonstoichiometry segregation upon annealing. The second control experiment consisted in post-annealing the films at elevated temperatures after deposition (specifically, the films were annealed for 4 h at 1 000 °C and 6×10^{-6} mbar O_2). After such treatment, the cation nonstoichiometry possibly accumulated in the bulk of the film could segregate to the surface or get diluted into the substrate. Either case would cause a change of the surface composition and structure. The change of surface structure was quantitatively determined upon post-annealing on a homoepitaxial $SrTiO_3$(110) film, and estimated a maximum total amount of Sr excess in the bulk of $-0.10 \pm 0.08\%$ (more details in ref. 69). This supports the hypothesis that, under the employed experimental conditions, a negligible fraction of the deposited cation excess is incorporated in the bulk of the film. Most of the excess cations deposited accumulates at the surface during growth.

7.3.2 Pushing the detection of cation nonstoichiometry to the limit

The fact that all nonstoichiometry segregates to the surface has an important implication: Arbitrarily small cation imbalances can be detected by growing appropriately thick films. In particular, if the same two reconstructions are present, at equilibrium with one another, on the substrate and on the film, the minimum detectable cation excess amounts to

$$x_{\text{min}} = \frac{\Delta\theta_{\text{min}}\Delta s_{1,2}}{n}, \tag{7.6}$$

as obtained from inserting Eq. (7.5) into Eq. (7.2). The quantity $\Delta\theta_{\text{min}}$ in Eq. (7.6) corresponds to the minimum detectable change of fractional coverage of one of the two reconstructions, and it is defined by the experimental technique used. It is estimated that STM allows to discriminate a $\Delta\theta_{\text{min}}^{\text{STM}} = 0.05$ areal coverage change with reasonable statistical efforts. For a film of 15 ML showing a mixture of (4×1) and (5×1) both before and after the growth, such as the one shown in Fig. 7.3, one then derives that x_{min} = 0.05%. This value is in perfect agreement with experimentally derived one: By dividing the measured surface nonstoichiometry on the film of Fig. 7.3 of (11.22 ± 0.80)% ML Sr by the film thickness of 15 ML, one obtains a total introduced cation excess of x = 0.74 ± 0.05%. The minimum detectable cation imbalance is determined by the 0.05% statistical uncertainty, and this is in perfect agreement with the value of x_{min} = 0.05% derived theoretically. Importantly, by growing thicker and thicker film, one can further decrease the minimum detectable cation excess.

7.3.3 Why do nonstoichiometries segregate?

It is likely that the surface reconstructions of $SrTiO_3$(110) themselves are key to the segregation of excess cations to the surface: Accommodating the excess cations at these reconstructions is less costly than introducing bulk defects.[230] In fact, in $SrTiO_3$, bulk defects consist of antisite point defects or of {001}-oriented SrO planes.[39] The formation of antisite point defects requires significantly larger energy (1–4 eV per defect)[262] than modifying the surface reconstruction [0.2 eV/(1×1) unit cell][230] while Ruddlesden-Popper planes [0.5 eV per $SrTiO_3$(001) unit cell][263] would inevitably result in energetically expensive crystallographic defects at the (110)-oriented surface.

Note that the higher cost associated to bulk defects than for reconstructuring the surface (> 1 eV/defect[39,262–268] vs. a few fractions of an electronvolt per unit cell[228,248]) is not a specific property of $SrTiO_3$(110): Surfaces will tend to reconstruct over forming bulk defects, when kinetics allows it. The deposited cation imbalance are expected to segregate to the surface under the following conditions:

(i) The material exhibits (at least two) surface-composition-driven reconstructions. As mentioned in the previous Chapter 6, this appears to be the case for a variety of complex oxide surfaces other than $SrTiO_3$(110),[224,228,231,238,246–250] and is likely true for other non-oxide materials.

(ii) The nonstoichiometry introduced during growth is small enough, such that surface restructuring allows its accommodation. Introduction of nonstoichiometric bulk defects[39,47] or precipitation of secondary phases is likely to occur if the deposited cation imbalance exceeds the largest excess that can be accommodated in the surface reconstructions. If this is the case, traditional techniques will be more suited. Chapter 9 shows that in the case of LSMO(110), ill-defined oxide clusters nucleate and grow on the surface when the deposited cation imbalance exceeds the capability of the surface to accommodate it.

(iii) The growth temperature and rate are chosen such that equilibration of the surface structures is appropriately established. The cation chemical potentials during deposition are uniquely determined by the combination of surface reconstructions, and are fixed in case only the same two reconstructions are present at all stages. This makes the inclusion of nonstoichiometric bulk defects unfavorable.

When these conditions are met, and the deposited cation imbalance is largely accommodated at the surface, the prowess of the method presented here can be fully exploited via Eq. (7.2). This should be possible for several materials other than $SrTiO_3$(110).

7.4 Conclusions

This Chapter has presented an unconventional approach to determine with unprecedented accuracy the cation excess deposited during the growth of complex-oxide thin films such as $SrTiO_3$(110). The method is based on the characterization the surface structure of films via STM, and exploits an existing surface phase diagram that relates specific reconstructions to one another and to the corresponding difference in their near-surface cation stoichiometry. It was shown that deposited cation imbalances deviating by less than 0.1% from the ideal bulk concentration can be readily detected. Importantly, in cases where the cation excess is mainly accommodated at the surface, as demonstrated for $SrTiO_3$(110) homoepitaxial films, this method does not suffer from a fundamental detection limit.

As seen in the previous Chapter 6, such utmost control of defects and composition is crucial to produce atomically flat film surfaces of complex oxides. Controlling both film stoichiometry and its surface morphology to such a degree is the key to making all-oxide electronics a reality, allowing to fully exploit the many functionalities of complex-oxide materials. As it will be shown in Chapter 9, this method was used to pinpoint optimal growth conditions for another oxide material, LSMO, which, just like $SrTiO_3$, exhibits a variety of composition-related surface reconstructions distinguishable from one another in STM. The growth of other oxide materials that share a similar behaviour to $SrTiO_3$ and LSMO could be also optimized by using the STM-based method described in this Chapter.

8. $La_{0.8}Sr_{0.2}MnO_3(110)$: Establishing a model system

8.1 Introduction

This Chapter deals with the most complex material explored within this Thesis: strontium-lanthanum manganite ($La_{1-x}Sr_xMnO_3$, LSMO), a four-element perovskite oxide with many exotic properties and exciting promises for applications. Breaking up the flow about the influence of the PLD parameters on the film properties if only for a moment, this Chapter is rather focused on the atomic-scale properties of the material itself. Because single-crystalline LSMO samples are not available commercially, and because single-crystalline films with ideal surfaces had not been synthesized yet, nothing is known about the surface details of LSMO. This Chapter gives a detailed overview of the first-time atomically resolved surface reconstructions of LSMO(110). The investigation was performed on high-quality LSMO(110) films that were synthesized via the STM-based method described in Chapter 7, as discussed in Chapter 9.

LSMO is a truly fascinating material, and it is used in the most diverse areas of application. Its excellent thermal stability, electron mobility, and redox abilities, plus its wide availability and environmental friendliness, have appointed it as the prototypical cathode material in solid-oxide fuel cells,[269,270] and as a viable and cheap catalyst for methane combustion and NO oxidation.[271–274] Because of its half-metallicity and colossal magnetoresistance, LSMO is also employed in spintronic applications.[275–279] Last but not least, the subtle interaction of spin, charge, orbital and lattice degrees of freedom in LSMO produce a rich phase diagram including doping- and thickness-dependent metal-to-insulator transitions, as well as ferromagnetic to anti/paramagnetic transitions,[280–282] which can be exploited to achieve new functionalities in well-controlled thin-film heterostructures grown by PLD.[281,283]

As always, a precise knowledge of the surface details of LSMO is essential for most

applications. In catalysis, it enables to control the material's activity that can be affected by the surface atomic structure,[71] composition, and oxidation state of Mn species;[274,284] in thin-film heterostructures, it allows for a fine engineering of electronic and magnetic properties;[285,286] it is also paramount for gaining fundamental insights about the LSMO electronic structure and excitations.[286,287] Establishing the details of the surface structures of LSMO at given experimental conditions is not enough, though: The surface properties will be affected by the environmental conditions, thus influencing their interaction with the external world or interfacing materials in epitaxial heterostructures. For instance, the polarization applied to the LSMO cathode in solid-oxide fuel cells (Chapter 10) will determine the effective oxygen chemical potential felt by the surface, which might affect its properties in turn. Hence, one also needs to understand how the environmental conditions affect the properties of given LSMO surfaces.

However, the knowledge on the atomic surface properties of LSMO, both at given and evolving experimental conditions, is still scarce. This is partly because single-crystalline samples are not easily available, and synthesizing single-crystalline films with well-defined surfaces has proven to be challenging (see Chapter 9). $SrTiO_3$ crystals with both (001) and (110) orientation have often been used as substrates for LSMO films, thanks to their reasonable lattice mismatch with LSMO.[288–292] While a few authors have shown that atomically flat surfaces of thin films on $SrTiO_3$ could be achieved after finely tuning the growth parameters,[289,290,293,294] the attempts of imaging LSMO surfaces at the atomic scale have so far been unsuccessful, possibly because of the widely reported segregation of SrO at LSMO surfaces,[295–297] although some authors have also blamed charge delocalization.[290,291] As a consequence, there exists no real systematic study on the surface atomic details of LSMO.

This Chapter investigates the atomic-scale properties of atomically flat films with (110) orientation and a $La_{0.8}Sr_{0.2}MnO_3$ composition, of interest for solid-oxide fuel cells where LSMO is used as a cathode[270] (details about the growth of these films and their bulk properties are given in Chapter 9). A variety of reconstructions are unveiled and investigated by combining atomically resolved STM with LEIS, LEED, XPS, and, for some structures, DFT.

After introducing the bulk-truncated structure of the system in Section 8.1.1, Section 8.2 focuses on surface reconstructions that are stable at pressures above 10^{-3} mbar O_2 at 700 °C, *i.e.* at conditions that bridge the gap between UHV and the operation conditions of solid-oxide fuel cells. Deposition of sub-monolayer amounts of Mn and La (followed by O_2 annealing) was used to tune the surface composition, and quantitative relations between the reconstructions were established by using the movable QCM de-

scribed in Section 2.5. The results, summarized in ref. 70, show that the reconstructions are characterized by distinct structural, compositional, and electronic properties, vary in their ability to accommodate the deposited cations, and have a likely origin in polarity compensation. The discussion then goes in more depth for one structure, namely the (1 × 1), focusing on its DFT-derived model (Section 8.3). Finally, Section 8.4 addresses the behavior of the high-pressure reconstructions of LSMO(110) as a function of the oxygen chemical potential μ_O, to unveil the stability regions of each reconstruction. It is shown that the plethora of surface reconstructions intrinsic to LSMO(110) can be conveniently summarized in a two-dimensional surface phase diagram, as a function of the content of Mn in the surface and of μ_O.

8.1.1 Bulk structure of $La_{0.8}Sr_{0.2}MnO_3$

In the ABO_3 perovskite structure of LSMO, the A site is occupied either by La or Sr, and the B site by Mn. Depending on the La-to-Sr ratio, the bulk structure exhibits slight variations of the rhombohedral and cubic symmetry (the transition to cubic occurs for Sr contents above 40%).[298] For the 80:20 stoichiometry possessed by the films presented here (see Chapter 9), LSMO crystallizes in a rhombohedral structure (a_R=5.4732(2) Å, α_R=60.5120(2)°),[299] but can be viewed as pseudocubic, *i.e.*, a distorted version of the ideal cubic symmetry, with lattice parameter a_{pc}=7.7702(2) Å, and angle between lattice vectors of 90.4420(2)°. [only half of the unit cell along (001) is shown in Fig. 8.1(a)]. Crystallographic directions given in this work are based on this pseudocubic lattice. The skeleton is built by perovskite 'cubes' with sides a=a_{pc}/2 =3.8851(1) Å with A cations (Sr or La) at the corners and octahedrally coordinated Mn (B site) in the center. Differently from the ideal cubic perovskite, the octahedra are slightly rotated and tilted in alternating directions [see black arrows in Fig. 8.1(a) for the tilt], resulting in a periodicity twice as large as the unit cell of the ideal cubic system along ⟨001⟩. Notice that the model of Fig. 8.1 does not include Jahn-Teller distortions that would produce also rotation and tilting of the A-site cations.[300] These are later included in the models presented in Section 8.3.

The side and top views of bulk-truncated LSMO(110) surfaces, of interest in this work, are shown in Figs. 8.1(b, c), respectively. The side view shows that LSMO(110) is polar, having planes of opposite charge ($\pm 8e$ per bulk unit cell assuming fully ionic species) alternating along the [110] direction. The top view highlights the (110) surface unit cell: it is twice as long in the [001] direction as the unit cell of a cubic perovskite, and identified by unit vectors **a** and **b** along [001] and [1$\bar{1}$0], respectively.

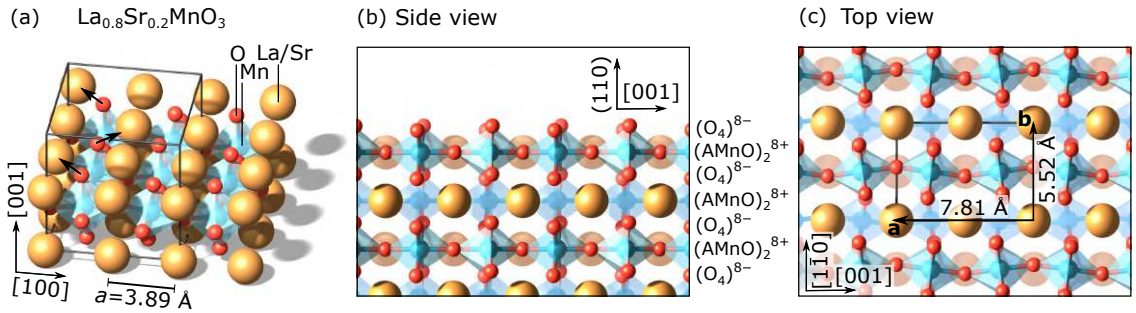

Figure 8.1. Bulk structure of $La_{0.8}Sr_{0.2}MnO_3$. (a) Perspective view of the bulk-truncated (001) orientation. (b, c) Side, and top views of the bulk-truncated (110) orientation. The (110) direction in panel (b) is reported in round brackets because there is no integer index vector perpendicular to (110) planes. Reprinted from ref. 70.

8.2 'High-pressure' surface phase diagram

Figure 8.2 summarizes the surface reconstructions obtained on LSMO(110) films at 'high' pressure, *i.e.*, by systematically depositing sub-monolayer amounts of Mn and La in PLD (RT, 0.2 mbar, 2 Hz, 2.0 J/cm^2, followed by O_2 annealing at 700 °C, 0.2 mbar, for $\geq$ 45 min). They are labeled as 'high-pressure' in virtue of the unusually high value (for UHV-compatible experiments) of the O_2 pressure employed during annealing, 0.2 mbar. As argued in Chapter 10, these preparation conditions bridge the gap between UHV and the conditions used for solid-oxide fuel cells, where LSMO is used as cathode. They are thus suited to investigate how O_2 is split and incorporated at LSMO surfaces under realistic, but controlled, conditions. The reconstructions, as seen in atomically resolved STM (top and middle row), and in the corresponding LEED patterns (bottom row), are displayed as a function of the cation composition [bottom axis; one monolayer, or ML, is defined as the number of Mn sites in an $(AMnO)_2$ plane of LSMO(110), *i.e.*, 4.64×10^{14} at./cm^2]. Section 8.2.6 will explain in detail how this bottom axis has been established. Importantly, the same reconstructions reported in Fig. 8.2 are observed on the surfaces of as-grown LSMO(110) films grown at different O_2 pressures (details in Chapter 9).

Deposition of Mn and La with PLD is the most reliable handle to select a specific surface termination among those shown in the phase diagram, but it is not the only one: As already anticipated, the O_2 background pressure employed during film growth can be used to change the composition of the film, and hence, of the surface (see Chapter 9). Moreover, Ar^+ sputtering (plus O_2 annealing) removes Mn (and O) preferentially over A-site species, and can thus also be used to move towards the left-hand side of the phase diagram. As a rule of thumb, 12 min of sputtering (defocused gun, 1 keV, 9×10^{-6} mbar, roughly 6 μA) roughly equals the deposition of 2 ML of La in PLD. It is likely that the preferential removal of Mn by Ar^+ is, in fact, a consequence of preferential sputtering

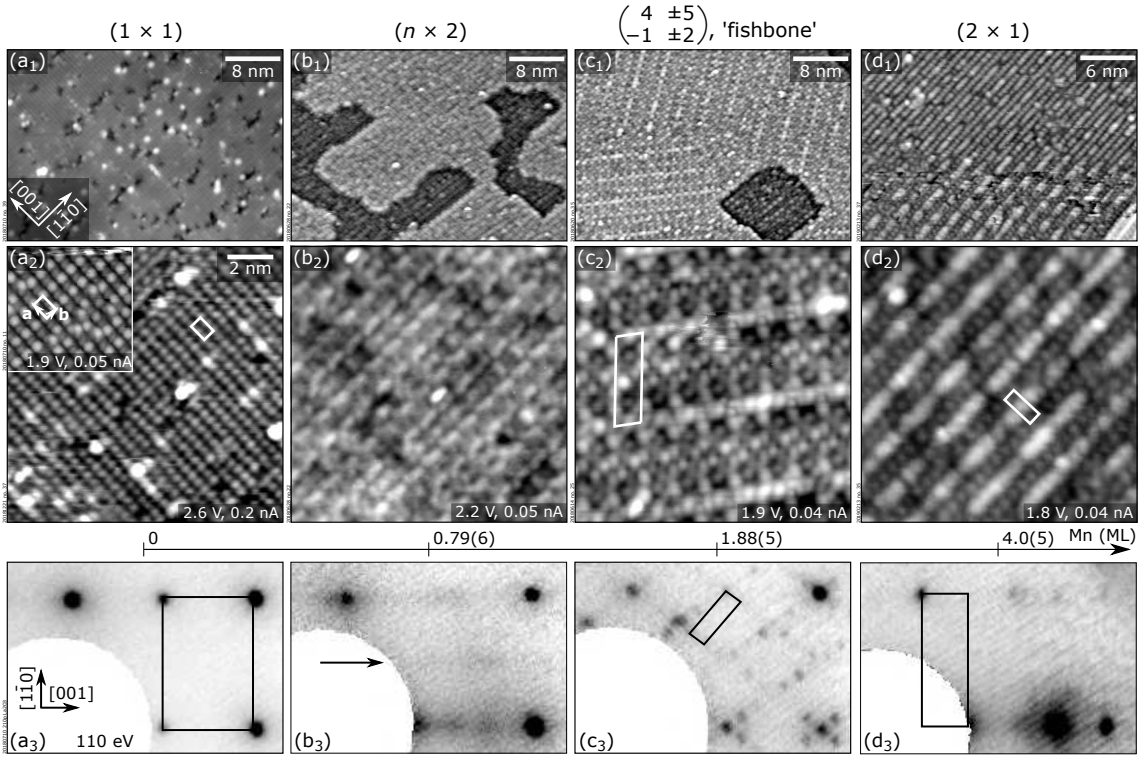

Figure 8.2. 'High-pressure' surface phase diagram of LSMO(110). The stable 'high-pressure' surface reconstructions of LSMO(110) are shown, as they appear in STM (top row, 40 × 27.7 nm^2, middle row, 12 × 12 nm^2), and LEED (bottom row). The reconstructions have been obtained by depositing submonolayer amounts of LaO_x and MnO_x on atomically flat LSMO(110) films, followed by oxygen annealing at 700 °C, 0.2 mbar, 1 h [see bottom axes for exact doses of Mn cations; uncertainties are indicated in parentheses; 1 ML is defined as the number of Mn sites in an $(AMnO)_2$ plane of LSMO(110), *i.e.*, 4.64 × 10^{14} at./cm^2]. They can also be obtained on as-grown films with slightly nonstoichiometric fluxes (Fig. 9.2), while Ar^+ sputtering can be used to shift the reconstructions towards the left-hand side of the phase diagram. The (1 × 1) surface in panel (a_2) and the (2 × 1) surface in panel (d_1) are shown with two characteristic tip terminations. The unit cells are highlighted in the close-up images and in the LEED patterns. Adapted from ref. 70.

of oxygen that is a well-established effect on oxides:[11] Among the undercoordinated cations left-behind, Mn and Sr preferentially re-evaporate over La because of their higher vapor pressure,[301] and Mn is preferentially removed over Sr because of the higher oxygen affinity of Sr.

The following analysis identifies the characteristic building blocks of each structure and discusses their geometric arrangement and periodicity, setting the stage for building the corresponding structural models. The discussion follows transitions from A-site rich towards B-site rich reconstructions, as achieved by depositing Mn in PLD (followed by O_2 annealing). If not specified otherwise, the same qualitative observations hold true when moving in the opposite direction by depositing La (or by Ar^+ sputtering), and the transitions between the reconstructions are reversible.

8.2.1 (1×1)

The (1×1) is the left-most (*i.e.*, most A-site rich) reconstruction of the phase diagram. It reproduces the periodicity of the bulk truncated LSMO(110), *i.e.*, a cell twice as large as the unit cell of $SrTiO_3$(110) along the [001] direction. The (1×1) periodicity is well visible both from the LEED pattern of Fig. 8.2(a_3) and the STM image of Fig. 8.2(a_2), where two common appearances of the surface are shown, as achieved with two distinct (yet unknown) tip terminations. Lines of round features with 25 pm-high corrugation run along the [001] direction. Depending on the tip termination, all features may appear identical (main panel), or every other feature along the [001] direction may appear brighter (inset). The rectangular unit cell [white in Fig. 8.2(a_3), 7.8×5.5 Å^2] is defined by the unit vectors **a** and **b** running along the [001] and the $[1\bar{1}0]$ directions, respectively [see inset of Fig. 8.2(a_3)]. Frequent defects (their amount depending on the preparation conditions) are present. A more thorough description of this surface and its defects, accompanied by its proposed DFT model, is given in the dedicated Section 8.3.

Deposition of Mn causes a phase separation of the surface: Discrete patches of the $(n \times 2)$ superstructure of Fig. 8.2(b_1) form and coexist with the remaining, structurally unchanged (1×1) areas. With more Mn deposited, the $(n \times 2)$ patches become more numerous and grow in size. Depending on the tunneling conditions and on the tip termination, the apparent height of the (1×1) phase may appear as either higher or lower than the $(n \times 2)$, suggesting that the apparent contrast is dominated by electronic effects.

8.2.2 $(n \times 2)$

The $(n \times 2)$ is a poorly ordered structure, characterized by a large number of structural defects. However, a few building blocks can be identified, as seen from Fig. 8.3, where the surface is shown as imaged with two different, yet unknown, tip terminations. Lines of 'boomerang' features (outlined in yellow in Fig. 8.3) run along the $[1\bar{1}0]$ direction. These boomerangs are separated from one another by two lattice units along **b**. This two-fold periodicity along $[1\bar{1}0]$ is visible also in the LEED pattern of Fig. 8.2(b_3) as a faint horizontal line (highlighted by an arrow) midway between integer-order spots. Two boomerangs, mirrored by a $[1\bar{1}0]$ line, enclose two sites marked by circles and '+' symbols in Fig. 8.3. The entities consisting of two boomerangs and the enclosed features as referred to as 'blocks'. Two types of blocks, mirrored by a [001] line, are generally present on the surface (Fig. 8.3 shows only one of them). Adjacent lines of blocks are separated by $n = 2, 3$,or 5 lattice units along **a**, and can be stacked in phase (*i.e.*, with no shift along $[1\bar{1}0]$), or can be shifted by one **b** lattice vector. 'Linker' structures connecting adjacent lines correspondingly appear aligned along [001], or as a zig-zag line,

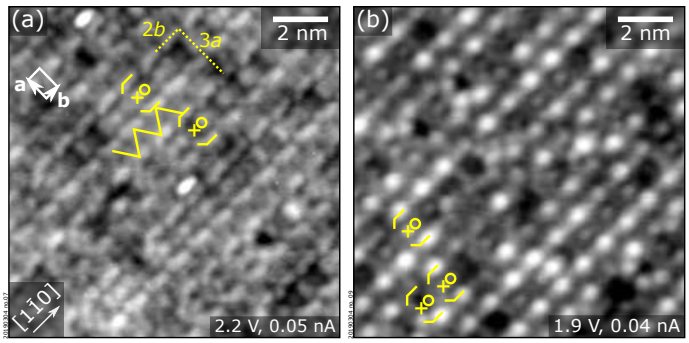

Figure 8.3. $(n \times 2)$ reconstruction of LSMO(110). (a, b) 12×12 nm^2 STM images obtained with two distinct, yet unknown tip terminations. See text for details.

as outlined in Fig. 8.3(a). The large variety of possible combinations within the $(n \times 2)$ (internal structure of blocks, spacing among adjacent lines in both in-plane directions) is the cause for the poor order of the structure. This is also reflected in the LEED pattern of Fig. 8.2(b_3), which shows an increased intensity along the [001] direction in between integer-order spots rather than well-defined maxima. As a consequence, a single well-defined unit cell cannot be identified.

The $(n \times 2)$ reconstruction can only be prepared in monophase form when La is deposited starting from the 'fishbone' reconstruction of Fig. 8.2(c). When depositing Mn from the (1×1), small, discrete patches of $(n \times 2)$ initially form that coexist with the remaining (1×1) areas, but, upon further deposition, they do not grow big enough to fill the whole surface: They soon transform into the fishbone reconstruction described below, such that (1×1) and fishbone areas coexist. This hysteretic behavior suggests that the $(n \times 2)$ reconstruction may be a metastable phase.

8.2.3 'Fishbone'

More details about the so-called 'fishbone' reconstruction of Fig. 8.2(c) are reported in Fig. 8.4. The large scale STM image in Fig. 8.4(a) reveals the presence of two domains that are mirror-symmetric with respect to the [1$\bar{1}$0] direction. Their size depends on the preparation conditions (longer annealing treatments yield larger domains). Their size, of a few tens of nanometers observed in the STM image reported here, is representative of most of the obtained fishbone-reconstructed surfaces. It was achieved by Ar^+ sputtering an as-grown LSMO film for 6 min (1 keV, 9×10^{-6} mbar), followed by deposition of 1.9 ML Mn in PLD and annealing at 700 °C and 0.2 mbar O_2 for 45 min. The two domains contribute to the complex Fast Fourier transform (FFT) and LEED pattern of Figs. 8.4(b, c). The simulated LEED pattern[302] overlaid to the experimental one in Fig. 8.4(c) allows one to derive the exact periodicity of the structure. It can be expressed in matrix notation

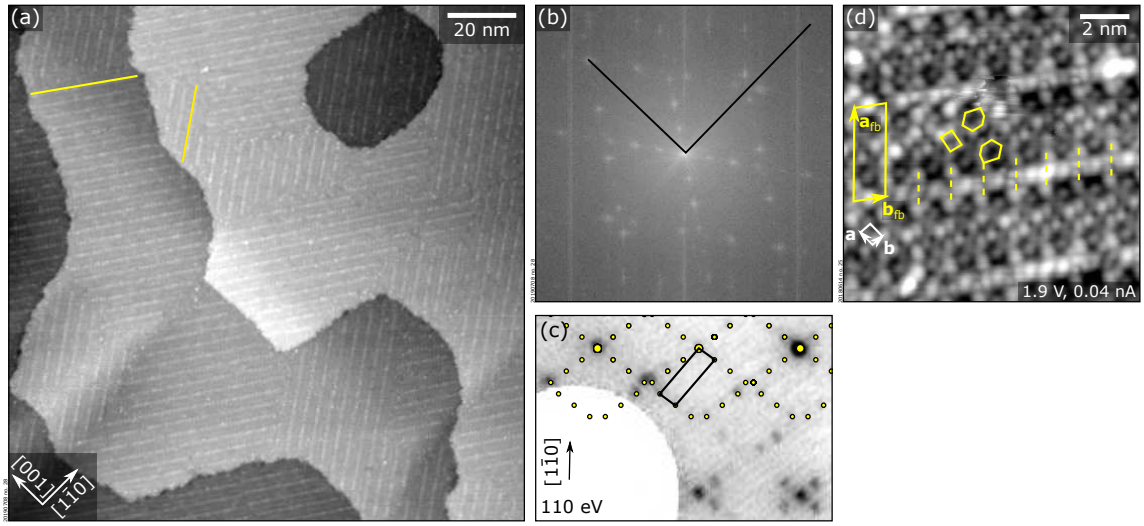

Figure 8.4. 'Fishbone' reconstruction of LSMO(110). (a) 150 × 150 nm^2 STM image. Two domains are visible and indicated by the yellow lines. (b) Corresponding Fourier transform [black lines indicate the unit cell of the (1 × 1)]. (c) Representative LEED pattern on which the simulated LEED pattern is overlaid. (d) 12 × 12 nm^2 STM image of one of the two fishbone domains. The characteristic features of the reconstruction and its unit cell are indicated in yellow (see main text for reference). The unit cell of the (1 × 1) reconstruction is indicated by the white rectangle.

as

$$\begin{pmatrix} \mathbf{a}_{\mathrm{fb}} \\ \mathbf{b}_{\mathrm{fb}} \end{pmatrix} = \begin{pmatrix} 4 & \pm 5 \\ -1 & \pm 2 \end{pmatrix} \begin{pmatrix} \mathbf{a} \\ \mathbf{b} \end{pmatrix},$$

where the vectors **a**, **b**, and $\mathbf{a}_{\mathrm{fb}}$, $\mathbf{b}_{\mathrm{fb}}$ identify the unit cell of the (1 × 1), and of the of the 13-times bigger unit cell of the fishbone, respectively [see close-up STM images in Fig. 8.4(d)]. Because the angle between $\mathbf{a}_{\mathrm{fb}}$ and $\mathbf{b}_{\mathrm{fb}}$ is different than the one between **a** and **b**, it is not possible to express this periodicity in Wood's notation. The different signs in the matrix correspond to the two mirror-symmetric domains.

Figure 8.4(d) shows the detail of one domain. Bright rows parallel to $\mathbf{b}_{\mathrm{fb}}$ are visible, interrupted by short lines parallel to $\mathbf{a}_{\mathrm{fb}}$ (dashed yellow lines). Between two adjacent $\mathbf{b}_{\mathrm{fb}}$ rows run two sets of six-membered rings (highlighted in yellow). These sets are shifted with respect to each other by $\mathbf{b}_{\mathrm{fb}}/2$ along the bright row, and rotated by 180°. One of the vertices of each ring coincides with the endpoint of the short lines parallel to $\mathbf{a}_{\mathrm{fb}}$. The closest four vertices of two neighboring rings arrange in a rectangle (also highlighted in yellow) that has the same shape and dimensions of a (1 × 1) unit cell, albeit rotated by ≈10°.

Transition between 'fishbone' and (2 × 1)

Figure 8.5 illustrates the transition between the fishbone and the (2 × 1) structure. The transition is continuous and without any phase separation, exposing different recon-

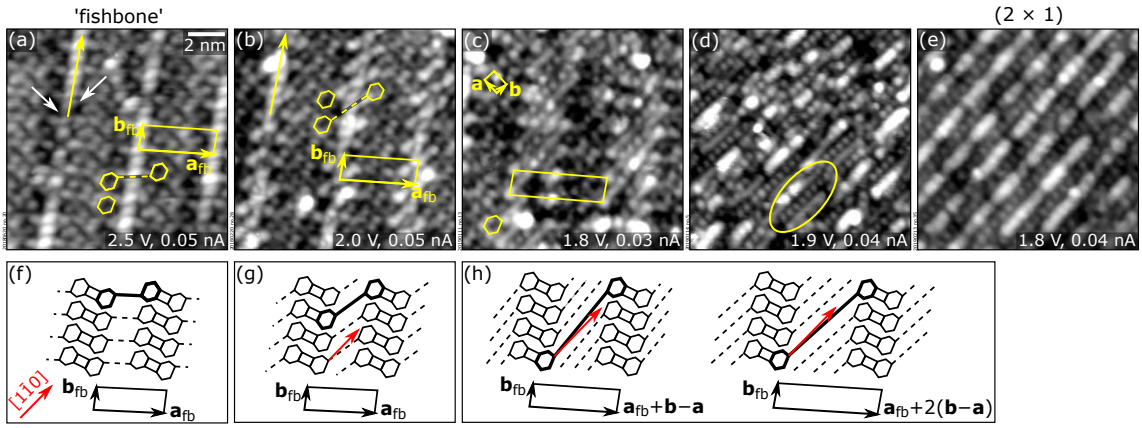

Figure 8.5. Transition from the 'fishbone' to the (2 × 1) surface reconstruction of LSMO(110). (a–e) 12 × 12 nm^2 STM images revealing a continuous transition between the 'fishbone' and the (2 × 1) reconstructions with increasing Mn concentration. (f–h) Sketches of the main structural changes during the transition from panel (a) to panel (c). Red arrows in (g, h) are oriented along [1$\bar{1}$0]. The tilt of the connecting short lines in panel (g) with respect to the [1$\bar{1}$0] direction is ≈10°. By depositing more Mn, the superstructure periodicities change from $\mathbf{a}_{fb}$ = 4**a** ± 5**b** [panels (f, g)] to $\mathbf{a}_{fb}$ + n(**b** ± **a**) with $n = 1$ at moderate Mn doses, and $n = 2$ at larger deposited amounts (the two signs correspond to the two mirror-symmetric domains). The periodicities in the sketches of panel (h) are indicated. The tilts of the connecting short lines in panel (h) with respect to the [1$\bar{1}$0] direction is are ≈4.5° and ≈4° for $n = 1, 2$, respectively. Reprinted from ref. 70.

structions with common structural building blocks. In Fig. 8.5, STM images of the structures (top row) are accompanied by corresponding sketches (bottom row).

For small Mn doses [Figs. 8.5(b, g)], minor changes are observed in the initial fishbone structure of Figs. 8.5(a, f). The structure has the same shape and size of the unit cell, and retains the main features of the fishbone, *i.e.*, bright ridges (yellow arrows '$\mathbf{b}_{fb}$') and rows of rings coupled by rectangles along $\mathbf{b}_{fb}$. The only difference is how the rings are connected with each other across the bright ridges. In the structure of Fig. 8.5(b), two additional features are introduced at the positions indicated by the white arrows in Fig. 8.5(a). This causes an apparent rotation towards [1$\bar{1}$0] of the 'connection lines' (dashed) between the rings, now connecting next-nearest-neighbors rather than nearest-neighbors [compare the sketches in Figs. 8.5(f, g)].

Further deposition of Mn [see Figs. 8.5(c, h)] increases the spatial periodicity of the superstructure and produces longer connecting lines (now appearing as either continuous or dotted) that again rotate towards the [1$\bar{1}$0] direction [see sketches in Fig. 8.5(h) and caption]. Two structures with different periodicities, shown in the sketches of Fig. 8.5(h), tend to coexist at the surface, the one with larger periodicity being predominant on Mn-richer surfaces. As a result of the many possible shifts required to create the two coexisting superstructures, the surface appears increasingly disordered in this regime as the Mn dose increases. Eventually the rings disappear [see Fig. 8.5(d)], and the connecting lines locally appear as alternating dotted and continuous lines [oval in Fig. 8.5(d)], parallel to,

or slightly rotated, with respect to [1$\bar{1}$0]. Finally, small, bright features appear on top of the continuous line, which grow longer with more Mn deposited, until the (2 × 1) surface of Fig. 8.5(e) is formed. Notice that because the structures of Fig. 8.5 tend to coexist at the surface rather than forming monophase samples, determining the corresponding Mn coverages is not trivial.

8.2.4 (2 × 1)

The periodicity of the (2 × 1) surface is seen in LEED [Fig. 8.2(d_3)], and in STM images acquired at high biases [above +2 V, see Fig. 8.2(d_2)]. The structure consists of dotted lines with alternating apparent height, all oriented along the [1$\bar{1}$0] direction. The brighter lines (larger apparent height) appear fragmented, and their maxima are shifted by **b**/2 with respect to the maxima of the darker lines. Notice that at low bias voltages the surface commonly appears as in the top part of the STM image of Fig. 8.2(d_1), where both lines show similar apparent height—a tip change made the bottom part of Fig. 8.2(d_1) appear as in Fig. 8.2(d_2). This suggests that the difference in apparent height observed at high bias voltages has significant electronic contributions.

Further deposition of Mn starting from the (2 × 1) results in other structures not included in the phase diagram of Fig. 8.2 [see Fig. 8.6(b) below]. It is worth mentioning the challenges in preparing a monophase sample with the (2 × 1) reconstruction: At times, only limited patches of the surface reconstruction described in Fig. 8.6(b) were observed before realizing the monophase (2 × 1). This difficulty is possibly due to kinetic limitations at the conditions used during post-deposition annealing.

8.2.5 Beyond the high-pressure surface phase diagram

Figure 8.6 shows LSMO(110) surfaces that are La- and Mn-richer [panels (a) and (b), respectively] than those reported in the phase diagram of Fig. 8.2. Deposition of La on the (1 × 1) surface [Fig. 8.2(a)] induces the formation of [1$\bar{1}$0]-oriented chains of white protrusions with a typical periodicity of 2**b**, appearing white in the STM images of Fig. 8.6(a_1, a_2). Depending on the tunneling conditions and/or the tip termination, the chains can be also imaged as depressions (not shown). The (1 × 1) structure is otherwise preserved. Because the A-site signal in XPS and LEIS is higher than on the (1 × 1) (not shown), it is reasonable to assume that the bright protrusions correspond to LaO_x complexes. Such features can be obtained also with sufficiently long Ar^+ sputtering starting from any of the structures shown in Fig. 8.2 (the Mn-richer the structure, the longer the sputtering time required).

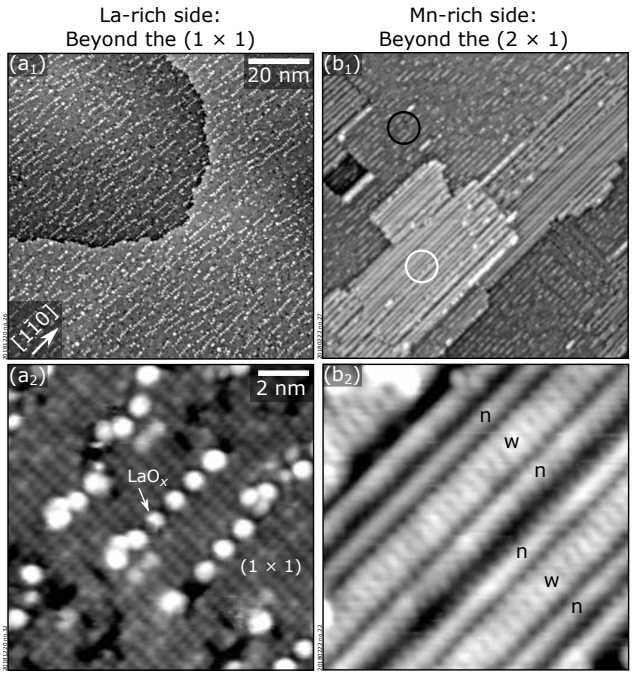

Figure 8.6. La-rich and Mn-rich surface structures beyond the phase diagram of Fig. 8.2. (a_1, a_2) 100 × 100 nm^2 and 12 × 12 nm^2 STM images (V_t = 2 V, I_t = 0.2 nA) of a surface of LSMO(110) La-richer than the (1 × 1). The periodicity of the (1 × 1) surface is largely preserved, but additional bright features aligned along the [1$\bar{1}$0] direction appear. (b_1, b_2) STM images—same sizes and similar tunneling parameters as those shown in panels (a_1, a_2)—of surfaces Mn-richer than the (2 × 1). While the majority of the surface (black circle) retains the (2 × 1) reconstruction, some patches (white circle) form bright lines as in the 12 × 12 nm^2 STM image of panel (b_2). Reprinted from ref. 70.

Figure 8.6(b) reports instead the typical morphology observed upon deposition of Mn on the (2 × 1) surface of Fig. 8.6(d). The majority of the surface preserves the (2 × 1) appearance [black circle in Fig. 8.6(b_1)], but patches of a new structure are formed [white circle in Fig. 8.6(b_1), close-up image in Fig. 8.6(b_2)]. The new (m × 1) structure consists of bright lines of different width and separation, all oriented along the [1$\bar{1}$0] direction. For small doses of Mn, narrow lines such as those labeled by 'n' in Fig. 8.6(b_2) form and patch together. As the Mn dose increases, also wider lines ['w' in Fig. 8.6(b_2)] are formed, which tend to be sandwiched by the narrow lines in a narrow–wide–narrow arrangement. As the amount of Mn increases further, this reconstruction covers an increasingly larger fraction of surface, at the expense of the (2 × 1) areas. However, a monophase sample with this (m × 1) superstructure was never observed, likely because deposited Mn species stick less on Mn-richer surfaces, as is elucidated in the next Section.

8.2.6 Relative compositions

As one moves along the phase diagram (deposition of Mn or La plus O_2 annealing), the reconstructions appear increasingly Mn-richer from the left- to the right-hand side of

Fig. 8.2, both from LEIS [Figs. 8.7(a, b)] and from analysis of the intensity of XPS core-level peaks [Fig. 8.7(c)]. Thanks to the sufficiently large compositional differences, both techniques allow to identify any given surface reconstruction. On the other hand, the La 4*d*/Sr 3*d* XPS intensity ratios are identical (within the error bars) for all the phases of Fig. 8.2, and no apparent trend in the La-to-Sr ratio is visible from the available LEIS spectra.

In LEIS, the Mn-to-A-site area ratios on the (1 × 1) and the (2 × 1) differ by more than one order of magnitude, while the changes in the XPS signal are less dramatic [Fig. 8.7(b, c)]. This indicates that the Mn-rich surfaces have their Mn mainly in their top-most layers, while the layers below (still within the escape depth of the XPS) are closer to an $AMnO_3$ stoichiometry. This notion is supported by prolonged LEIS acquisition. Figure 8.7(b) compares two sets of consecutive acquisitions on each reconstruction (each acquisition corresponds to the average of 20 consecutive spectra; full and empty circles correspond to the first and second acquisition, respectively). The Mn signal decreases over time on the fishbone and on the (2 × 1) structures. This is because He^+ ions cause a mild sputtering/scrambling of the surface just like Ar^+ ions, preferentially removing/scrambling the abundant surface Mn species. In contrast, the Mn signal of the (1 × 1) surface increases over time, possibly because Mn species are less abundant at the top surface layer (if at all present), and Mn species in the subsurface are made accessible with longer LEIS acquisition as a result of the mild sputtering/scrambling. This behavior suggests that the (1 × 1) belongs to another family with respect to the other structures of the phase diagram of Fig. 8.2.

Calibration of the Mn doses and surface-dependent re-evaporation

This Section addresses how the horizontal axis of Fig. 8.2 and Figs. 8.7(b, c), *i.e.*, the relative compositions of the surface structures in terms of Mn cations, have been established. The first step was to evaluate the number of laser pulses shot on the MnO target required to move between adjacent reconstructions, accounting for re-evaporation effects that affect the effective amount of material deposited. The second step was to translate these amounts into cation monolayers by means of the movable QCM (refer to Section 2.5).

During the first step, pronounced differences in the incorporation of the deposited species were observed among the different surface phases, similarly as for $SrTiO_3(110)$ (cf. Chapter 6). These must be taken into account to determine the effective amount of material needed to switch between the reconstructions. Figure 8.8(a) shows the XPS intensity ratio of Mn 2*p*/La 4*d* corresponding to well-defined LSMO(110) surfaces that were produced by depositing incremental amounts of Mn at 0.2 mbar O_2 at RT followed by O_2 annealing at 700 °C, starting from the (1 × 1) surface of Fig. 8.2(a). The intensity

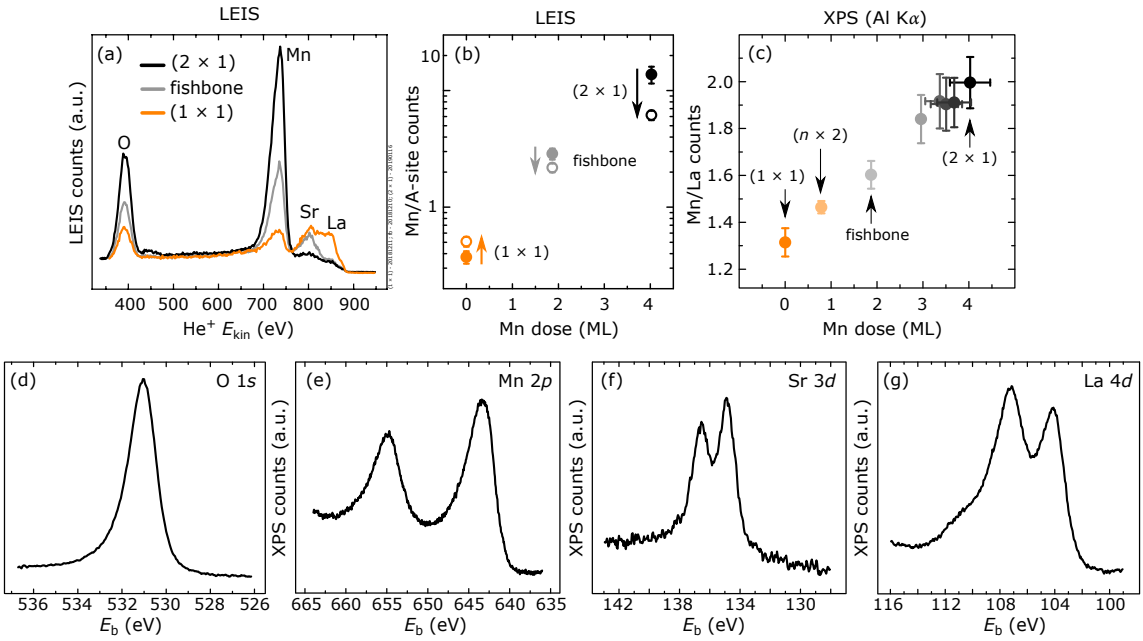

Figure 8.7. Relative composition of the LSMO(110) 'high-pressure' reconstructions. (a) LEIS spectra of the (1 × 1) (orange), fishbone (grey), and (2 × 1) (black) structures (each LEIS spectrum corresponds to the average of 20 consecutive scans with a total acquisition time of 10 min). (b) Mn-to-A-site area ratios from LEIS. Peak intensities were evaluated after subtraction of linear backgrounds. The area ratios obtained from the measured peak intensities do not include corrections due to different scattering cross sections or neutralization probabilities. Full circles: values extracted from spectra in (a); Empty circles: subsequent acquisition. (c) Mn-to-La area ratios from XPS. (d–g) Reference core-level XPS spectra, acquired on a fishbone-reconstructed surface (normal emission, 10 eV pass energy). Adapted from ref. 70.

ratios are plotted as a function of the number of laser pulses shot on the MnO target. The intensities increase linearly for small amounts deposited, in agreement with the expected enrichment in Mn of the surface, but above a critical Mn enrichment (dashed line), their slope with the deposited pulses decreases drastically. The critical point corresponds to a surface with a structure between those shown in Fig. 8.5(b) and Fig. 8.5(c), *i.e.*, slightly Mn richer than the fishbone reconstruction. Correspondingly, after overcoming this critical composition, a large number of pulses is required to detect appreciable changes in the surface structure in STM. XPS measurements reveal that the observed change in slope is obtained after the post-annealing step: Right after RT deposition, the Mn/La signal increases linearly, as expected (not shown); the signal decreases after annealing at 0.2 mbar O_2 and 700 °C for 1 h.

A similar behavior is observed also during the deposition of La. Figure 8.8(b) shows the La 4*d*/Mn 2*p* XPS intensity ratios as a function of the number of laser pulses shot on the La_2O_3 target (again, deposition at RT in 0.2 mbar O_2 and 700 °C post-annealing in 0.2 mbar O_2). For this set of experiments, the starting point was the Mn-rich structure of Fig. 8.5(c). The surface becomes increasingly La-richer the more La is deposited. Also in this case the initially linear trend suddenly changes slope after a critical stoichiometry

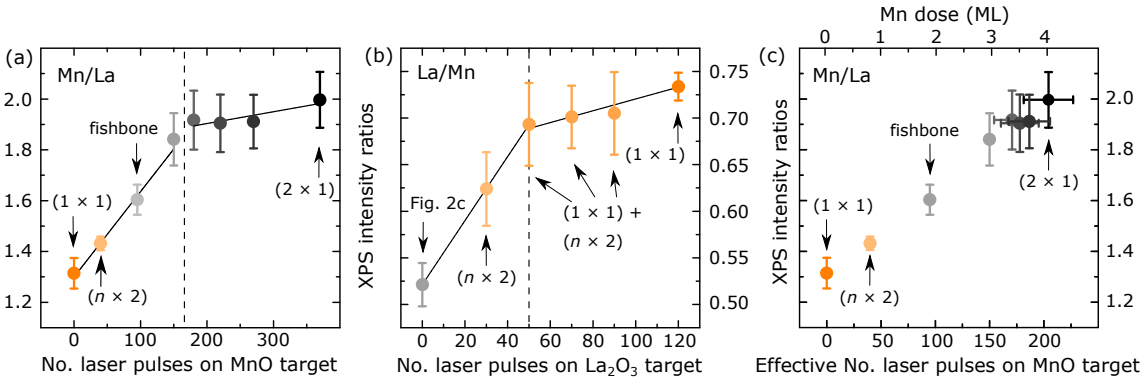

Figure 8.8. Surface-dependent sticking of Mn and La species on LSMO(110). (a, b) Mn 3*d*/La 4*d* and La 4*d*/Mn 3*d* XPS peak intensity ratios as a function of the laser pulses shot on the MnO and La_2O_3 targets, to enrich well-defined LSMO(110) surfaces in Mn and La, respectively. The XPS intensities are not linear with the amount of deposited material: Mn (La) species stick less on Mn- (La-) rich surfaces. (c) Mn 3*d*/La 4*d* intensity ratios as a function of the 'effective' laser pulses shot on the MnO target, derived from the data in panel (a) by correcting for the slope differences in the two regimes. The horizontal error bars on the last four points in (c) are due to this correction. Reprinted from ref. 70.

is reached (dashed line). This corresponds to a surface structure between the $(n \times 2)$ and the (1×1).

The data in Figs. 8.8(a, b) show that, on well-defined LSMO(110) surfaces, Mn (La) species tend to be incorporated less easily in surfaces that are richer in Mn (La), as if there was a large barrier to incorporate additional cationic species when the composition of the surface is brought towards the extremes of the surface phase diagram. Similar trends have been observed previously on $SrTiO_3(110)$, where it was shown they occur because of surface-dependent sticking (see Chapter 6). One can exclude that the changes in the XPS slopes are associated with the formation of 3D structures, as judged from large-area STM (images not shown). One can also rule out that the change of slope is due to the development of a second layer, as this occurs at Mn doses well above 1 ML. The XPS data acquired right after RT deposition and after post-annealing suggest that that cation re-evaporation is the dominant mechanism driving this effect.

The 'effective' number of pulses needed to switch between adjacent reconstructions (accounting for the re-evaporated material during the annealing step) has been derived by scaling the number of laser pulses with the slopes of the XPS intensity ratios (obtained from linear fits to the data). The outcome is shown in Fig. 8.8(c), which reports the horizontal axis both, in terms of the effective number of laser pulses shot on the MnO target (bottom), and in terms of ML of Mn (top). The translation to ML of Mn has been performed by using the amount of Mn deposited per pulse derived with the movable QCM, as discussed below. This quantity amounts to $(1.97 \pm 0.03) \times 10^{-2}$ ML, and the translation was performed under the assumption of that sticking on the QCM is the same as on LSMO(110) surfaces with a surface composition between (1×1) and fishbone, and

considering the MnO_2 composition of the film deposited (see below).

Express Mn doses in ML

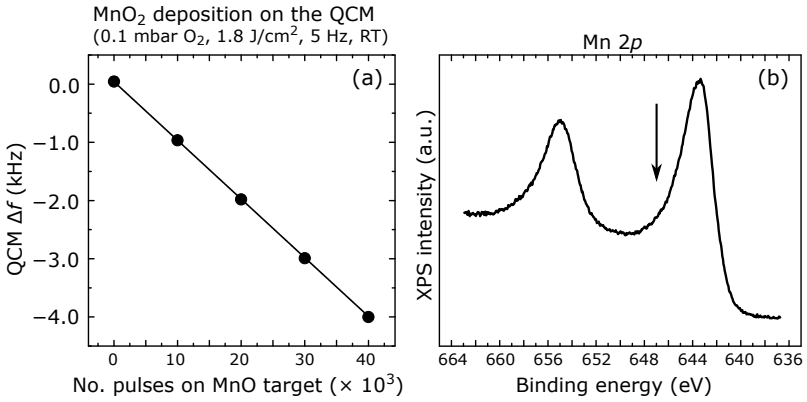

Figure 8.9. (a) Shifts in the QCM resonance frequency as a function of the amount of MnO_2 deposited (number of laser pulses shot on the MnO target). (b) Corresponding Mn 2*p* peak. Adapted from ref. 70.

The amount of Mn cations (in ML) needed to switch between the reconstructions starting from the known number of effective laser pulses shot on the MnO target were established with the home-designed QCM device described in Section 2.5. Thick MnO_x films were incrementally grown at the same conditions employed for the growth on LSMO(110), and measured the QCM resonance frequency at each step. The results are shown in Fig. 8.9. From a linear fit of the data, one derives a rate of change of the resonance frequency of -0.1062 ± 0.0007 Hz/pulse. This corresponds to a mass growth rate $\Delta m/A = 1.32 \pm 0.02$ ng/(cm^2 pulse).

Since manganese oxide can exhibit a variety of oxide species (MnO, Mn_2O_3, Mn_3O_4, or MnO_2) depending on the growth conditions, XPS was used to determine the composition of the films grown on the movable QCM at the employed conditions. As shown below, the composition is MnO_2. By accounting for the 1:2 Mn:O stoichiometry and the known atomic masses of O and Mn, one can then derive a deposition rate of Mn of $(9.16 \pm 0.15)\ 10^{12}$ Mn at./(cm^2 pulse), or $(1.97 \pm 0.03) \times 10^{-2}$ ML_{Mn}/pulse [recall that 1 ML is defined as the number of Mn sites in an $(AMnO)_2$ plane of LSMO(110), *i.e.*, 4.64×10^{14} at./cm^2].

The composition of the manganese oxide film deposited on the QCM at the employed growth conditions was determined based on the abundant XPS literature on manganese oxides.[303–308,310–314] The shape and the relative positions of several relevant peaks are uniquely associated with a specific compound. MnO is most easily distinguishable, since it displays a characteristic shake up peak in its Mn 2*p* spectrum.[311,313] Since this satellite is not present in the spectra of Fig. 8.9(b) (the position of the missing satellite is indicated

Table 8.1. Selected XPS data for different manganese oxides. The Mn 3*s* splitting, relative position of Mn2$p_{3/2}$ and O 1*s*, and Mn($2p_{3/2}$, $L_3M_{23}M_{45}$) Auger parameter of several manganese oxide compounds extracted from the literature are compared with values from films grown on the QCM in the present work (rightmost column). Values are expressed in electronvolts.

	MnO	Mn_3O_4	Mn_2O_3	MnO_2	Experiment[a]
Mn 3*s* splitting	–	–	5.4[303]	4.4[304]	4.55±0.22
	–	–	–	4.6[305],4.7[306]	
	5.8[307]	5.2[307]	5.3[307]	4.7[307]	
	6.1[308]	–	5.5[308]	4.5[308]	
	5.9[309]	4.6[309]	5.2[309]	4.5[309]	
	5.6[310]	5.6[310]	5.4[310]	4.5[310]	
	6.1[311]	5.3[311]	5.4[311]	4.5[311]	
	6.05[312]	–	5.5[312]	4.58[312]	
O 1*s* – Mn $2p_{1/2}$	–	–	111.8[303]	112.8[304]	112.25±0.05
	–	–	–	112.5[305]	
	–	111.8[307]	111.8[307]	112.6[307]	
	110.9[310]	111.1[310]	111.4[310]	112.4[310]	
	–	111.34[313]	111.93[313]	112.36[313]	
	–	111.6[314]	–	112.2[314]	
Auger param.[b]	–	–	1226.91[303]	1227.21[304]	1227.24±0.08
	–	–	–	1228.1[305]	
	1223.8[310]	1224.4[310]	1224.6[310]	1225.5[310]	
	1225.6[314]	1224.8[314]	1226.6[314]	1227.3[314]	

[a]Peak positions were obtained with CasaXPS by fitting Gaussian-Lorentzian [GL(30)] line shapes to Mn 3*s*, O 1*s*, and Mn $L_3M_{23}M_{45}$ spectra; an asymmetric line shape [LA(1.9, 3.2, 60)] was used for Mn $2p_{3/2}$. A Shirley-type background was used in all cases. Errors on the peak positions were derived by the automated Monte Carlo procedure available in CASAXPS, combined by linear error propagation, and scaled by a factor of 2 to represent 95% confidence intervals. [b]Mn($2p_{3/2}$, $L_3M_{23}M_{45}$) = E_B(Mn $2p_{3/2}$) + E_{kin}(Mn $L_3M_{23}M_{45}$), where E_B and E_{kin} correspond to binding and kinetic electron energies, respectively, when using an Al Kα source.

by an arrow), one can exclude MnO as the dominant composition of the film. It is less straightforward to discern between Mn_3O_4, Mn_2O_3, and MnO_2 based on the shape of their peaks is less straightforward, as it hinges on a very accurate fitting of the data, ideally acquired with a monochromatic source.[313] For this reason, the relative positions of Mn $2p_{3/2}$ and O 1*s*, the final-state splitting of Mn 3*s*, and the Mn($2p_{3/2}$, $L_3M_{23}M_{45}$) Auger parameter[310] were chosen as indicators. Table 8.1 summarizes the values extracted from several literature sources. Comparison with the XPS data obtained here (rightmost column in Table 8.1) suggests that the composition of the film deposited on the QCM is largely MnO_2.

8.2.7 Electronic diversity

To gain insights into the electronic properties of the surface phases of LSMO(110), the distance between Mn $2p_{3/2}$ and O 1*s* core level positions and the Mn($2p_{3/2}$, $L_3M_{23}M_{45}$) Auger parameter were evaluated as a function of the surface composition. These two quantities, shown in Figs. 8.10(a, b), respectively, yield information about the oxidation state of Mn species at the surface, and about the character of the metal–oxygen bonding among the different surface phases of Fig. 8.2. Most commonly, the oxidation state of Mn in Mn-containing compounds is determined based on the shape of a few relevant peaks. This was not possible in the present work, due to (i) the overlap of the Mn 3*s* with Al K$\alpha_{3,4}$s-induced La 4*d* satellites, (ii) the rather large full-width at half-maximum of the Mn 2*p* peaks [see Fig. 8.7(e)], and (iii) the low surface sensitivity due to the normal-

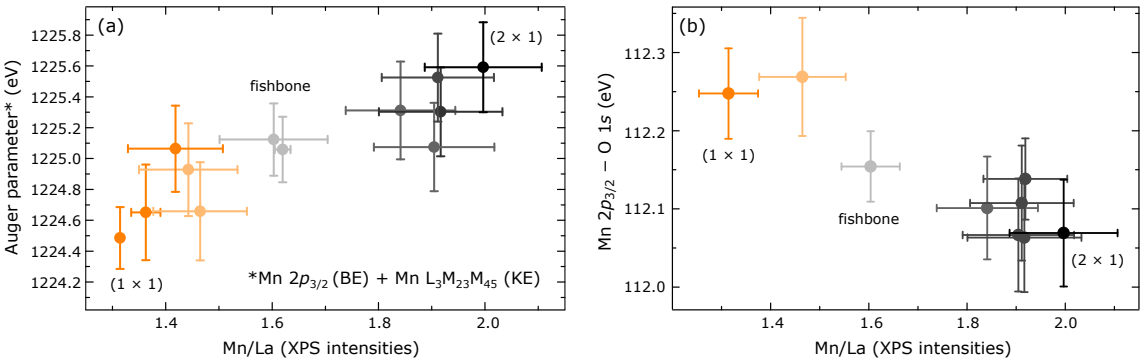

Figure 8.10. XPS characterization of the reconstructions of LSMO(110). (a) Mn($2p_{3/2}$, $L_3M_{23}M_{45}$) Auger parameters of the different surface phases of LSMO(110). A trend is visible in the Auger parameters upon increasing the Mn content of the surface, consistent with the increasingly covalent character of the surface. (b) (Mn $2p_{3/2}$ – O 1*s*) core-level shifts as a function of the surface stoichiometry. The intensities and positions of the Al-Kα-excited XPS peaks were evaluated with CasaXPS after subtraction of a Shirley-type background. For the evaluation of core-level shifts and Auger parameters, peak positions were obtained by fitting Gaussian-Lorentzian [GL(30)] line shapes to Mn 3*s*, O 1*s*, and Mn $L_3M_{23}M_{45}$ spectra; an asymmetric line shape [LA(1.9, 3.2, 60)] was used for Mn $2p_{3/2}$. Errors in the peak positions were derived by the automated Monte Carlo procedure available in CasaXPS, combined by linear error propagation, and multiplied by a factor of 2 to represent 95% confidence intervals. Reprinted from ref. 70.

emission configuration (grazing exit was precluded by geometrical constraints of the apparatus). Instead, the distance between Mn $2p_{3/2}$ and O $1s$ peaks was used for this purpose. Since this quantity does not depend on band shifts with respect to the Fermi level,[315] it is a good metric to gain information about the Mn oxidation state. The values for reference manganese oxide compounds in Table 8.1 show a clear decreasing trend of the distance between Mn $2p_{3/2}$ and O $1s$ peaks with decreasing Mn oxidation state (*i.e.*, increasing Mn content in the reference compound). A consistent trend is visible in Fig. 8.10(a), suggesting that Mn-richer surface phases in LSMO(110) are associated to lower Mn oxidation states. However, because the XPS signals are dominated by bulk contributions (normal emission setup, inelastic mean free path of ≈2 nm), the shifts measured are much smaller than the those that would originate from the surface layers alone, and one cannot pinpoint absolute values of the oxidation state of Mn atoms at the surface. The fact that a difference is observed at all is a strong indication that the different reconstructions are characterized by different Mn oxidation states. Notice that the absolute value of the shifts in Fig. 8.10(a) would indicate the oxidation state expected for bulk LSMO, *i.e.*, between 3+ and 4+ (cf. Table 8.1), consistent with the fact that the XPS signals are dominated by bulk contributions.

The Mn($2p_{3/2}$, $L_3M_{23}M_{45}$) Auger parameter in Fig. 8.10(b) shows an approximately linear trend with increasing Mn enrichment at the surface. As already discussed in Chapter 5, Auger parameters are calculated as the sum of the energy positions of a core level peak (expressed in binding energy) and an Auger peak (expressed in kinetic energy), and they effectively describe the extent to which photo-induced core holes are screened by ligands (O) surrounding the ionized atom (Mn) and by conduction-band electrons (resulting from the ionization of cations).[212] Effective screening is typically achieved in small-bandgap materials, where a large number of delocalized electrons is available to participate, and/or when the metal–oxygen bonds have strong covalent character. Hence, the data in Fig. 8.10(b) suggest that the different phases of LSMO(110) are characterized by increasingly covalent Mn–O bonds and/or decreasing bandgaps as a function of the Mn enrichment. For completeness, the Auger parameters of oxygen [O(1_s, $KL_{23}L_{23}$)] and La [La($3d_{5/2}$, MNN)] were also determined (not shown). These Auger parameters do not substantially change with the Mn content at the surface. The absence of a trend in the oxygen Auger parameter is at odds with the correlation between metal and oxygen Auger parameters observed for other oxide compounds.[316]

8.2.8 Discussion

Structural, electronic, and compositional diversity

The experimental data presented here on the reconstructions of LSMO(110) testify to their remarkable structural and electronic variety as a function of the surface composition. Importantly, each reconstruction can be uniquely identified by its appearance in STM, by its Mn-to-A-site content (as determined with XPS or LEIS), and by the corresponding value of the Auger parameter. This level of control over the single surface phases sets the stage to isolate a few critical factors that are known/expected to affect the surface reactivity of LSMO to specific reactions, namely its composition,[317] the surface atomic structure (through the surface coordination chemistry),[71] the Mn oxidation state,[284] and the ionicity of the metal–oxygen bonds. Notably, because the presented phases are stable at realistic operation conditions of solid-oxide fuel cells (notwithstanding UHV compatibility), they are an ideal test bed to address the oxygen incorporation driving these devices, as discussed in Chapter 10.

While presenting the appearance of the surface structures in STM, the building blocks of each structure and their geometric arrangements have been identified and discussed. Among the presented phases, the A-site rich (1×1) [Fig. 8.2(a)] is a particularly promising and appealing candidate for *ab-initio* methods. Section 8.3 will delve into the details of this structure, and illustrate a proposed DFT model. Note that the A-site richness of the (1×1) is consistent with the trend of the Mn Auger parameter as a function of the surface composition [Fig. 8.10(b)]. The comparatively small value measured on the (1×1) speaks for an ionic character, which is expected for a surface dominated by AO_x bonds. Consistently, the Mn-richer structures are characterized by an increasingly more covalent bonding environment.

Increasing the Mn content of the surface moves the surface reconstructions beyond the (1×1) phase, and more complex structures with larger unit cells are encountered. Figure 8.5 reveals that one can move between these Mn-rich reconstructions via a smooth transition in which common building blocks are retained, and whose relative arrangement changes as a function of the Mn content. Identifying these building blocks is the first step to build quantitative structural models: the identification of structural units and their relative arrangement has been crucial to solve many of the surface reconstructions forming on (001)-, (110)-, and (111)-oriented $SrTiO_3$ and related perovskite oxides.[318] Similarly to these systems, also the Mn-rich reconstructions of LSMO possibly consist of variously arranged tetrahedra and octahedra. Notice that other multi-element oxides (mostly ternary) besides LSMO(110) were shown to display numerous and complex surface reconstructions depending on the cation and/or oxygen stoichiome-

try.[64,223,224,228,231,319] This suggests that the rich structural variety shown by the LSMO(110) surface may be the rule rather than the exception among multielement oxides.

The XPS data in Fig. 8.10 show that the structural diversity witnessed among the surface phases of LSMO(110) is accompanied by similar variety in their electronic properties. The trend in the difference of Mn $2p_{3/2}$ and O $1s$ peaks [Fig. 8.10(a)] suggests that Mn-richer structures are associated to lower oxidation states of Mn. The fact that these differences are present does not surprise: The oxidation state of Mn in A-doped manganites such as LSMO is sensitive to the doping level[320–322] and the oxygen chemical potential (*i.e.*, concentration of oxygen vacancies).[323] While most generally a mixture of 3+/4+ with variable ratio is probed, 2+ was observed under reducing conditions,[286,324] at the surface of LSMO films. Given the large compositional differences among the surface phases of LSMO(110) (see bottom axis of Fig. 8.2), differences in the corresponding Mn oxidation state are to be expected.

Origin of the surface reconstructions

As seen from Fig. 8.1(b), the unreconstructed LSMO crystal is polar along the (110) orientation, consisting of alternating planes with a charge of $+/-8e$ per unit cell (taking oxidation state as charges, and neglecting the contribution of the small equilibrium concentration of oxygen vacancies at 700 °C and 0.2 mbar O_2, *i.e.*, $\approx 2 \times 10^{-8}$ of the O sites[325]). Without any polarity-compensating mechanism, this would result in a diverging dipole moment with increasing crystal thickness, *i.e.*, an unstable system, similarly to the $SrTiO_3$(110) system described in Chapter 6. Realizing reconstructions with appropriate net charge [$-4e$/unit cell on top of the $(AMnO)_2$ termination, $+4e$/unit cell above O_4 planes] could compensate for this polar catastrophe. Generally, for the reconstructions to bear the same formal charge per unit cell despite a change in cation composition, the oxygen stoichiometry and/or the oxidation state of the cations must change. For example, the polarity-compensating reconstructions of $SrTiO_3$(110) are distinguished by (i) different Ti-to-O compositions, (ii) different coordination of the cations to the oxygen species,[242] and possibly (iii) slight differences in the oxidation state of Ti.[326]

There is evidence that similar mechanisms are also at play in LSMO(110): First, its reconstructions display clear compositional differences. Moreover, the trend between Mn $2p_{3/2}$ and O $1s$ peaks speaks for differences in the Mn oxidation states. The high-quality of the film's surface will allow, *e.g.*, to perform X-ray absorption spectroscopy to pinpoint the coordination and/or oxidation state of the surface species in the future.[242]

La/Sr content

The Sr doping level in LSMO is important for its performance: It defines many of the bulk properties [LSMO undergoes metal–insulator and (anti)ferromagnetic–paramagnetic transitions as a function of the Sr content, and also the crystallographic structure depends on the Sr doping[282]], and can also affect surface reactivity. Particularly critical for the operation of solid-oxide fuel cells is the widely reported segregation of Sr-rich phases at operation conditions, which tends to degrade the oxygen exchange activity at the surface.[317] Sr segregation and the formation of insulating Sr-rich clusters is a very common phenomenon observed in LSMO and other perovskite oxides at conditions comparable to those employed in this work,[296,327] and it has been widely investigated, both experimentally and theoretically.[317,328] Notably, the films presented in this work do not show this phenomenon. XPS does not indicate any substantial deviation of the La-to-Sr ratio from the nominal composition in the near-surface region. Moreover, the films do not show the expected Sr segregation nor the formation of insulating, Sr-rich clusters upon prolonged (> 5 h) annealing at 700 °C and 0.2 mbar O_2: The A-site-to-Mn and the La-to-Sr XPS intensity ratios stay unaltered, and the surface structures appear unchanged in STM, always retaining atomically flat morphologies. It is likely that the Sr segregation observed in polycrystalline and textured films and in ceramic samples at comparable conditions is due to grain and twin boundaries that favor Sr diffusion,[329,330] which are absent in the single-crystalline films presented here.

Regarding the La/Sr ratio among the different surface phases of Fig. 8.2, there seems to be no evident trend as a function of the Mn content. As mentioned in the Results Section, the La 4*d*/Sr 3*d* XPS ratio among the surfaces of Fig. 8.2 appears unchanged within the error bars (*i.e.*, within ≈10%). However, this could be due to the low surface sensitivity of XPS at the high kinetic energies where the Sr 3*d* and La 4*d* peaks are found (≈1350 eV and ≈1380 eV, respectively). Similarly, the La/Sr LEIS intensity ratios show a strong scatter (≈50% of the average) without apparent trend, but it is hard to determine whether the measured differences are to be assigned to slightly different sample treatments. Small variations in the La/Sr ratio in LEIS have also been observed among surface structures that appear identical in STM. These differences are likely due to different sample history that can alter the near-surface composition (*e.g.*, sputtering–annealing treatments preferentially remove Sr over La). It is possible that small variations in the La/Sr ratio (with same Mn/A-site ratio) are compensated by introducing small amounts of oxygen vacancies or by changing the oxidation state of Mn, without changing the overall appearance of the surface phase. A systematic investigation of the LSMO(110) surface as a function of the Sr content, by deposition of Sr or SrO_2, accompanied by a detailed characterization of surface point defects, would be needed for an increased

understanding of the effect of the Sr/La ratio on the surface properties of LSMO(110).

Hints for a structural model for the fishbone reconstruction

As mentioned above, structural models for the Mn-rich reconstructions have not been developed yet. Nonetheless, valuable hints can be gathered from the structural model proposed for the (1×1) structure (see Section 8.3 below). As will be discussed in more detail, the (1×1) structure can be obtained starting from an $(AMnO)_2$-terminated LSMO(110) slab, and removing all Mn atoms from the top layer and one subsurface O atom. According to the established compositional axis in Fig. 8.2, the fishbone structure is characterized by 1.88(5) ML Mn more than the (1×1). Hence, the fishbone is obtained from the (1×1) by filling up the missing Mn in the (1×1) layer (1 ML), and adding an extra 0.88(5) ML Mn. This additional 0.88(5) ML Mn correspond to 23 ± 1 Mn atoms in the fishbone unit cell (out of the 26 in the 13 $(AMnO)_2$ units within the fishbone surface unit cell). Polarity compensation [$-4e$/(1×1) unit cell in the surface reconstruction] can be ensured by increasing also the amount of O atoms in the surface structure. Indeed, the fishbone structure is characterized by a higher O-to-Mn signal both in XPS and in LEIS (see Section 8.2.6). The exact number of O atoms will depend on the valence of Mn. For instance, for a valence of $4+$, 72 ± 3 atoms are required to keep a net charge of $-4e$/unit cell required for polarity compensation. Less O will be required if Mn atoms are more reduced than $4+$. In all cases, the numbers are significantly smaller than 130, *i.e.*, the number of O atoms present when 26 Mn atoms realize corner-sharing octahedra. This means that the fishbone structure is likely made by numerous edge/face sharing (truncated) octahedra or tetrahedra.

8.3 Deeper insights on the (1×1) phase

As mentioned above, the (1×1) phase of LSMO(110) [Fig. 8.2(a)] is a particularly appealing candidate for *ab-initio* methods. Not only does it show a comparatively simple appearance and a small-enough unit cell. It may also be the first example among complex multi-element oxides of a strongly A-site-rich reconstruction that is stable at close-to-realistic conditions. A-site structures are rarely resolved in complex multi-element oxides, which tend to consist of one or two layers of B-site cations coordinated with oxygen.[318] Nonetheless, the formation of A-site rich structures is often held responsible for the deactivation of perovskite oxide surfaces in solid-oxide fuel cells.[327,328,331–334] Obtaining a structural model for an A-site rich surface such as the (1×1) would be valuable to better understand this process.

The following Section discusses the proposed DFT model for this structure. A model is proposed also for another (1 × 1) structure that forms at more reducing conditions. All calculations were performed by Michele Reticcioli from the University of Vienna. Because the analysis is preliminary, only the most relevant results are reported and discussed. LEED-IV curves have been recently acquired on both structures (not shown) and will be used to validate the DFT models by comparison with theoretical curves.

8.3.1 Methods

Theoretical methods

First principles calculations were performed in the framework of DFT, using the Vienna *ab-initio* simulation package (VASP),[150,335,336] under the generalized gradient approximation (GGA) within the Perdew, Burke, and Ernzerhof parametrization (PBE).[153] The approximation to the correlation energy was corrected with the inclusion of an on-site effective U of 4.0 eV on Mn d states.[337]

The $LaMnO_3$(110) surface was modeled with an orthorhombic unit cell, and using symmetric slabs built by 13 LaMnO layers and a 30 Å-thick vacuum region; $\sqrt{2}\times\sqrt{2}$-large unit cells were used in order to accommodate the typical lattice distortions of the material.[300] Notice that the Jahn-Teller distortions of the A-site cations considered in the presented DFT models are not present in perfectly rhombohedral LSMO (space group $R\bar{3}c$). A more detailed analysis of the XRD data in Chapter 9 will be needed to establish whether the films deviate from the rhombohedral structure, and whether Jahn-Teller distortions are indeed present. One expects that the absence of Jahn-Teller distortions should not alter dramatically the results presented below.

Different surface reconstructions were investigated in a two-step process: First, all models were relaxed using standard convergence criteria with a plane-wave energy cutoff of 275 eV and approximately 20 k points in the irreducible Brillouin zone for the integration in the reciprocal space. Finally, the most stable and promising models were further relaxed using a more refined setup with a cutoff of 600 eV. The electronic properties of the relaxed models were calculated by using a Gaussian smearing for the orbital occupancy. The spin-polarized calculations considered both ferromagnetic and antiferromagnetic ordering of the Mn magnetization. The spatial extension of the electronic charge has been visualized in STM images using the Tersoff-Hamann approximation.[338]

Experimental methods

Surface preparation. Two types of (1 × 1) surfaces are discussed below: The 'high-pressure' (1 × 1), already introduced in Section 8.2 when discussing the high-pressure surface phase diagram of LSMO(110), and the and 'low-pressure' (1 × 1), that forms at more reducing conditions. To achieve the high-pressure (1 × 1), a fishbone-reconstructed surface [Fig. 8.2(c)] was sputtered for 6 min at 1 keV, 9×10^{-6} mbar Ar, followed by annealing at 700 °C at 0.2 mbar O_2 for 45 min.

The low-pressure structure was obtained by annealing the high-pressure structure at 700 °C and 7×10^{-6} mbar O_2 for 45 min (as discussed below, this structure forms and it is stable at 700 °C below 1×10^{-3} mbar O_2). With support from Martin Setvin, this surface has also been imaged with non-contact AFM, in an Omicron q-Plus LT head at T = 4.8 K with a custom cryogenic preamplifier,[339] and tuning-fork sensors (f_0 ≈31 kHz, Q ≈20 000)[340] with etched W tips. These were prepared by self-sputtering and checked on a Cu sample before being used on the LSMO sample. However, Cu-terminated tips have been unsuccessful in delivering atomic resolution. Atomic resolution was achieved only after harsh tip treatments, which probably terminated the tip with some constituents of the LSMO surface. As a result, the tip termination and shape was unknown, and no scanning tunneling spectroscopy could be performed. The (1 × 1) was prepared in the PLD surface science apparatus and transferred through air to the nc-AFM chamber, where it has been imaged after annealing at 700 °C and 7×10^{-6} mbar O_2. The surface was not prepared in the AFM chamber due to time constraints. The LSMO(110) surfaces are highly sensitive to sputtering treatments, and achieving a precise surface stoichiometry and surface structure requires iterative cycles of sputtering and Mn deposition (both requiring precise calibration in each chamber). Remarkably, the oxygen treatment alone was sufficient to recover the surface cleanliness required for atomic-scale imaging, as already witnessed for the (n × 1) reconstructions of $SrTiO_3$(110).

LEED-IV data. LEED-IV is planned to validate the structural models provided by DFT.[341] In LEED-IV, the intensities of diffracted beams are recorded as a function of incident electron energy to generate the so-called I-V curves. These curves can be compared with theoretical ones calculated from a proposed structural model. A quality factor—the so called Pendry R factor—measures the quality of the fit. Preliminary experimental curves were acquired, and will be compared to the theoretical ones calculated from the proposed DFT models. A new software (ViPErLEED) under development by Michele Riva, Florian Kraushofer, and Michael Schmid, in collaboration with Lutz Hammer from the Friedrich-Alexander-Universität Erlangen-Nürnberg, will be used for this task.

8.3.2 DFT models

High-pressure (1 × 1)

Figures 8.11(a–c) report once again the appearance in STM and LEED of the high-pressure (1 × 1) reconstruction, the A-site richest reconstruction of the surface phase diagram of Fig. 8.2. Figure 8.11(a) shows an STM image where a spontaneous tip change has allowed to image the same surface with two common appearances. In both cases, lines of round features with 25 pm-high corrugation run along the [001] direction. Depending on the tip termination, all features may appear identical (top half), or every other feature may appear brighter (bottom half). Figure 8.11(c) shows a small-scale STM image of the most common appearance of the surface, where all features appear identical.

This Section discusses the proposed DFT model for this surface. Crucial hints for the development of the DFT model have been given by the experimental data, in particular the LEIS data reported in Fig. 8.7. The LEIS data show that the (1 × 1) is significantly A-site richer than the other reconstructions. They also reveal the unique behavior of the (1 × 1) upon longer LEIS acquisitions: The Mn peak increases, instead of decreasing like for the other reconstructions [see Fig. 8.7(b)]. The decrease in the Mn signal is expected if Mn is present at the surface: Assuming only binary collisions between the impinging He^+ ions and the surface atoms, Mn atoms should be sputtered/scrambled preferentially than the rest, causing the Mn signal to decrease. The increase in the Mn signal with prolonged acquisition can be understood if one assumes a very small (if not zero) presence of Mn cations at the very surface of the (1 × 1). As acquisition proceeds, the He^+ ions produce a mild sputtering and scrambling of the surface, making the Mn species in the sub-surface layers more and more accessible. This crucial difference between the (1 × 1) and the other surface phases is amplified by the peculiar behavior during the transition to the adjacent reconstructions in the surface phase diagram: While a continuous transition allows to move between the Mn-richer structures (see Fig. 8.5), the transition between the (1 × 1) and the (n × 2) occurs via a phase separation.

Based on the observations from LEIS and for the sake of simplicity, one can assume that the (1 × 1) surface is free from Mn, only consisting of Sr, La, and O. One can then, just initially, make another simplifying assumption and neglect the presence of Sr atoms. The composition of the surface layer is easily derived by remembering that each reconstruction must bear $-4e$ per surface unit cell to compensate for the polarity of the bulk-truncated LSMO(110) (see Section 8.2.8). Given the formal charge states of O and La of -2 and $+3$, respectively, each unit cell must then contain 2 La atoms and 5 oxygen atoms, yielding the unit formula of $(La_2O_5)^{4-}$ (for simplicity, the oxidation state of Mn in the subsurface is assumed to be 4+, unaffected by the reconstruction).

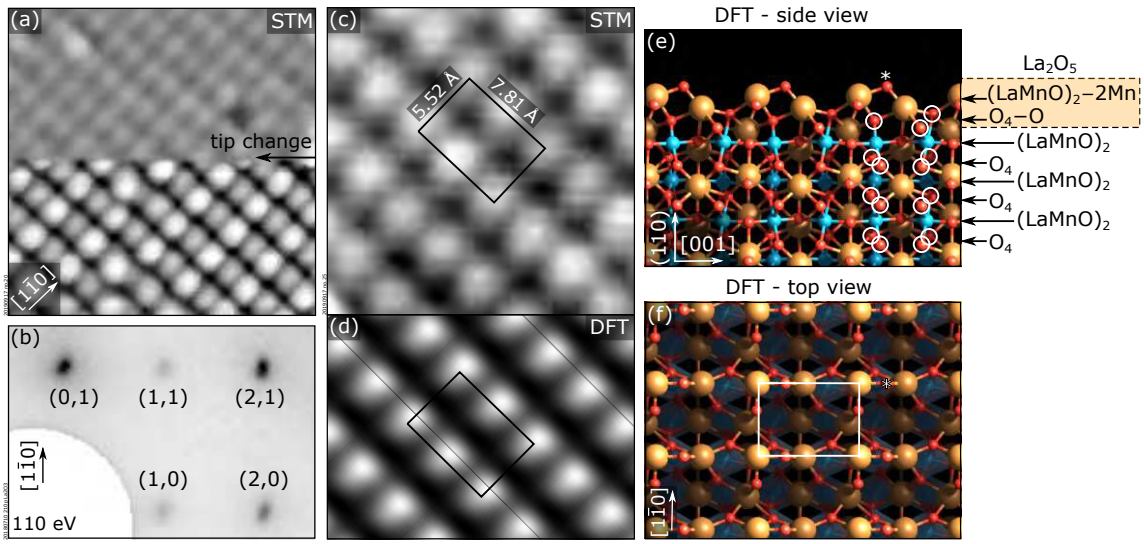

Figure 8.11. High-pressure (1 × 1) structure of LSMO(110). (a) 5 × 5 nm^2 STM image of the (1 × 1) structure, imaged with two distinct, yet unknown, tip terminations (U = +3.4 V, I_t = 0.2 nA). A spontaneous tip switch has occurred in the middle of the image. (b) LEED pattern. (c) 2.25 × 2.25 nm^2 STM image of the most common appearance of the surface (U = +3.3 V, I_t = 0.3 nA). (d) STM simulation, obtained from the proposed DFT model whose side, and top views are reported in panels (e, f), respectively. The image is calculated for a tip positioned 3 Å above the surface, and is obtained by integrating the density of states in a 5 eV range above the Fermi level.

The formation energy of several structures complying with this constraint has been tested with DFT. Figure 8.11 shows the most stable structure found, consisting of a La_2O_5 layer lying above a slightly relaxed bulk-truncated $(AMnO)_2$ plane of LSMO(110). Figure 8.11(e) shows the side view of this structure. As mentioned in Section 8.1.1, the bulk of LSMO(110) consists of $(O_2)_2$ and $(AMnO)_2$ planes that alternate along the [110] direction. When considering Jahn-Teller distortions, Mn and La atoms buckle along the [110] direction[300] (≈0.73 Å). The La_2O_5 structure can be obtained starting from a bulk-truncated system terminated by an $(AMnO)_2$ plane, and by removing two Mn atoms from the $(AMnO)_2$ plane and one subsurface O atom. Notice that this structure would be consistent with the presence of a Mn peak in LEIS, even during the first stages of the acquisition (see Fig. 8.13): As seen from the top view in Fig. 8.11(f), the proposed structure is somewhat open, and the subsurface Mn atoms could be accessed by the He^+ ions during LEIS acquisition.

Underneath the La_2O_5 layer, the bulk structure is only slightly relaxed (0.1–0.2 Å expansion/contraction of subsurface Mn and La atoms with respect to the bulk). On the other hand, La and O atoms in the La_2O_5 surface structure are significantly displaced with respect to the bulk positions along [001]. Because of the missing Mn atoms at the surface, La atoms have dimerized along the [001] direction, sharing a bridging O (white star) that would otherwise bridge adjacent Mn atoms. The La atoms in each dimer have different coordination to oxygen (four- and five-fold, respectively), and this causes

a strong buckling (≈0.9 Å) along the [110] direction, with the higher-coordinated La atom lying closer to the subsurface. This strong buckling could be consistent with the alternating apparent heights measured in STM with specific tip/tunneling conditions [see Fig. 8.11(a)]. Since the buckling is directly related to the oxygen coordination of the surface La atoms, one can expect a similar buckling to be present even when not considering Jahn-Teller distortions in the bulk of the slab (see Methods).

Figure 8.11(d) shows the STM simulation derived from the model discussed above, obtained by integrating the density of states in a 5 eV range above the Fermi level (dominated by La states, not shown). The simulation matches the experimental STM image of Fig. 8.11(c). LEED-IV will be used to conclusively validate the model.

Note that the DFT analysis presented here is still in its preliminary stages. A more thorough analysis should account for the presence of defects, which are invariantly observed on the (1 × 1) surfaces (see Section 8.3.3), and for the presence of Sr, which has not been considered here. So far, the presence of Sr was neglected because accounting for the appropriate amount is not trivial experimentally. While the bulk composition of the films is known (≈80:20 La:Sr ratio), the composition of the surface is uncertain. In fact, the surfaces are prepared by repeated sputtering–annealing cycles (during which Sr is sputtered preferentially over La, not shown), and Mn deposition followed by O_2 annealing. This makes the Sr content at the surface history-dependent, and an unknown input for DFT. Additionally, the distribution of the Sr atoms at the surface is not known a priori (it was not yet investigated whether Sr can be distinguished from La in STM). Nonetheless, it was observed that small deviations in the relative Sr/La composition due to the specific sample history do not affect the overall appearance of the surface. It is likely that these small variations in the La/Sr ratio (with same Mn/A-site ratio) are compensated by introducing small amounts of oxygen vacancies or by changing the oxidation state of Mn (from polarity considerations, one expects to remove 1/2 O per Sr atom, or to reduce the oxidation state of one Mn atom by 1). Hence, one can expect that the model proposed would hold also in the presence of Sr. A systematic investigation of the LSMO(110) surface as a function of the Sr content, by deposition of Sr or SrO_2, accompanied by a detailed characterization of surface point defects, would be needed for an increased understanding of the effect of the Sr/La ratio on the surface properties of LSMO(110).

Low-pressure (1 × 1)

At sufficiently reducing conditions, another (1 × 1) structure appears and is stable. The following Sections will refer to the two (1 × 1) reconstructions as $(1 \times 1)_{HP}$ and $(1 \times 1)_{LP}$, where HP and LP stand for high pressure and low pressure, respectively. Starting from

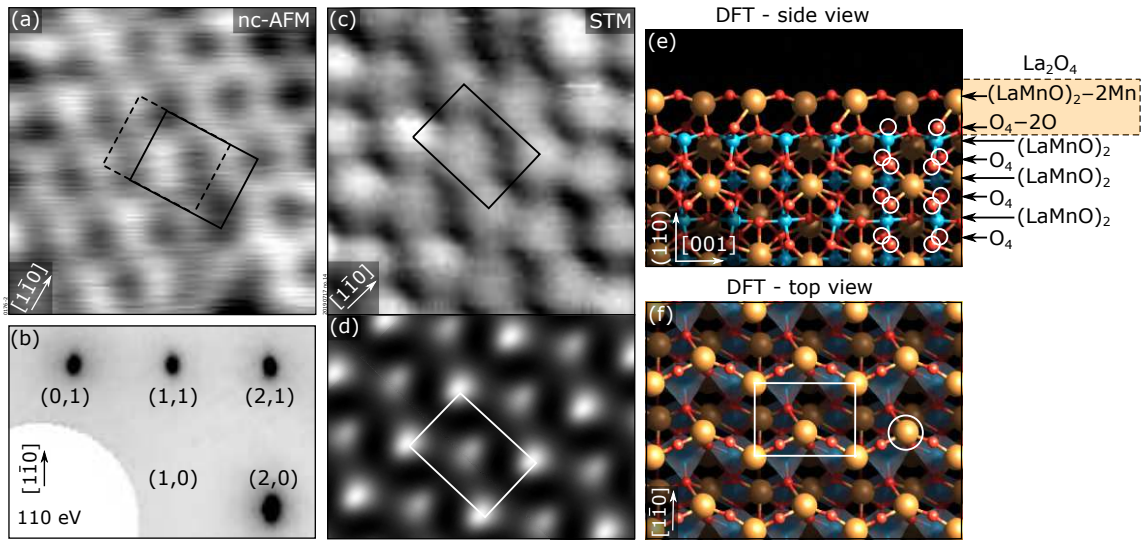

Figure 8.12. Low-pressure (1 × 1) structure, prepared at 7 × 10^{-6} mbar O_2. (a, c) 2.25 × 2.25 nm^2 nc-AFM images and STM images, respectively (tunneling parameters during STM acquisition: U= 1.8 V, I_t= 0.04 nA. (b) Representative LEED pattern. (d) STM simulation, obtained from the DFT model whose side, and top views are reported in panels (e, f), respectively. The image was calculated with a tip positioned 2 Å above the surface La atoms, and integrates the density of states in a 5 eV range above the Fermi level (dominated by La states, not shown).

a monophase $(1 \times 1)_{HP}$ surface, a transition to the $(1 \times 1)_{LP}$ occurs at 700 °C below 10^{-3} mbar O_2. This reconstruction is then stable at 700 °C down to UHV.

Figures 8.12(a, c) show non-contact AFM and STM images of the $(1 \times 1)_{LP}$ surface, while Fig. 8.12(b) shows the corresponding LEED pattern. The (1 × 1) unit cell (same size as for the HP structure) can be easily identified [black rectangles in panels (a) and (c)]. In the STM image, two protrusions per unit cell are visible, one at the corner, the other one roughly in the center of the cell (midway along [001], and slightly shifted along $[1\bar{1}0]$). This shift produces zig-zag rows along the [001] direction. Two symmetry-equivalent domains exist, in which the second atom is displaced along $[1\bar{1}0]$ or along $[\bar{1}10]$. The zig-zag of the surface features produces a glide plane parallel to the [001] direction, whose presence is also visible in the LEED pattern of Fig. 8.12(b): The (1,0) spot (and all its odd multiples) cannot be distinguished from the background at any electron energy [compare with the (1,0) spot that is instead present in the high-pressure counterpart, Fig. 8.11(b)]. In the nc-AFM image of Fig. 8.12(a), two levels of contrast are visible, 'bright' and 'dark' [see solid and dashed rectangles], speaking for the presence of two atomic species at the surface (in nc-AFM, the contrast relates to the strength of the interaction between the tip and the surface at each location, in turn sensitive to the local chemistry of the surface). However, because of the unknown tip termination (see Methods above), no additional information can be inferred from the contrast.

Once again, LEIS was used to gain information about the composition of the surface structure under investigation: Figure 8.13 compares LEIS spectra acquired on a $(1 \times 1)_{LP}$

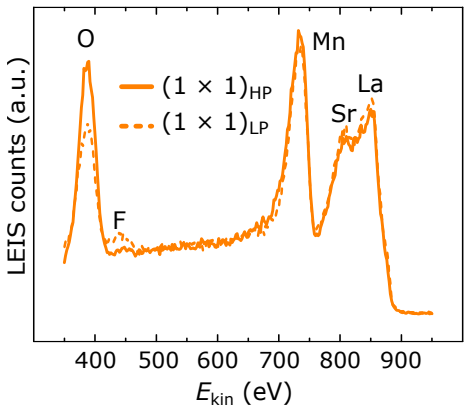

Figure 8.13. LEIS spectra acquired on the high- and low-pressure (1 × 1) structures of LSMO(110) (solid and dashed lines, respectively). The cation signals are comparable on both surfaces, while a higher O signal is detected on the high-pressure structure. The small F signal is caused by minor contamination in the chamber.

surface (dashed) and on the HP counterpart (solid). The two phases appear to be characterized by a comparable cation composition, while a difference is evident in their O content (smaller on the LP phase). This suggests that, like the $(1 \times 1)_{HP}$, the LP phase consists of a layer of La, Sr, and O atoms. [Note that the small contribution from F originates from a small contamination in the chamber, that is especially visible on samples after a few hours from their preparation. Note also that the Mn signal is slightly higher than the A-site signals in these spectra, differently from what reported in Fig. 8.7. One possible reason is that the surface exhibited small patches of the $(n \times 2)$ reconstruction, which is slightly Mn-richer than the (1 × 1) (see Fig. 8.2) (small coverages of this reconstruction are not visible in LEED).]

Based on the hypothesis that the only difference in the composition of the two (1 × 1) structures lies in their oxygen content, Michele Reticcioli has tested several structures that have the same cation composition of the $(1 \times 1)_{HP}$, *i.e.*, two La atoms per unit cell, and that have at least one O atom less per unit cell with respect to the $(1 \times 1)_{HP}$. The side and top views of the most stable structure that was found are shown in Figs. 8.12(e, f), respectively. Like the HP phase, the structure consists of a single layer of La and O (in this case, La_2O_4 instead of La_2O_5) lying on a (slightly relaxed) bulk-truncated $(AMnO)_2$ plane of LSMO(110). Like the HP phase, it can be obtained from a bulk-truncated LSMO(110) slab terminated by an $(AMnO)_2$ plane, by removing two Mn atoms from the top plane, and *two* subsurface O atoms. Note that polarity compensation can be still ensured by reducing all Mn atoms in the subsurface layer from 4+ to 3+ (*i.e.*, forming small polarons), or by distributing the extra two electrons per unit cell over several $(AMnO)_2$ layers (*i.e.*, forming large polarons or delocalized states). With the DFT level used, the extra electrons appear to be delocalized over the whole slab. However, one cannot exclude that the charge is, in fact, localized on Mn atoms. More detailed investigations on this matter

are planned for the future.

The additional subsurface O atom missing in the LP phase produces a few changes with respect to the HP phase. Now both La atoms in the unit cell miss a bond with subsurface O, hence they are both four-fold coordinated. For the same reason, the buckling of these surface La atoms along the [110] is now essentially suppressed: In the HP phase, the buckling originated from the fact that one of the two atoms in the unit cell was five-fold coordinated, and hence more tightly bound to the atoms underneath. Removing one sub-surface O bond makes this atom relax upwards (white circle). Moreover, the missing bond with subsurface O makes this atom also shift by 1.6 Å along the [001] direction. This shift is the cause of the zig-zag lines and the glide plane characteristic of this surface.

Figure 8.12(d) shows the STM simulation derived from the proposed model, which matches nicely with the experimental STM image of Fig. 8.12(c). The simulation is obtained from the density of states integrated in a 5 eV range above the Fermi level, which is dominated by La states (not shown). The nice match of the simulated image obtained from La states supports the hypothesis that the atomic features observed in the STM image correspond to La atoms. Nonetheless, comparison of experimental and theoretical LEED-IV curves is planned to conclusively validate the DFT model. Note that, like in the case of the high-pressure structure, the DFT analysis presented here does not account for the presence of Sr and atomic defects.

8.3.3 Defects

So far, defect-free (1×1) surfaces have been assumed. In reality, both the high- and the low-pressure (1×1) exhibit atomic defects, which are briefly pointed out and described in the following. A more detailed characterization of the observed defects is planned for the future.

High-pressure (1×1)

Figure 8.14 highlights the STM appearance of the four most common types of defects found on the high-pressure (1×1) surface. They consist of: (A) bright protrusions that bridge two [001] rows; at certain tunneling conditions, these features can be dragged across the surface, producing the artificial chain observed at the top left of panel (b); (B) brighter appearance of a single atomic feature characteristic of the reconstruction, which appears slightly displaced along the $[1\bar{1}0]$ or the $[\bar{1}10]$ direction with respect to the ideal (1×1) grid (see the features indicated by B and B', respectively); (C) H-like features bridging two [001] rows—notice that the central feature is slightly displaced

along [1$\bar{1}$0] with respect to the ideal bridging position; (D) dark features in between two rows. Notice also that slight La enrichments produce the atomic chains observed on Fig. 8.6(a) (Section 8.2.5).

The nature of these defects is to this date unknown. They could be associated to adsorbates, oxygen vacancies, structural defects, Sr atoms, or bulk impurities. Experiments are planned to pinpoint such defects in the future.

Low-pressure (1 × 1)

Figure 8.15(a) shows a low-pressure (1 × 1) prepared at 7×10^{-6} mbar O_2. A few defects are observed. They appear as brighter (A), slightly darker (C), and darker (B) than the single atomic features that are characteristic of this reconstruction. Some clusters (D) are also observed.

When the same surface is annealed in UHV, the atomic structure is preserved, but new bright features are observed at the same atomic position of the underlying (1 × 1) structure [panels (b–f); the corresponding LEED patterns appears identical]. It is likely that these features consist of carbon-containing adsorbates. First, species appear to be very mobile—compare their positions in the consecutive images shown in panels (d–f). This supports the idea that they consist of weakly bound adsorbates. Moreover, XPS reveals the appearance of a new C peak that was not observed on the surface prepared in an oxygen environment (not shown). No change is observed in the shape of the oxygen peak, suggesting that the adsorbates are not related to, *e.g.*, dissociated water.[167] Notice that the coverage of these adsorbates depends on the duration of the reducing treatment (the longer the annealing, the larger their number), and of the time after which the surface is imaged (higher coverages with longer times). The preliminary interpretation is that the reducing treatment induces oxygen vacancies, making the surface more reactive to C species present in the UHV system (*e.g.*, CO, CO_2). The mechanism driv-

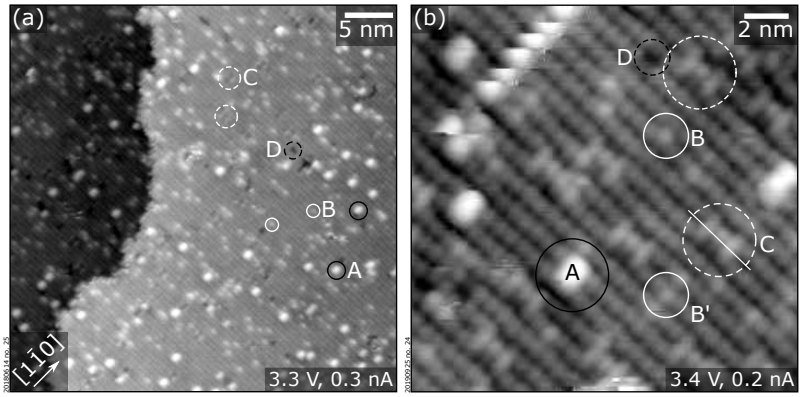

Figure 8.14. Defects on the high-pressure (1 × 1) structure of LSMO(110), as seen from (a) 40 × 40 nm^2 and (b) 12 × 12 nm^2 STM images. Labels identify the different types of defects (see main text).

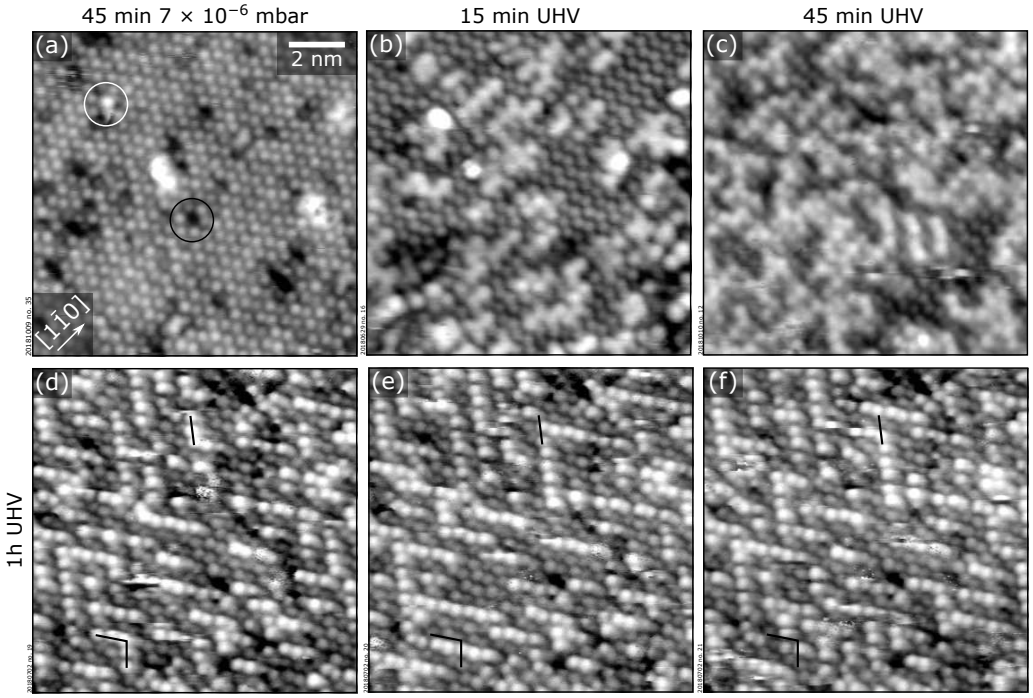

Figure 8.15. Defects on low-pressure (1 × 1) surfaces of LSMO(110) prepared at slightly different conditions, as seen from 12 × 12 nm^2 STM images. (a) Surface obtained by annealing for 45 min at 7 × 10^{-6} mbar O_2. Defects consist of different appearances of the single features of the reconstruction (brighter, darker, and missing—A, C, and B, respectively), or of a bright clusters (D). (b, c) surfaces prepared by annealing in UHV for 15 min and 45 min, respectively. New features appear at the surface, assigned to carbon species (see main text). (d–f) Surface prepared by annealing for 1 h in UHV. A labyrinth-like structure of brighter features is observed. Consecutive imaging reveals the high mobility of these features.

ing the adsorption is possibly that of polarity compensation. When positively charged oxygen vacancies are introduced in the system, adsorption of negative species (possibly C-related species) can reintroduce charge neutrality. The labyrinth arrangement of the adsorbates in panels (d–f) could be caused by the minimization of the electrostatic repulsion between the charged adsorbates. More experiments are planned to explore these phenomena in more depth. Notice that high reactivity to CO adsorption at RT on AO_x-terminated surfaces of perovskite oxides was already reported in the literature.[342,343]

8.4 '2D' surface phase diagram (μ_O vs. μ_{Mn})

Section 8.2 has been focused on the surface properties of LSMO(110) explored as a function of the cation composition, at a fixed value of oxygen chemical potential, μ_O, given by the annealing conditions of 700 °C and 0.2 mbar O_2. This Section extends the characterization of the LSMO(110) surface to smaller values of μ_O. It is shown that the surface of LSMO(110) has a strong tendency to phase-separate into A-site-rich and Mn-rich areas at pressures below 2 × 10^{-3} mbar O_2 (at 700 °C). The A-site-rich areas become larger

at more reducing conditions, while the Mn-rich regions become Mn richer. New surface reconstructions are revealed within these Mn-rich areas, which were characterized with STM, LEED, and LEIS, as described in Section 8.4.2. It is argued that the observed phase separation is achieved by transferring Mn across the surface, while leaving the overall surface cation composition unchanged. Section 8.4.3 discusses a strategy to organize all the reconstructions observed on the LSMO(110) films—both high- and low-pressure—in an experimental two-dimensional phase diagram as a function of both, μ_O, and the Mn content. These results are collected in ref. 344.

8.4.1 Behavior with decreasing oxygen chemical potential

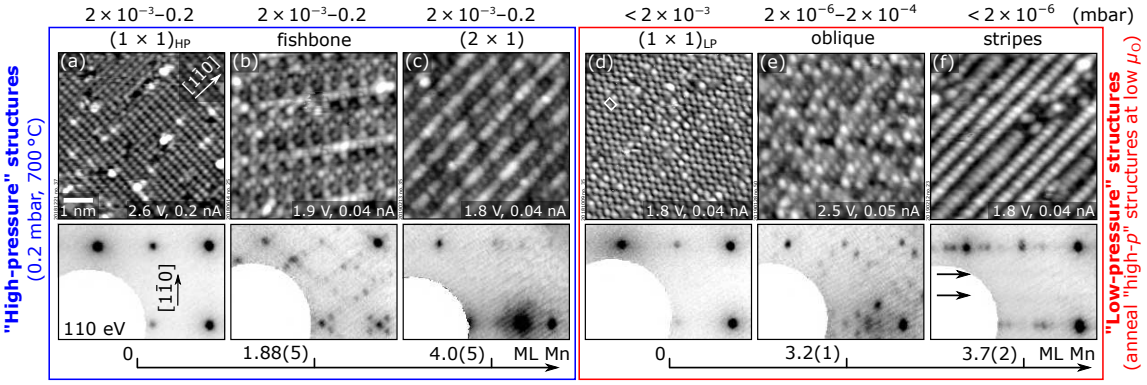

Figure 8.16. Summary of the surface structures of LSMO(110). (a–c) 'High-pressure' structures, obtained by tuning the surface composition by depositing controlled amounts of manganese- or lanthanum-oxide in PLD (plus annealing 1 h, 700 °C, 0.2 mbar O_2). They are stable at 700 °C above 2×10^{-3} mbar O_2. The (1×1) surface in panel (a) transforms to the surface in panel (d) when annealed below 2×10^{-3} mbar. It preserves the (1×1) periodicity, but develops a glide symmetry. When annealing the surfaces in panels (b or c) below 2×10^{-3} mbar O_2, they phase-separate, forming patches of the $(1 \times 1)_{LP}$ in panel (d) and of the 'low-pressure' structures in panels (e, f). Since the $(1 \times 1)_{HP}$ and the $(1 \times 1)_{LP}$ surfaces have the same cation composition, they are taken as common reference for the stoichiometry of the other structures (see bottom axis). 1 ML is defined as the number of Mn sites in an $(AMnO)_2$ plane of LSMO(110), *i.e.*, 4.64×10^{14} at./cm^2. Adapted from ref. 344.

This Section addresses the behavior of the high-pressure reconstructions of Fig. 8.2 with decreasing oxygen chemical potential. Unless otherwise specified, lower values of μ_O have been achieved by decreasing the O_2 pressure while keeping the temperature at the fixed value of 700 °C. For convenience, Fig. 8.16 summarizes all the stable surface reconstructions observed on the LSMO(110) films: On the left-hand side are the high-pressure structures discussed in Section 8.2. On the right-hand side, the low-pressure structures to be presented shortly. In both cases, the bottom axis reports the relative composition in terms of monolayers of Mn.

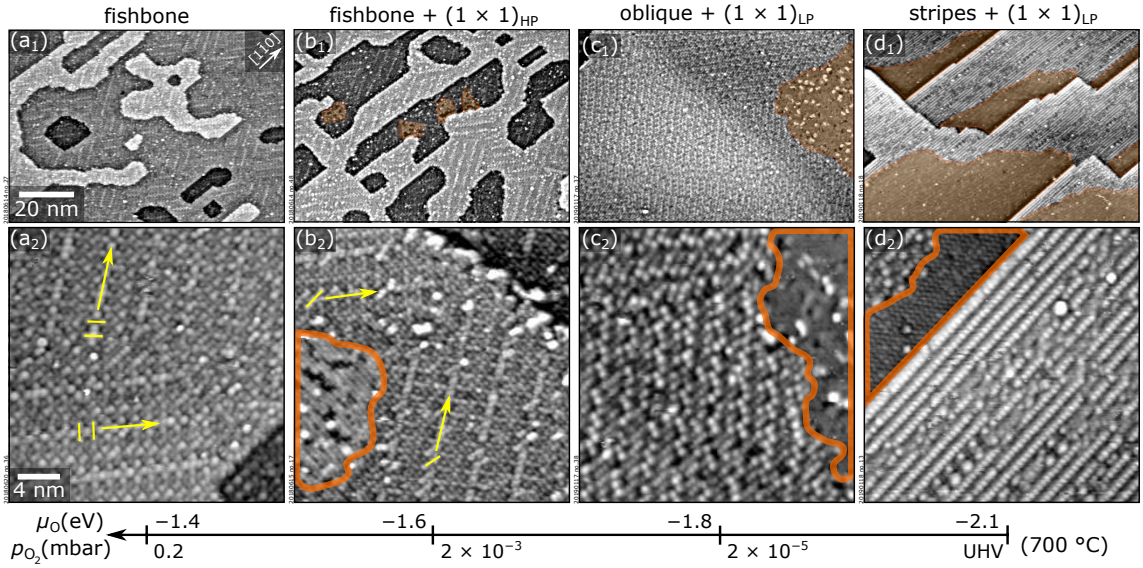

Figure 8.17. Evolution of the 'fishbone' surface of LSMO(110) with annealing at lower μ_Os. (a_1–d_1, a_2–d_2) STM images of 100 × 70 nm^2, and 26 × 26 nm^2, respectively. (a_1,a_2) Monophase fishbone surface of LSMO(110). After annealing at 2×10^{-3} mbar (b_1,b_2), small $(1 \times 1)_{HP}$ patches appear, and small structural changes occur in the fishbone. Annealing at 2×10^{-5} mbar (c_1,c_2) results in the formation of $(1 \times 1)_{LP}$ areas, while the rest of the surface evolves towards a new low-pressure structure, *i.e.*, the 'oblique' of Fig. 8.16(e). Annealing in UHV (d_1,d_2) causes the enlargement of the $(1 \times 1)_{LP}$ areas, while the rest of the surfaces transforms in the 'stripes' of Fig. 8.16(f). The process is fully reversible. Adapted from ref. 344.

The first stability test with decreasing μ_O was done on the A-site richer reconstruction of the high-pressure phase diagram, *i.e.*, the $(1 \times 1)_{HP}$ shown in Fig. 8.16(a). This stays unaltered upon annealing at 700 °C and above 2×10^{-3} mbar. At lower pressures and down to UHV, it transforms to the $(1 \times 1)_{LP}$ monophase of Fig. 8.16(d). Both structures have been discussed in detail in Section 8.3, which also presents their proposed DFT models. In a nutshell, the low- and high-pressure (1×1) phases are both characterized by a layer of Sr, La, and O over an essentially bulk-truncated $(AMnO)_2$ plane of LSMO(110). They are characterized by different amount of O (one O atom less per unit cell in the LP phase), and same cation composition. Hence, the cation composition of a surface initially monophase $(1 \times 1)_{HP}$ does not change upon annealing at decreasing μ_O. Since the following discussion pivots around the cation composition of given surface reconstructions, and this is the same for the high- and low-pressure (1×1) structures, either of the two will simply be referred to as (1×1), disregarding the change in oxygen content and in the atomic structure with μ_O.

The stability with decreasing μ_O of the other high-pressure structures of LSMO(110) (Fig. 8.5) was also tested. These 'Mn-rich' structures [as opposed to the AO_x-terminated (1×1)] behave differently that the (1×1). Figure 8.17 exemplifies the evolution of an initially monophase fishbone-reconstructed surface with decreasing μ_O [the same qualitative behavior was also observed for reconstructions and compositions between

the fishbone and the (2 × 1), as shown below]. Between 0.2 mbar and 2×10^{-3} mbar, small (1 × 1) areas appear on the fishbone surface that get larger with lower pressure [orange in Figs. 8.17(b_1, b_2)]. At the same time, the fishbone undergoes a minor structural change: part of the small features orthogonal to the bright line indicated by the yellow arrow tilt towards the $[1\bar{1}0]$ direction [cf. Figs. 8.17(a_2, b_2)]. As seen from Fig. 8.5, this is indicative of a higher Mn content in the structure.

Annealing at lower μ_O produces more dramatic changes: Between 10^{-4} and 10^{-6} mbar [Figs. 8.17(c_1, c_2)], most of the surface exposes a new structure that has not been observed at high pressure, *i.e.*, the 'oblique' of Fig. 8.16(e), described in more detail below, while the rest of the surface exhibits the (1 × 1) reconstruction. The (1 × 1) areas are larger than the ones formed above 2×10^{-3} mbar, while the rest of the surface is richer in Mn: The LEIS spectra in Fig. 8.18(a) performed on monophase fishbone (light gray) and oblique (dark gray) surfaces reveal that the oblique reconstruction is Mn richer than the fishbone.

Decreasing the pressure even further [below 10^{-6} mbar and down to UHV, see the STM images in Figs. 8.17(d_1, d_2)] produces yet another major change of the surface: Even larger (1 × 1) patches are observed, while the rest of the surface has evolved towards yet another structure, the 'stripes' of Fig. 8.16(f), described in more detail below. This structure qualitatively resembles the high-pressure (m × 1) structure observed upon depositing around and above 1 ML Mn on a (2 × 1) surface [Fig. 8.6(b)]: In both cases, stripe features run along the $[1\bar{1}0]$ direction. Due to the pronounced surface-dependent sticking effects discussed in Section 8.2.6, it was not possible to prepare a monophase surface of the low-pressure stripes, and acquire the corresponding LEIS spectra. The strong resemblance to the (m × 1) structure of Fig. 8.6(b) could be indicative of an equivalent Mn enrichment of this surface. It is worth mentioning that around 10^{-4} mbar, *i.e.*, between the fishbone and the oblique regimes, a semi-ordered phase is observed that is assigned to a transition state between these two reconstructions (not shown).

XPS was used to monitor the composition of the surface presented in Fig. 8.17 at each annealing step—see Fig. 8.18(b). The data show no trend (within the error bars) as a function of the oxygen chemical potential.

Interpretation

To understand the mechanism that drives the observed phase separation, causing the exposure of larger and larger (1 × 1) patches, while the rest of the surface gets more and more Mn enriched, a few crucial observations are helpful. (i) The process illustrated in Fig. 8.17 is fully reversible: The initial surface is recovered when annealing back at high

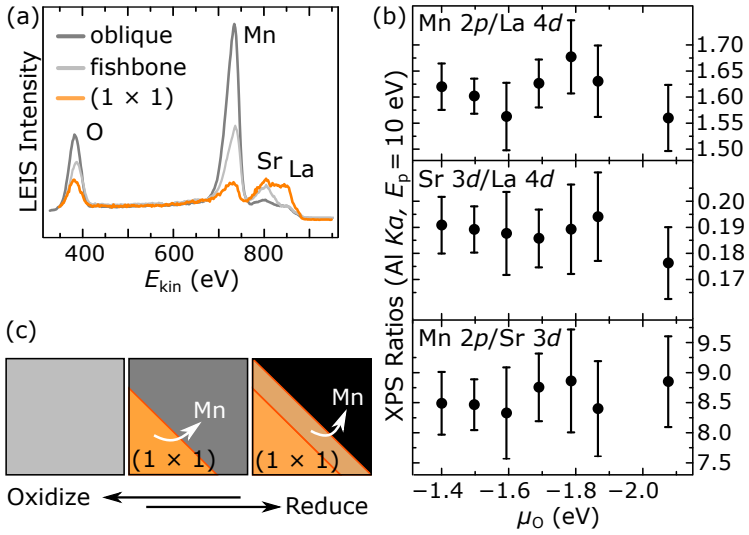

Figure 8.18. (a) Comparison of LEIS spectra of monophase $(1 \times 1)_{HP}$ (orange), fishbone (ligth grey), and oblique (dark grey) surfaces. The oblique forming during the phase separation is Mn-richer. (b) XPS intensity ratios acquired at each annealing step: there is no trend within the error bars. (c) Mn is transferred across the surface to expose $(1 \times 1)_{HP}/(1 \times 1)_{LP}$ areas (that have the same cation composition) and form new Mn-richer structures, while preserving the overall cation composition. Adapted from ref. 344.

pressure. (ii) The XPS data of Fig. 8.7(c) do not show any trend as the phase separation proceeds. However, Fig. 8.7(c) has demonstrated that XPS is very sensitive to changes in the surface composition of LSMO(110), showing clear differences between the composition of monophase samples of the (1×1) and the fishbone. One can thus conclude that the average cation composition of the first few nanometers probed by XPS is preserved at each annealing step. (iii) The bulk diffusivity of cations in LSMO is very slow at the employed conditions: Each cation can travel at most one atomic layer.[330]

Points (i) and (ii) rule out cation evaporation, while point (iii) rules out that the phase separation originates from local preferential exchange of cations with the bulk [local segregation of Mn/interdiffusion of A-site to form the Mn-rich regions, and local segregation of A-site/interdiffusion of Mn to realize the (1×1) areas]. The simplest explanation is that Mn is transferred across the surface, depleting those areas that will expose the (1×1) reconstruction, while enriching the rest of the surface, as sketched in Fig. 8.18(c).

8.4.2 A closer look at the low-pressure structures

The following Section briefly describes the low-pressure structures of LSMO(110) that are observed during the pressure-dependent phase separation discussed above.

'Oblique'

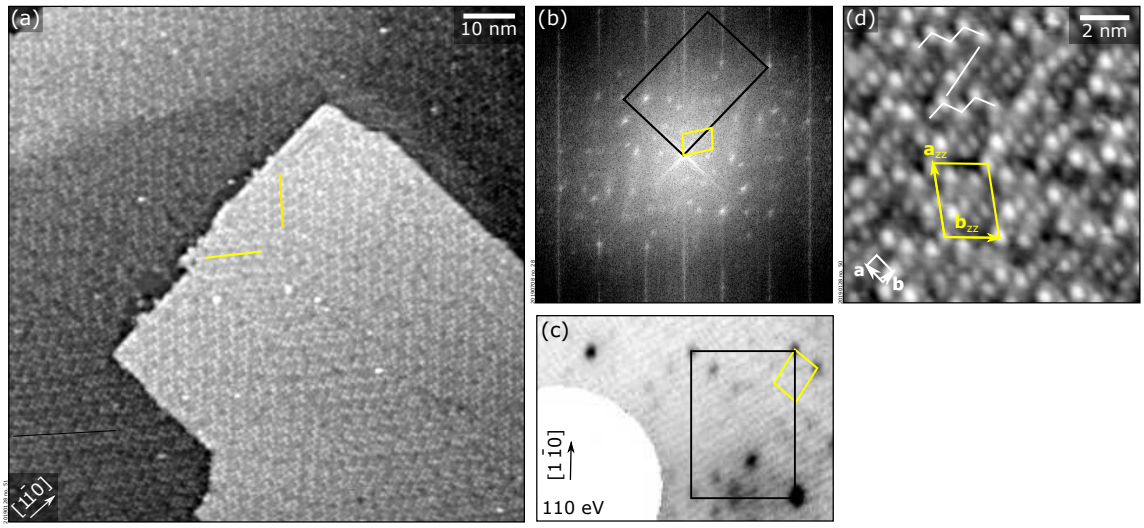

Figure 8.19. Low-pressure, oblique reconstruction of LSMO(110). (a) 100 × 100 nm^2 STM image. Two mirror-symmetric domains with respect to the [1$\bar{1}$0] direction are visible (yellow lines). (b, c) Corresponding Fourier transform and LEED pattern. The unit cells of the (1 × 1) and of one of the two oblique domains are highlighted in black and yellow, respectively. (d) 12 × 12 nm^2 STM image on one of the two oblique domains. The unit cells of the (1 × 1) and of the oblique are indicated in white, and yellow, respectively. Adapted from ref. 344.

The oblique reconstruction (Fig. 8.19) is observed between 10^{-4} and 10^{-6} mbar O_2. The large-scale STM image of Fig. 8.19(a) shows that it is characterized by two domains that are mirror-symmetric with respect to the [1$\bar{1}$0] direction, similarly to the high-pressure fishbone reconstruction (Section 8.2). These contribute to the complex Fourier transform and LEED pattern of Figs. 8.19(b, c). The unit cells of one of the two domains is indicated in yellow. The periodicity of the structure can be expressed in matrix notation as

$$\begin{pmatrix} \mathbf{a}_{ob} \\ \mathbf{b}_{ob} \end{pmatrix} = \begin{pmatrix} 3 & \pm 3 \\ -2 & \pm 3 \end{pmatrix} \begin{pmatrix} \mathbf{a} \\ \mathbf{b} \end{pmatrix},$$

where the vectors **a**, **b**, and $\mathbf{a}_{ob}$, $\mathbf{b}_{ob}$ identify the unit cell of the (1 × 1), and of the oblique, respectively [see close-up STM images in Fig. 8.19(d)]. Similarly to the fishbone reconstruction, because the angle between $\mathbf{a}_{ob}$ and $\mathbf{b}_{ob}$ is different than the one between **a** and **b**, it is not possible to express this periodicity in Wood's notation. The two signs correspond to the mirror-symmetric domains.

The close-up STM image in Fig. 8.19(d) shows the atomic details of the oblique reconstruction. It is composed of 'tiles' (yellow overlay) outlined by bright protrusions forming a ring, and with additional protrusions approximately running along **b** (and separation between protrusion close to |**b**|). A monophase oblique (as determined by

STM) was realized starting from a mixed $(1 \times 1)_{LP}$ and oblique surface, and iteratively depositing small amounts of Mn at high O_2 pressure (≈0.2 ML Mn, RT, 0.2 mbar), followed by annealing at 700 °C and 7×10^{-6} mbar O_2.

'Stripes'

The low-pressure 'stripes' (Fig. 8.20) are observed after UHV annealing. STM reveals that they consist of several coexisting structures—all preferentially oriented along the $[1\bar{1}0]$ direction and contributing to the $(n \times 1)$ periodicity seen in the LEED pattern of Fig. 8.16(f) (an additional faint 3-fold periodicity is also observed along the $[1\bar{1}0]$ direction, as highlighted by the black arrows). In the STM images in Fig. 8.20, the different structures are uniquely identified by colors and labels.

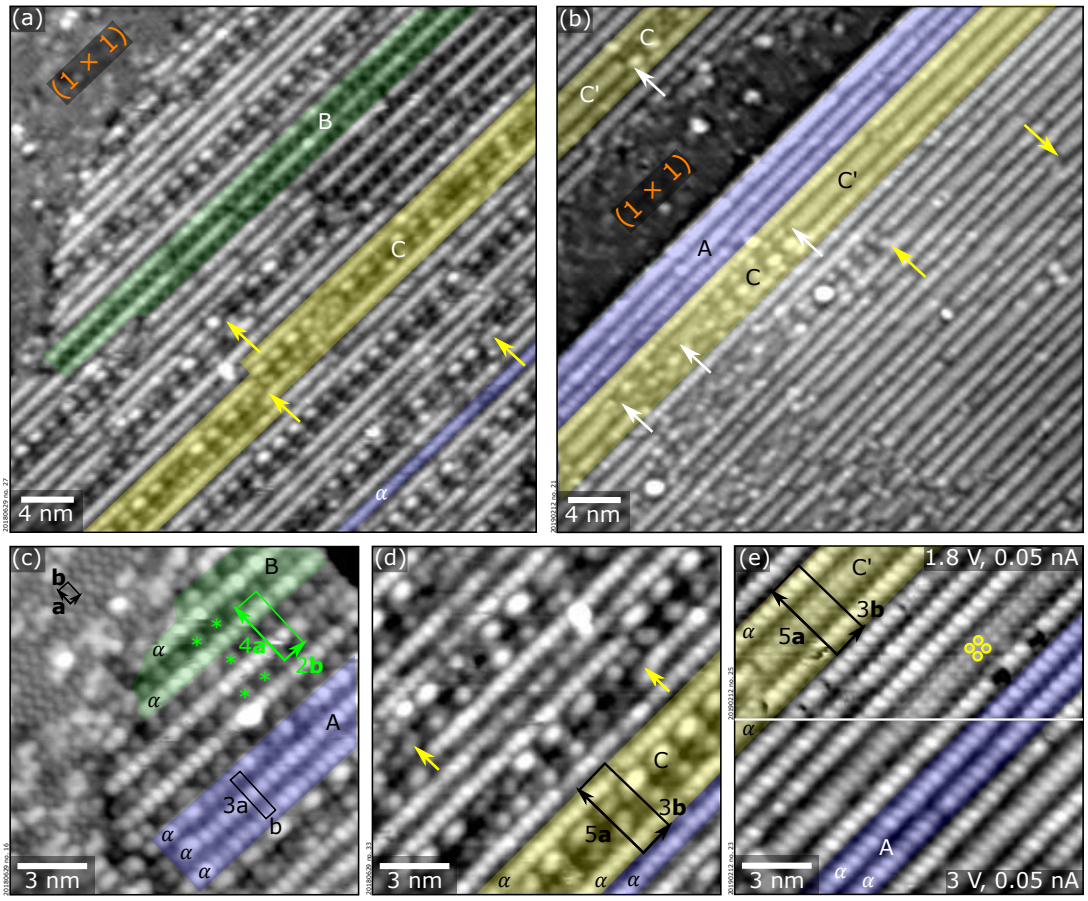

Figure 8.20. Low-pressure, $(n \times 1)$ reconstructions of LSMO(110). (a, b) 40 × 40 nm^2 STM images of the surfaces of two LSMO(110) samples annealed at 700 °C, UHV, 15 min, starting from (a) fishbone reconstruction, and (b) from the (2×1). In each case, both (1×1) areas and $(n \times 1)$ areas are visible. The $(n \times 1)$ comprises several structures, highlighted by different colors, and present at different concentrations in panels (a) and (b). In panel (a), three types of structures coexist, shown in detail in the (15 × 15) nm^2 images of panels (c, d)—the α lines and A-type (blue), B-type (green), and C-type stripes (yellow). Yellow arrows highlight the jump of C-type stripes along the [001] direction. In panel (b), α lines coexist with C'-type stripes, which originate from C-type stripes (white arrows). (f) α lines and C'-type stripes imaged at two different bias voltages. Adapted from ref. 344.

The large-scale STM images in Figs. 8.20(a, b) correspond to two high-pressure, Mn-rich surfaces with slightly different composition [Mn-richer in panel (b)] that have both been annealed at 700 °C and UHV for 45 min. Both show (1×1) patches and patches of the stripes reconstruction. As expected from the reasonings above, the initially Mn-richer surface exhibits smaller patches of the (1×1). Slight differences are also observed in the regions with the stripes.

The surface of panel (a) displays four types of structures: α lines, and structures A, B, and C. These are explored in more detail in panels (c) and (d). For reference, the top left of panel (c) reports the unit cell of the (1×1) structure, identified by the unit vectors **a** and **b**, oriented along the [001] and $[1\bar{1}0]$ directions, respectively.

- ***α* lines.** All structures discussed below share the same building block, the so-called 'α lines', some of which are highlighted in blue in Fig. 8.20. These lines run along **b**, appear with a bright contrast, and are made of round features separated by $|\mathbf{b}|$. 'α lines' can also patch together and realize the structure labeled by A in Figs. 8.20(b, c, e).

- **Structure A.** Structure A is realized when more α lines are patched together—see, *e.g.*, the three lines in Fig. 8.20(c) (notice that the outer lines realize structures B, and C, respectively). The unit cell of this structure is a $c(3 \times 1)$ centered rectangle [black, in panel (c)].

- **Structure B.** Structure B [green, see panels (a) and (c)] is the most rarely observed. It consists of two types of lines oriented along **b** that alternate along **a** with a separation equal to $|\mathbf{a}|$. One of the two is an α line. The other line possesses half the features of the α line, and appears with darker contrast. Each α line is aligned with the next α line, while closest dark lines are shifted with respect to each other by **b** [see the features highlighted by green stars in panel (c)]. The resulting unit cell (green) is a $c(4 \times 2)$ centered rectangle.

- **Structure C.** Structure C [yellow, present in all panels except panel (e)] consists of 4 lines running along **b**: The outer lines are α lines, shifted with respect to each other by half a (1×1) unit cell along **b**. The two inner lines of structure C consist of oval features with a periodicity of 3**b**. The unit cell of this structure is a (5×3) rectangle. The $3\times$ periodicity along **b** is likely the cause for this faint periodicity to be visible in the LEED pattern of Fig. 8.16(f). Notice that several C-type stripes commonly appear near one another. At times, two type-C stripes appear separated by a single α line (or, more rarely, by two α lines).

The surface of panel (b) displays again the α lines, and structures A and C. A new structure, C', is also observed:

- **Structure C'.** Structure C' [yellow, panels (b, e)] closely resembles structure C. In fact, it appears to always originate *from* structure C [white arrows in Fig. 8.20(b)]. It consists of two α lines that sandwich a wider line [see bottom half of panel (e)]. Like in the structure C, the α lines are shifted with respect to each other by half a (1×1) unit cell along **b**. Rare combinations of tip termination and tunneling conditions give the contrast observed in the top half of panel (e), where the wide line actually appears as two lines of small, round features (see yellow circles), with a periodicity of half the (1×1) unit cell along **a**.

The slight differences between the reconstructions of surfaces with different composition [such as the ones in panels (a) and (b) discussed above] are likely associated to different compositions in the stripes structures themselves.

Similarities with the $(n \times 1)$ reconstructions of $SrTiO_3(110)$. The structures described above show many similarities with the $(n \times 1)$ reconstructions of $SrTiO_3(110)$ discussed in Section 6.2.1. Not only they are all oriented along the $[1\bar{1}0]$ direction. They also all coexist at the surface and mix evenly with one another. For instance, structure C (or C') tends to alternate with a one-to-one ratio with the α lines—although deviations (*e.g.*, two α lines in between two structures C) are also observed.

Moreover, while all discussed structures run along the $[1\bar{1}0]$ direction, they tend to realize frequent jumps along the [001] direction, in a very similar fashion to the $(n \times 1)$ reconstructions of $SrTiO_3(110)$ (see Fig. 6.6 in Chapter 6). Some of the jumps realized by structure C are highlighted by yellow arrows in Fig. 8.20. These similarities support the idea that the different stripes structures are characterized by slightly different cation compositions, similarly to the $(n \times 1)$ structures of $SrTiO_3(110)$.

8.4.3 Building a 2D surface phase diagram

The complexity of the structures discussed above hinders us from building the corresponding atomic models at the present stage. As already discussed for the high-pressure phase diagram of LSMO(110) (Section 8.2), a first necessary step to reach this goal is to identify the relative compositions of the surface structures. Section 8.2 has shown that monophase samples can be realized by depositing a controlled amount of Mn in PLD, and relative compositions can be determined by exploiting the movable QCM device. However, because of the phase separation discussed above, this approach cannot be implemented to derive the relative compositions of the low-pressure structures.

This Section presents another strategy, based on STM, that can be used to derive the composition of given surface structures forming during a phase separation. This ap-

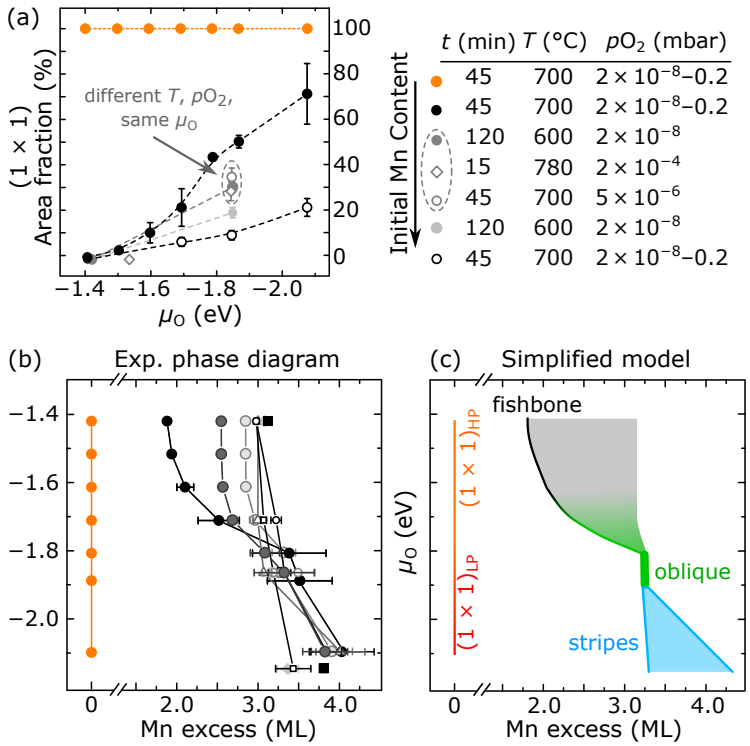

Figure 8.21. Building a 2D surface phase diagram for the surface reconstructions of LSMO(110). (a) STM quantification of $(1 \times 1)_{LP}/(1 \times 1)_{HP}$ areal coverages as a function of μ_O (refer to Section 5.2 for the definition of μ_O). The monophase (1×1) surface that is stable over a wide range of μ_Os (orange), while Mn-rich surfaces phase-separate into Mn-richer areas and (1×1) areas that grow larger with decreasing μ_O. Full circles correspond to Fig. 8.17 (starting surface: fishbone). The other curves were obtained starting from Mn-richer surfaces. When employing different combinations of T, p_{O_2}, but all equivalent to the same value of μ_O [dashed circle], similar coverages are obtained. (b) Experimental two-dimensional surface phase diagram of LSMO(110), mapping out the stability regions of the surface reconstructions of LSMO(110) as a function of the oxygen chemical potential (vertical axis) and the Mn chemical potential (bottom axis, expressed in monolayers of Mn referred to the (1×1) structure). Each curve describes the evolution with decreasing μ_O of a surface with a given composition prepared at high pressure (0.2 mbar, 700 °C). The curves are obtained under the assumption that the average surface composition is preserved, and based on the relative coverage of the coexisting phases. Adapted from ref. 344.

proach allows organizing all the reconstructions observed on LSMO(110)—both high- and low-pressure—in a two-dimensional surface phase diagram as a function of the cation composition and the oxygen chemical potential. Crucial to this approach is the fact that the overall surface cation composition is preserved at each annealing step, and that the changes in local composition are induced by Mn traveling across the surface: As argued below, under these circumstances the relative composition of the coexisting reconstructions can be derived from their relative coverage, which is measurable by STM.

To realize the two-dimensional phase diagram, the (1×1) surface was taken as a reference, since its cation composition does not change with the oxygen chemical potential. Several high-pressure surfaces with different Mn composition were prepared, and annealed at decreasing p_{O_2}. At each step, the coverage of the (1×1) areas was quantified by acquiring 10–12 STM images on a 300×300 nm^2 scale on different positions on the

sample. Each surface was also regularly annealed back to oxidizing conditions to cross check the reproducibility of the changes. Figure 8.21(a) reports the quantification of (1×1) coverages for a few selected examples. In orange, the coverage of the (1×1) areas starting from a (1×1) monophase surface: Since the surface remains monophase and (1×1) at all conditions, the plot with μ_O is simply a constant, 100% coverage. The full circles represent the quantification for the experiment illustrated in Fig. 8.17, *i.e.*, starting from a monophase fishbone surface. As anticipated, the coverage of the (1×1) areas steadily increases with more reducing conditions. This increase of (1×1) areas with decreasing μ_O is also observed for starting Mn-richer surface compositions (gray), albeit with a smaller slope: Mn-richer surfaces tend to form less of the Mn-poor (1×1) areas. Importantly, when different combinations of temperature and oxygen pressure are employed for annealing the same surface, but all resulting in the same value of μ_O (dashed circle), the same phases are observed on the surface, and with the same quantitative coverages: This means that, for a given initial Mn enrichment, the value of μ_O uniquely determines the resulting surface phases. In turn, this means that the phase separation observed is the result of thermodynamic equilibrium at the surface. This is further supported by the fact that no quantitative difference was observed upon annealing selected surfaces at fixed parameters for longer times.

Figure 8.21(b) shows the quantitative two-dimensional phase diagram of LSMO(110) as a function of both, the Mn content on the surface, and the oxygen chemical potential, as derived by the quantitative evaluation of the (1×1) coverages of Fig. 8.21(a). In Fig. 8.21(b), each curve describes the evolution of a surface with given composition (horizontal axis) prepared at high pressure (0.2 mbar, 700 °C), and then annealed at decreasing μ_O (vertical axis). For instance, the left-most curve represents the evolution of the initially monophase (1×1) surface. As its composition does not change upon annealing at reducing conditions, its evolution with μ_O is simply represented by a straight line as a function of the Mn content. The solid black circles represent instead the evolution of the initially monophase fishbone reconstruction of Fig. 8.17, which at lower pressures phase-separates into (1×1) areas and regions characterized by low-pressure, Mn-richer structures (the tilted fishbone, and the oblique and stripes described above). The other curves represent surfaces that have been initially prepared to exhibit a slightly Mn-richer structure [between the fishbone and the (2×1)]. Notice that the plot reveals the composition of the low-pressure structures of LSMO(110). For instance, the oblique possesses $\approx$3.2 ML Mn more than the (1×1).

To plot the phase diagram, the number of cations on the whole surface was taken as constant at each annealing step, as justified by the reasonings above. This hypothesis can

be expressed as $n = \sum_i n_i \times \theta_i = const$, where n is the density of Mn cations for a surface with one or two structures exposed, characterized by density of Mn cations n_i and areal coverage θ_i, which is quantified as in Fig. 8.21(a). Initially (at high pressure) the surface exposes only a monophase, Mn-rich surface. Since in this case the coverage of the (1×1) is zero, the density of Mn cations at the surface is simply the one of the exposed high-pressure structure, henceforth labeled as 'HP'. This reads as $n = n_{HP}$, or, when referring the densities to the one of the (1×1) structure, as $n' = n_{HP} - n_{(1\times1)} = n'_{HP}$, where n'_{HP} is known from the phase diagram of Fig. 8.16 (for instance, for the fishbone, n'_{HP}=1.88). When annealing at low pressure, and the surface phase separates into (1×1) areas and new Mn-rich areas ('LP'), one has that $n' = n'_{LP} \times \theta_{LP}$, where n'_{LP} is the (unknown) density of Mn cations on the new LP phase, referred to the density of Mn cations of the (1×1), and θ_{LP}=1–$\theta_{(1 \times 1)}$ is the corresponding areal coverage (known from STM). Since $n' =$ const by assumption (see Fig. 8.18), one obtains that $n'_{LP} \times$(1–$\theta_{(1 \times 1)}$)=n'_{HP}. The only unknown, n'_{LP}, *i.e.*, the composition of a given low-pressure structure relative to the composition of the (1×1), can be derived and plotted in the phase diagram of Fig. 8.21(b). A simplified sketch of the diagram is reported in Fig. 8.21(c).

It is worth noting that most of the investigated structures belong to a single family in which a minor change of the cation composition induces a slight modification of the surface structure. This was previously observed for the high-pressure reconstructions between the fishbone and the (2×1) (Fig. 8.5), and for the low-pressure 'stripes' described above. In both cases, these related structures are identified by 'coexistence' regions in the sketch of Fig. 8.21(d) (gray and blue, respectively).

It is premature to generalize whether the reported surface phase separation with μ_O is a shared property of multi-component perovskite oxides. However, phase separations as a function of the cation content has been observed in several other cases. The approach outlined in this Section is an unconventional and powerful tool to experimentally establish the stability regions of the surface reconstructions of complex materials in the presence of a surface phase separation. At the same time, it allows for quantitatively determining the cation composition of complex reconstructions.

8.5 Conclusions

This Chapter has unveiled for the first time the surface reconstructions intrinsic to the (110) termination of LSMO. PLD has been combined with surface science tools to explore in depth the details of these surface reconstructions and the relations between them. It was shown that LSMO(110) exhibits several composition-related surface phases with

unique structural and electronic properties, which can be controlled in various ways: (i) By depositing sub-monolayer amounts of La or Mn by PLD (accurately quantified with the movable QCM of Section 2.5), (ii) by Ar^+ sputtering (both followed by O_2 annealing), or (iii) by annealing at different oxygen chemical potentials. The latter forces an unusual phase separation of the surface, in distinct A-site-rich and Mn-rich areas, while the overall cation composition is preserved. With decreasing μ_O, larger areas of the A-site-rich reconstruction are exposed, while the rest of the surface gets enriched in Mn, producing a corresponding change in the surface atomic structure. Based on the evaluation of the relative coverages of A-site-rich and Mn-rich areas at each step, the two-dimensional phase diagram of the surface reconstructions of LSMO(110) was drawn, as a function of both, the Mn content, and the oxygen chemical potential.

A DFT model has been proposed for the simplest of the structures, an AO_x-terminated (1×1). The other reconstructions are too complex and possess too large unit cells for standard DFT methods. New theoretical tools, *e.g.*, based on machine-learning concepts, could be successful in solving these structures in the future.

The results outlined in this Chapter portray a first full, albeit preliminary, picture of the atomic-scale details of the LSMO(110) surfaces. They build the foundation for developing quantitative structural models needed to understand basic phenomena driving LSMO-based devices at different environmental conditions. On a more fundamental level, the knowledge built for the LSMO(110) surfaces might be insightful for other, similarly complex, materials.

9. $La_{0.8}Sr_{0.2}MnO_3$(110): Understand and optimize film growth

9.1 Introduction

As anticipated in the previous Chapter 8, there exist no literature reports of LSMO films thicker than a few nanometers and with atomically smooth surface topologies suited for atomic-scale investigations. The likely reason is that film morphology of LSMO—along with its composition, and its transport and magnetic properties—appears to be very sensitive to the growth conditions.[41,58,288,289,293,345,346]

Motivated by the need of growing atomically flat LSMO films of the desired stoichiometry ($La_{0.8}Sr_{0.2}MnO_3$), this Chapter addresses the role of one crucial growth parameter, the oxygen pressure (p_{O_2}), on the composition and morphology of LSMO films grown on $SrTiO_3$(110), along the lines of the STM studies on the $SrTiO_3$(110) homoepitaxy performed as a function of the laser fluence (see Chapters 6 and 7). Similarly to the case of $SrTiO_3$, the surface atomic structure appears to play a crucial role for the development of given morphologies. Once again, (at least part of) the nonstoichiometry introduced during growth segregate to the film's surface, thus changing the surface atomic structure according to a given compositional surface phase diagram (in the case of LSMO, the one established in Chapter 8, see Fig. 8.2). However, when the introduced nonstoichiometry overcomes a certain limit, the surface no longer manages to incorporate it by changing its atomic structure: A phase separation takes place, with clusters of the excess material appearing at the surface.

Section 9.2 will first address the changes observed in thin films (of ≈2.5 nm thickness) as a function of the value of p_{O_2} used during growth. The focus will shift then to thicker films, showing how non-ideal conditions can cause the excess cations to form undesired, ill-defined clusters. Section 9.3 is devoted to the experimental strategies that can be used to remove these clusters and recover ideal morphologies. Finally, Section 9.4

shows how STM can be used to pinpoint the growth conditions that yield LSMO(110) films with ideal composition and morphology, by monitoring the changes of the surface structure with STM at different steps of the growth, and changing the O_2 pressure accordingly. Section 9.5 summarizes the bulk properties of the films grown at the most promising conditions, as addressed by XRD, TEM, and RBS.

9.2 Role of growth parameters on film composition and morphology

9.2.1 Thin films (≈2.5 nm-thick)

Several thin films have been grown at the same nominal conditions (700 °C, 1 Hz, 2 J/cm^2), except for the O_2 pressure, ranging from 7×10^{-6} to 0.2 mbar. All films have the same thickness of 2.5 nm, or nine layers, where one layer corresponds to one full RHEED oscillations measured during growth [for one representative example, see Fig. 9.3 below], or the separation between two (110) planes, *i.e.*, 0.276 nm. The XPS analysis of the relevant core-level peaks (Mn 2*p*, La 4*d*, Sr 3*d*) in Fig. 9.1(a) reveals that the film composition is in-

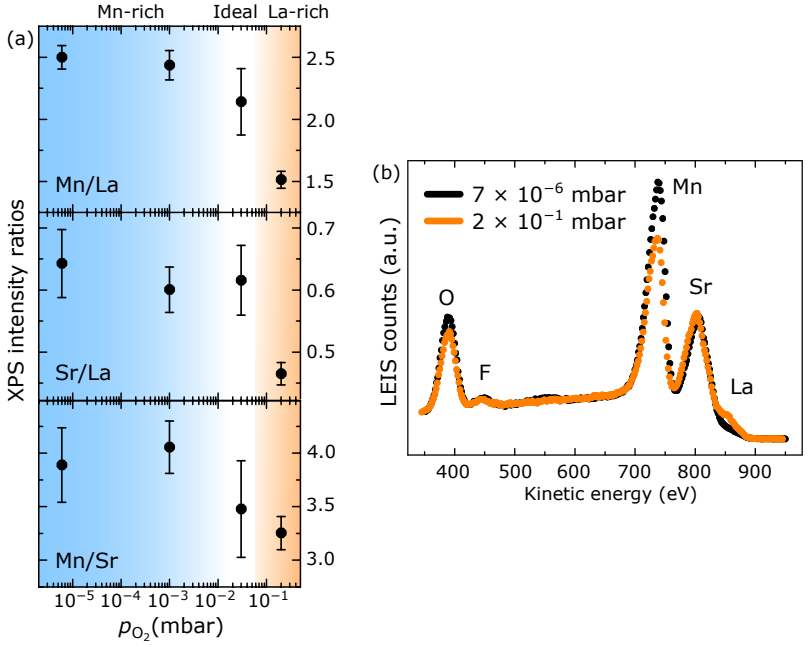

Figure 9.1. XPS (a) and LEIS (b) analysis of the surface composition of thin (≈2.5 nm) LSMO(110) films as a function of the oxygen pressure used during growth, while keeping the other parameters unchanged. Lower growth pressures are associated with a higher Mn content in the film surface. All areas of the XPS peaks (Mn 2*p*, Sr 3*d*, La 4*d*) were evaluated after subtraction of a Shirley-type background. The small F peak in the LEIS spectra originates from contamination in the analysis chamber (the peak is not present when samples are measured immediately after growth).

fluenced by the O_2 pressure employed during growth. The peak intensity ratios of light elements over heavier elements always decrease with the pressure. As a result, films grown at low pressure are richer in Mn (the lightest cation) than those grown at more oxidizing conditions. For reference, the LEIS spectra of the films grown at the highest and lowest pressures is also reported [Fig. 9.1(b)]. Consistent with the XPS results, the surface of the film grown at the lowest pressure is richer in the A-site species.

The STM morphologies of the corresponding films are shown in Figs. 9.2(a–d). On the scale of few hundreds of nanometers (top row), all films appear atomically flat, with terrace sizes up to hundreds of nanometers separated by monoatomic steps, and exposing up to four layers. On a smaller scale (bottom row), different reconstructions are evident. Note that the reconstructions of Figs. 9.2(a, b, c) are the same obtained by purposely changing the composition of the surface of LSMO(110) films by depositing submonolayer amounts of Mn followed by high-pressure O_2 annealing (Fig. 8.2, Section 8.2): Panels (a), (b), and (c) display the $(n \times 2)$, fishbone, and a reconstruction between the fishbone and the (2×1), respectively. The reconstruction of Fig. 9.2(d) was not observed while tuning the surface composition of LSMO(110) at high p_{O_2}, likely because the corresponding film was grown at low values of p_{O_2}. Consistent with the XPS findings, the reconstruction present on the films grown at low pressure are richer in Mn (cf. bottom

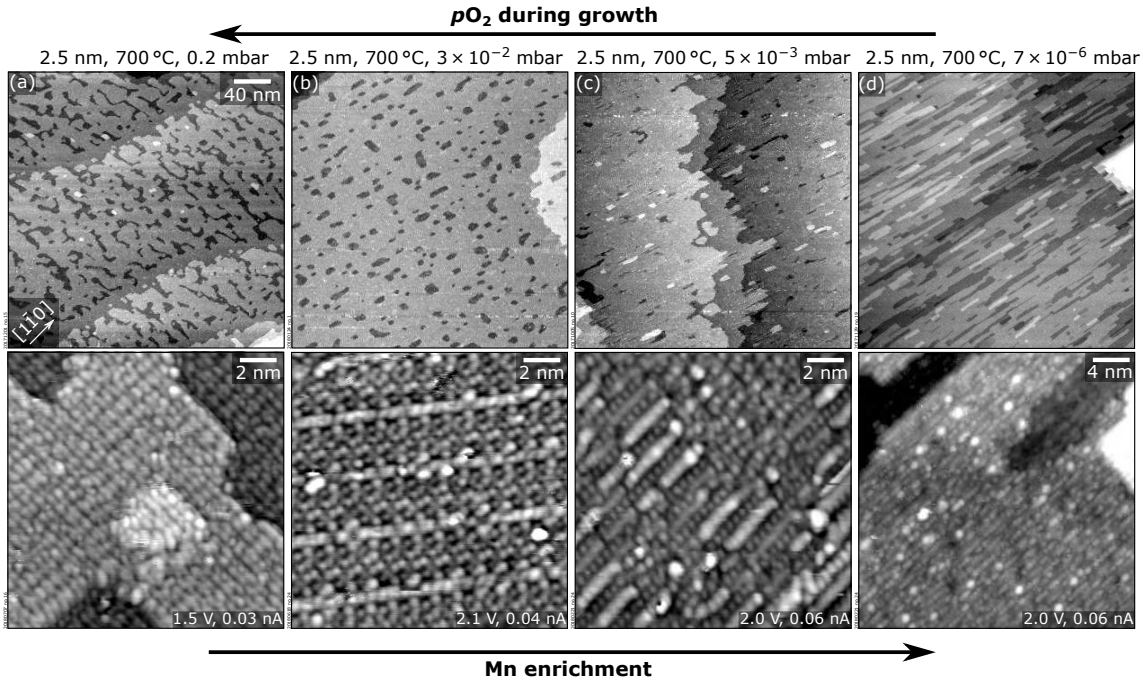

Figure 9.2. Effect of the oxygen growth pressure on the morphology of LSMO(110) films. (a–d), top row: 300 × 300 nm^2 STM images (U_{sample} = 2 V, I_t = 0.2 nA) of films of 2.5 nm thickness grown at pressures ranging from (a) 0.2 mbar to (d) 7 × 10^{-6} mbar (700 °C, 1 Hz, 2 J/cm^2); bottom row: corresponding close-up STM images [(a–c) 15 × 15 nm^2; (d) 30 × 30 nm^2, high-pass-filtered for displaying purposes], highlighting the differences in the atomic-scale morphologies.

axis of Fig. 8.2).

Monitoring the specular spot of the RHEED intensity in real time reveals that the growth occurs in a layer-by-layer fashion over the entire pressure range (Fig. 9.3). Qualitative differences are evident in the shape and in the intensities of oscillation minima and maxima. As argued in Chapter 6, these differences are at least partially caused by the different reconstructions that form at different pressures, which produce changes in the diffraction geometry, originally optimized for the $SrTiO_3$(110)-(4 × 1) substrate. The more pronounced decay observed when growing at the lowest pressure [Fig. 9.3(c)] may be also partially due to the slightly rougher surface morphology. Notice that the period of the oscillations increases with the pressure, suggesting that less and less material reaches the substrate.

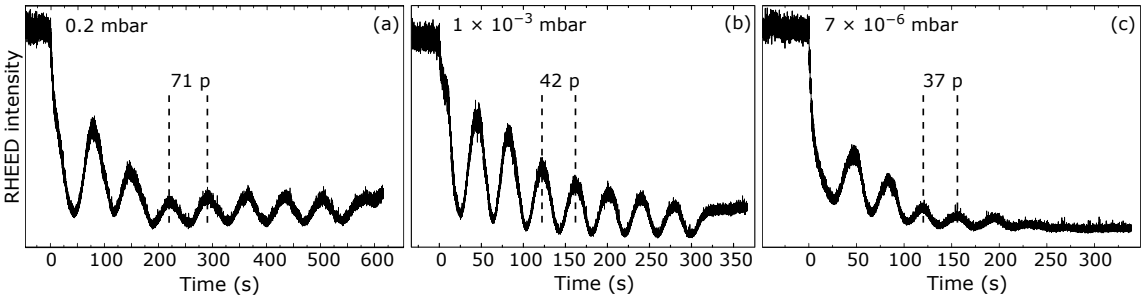

Figure 9.3. RHEED oscillations during the growth of thin LSMO(110) films (≈2.5 nm-thick) at different O_2 pressures (indicated in the respective panels), and otherwise identical parameters (700 °C, 1 Hz, 2 J/cm^2).

9.2.2 Thicker films

When thicker films are deposited at the same conditions as per Figs. 9.2(a–d), the surface remains atomically flat only in a narrow range of pressures, see Fig. 9.4. Figure 9.4(b) shows an atomically flat film of 132 nm thickness grown at 3×10^{-2} mbar O_2. At higher and lower p_{O_2} [0.2 mbar, Fig. 9.4(a), and 5×10^{-3} mbar, Fig. 9.4(c), respectively], clusters appear on the surface that are few nanometers high and poorly conductive. Note that the defected films are significantly thinner, *i.e.*, only 11 and 5.5 nm-thick in Figs. 9.4(a) and (c), respectively. Growing thicker films at these conditions results in severely roughened surfaces that cannot be measured in STM.

9.2.3 Discussion

Growth parameters and film composition

As seen above, the O_2 background gas dramatically affects the composition and the surface morphology of the LSMO(110) films. As argued already in Section 2.3.1, changes in

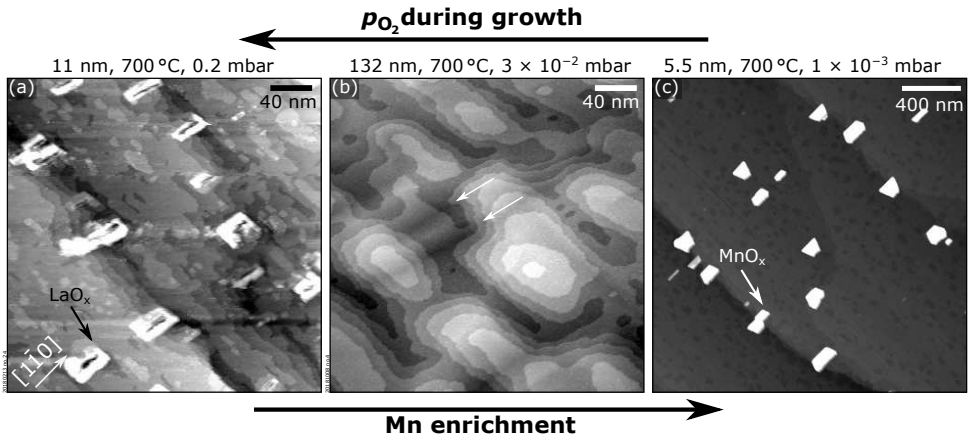

Figure 9.4. Accumulation of nonstoichiometry at the surface of LSMO(110) films. (a, b) 300 × 300 nm^2 STM images and (c) 2.1 × 2.1 µm^2 AFM image of LSMO(110) films thicker than 15 ML (5.5 nm). (a, c) Nonstoichiometric growth conditions result in poorly conductive, few nanometers-high features on the surface that are identified as lanthanum- and manganese-oxide-rich clusters from XPS analysis, respectively; (b) ideal stoichiometries correspond to atomically flat films.

the film composition as a function of p_{O_2} are expected, and can be qualitatively explained in the three-pressure-regimes framework: At sufficiently low p_{O_2}, the ablated material is transferred congruently to the substrate. In some intermediate range, lighter species are scattered more than heavier ones, such that the film is enriched with the heavier species as the pressure increases.[41] At very high pressures, in the so-called shock-wave regime, all species are slowed down equally and kept confined, and are transferred congruently from target to substrate.[41,52,74] As already mentioned, these three pressure regimes cannot be identified with the value of p_{O_2} alone, as the target-to-substrate distance (D) can also affect the transfer of material from target to substrate.[58] For the specific value of D = 55 mm used in this work, the low-pressure regime is realized at $p_{O_2} \leq 5 \times 10^{-3}$ mbar: Below this pressure, there is no change in the XPS signal in Fig. 9.1, a strong indication of congruent transfer of the ablated species typical of this regime. The intermediate pressure regime corresponds to $3 \times 10^{-2} \leq p_{O_2} \leq 0.2$ mbar: Within this range, the Mn content decreases with increasing pressure (Mn is the lightest cation in LSMO). Above 0.2 mbar, the shock-wave regime takes place: The growth rate at 1 mbar is roughly ten times smaller with respect to the lower pressures (not shown). This model is consistent with the increased period of the RHEED oscillations with increasing pressure (Fig. 9.3). Note, however, that the model is overly simplistic, as it does not account for any interaction among the ionized species in the plasma plume. Nonetheless, it describes qualitative trends accurately.

As argued in Chapter 6 while discussing the homoepitaxial growth of $SrTiO_3(110)$, not only the oxygen background pressure, but also the laser fluence can affect the film composition, as it determines which species are preferentially ablated from the target.

As a result, near-ideal stoichiometries can be achieved in two ways: (i) with congruent ablation and congruent transfer, by using perfectly calibrated laser fluences and depositing within the low-/high-pressure regimes; (ii) with incongruent ablation and incongruent transfer, by mitigating the nonstoichiometry caused by preferential ablation of the target via interaction with the background gas in the intermediate-pressure regime. Despite its appeal, the first scenario is not easy to implement: The laser fluence is scarcely reproducible among different PLD setups,[68] and the most common way to adjust the UV pulse energy, by changing the discharge voltage of the UV laser, hinders accurate calibration.[76] LSMO(110) films with ideal stoichiometry have been grown within the second scenario. In fact, the RBS analysis performed on the film of Fig. 9.4(b) grown in the intermediate pressure regime reveals its stoichiometry to be nearly ideal, *i.e.*, very close to that of the target (see Section 9.5). From comparison with the XPS data in Fig. 9.2(d), one then infers that films grown at lower and higher pressures are Mn rich and Mn deficient, respectively. One thus concludes that at the chosen laser fluence Mn is preferentially ablated at the target: Mn-rich films are obtained at low pressures because the composition of the Mn-enriched plume is not affected by scattering with the background gas. The ideal stoichiometry is achieved at a specific value of the intermediate pressure such that the excess Mn is scattered preferentially over the heavy La species, until, at even higher pressures, more than the excess Mn is preferentially scattered, and the films grow La-rich. The preferential ablation of Mn at the target is possibly caused by a too-low laser fluence (Mn is characterized by a higher vapor pressure than La). Section 9.4 will lay out an STM-based strategy to pinpoint the optimal background pressure that yields ideal film composition and morphology.

Link between composition, surface structure, surface morphology

When the films are sufficiently thin, the morphology remains atomically flat regardless of the composition. The surface structure evolves along the compositional phase diagram of Fig. 8.2, similarly to what observed during the homoepitaxy of $SrTiO_3$(110) (Chapter 6). This suggests that the nonstoichiometry introduced during growth segregates (at least partially) to the surface. As the film thickness increases, this nonstoichiometry keeps accumulating at the surface, up to the point where the surface is not able to accommodate it anymore by modifying its atomic structure: A secondary phase caused by the excess cations develop in the form of the observed clusters [Figs. 9.4(a, c)], which are assigned to secondary MnO_x and LaO_x phases [similar clusters were also observed after excessive deposition of MnO_x and LaO_x on well-defined LSMO(110) surfaces].

Note that for very slightly nonstoichiometric conditions and/or sufficiently thin films, the surface-dependent re-evaporation discussed in Section 8.2.6 (less Mn and La species

incorporated on Mn-rich and La-rich surfaces, respectively, see Fig. 8.8) could act as a beneficial feedback mechanism for the film stoichiometry (and morphology). For example, if the flux is slightly La-rich, the surface will gradually shift towards A-site richer reconstructions, onto which Mn 'sticks' more, such that the surface shifts back towards Mn-richer structures. Now La sticks more, and so on. The forgiveness of this growth mechanism may allow to grow atomically flat and stoichiometric films even under slightly nonstoichiometric conditions. Oxide clusters will be formed when the introduced cations become excessive for the surface. Note that, with respect to the case of $SrTiO_3$(110), the surface reconstructions of LSMO(110) are separated by larger compositional differences (cf. bottom axis of Fig. 6.3 and of Fig. 8.2). As a result, larger deposited nonstoichiometry can be accommodated at the surface of LSMO(110) films, yielding the growth of atomically flat films over a larger window of growth parameters.

9.3 Recovering ideal morphologies

The previous Section has shown that rough morphologies tend to develop if the growth is not realized under optimal conditions. This Section discusses how ideal morphologies can be recovered with appropriate UHV treatments. One must distinguish between two situations. The first one is the best-case scenario, when clusters are present on the film's surface, but most of it still consists of atomically flat terraces, *e.g.*, as per the films in Figs. 9.4(a, c). In this case, ideal morphologies can be recovered by Ar^+ sputtering followed by O_2 annealing at high pressures (0.2 mbar). Figures 9.5(a–c) show the evolution of the morphology of the film of Fig. 9.4(a), *i.e.*, with LaO_x-rich clusters at the surface, as a function of the sputtering time (after each sputtering cycle, the sample was annealed for 1 h at 700 ° and 0.2 mbar O_2). After 13 min [Fig. 9.5(b)], the clusters reveal themselves as

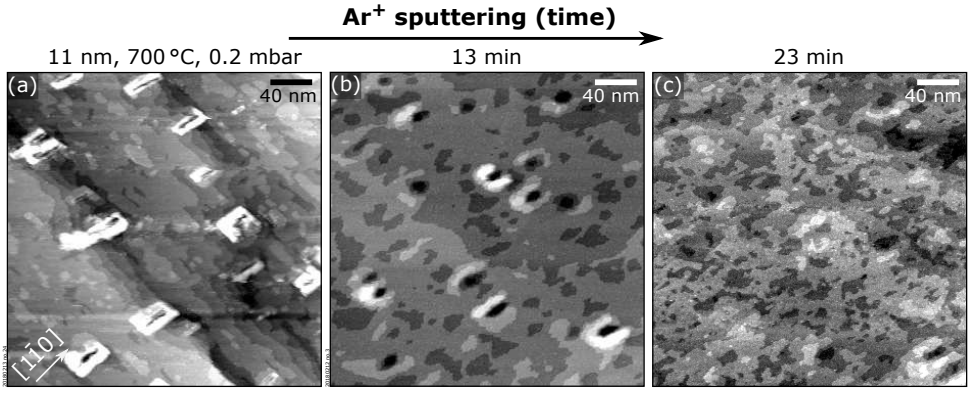

Figure 9.5. Recovering ideal morphologies of LSMO(110) films by sputtering-annealing cycles. (a–c) 300×300 nm^2 STM images, showing the improvement of the surface morphology of a LSMO(110) initially exhibiting a few $LaOx$-rich clusters.

pits similar to those formed on $SrTiO_3(110)$ homoepitaxial films grown at Ti-rich conditions [Fig. 6.11(d_1)]: Few-layers-high rims surround few-layers-deep holes, whereas the rest of the surface consists of flat terraces. This strengthens the hypothesis discussed in Chapter 8 that sticking/re-evaporation effects similar to those observed during the nonstoichiometric growth of $SrTiO_3$ (Chapter 6) are in play also for LSMO(110). Further sputtering the surface removes almost all the pits [Fig. 9.5(c)]. Note that Ar^+ sputtering plus O_2 annealing preferentially removes Mn over A-site species (see Chapter 8). Consistently, the surface structure of the film shown in Fig. 9.5 progressively evolve towards A-site richer structures, as inferred by comparison with the high-pressure surface phase diagram of Fig. 8.2.

The other seemingly unfortunate scenario is when the clusters dominate the film morphology [see, for example, Fig. 9.6(a)]. In this case, the surface cannot be recovered by Ar^+ sputtering plus annealing at high p_{O_2}, as demonstrated by Figs. 9.6(b–d). While the number of exposed layers diminishes with increasing sputtering–high-pressure-annealing cycles, many pits remain present [see Fig. 9.6(c) after 5 cycles]. Annealing significantly longer at the same conditions gives only a minor improvement

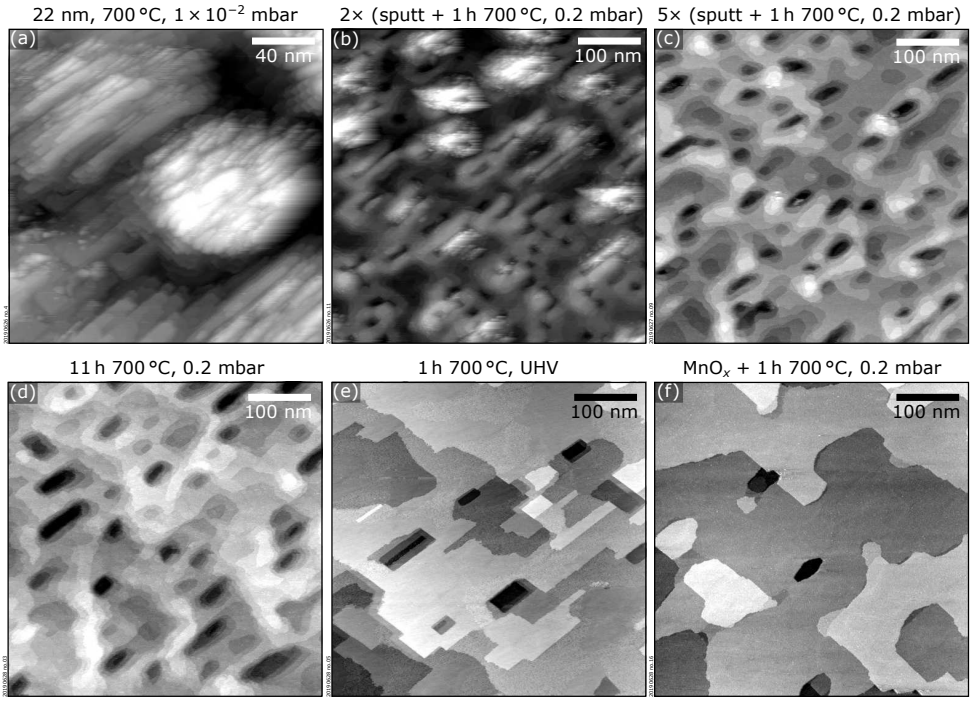

Figure 9.6. Recovering ideal morphologies of LSMO(110) films by annealing at reducing conditions, as seen from 200 × 200 nm^2 (a) and 500 × 500 nm^2 (b–f) STM images. Sputtering plus high-pressure oxygen annealing (1 h, 700 °C, 0.2 mbar) is partially effective in removing the excess material localized at the clusters (b, c). However, holes that are a few nanometers deep remain present at the surface (c), even after 11 h annealing at the same conditions (d). With only 1 h annealing at reducing conditions (700 °C, UHV), the surface morphology improves dramatically (e). An ideal morphology is obtained after depositing MnO_x (followed by high-pressure oxygen annealing), meant to recover the desired stoichiometry and surface structure (f).

[Fig. 9.6(d)]. It was found that the quicker and most effective way to recover the surface is to anneal at more reducing conditions: After annealing for 1 h at the same temperature but in UHV, only a few pits remain on the surface, and the number of exposed layers decreases drastically [Fig. 9.6(e)]. As discussed later in Chapter 11, this is assigned to the oxygen chemical potential during annealing that determines the diffusivity of the surface species, hence, in large part, the surface morphology. Note that the multiple sputtering cycles have depleted the surface from Mn, changing its surface reconstruction. To recover the surface termination of interest, Mn was deposited followed by annealing again at high p_{O_2} [Fig. 9.6(f)]. The final quality of the surface is ideal: It exhibits hundreds-of-nanometers-wide, atomically flat terraces, with the desired reconstruction exposed.

9.4 STM helps to grow atomically flat, stoichiometric films

Chapter 7 has shown how non-ideal values of the laser fluences during the homoepitaxial growth of $SrTiO_3$(110) introduce cation excesses. These accumulate at the film's surface, changing its atomic structure according to a known compositional surface phase diagram. By measuring the changes in the surface structure upon growth with STM, one can quantify the introduced nonstoichiometry with great accuracy.

As discussed above, there are multiple indications that the nonstoichiometry introduced in LSMO(110) films grown under non-optimal conditions also accumulate (at least partially) to their surface. As a result, also in this case, the film surface structure changes according to an established compositional surface phase diagram (Fig. 8.2). The following discussion shows how one can pinpoint the optimal growth conditions by exploiting these changes in the surface structure during growth.

To identify the exact value of p_{O_2} for the growth of LSMO(110), several thin films were grown at values of p_{O_2} in the optimal range identified by RBS and XPS (*i.e.*, around 10^{-2} mbar, Section 9.5), and the corresponding changes in the surface structure were monitored by STM. To start from a reproducible starting point, prior to each growth experiment the surface was prepared to exhibit the fishbone reconstruction of Fig. 8.2(c). Figure 9.7 summarizes the results [for reference, the top row reports the high-pressure surface phase diagram of LSMO(110)]. At first, 5 nm were grown at 2.0×10^{-2} mbar. The resulting surface [Fig. 9.7(g)] is still atomically flat, but it exhibits patches of the $(m \times 1)$ structure of Fig. 9.7(d), an indication for this pressure to cause a strong Mn enrichment. In fact, by growing a film twice as thick at these conditions, one observes the formation

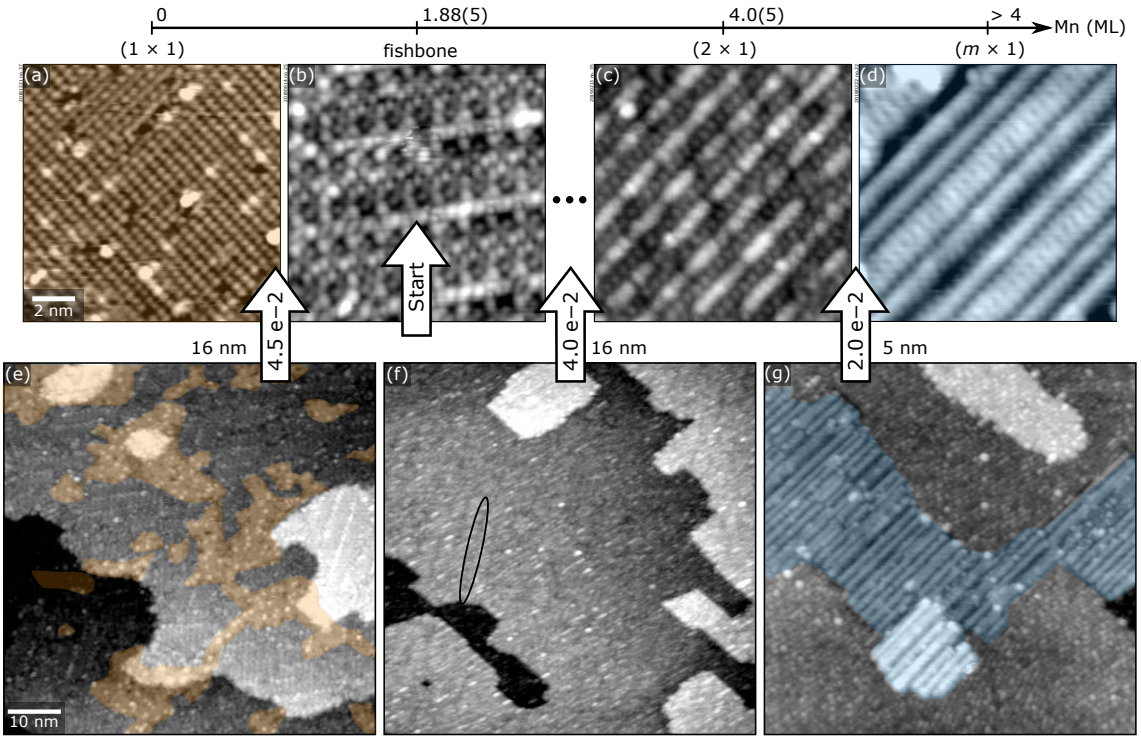

Figure 9.7. Using STM to pinpoint the optimal value of oxygen pressure to grow LSMO(110) films. (a–d) 12 × 12 nm^2 STM images of selected reconstructions of the 'high-pressure' surface phase diagram of LSMO(110) of Fig. 8.2. (e–g) 70 × 70 nm^2 STM images of LSMO films of various thicknesses, grown at different oxygen background pressures, and always starting from LSMO(110) films displaying the fishbone reconstruction of panel (b). (g) 5 nm-thick film grown at 2 × 10^{-2} mbar O_2, displaying patches of the Mn-rich (m × 1) structure of panel (d). (f) 16 nm-thick film grown at 4 × 10^{-2} mbar O_2, showing a surface reconstruction in between the fishbone and the (2 × 1). (e) 16 nm-thick film grown at 4.5 × 10^{-2} mbar O_2, showing patches of the (1 × 1) and of the fishbone reconstructions.

of clusters similar to those of Fig. 9.4(c).

As suggested by the results in Fig. 9.1, one can increase the value of p_{O_2} to reduce the amount of Mn introduced in the film during growth. By growing a film of the same thickness (5 nm) at double the value of pressure, *i.e.*, 4.0 × 10^{-2} mbar, no appreciable change in the surface structure is observed (not shown). However, by increasing the film thickness, a slight Mn enrichment of the surface is again detected: The surface of the 16 nm-thick film of Fig. 9.7(f) shows a co-existence of the fishbone reconstruction (solid oval) and of the 'advanced' fishbone reconstruction of Figs. 8.5(c, d). Also in this case, one cannot increase the thickness indefinitely, as the excess Mn cations, progressively accumulated at the surface, soon cause the formation of MnO_x clusters. By further increasing the value of p_{O_2} to 4.5 × 10^{-2} mbar, one moves to the opposite side of the surface phase diagram, realizing patches of the (1 × 1) reconstruction that coexist with fishbone-reconstructed areas. Figure 9.7(e) shows the STM appearance of the surface of a film of 16 nm thickness grown at such conditions. By choosing a growth pressure intermediate between the last two trials, *i.e.*, 4.2 × 10^{-2} mbar O_2, a smaller areal cover-

age of the (1 × 1) patches is observed for a comparable thickness [Fig. 9.8(a)]. At these conditions, one can grow a film up to 80 nm thickness that is atomically flat [Fig. 9.8(b)]. Atomically flat films were subsequently achieved by growing in one shot at these conditions. Note that each set of experiments require independent optimization (still within the optimal range of pressure identified): For instance, it was found that the composition of the plasma plume is highly sensitive to the aging of the UV laser.

The films described above have been grown at different pressures, each time repreparing the surface to exhibit the fishbone reconstruction. Another strategy to obtain ideal morphologies does not involve repreparing the surface: One can grow at given parameters, observe the change of the surface structure with STM, and grow on top with some other parameters that counteract the effect of the previous ones. For example, if the chosen pressure gives a Mn enrichment (p_{O_2} too low), one can grow on top with a La-enriching (*i.e.* higher) pressure, letting the surface structure compensate for the introduced nonstoichiometry.

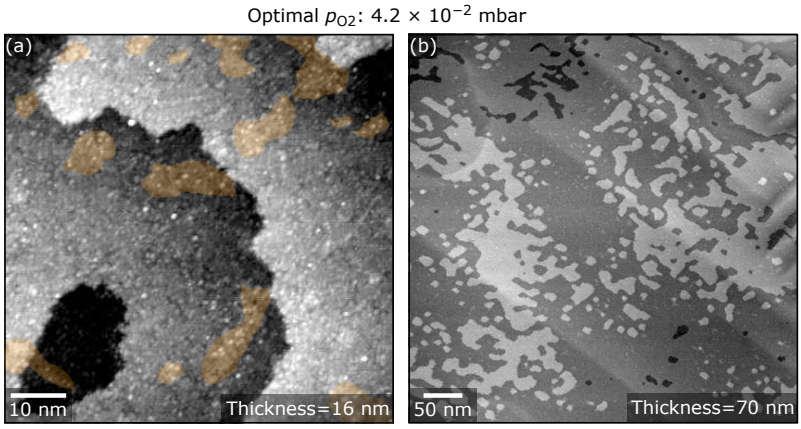

Figure 9.8. LSMO(110) film grown at optimized conditions. (a, b) 70 × 70 nm^2 and 500 × 500 nm^2 STM images of 16 nm-thick and of 70-nm-thick LSMO(110) films, respectively, grown onto a fishbone-reconstructed LSMO(110) surface at 4.2 × 10^{-2} mbar O_2. Both morphologies are atomically flat. At the atomic scale, (1 × 1) patches are visible [orange in panel (a)].

9.5 Bulk characterization of ideal films

The bulk properties of the films grown at the most promising conditions [yielding the atomically flat film of Fig. 9.4(b)] were investigated by means of XRD and RBS (Fig. 9.9) to establish the bulk structure and the composition of the film, and to provide the needed details for future computational modeling of the LSMO surfaces.

A preliminary analysis of the XRD results [Figs. 9.9(a, b)] shows that the LSMO films are largely pseudomorphically matched with the $SrTiO_3$ substrate, and do not exhibit the in-plane distortions expected for a rhombohedral structure. The small relaxation

visible from asymmetric XRD is possibly correlated with the modulation visible in STM [white arrows in Fig. 9.4(b)]. The film relaxation could cause the formation of buried dislocations that appear as a 0.1 nm-high modulation on the film surface. A deeper analysis is undergoing and will establish the exact value of the lattice parameter of the films and the relaxation.

RBS was used to quantify the stoichiometry of the films [Fig. 9.9(c)]. It corresponds to $(La_{0.78\pm0.03}Sr_{0.22\pm0.03})_{1.06\pm0.05}MnO_3$, which is in reasonable agreement with the intended $La_{0.8}Sr_{0.2}MnO_3$. Note that the oxygen content cannot be reliably evaluated from RBS measurements. Note also that other available techniques that were tested (XPS, TEM, ICP-MS) could not deliver a reliable estimate of the film stoichiometry. The use of XPS for quantitative estimates was hindered by significant forward focusing effects and the lack of reliable reference samples for the single elements. TEM was problematic due to the preparation of the lamellas by Ar^+ milling: Because Ar^+ preferentially removes Mn, different compositions were obtained as a function of the lamella's thickness. Preferential dissolution of cations and the presence of Sr both in the films and substrate hindered the use of ICP-MS.

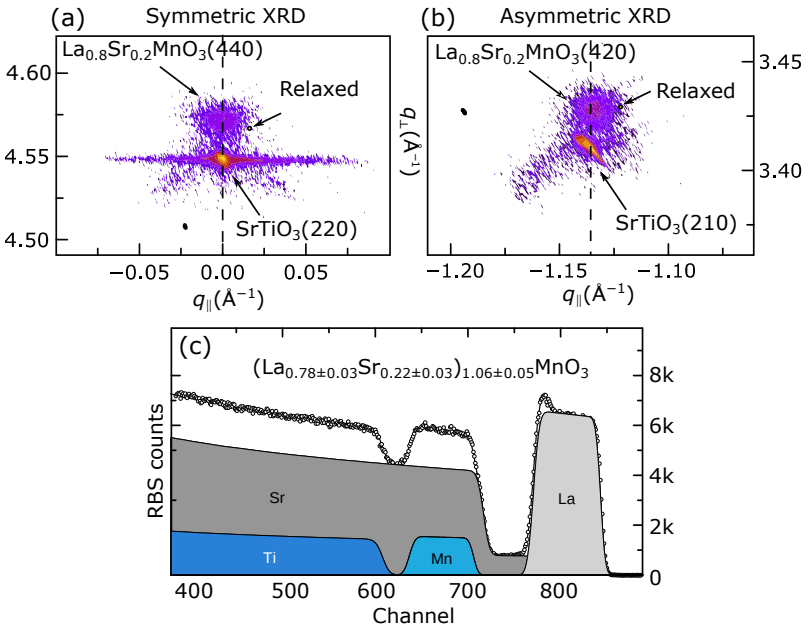

Figure 9.9. Bulk characterization of optimal LSMO(110) films. (a, b) XRD reciprocal-space maps acquired around (a) symmetric, and (b) asymmetric reflexes (grazing incidence); $q_{\parallel}$, and $q_{\perp}$ represent the in-plane, and out-of-plane components of the transfer momentum, respectively, where $q{=}2\pi/d$ when d is the distance between diffracting planes. (c) RBS counts, from which a composition of $(La_{0.78\pm0.03}Sr_{0.22\pm0.03})_{1.06\pm0.05}MnO_3$ is inferred. The RBS and the XRD analysis were performed by René Heller and Michele Riva, respectively.

9.6 Conclusions

This Chapter has shown that the nonstoichiometric growth of LSMO(110) and $SrTiO_3(110)$ (Chapter 6) share more than a few behaviors, including nonstoichiometry segregation that causes changes in the surface structures and surface-dependent sticking/re-evaporation of the deposited cations. It also testifies once again to the importance of controlling the surface atomic structure during growth: Uncontrolled surface structures call for rough surface morphologies. On the bright side, it was shown that these can be reversed back to ideal with appropriate UHV treatments.

Here nonstoichiometries were systematically introduced by acting on the O_2 background pressure. A combined STM and XPS analysis has revealed that stoichiometric, atomically flat films can be produced even with incongruent ablation at the target, by exploiting preferential scattering of light plasma species with the background gas in a specific window of pressures. For pressures other than these, nonstoichiometries are introduced and accumulate at the film's surface, causing the surface structure to evolve along the compositional phase diagram established in Chapter 8. The films become rough when the nonstoichiometry exceeds the capability of the surface to accommodate excess cations via a change in the surface structure, causing the formation of few-nanometers-high, poorly conductive oxide clusters. Atomically flat and stoichiometric films were produced by exploiting the STM-based method developed in Chapter 7.

While it is generally unwise to extrapolate conclusions from two data points, one can reasonably expect that the behaviors observed for $SrTiO_3$ and LSMO are shared by a larger number of multicomponent materials. The insights provided for these two systems might be useful to optimize the growth of other materials that, when grown by PLD, tend to display rough morphologies.

10. Oxygen exchange and surface structure

10.1 Introduction

This Chapter exemplifies the power of using crystalline surfaces with exactly controlled and established terminations to gain mechanistic insights into technologically relevant processes. Specifically, it investigates the details of oxygen incorporation—a key reaction for the functioning of solid-oxide fuel cells, see below—at atomically controlled surfaces of Nb-doped and undoped $SrTiO_3$(110) single crystals and of LSMO(110) single-crystalline films.

Key to the results presented here is a newly developed approach, published in ref. 71, that marries the world of surface science with solid-state ionics. Within this approach, surface science tools and facilities are used to prepare crystalline oxide surfaces that are controlled at the atomic scale. Exploiting the high-pressure UHV-compatible PLD chamber, these well-defined structures are exposed to O_2 pressures that are well beyond UHV-compatible ranges and are relevant for realistic applications, while retaining a high degree of control over the surface atomic details. The rates of incorporation of oxygen on differently reconstructed surfaces are then evaluated with kinetic oxygen exchange measurements such as secondary-ion mass spectrometry. The results, interpreted with support from DFT modeling, highlight the importance of the surface atomic details on the incorporation of oxygen: They demonstrate that the local arrangement and coordination of the surface atoms is truly critical to how and how much oxygen is incorporated in the system.

After introducing solid-oxide fuel cells and the scientific questions behind this work in more detail, Section 10.1.2 outlines the methodology. Before addressing the findings on a popular cathode material used in solid-oxide fuel cells, LSMO, the focus is on its simpler (and more established) relative: $SrTiO_3$. Specifically, on the results obtained on

(110)-oriented, 0.5 wt.% Nb_2O_5-doped $SrTiO_3$ single crystals. This is an ideal model system to study the effect of the surface on the oxygen exchange: First, DFT models exist for its surface reconstructions (see Chapter 6). Moreover, the n-type dopants suppress oxygen diffusion in the bulk, allowing to isolate the role of the surface. Section 10.3 takes a step forward and mirrors the same investigation on the undoped counterpart, where oxygen diffusion in the bulk is, instead, permitted. Finally, Section 10.4 discusses preliminary results obtained on (110)-oriented LSMO single-crystalline films.

10.1.1 Solid-oxide fuel cells

Solid-oxide fuel cells (SOFCs, see Fig. 10.1) are eco-friendly energy-conversion devices with a strong promise to surpass and eventually supplant traditional carbon-fueled technologies. The general operating principle of the SOFC is illustrated in Fig. 10.1(a), while Fig. 10.1(b) shows the cross-sectional TEM image of a device. Two porous electrodes (cathode and anode) are separated by a solid, oxygen-ion-conducting electrolyte that prevents electron transport. At the cathode, oxygen from the air is reduced and the resulting oxygen ions are transported through the electrolyte to the anode. Here they react with gaseous fuel yielding heat, water, CO_2 (in case of hydrocarbon-based fuels), and releasing electrons to the external circuit. As shown in Fig. 10.1(c), multiple cells can be combined to provide the desired voltage and power outputs. At present, YSZ is the most commonly used electrolyte, as it possesses an adequate oxide-ion conductivity (0.13 S/cm at 1 000 °C), and also shows a desirable phase stability in both oxidizing and reducing atmospheres.[347] A Ni-YSZ ceramic composite is used as anode. The current cathode material of choice for commercial use is $La_{1-x}Sr_xMnO_3$ (LSMO), in particular, for $x = 0.2$. LSMO has a thermal expansion coefficient compatible with the YSZ electrolyte, thus limiting stress buildup at the high operation temperatures of the SOFCs (between 600 °C and 1 000 °C).[270] Also, LSMO has low levels of chemical reactivity with YSZ, which extends the lifetime of the materials.

The potential of SOCFs is tremendous. SOFCs produce clean energy (when fueled by hydrogen, their only waste-product is water) with impressive efficiencies: between 45% and 65% for stand alone applications, and above 85% in combined heat and power applications. On top of that, their scalable nature allows using them in a variety of applications, from very small-scale ones where a few watts are needed, to large-scale distributed power generation of hundreds of megawatts, both stationary and mobile [Fig. 10.1(c)].[348,349] Finally, this technology could be integrated immediately within the existing hydrocarbon fuel infrastructure, since it can operate with a variety of fuels besides hydrogen.[350]

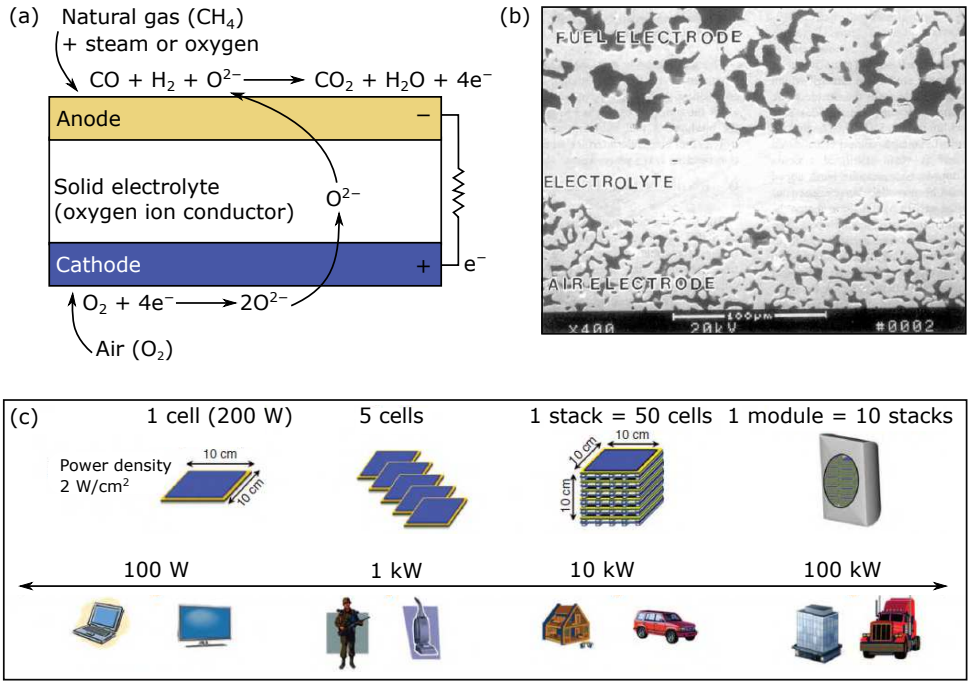

Figure 10.1. (a) Sketch of a solid oxide fuel cell (SOFC) running on natural gas. (b) Electron micrograph of the cross-section of an SOFC developed by Siemens Westinghouse. (c) Estimation of power output with LT-SOFC from a single cell to a module. Adapted from ref. 348.

Nonetheless, improvements are needed for large-scale commercialization. The main impediment is the high operating temperatures (800–1 000 °C) that are currently needed to guarantee an ionic conductivity in the range of 0.1 S/cm and the fantastic yields that follow. The main drawbacks connected to the high operating temperatures include issues of safety, electrode sintering, catalyst poisoning, interfacial diffusion between electrolyte and electrode materials, thermal instability, and mechanical (or thermal) stresses due to different coefficients of thermal expansion of the cell components. Additionally, complex cell and stack fabrication, high material cost, and concerns with regard to handling of gases and routine maintenance have limited the development and use of SOFCs to a great extent.[347] Experiments to overcome such limitations and device material selection are the focus of ongoing technology developments. One notable example is the recent development of low-temperature SOFCs with operation temperatures down to 350 °C.[348]

Understanding the details of the relevant reactions in SOFCs could provide a pathway to rationally design highly active electrode materials and improve the overall efficiency of SOFCs at lower temperatures. One known (and so far, poorly understood) limiting step is the oxygen incorporation at the cathode's side. Unveiling the fundamental mechanisms of this process is a worthwhile exercise, and it will be the main goal of this Chapter.

Models for the oxygen incorporation exist already. It is generally accepted that the

main factors affecting reactivity are (i) the availability of surface oxygen vacancies at the cathode,[99,351–354] (ii) the availability of electrons[355–359], and (iii) the position of the oxygen $2p$ band center.[360] Intriguingly, none of the standard reactivity models accounts for the (as it will be shown, all-but-negligible) role of the atomic-scale structure of the cathode's surface, in spite of the reaction taking place at the surface itself. This is due to the lack of adequate methods and to the nature of commercial cathode materials and their interaction with the environment. Indeed, commercial cathodes are either in powder form or consist of crystallites with different orientations. Different crystallographic orientations can produce different oxygen exchange and water splitting kinetics,[361–365] and resolving such samples at the atomic scale is an almost impossible task. Another complication arises from the presence of grain and twin boundaries that affect diffusion dramatically.[366,367] Moreover, many of the commonly used Sr-doped perovskite oxides segregate out Sr-rich insulating phases that are hardly controllable and resolvable.[327,328,331–334] Lastly, the surface structure may be affected by interaction with water and other gases, which are known to affect the surface-exchange rate constant.[368] As it will be expanded on in the next Section, a surface science approach can unfold this complexity and isolate the role of the surface atomic structure.

10.1.2 A surface science approach to unfold the complexity

This surface science approach is detailed in the work of ref. 71. It relies strongly on the ability to prepare atomically flat, single-crystalline samples with well-defined surface reconstructions. This removes many uncertainties connected with polycrystalline or powder-form cathodes, including the influence of grain or twin boundaries (also, the presence of a surface reconstruction suppresses Sr segregation[369]). Other common uncertainties are contained by exposing the well-characterized surfaces to very dry oxygen and under UHV-clean conditions. In a nutshell, the idea is to compare the reactivity of two well-defined surface reconstructions while all the other parameters are kept exactly constant. This is done by following these steps:

- Select two well-controlled and -understood surface reconstructions for the single-crystalline sample of interest. For $SrTiO_3$(110), these are the (4×1) and the (2×5) (refer to Chapter 6). For LSMO(110), the (1×1) and the fishbone reconstructions (refer to Chapter 8).
- Test the stability of the reconstructions under reaction conditions. In the works presented here, temperatures between 450 °C and 800 °C, and pressures between

0.001 and 0.1 mbar have been tested. The temperatures are realistic for SOFC operation, but the pressure values, while well beyond normally UHV-compatible values, are still much lower than the atmospheric pressure used during realistic SOFC operation.

- Realize a 'half sample', *i.e.*, a sample with two halves reconstructed differently. This way, one can exclude any effect from the bulk, *e.g.*, its history and stoichiometry.
- Equilibrate the half sample to ensure the stabilization of a steady-state oxygen vacancy concentration: The half sample was annealed at the reaction conditions with flowing O_2 gas of natural isotope composition (referred to as $^{16}O_2$) for an appropriate duration, and heating and cooling ramps of 60 °C/min and 120 °C/min, respectively (more details in the Sections to follow). Note that before this equilibration step, the vessel was continuously flushed with $^{16}O_2$ (20 sccm) for 1 h; this ensures reproducible conditions in the vacuum chamber. The pumping speed was regulated to stabilize a pressure of 1 mbar.
- Perform isotopically labeled oxygen exchange experiments (97.1% $^{18}O_2$, referred to as $^{18}O_2$ for brevity) without air exposure (60 °C/min and 120 °C/min heating and cooling ramps). Similar to the $^{16}O_2$ equilibration step, the chamber was preconditioned in $^{18}O_2$ at 0.5 mbar static pressure for 30 min prior to each experiment. To ensure a system as free from water as possible and avoid effects connected with the interaction with water,[368] the gas lines supplying the ^{18}O were baked prior to the exchange experiments.
- Analyze the exchanged samples *in situ* with LEED, XPS (both monophase and half samples), STM, and LEIS (monophase samples only). Perform *ex-situ* time-of-flight–secondary-ion mass spectrometry (ToF-SIMS).
- Quantify the amount of oxygen exchanged.
- Model oxygen incorporation by first-principles calculations.

More experimental details inherent to the approach are given in the following.

Half samples

Figure 10.2 illustrates the procedure to obtain a half sample for $SrTiO_3(110)$. In this case, the goal was to have the (4×1) reconstruction on one half of the sample, and the (2×5) on the other (see Chapter 6 for an introduction about these reconstructions). To achieve this, a substrate with a uniform (4×1) surface was placed in the back slot of the

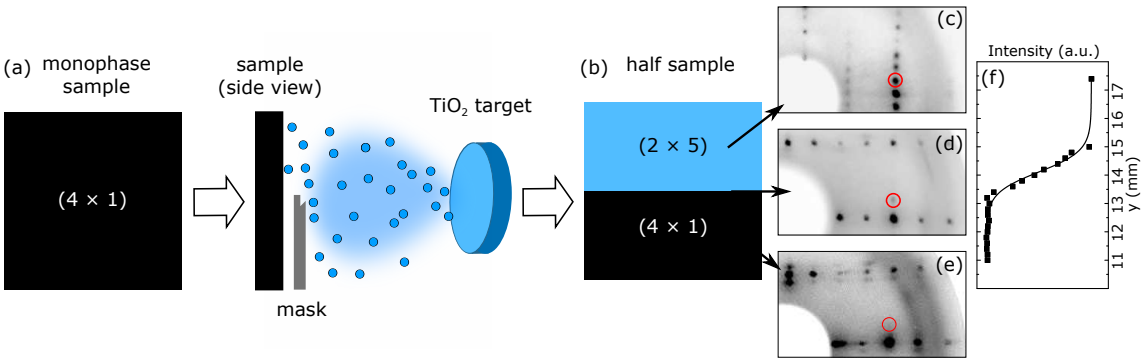

Figure 10.2. $SrTiO_3$(110) half samples. (a) (4 × 1)-reconstructed monophase sample. A mask shades half of the sample while Ti is deposited in PLD on the other half, where the (2 × 5) reconstruction is obtained (b). The LEED pattern evolves from a pure (4 × 1) (e) to a pure (2 × 5) (c) via a mixture of the two (d). (f) Intensity of the spot marked by the red circle across the transition.

double decker holder of the PLD, while the front slot was occupied by a home-made mask shading half of the sample. The amount of Ti needed to switch from the (4 × 1) to the (2 × 5), as inferred by the bottom axis of the phase diagram of Fig. 6.3, was then deposited by PLD. The LEED patterns in Figs. 10.2(c–e) show that the surfaces remains (4 × 1)-reconstructed when shaded, while the rest becomes (2 × 5)-reconstructed. Across the transition, the LEED pattern shows a mixture of the two reconstructions. Figure 10.2(f) shows the intensity of a spot characteristic of the (2 × 5) reconstruction and absent on the (4 × 1), as a function of the sample position [the spot is marked by a red circle in Figs. 10.2(c–d)]. The intensity is zero in the (4 × 1)-reconstructed region, it increases across the transition, and saturates within the (2 × 5) region. By fitting a sigmoidal step function to the curve, and by removing the contribution from the size of the LEED spot (0.7–0.8 mm), a width of the measured transition of about 0.4 mm was estimated. SIMS and XPS measurements on the two halves of half samples were always taken at least 1 mm away from the transition.

A similar approach was used to prepare the LSMO half samples. The reconstructions of interest here were the (1 × 1) and the fishbone introduced in Chapter 8. Shading a monophase (1 × 1) surface, appropriate amounts of manganese oxide were deposited to achieve the fishbone reconstruction on the exposed half. Note that at the 'high' pressure normally used to switch between the (1 × 1) and the fishbone reconstruction (0.1 mbar O_2, see Chapter 8), Mn species experience significant scattering with the background gas (see Chapter 9). This results in a very broad transition across the two reconstructions, due to shadowing effects caused by the mask. To obtain an acceptably narrow transition, one must deposit Mn at lower pressure. This was achieved by depositing Mn at 1×10^{-5} mbar O_2 (the deposition rate obtained at this value of pressure was calibrated with STM).

XPS measurements

It is commonly accepted that O_2 reactivity is promoted by the material's ability to transfer electrons to the O_2 molecules, which can be affected by the work function of the system and by the band bending.[355–358] XPS was used to address these effects. Work functions were derived from the cutoff of the X-ray-excited secondary electron emission spectra[370] acquired on the two regions of a half sample prior to the exchange experiments. The band alignment was checked by superimposing selected core-level XPS peaks acquired on the two halves. All secondary-electron spectra were acquired at normal emission, with the sample negatively polarized with a 9 V (nominal) battery. This confers the electrons a minimum kinetic energy higher than any analyzer work function (4–5 eV), thus preventing unwanted cutoffs due to the detection system. The horizontal axis was corrected with O 1*s* core-level spectra acquired on each region, with the sample held at both ground and at the polarization potentials. To minimize electric-field-lines distortion that can significantly affect work function measurements,[370] the X-ray source was retracted from the surface by approximately 50 mm. To limit the effect of any stray, time-varying magnetic fields, all measurements were performed overnight. Subsequent spectra acquired on both regions show a deviation in the measured cutoff smaller than the standard error of the fitted position. The secondary electron cutoff was evaluated by fitting a sigmoidal step function to the main, lowest-kinetic energy peak in each spectrum. The cutoff positions were evaluated as the energies corresponding to 5% of the step amplitude. Uncertainties in the derived work functions arise from the combined standard errors on the fitting parameters of the sigmoidal step, and the position of the O 1*s* core levels.

Note that this approach allows to unequivocally measure work function differences solely arising from the reconstructions, independent of any extrinsic influence.

Depth profiling and quantification of $^{18}O_2$

Oxygen-isotope depth profiles were performed and analyzed by Markus Kubicek via ToF-SIMS on a ToF-SIMS 5 instrument (ION-TOF, Germany). 25 keV Bi_3^{++} clusters (0.02 pA) were used as primary ions in collimated burst alignment mode optimized for oxygen isotope measurements.[371,372] Negative secondary ions were detected from areas of $100 \times 100\ \mu m^2$ using a raster of 512×512 measured points, and the secondary ion counts of $^{16}O^-$ and $^{18}O^-$ were used to determine the isotopic composition $f = {}^{18}O/({}^{18}O + {}^{16}O)$. For depth profiling, areas of $400 \times 400\ \mu m^2$ were sputtered using Cs^+ ions, and the depth information was calculated from the sputter coefficients and sputter currents, referenced by measuring the depth of the sputter craters via digital holography microscopy.

An electron flood gun (21 eV) was used for charge compensation. The average oxygen exchange coefficient $k^\star$ was calculated as

$$k^\star = \frac{\sum_{\text{meas. points}} (f_\text{m} - f_\text{bg}) d_\text{s}/t}{(f_\text{out} - f_\text{bg})}, \tag{10.1}$$

where f_m and f_out denote the measured fraction of ^{18}O incorporated in the surface, and the fraction in the UHV vessel, respectively, while f_bg stands for the background tracer fraction (approximated by the natural abundance f_bg = 0.00205). d_s is the sputter depth per measurement point. More details on the approximations employed and on the derivation of $k^\star$ are found in ref. 71.

First-principles calculations

Calculations were performed by Cesare Franchini using the VASP code [149,150] in the framework of DFT within the generalized gradient correction approximation of Perdew, Burke and Ernzerhof. [153] The computational methods are described in detail in ref. 71.

10.2 ^{18}O exchange on Nb-doped $SrTiO_3$(110)

As mentioned in the Introduction, Nb-doped $SrTiO_3$(110) single crystals are ideal model systems to investigate the role of the surface atomic structure on the incorporation of oxygen. Because of the n doping, the relevant bulk V_O concentration expected under the experimental conditions of this work is extremely low: A lower limit of 6×10^{-7} cm^{-3} (10^{-29} with respect to oxygen sites) is derived by defect chemical models, [373–375] while an upper limit of 6×10^{12} cm^{-3} (10^{-10} with respect to oxygen sites) is derived from the estimated decay length of the tracer profiles. [71] Because of this very low V_O concentration, the oxygen transport in the bulk is strongly suppressed, while the surface oxygen exchange reaction can still be probed in isotope exchange experiments. This enables one to isolate the influence of the surface on the oxygen incorporation. On a more technical note, dealing with a doped system gives the additional benefit of having sufficient conductivity for STM. Crucially, the surface reconstructions of this system have been modelled by DFT (see Chapter 6).

The role of the surface reconstruction on the oxygen incorporation was addressed by comparing the reactivity of the (4×1) and the (2×5) reconstructions at identical conditions. These reconstructions both consist of a layer of TiO_x polyhedra sitting on a bulk-like $(SrTiO)^{4+}$ plane, but the top titania overlayers have distinctly different structural properties: The (4×1) surface consists of a porous network of corner-sharing tetrahedrally-coordinated TiO_4 units, while the (2×5) consists of a bilayer of octahe-

drally coordinated Ti atoms (details in Chapter 6). The work presented here demonstrates that the different coordination and arrangements of the surface atoms in these two reconstructions is the main cause for different rates of incorporation of oxygen in the material.

The following Sections showcase the approach introduced in Section 10.1.2: First, Section 10.2.1 demonstrates that the reconstructions under investigations are stable at the chosen reaction conditions. Section 10.2.2 discusses the oxygen incorporation experiments, analyzing results both from LEIS and SIMS, taken both on monophase and half samples. Finally, Section 10.2.3 addresses the role of the availability of electrons, surface oxygen vacancies, and surface atomic structure on the reactivity to oxygen incorporation, respectively, complementing the experimental results with theoretical modeling. Most of these results have been published in ref. 71.

10.2.1 Stability of the surface structures under reaction conditions

Prior to the exchange experiments, the stability of the (4×1) and of the (2×5) reconstructions was tested at the chosen reaction conditions, *i.e.*, 450 °C, 0.1 mbar O_2. Figure 10.3 compares the morphology and the periodicity of monophase samples before and after 5 h annealing at these conditions (comparable results are observed also after 20 h, not shown). The reconstructions are largely unchanged. In wide-area STM images, (4×1)-reconstructed $SrTiO_3(110)$ surfaces retain large (20–300 nm), atomically flat terraces, separated by steps with single or multiple unit-cell heights, preferentially running along low-index directions [compare main panels of Figs. 10.3(a, c)]. No change is observed in the corresponding high-resolution STM images and LEED patterns. The same observations hold true for the (2×5) surface [cf. Figs. 10.3(b, d)], although a few additional islands are seen on the wide-scale STM. Since small changes in the surface Ti/Sr ratio would switch the surface to another reconstruction (see Chapter 6), one can exclude cation segregation.

10.2.2 $^{18}O_2$ exchange experiments

$^{18}O_2$ exchange was conducted on monophase samples and on half samples. The resulting tracer incorporation was evaluated with both LEIS and SIMS, as shown in Figs. 10.4. LEIS [Fig. 10.4(a)] was always acquired on monophase samples in UHV, right after the $^{18}O_2$ treatment (the He^+ beam is too broad to probe only half of the sample surface at a time). After the exchange, a new small peak (highlighted in red) appears. This peak,

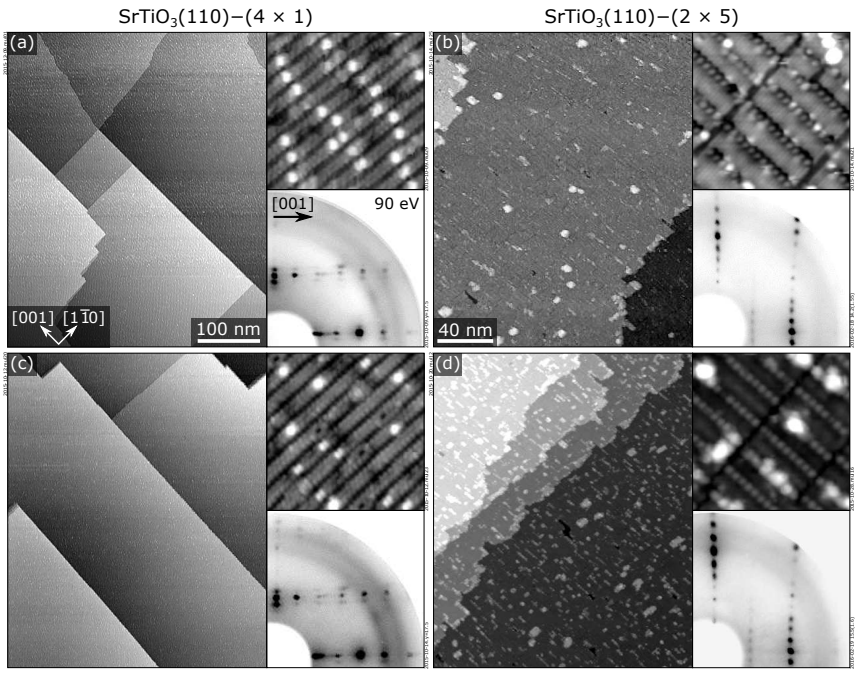

Figure 10.3. Surface structures of Nb:$SrTiO_3$(110) and their stability upon treatment in oxygen atmosphere (450 °C, 0.1 mbar O_2). (a, c) STM images (main panels: 410 × 500 nm^2; insets: 15 × 15 nm^2) and LEED patterns of a monophase $SrTiO_3$(110)-(4 × 1) surface, before and after 5 h at 450 °C and 0.1 mbar $^{18}O_2$. (b, d) STM images (main panels: 190 × 230 nm^2; insets: 15 × 15 nm^2) and LEED patterns of a monophase $SrTiO_3$(110)-(2 × 5) surface, before and after the $^{18}O_2$ annealing. The slightly different contrast observed in the high-resolution STM images of panels (b) and (d) are related to variations of the tip termination. Adapted from ref. 71.

corresponding to the incorporated $^{18}O_2$, is higher on the (4 × 1) sample. One can obtain the surface ^{18}O density by scaling the LEIS-measured tracer concentrations with the corresponding density of oxygen atoms in the topmost layer [8.81 × 10^{14} cm^{-2} and 1.04 × 10^{15} cm^{-2} for (2 × 5) and (4 × 1), respectively]. It amounts to (8.4 ± 0.4) × 10^{13} cm^{-2} for the (2 × 5), and to (1.33 ± 0.04) × 10^{14} cm^{-2} for the (4 × 1).

SIMS was performed both on half and monophase samples. Figure 10.4(b) shows the results acquired on a half sample (similar results were seen on monophase samples, not shown). Also in this case, the (4 × 1)-reconstructed surface appears to incorporate more $^{18}O_2$ during the exchange process than the (2 × 5)-reconstructed surface, as seen from the areas underlying the SIMS curves in Fig. 10.4(b). Integrating the SIMS profiles to quantify the tracer incorporation at the surface is the only viable approach in this case: Due to the virtual absence of oxygen vacancies in the bulk because of the donor doping, the profiles are extremely shallow. As a result, they are dominated by ion-beam-induced broadening effects (*i.e.*, mixing), and cannot be fitted to analytical or numerical solutions of Fick's law, as commonly done. The exchange rate coefficient $k^\star$ was estimated from the total amount of exchanged $^{18}O_2$ derived from the integration of the profiles.[71] With exchange times of 1 h and 4 h, $k^\star$ was found to be 4.5–6.0 × 10^{-13} cm/s for the (2 × 5)-

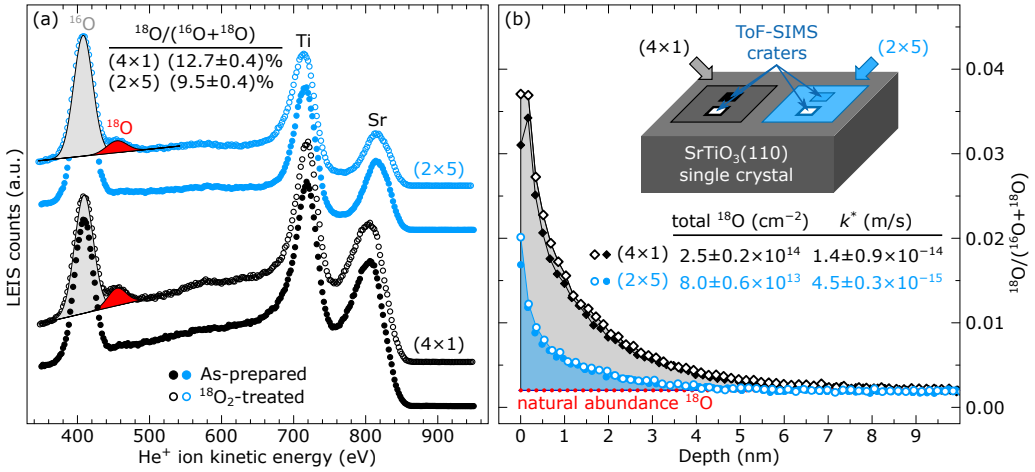

Figure 10.4. Isotope exchange experiments on Nb:$SrTiO_3$(110). (a) LEIS spectra (He^+ with 1000 eV primary energy) measured on (4 × 1)- (black), and (2 × 5)-reconstructed (blue) $SrTiO_3$(110) surfaces, respectively. Results from as-prepared, and $^{18}O_2$ exchanged samples are displayed with full, and open symbols, respectively. Each spectrum is normalized to the total O signal. The uncertainty (standard error) on the fractional $^{18}O_2$ signals reported in the table is 0.4% for both surfaces. (b) ToF-SIMS $^{18}O_2$ isotope exchange depth profiles measured on (4 × 1)- (black), and (2 × 5)- reconstructed (blue) $SrTiO_3$(110) surfaces of the same crystal. Here, open and full symbols correspond to two separate measurements on different spots on each half of the bi-crystal. Adapted from ref. 71.

reconstructed surface, and approximately three times as much (1.4–1.8 × 10^{-12} cm/s) for the (4 × 1). Note that the ratio of effective surface exchange constants $k^{\star}_{(4\times1)}/k^{\star}_{(2\times5)}$ remains constant over several hours (it amounts to 3.1 ± 0.3 and 3.1 ± 0.6 for the 1 h and 4 h annealing periods, respectively). This implies that the incorporation via the surface remains constant over this time. One can thereby exclude that either saturation effects, or different transport in the near-surface regions are responsible for the observed differences between the two reconstructions. Consequently, only the different activity of the respective surface structures is responsible for the threefold larger ^{18}O incorporation on the (4 × 1).

Note that, with respect to LEIS, SIMS measures a larger difference in incorporated oxygen between (4 × 1) and (2 × 5): On the (4 × 1), the $^{18}O_2$ density measured by SIMS is (2.5 ± 0.2) × 10^{14} cm^{-2}, roughly twice as large as than the one measured by LEIS. Instead, the value of (8.0 ± 0.6) × 10^{13} cm^{-2} for the (2 × 5) obtained by SIMS is essentially identical to that obtained by LEIS. Since SIMS probes the total amount of tracer ions incorporated in the sample, while LEIS probes the ^{18}O density in the topmost surface layer only, one can conclude that oxygen exchange is confined to the topmost surface layer on the (2 × 5), while a few atomic layers are involved on the (4 × 1). This argument is strengthened by DFT calculations showing that oxygen vacancies are more prevalent at the very surface on the (2 × 5), while subsurface sites are favored on the (4 × 1) (see Section 10.2.3 below).

10.2.3 Interpreting results

To understand the origin of the higher O_2 reactivity of the (4×1) surface as compared to the (2×5), the two most commonly considered factors have been addressed first: The ease of transferring electrons to the O_2 molecules, and the number of surface oxygen vacancies. As it will be argued, these commonly accepted mechanisms cannot explain the different O_2 reactivity of these two surfaces. Instead, it will be shown that the surface atomic structure itself is mainly responsible. Note that the experimental results could be directly related to first-principles calculations thanks to the available structural models for the surface reconstructions. Because the author was not directly involved in the calculations, this Section gives only a summary of the most relevant computational results. Additional details are found in ref. 71.

1. Role of electron transfer

It is commonly accepted that the easier it is to transfer electrons to the O_2 molecule adsorbed at a given surface, the easier it is to split it and incorporate the resulting oxygen ions.[355–360] XPS measurements (Fig. 10.5) were performed to address whether this effect dominates the ^{18}O incorporation at the (4×1) and (2×5) surfaces. First, work functions were measured on (4×1) and (2×5) areas present on the same half sample [Fig. 10.5(a)]. The results show that the work function of the (4×1) is 0.42 eV larger than the one measured on the (2×5). DFT qualitatively agrees, predicting a 0.7 eV larger work function for the (4×1) with respect to the (2×5). (Note that the features above 5 eV in the secondary emission spectra in Fig. 10.5 are possibly related to low-energy Auger emission—their characterization is beyond the scope of this Thesis). The role of band bending was then assessed by comparing the core-level energies of the two zones on the surface half sample [Fig. 10.5(c)]. The peaks are perfectly overlapped. Therefore, the surface potential or band bending (if it exists) is the same on these two surfaces.

Taken the results above—*i.e.*, no difference in band bending and smaller work function of the (2×5)—one can sketch the band alignment of the two reconstructions with respect to an O_2 molecule as in Fig. 10.5(b). According to this scenario, one would expect easier electron transfer to O_2 molecules from the (2×5) surface than from the (4×1). However, this is in contrast with the fact that (2×5) is *less* reactive than the (4×1) (Section 10.2.2). Hence, the ease of electron transfer cannot be the dominant mechanism governing oxygen incorporation.

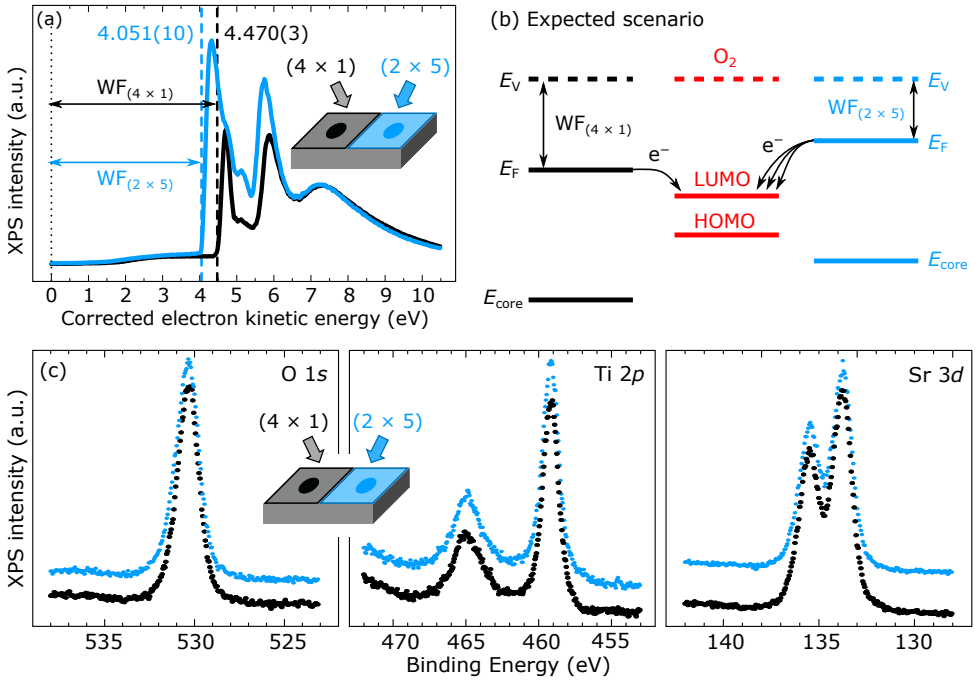

Figure 10.5. Work function measurement and band alignment on a Nb:$SrTiO_3$(110) half sample with (4 × 1) and (2 × 5) reconstructions. Spectra acquired on the two regions are represented in black and blue, respectively. (a) Secondary-electron emission spectra. Work-functions are highlighted by vertical dashed lines. (b) Sketch of the expected band alignment of the two surfaces with respect to one O_2 molecule, assuming no band bending. The (2 × 5) surface should transfer more electrons than the (4 × 1). (c) Core level XPS peaks. The peaks acquired on the two halves are perfectly overlapped. Adapted from ref. 71.

2. Role of surface oxygen vacancies

Another factor that is supposed to drive the incorporation of oxygen at perovskite surfaces is the number of surface oxygen vacancies.[99,351–354] Intuitively, the more oxygen vacancies are present at the surface, the more opportunities exist for O_2 molecules to readily dissociate and, thus, to result in the incorporation of oxygen anions. DFT was used to evaluate the importance of this effect for the (4 × 1) and (2 × 5) reconstructions. The formation energies for O vacancies were evaluated at various positions, both on the top of the surface and closer to the interface with the underlying $SrTiO_3$ bulk lattice, as shown in Fig. 10.6. The formation of the lowest-energy V_O on the (2 × 5) surface layer is more favorable by 2.2 eV than on the (4 × 1) surface. Recalling that the (4 × 1) surface is more reactive than the (2 × 5) (Section 10.2.2), one can conclude that the ease of surface V_O formation is not decisive for the $^{18}O_2$ exchange.

3. Role of surface atomic structure

The previous two Sections have excluded two important mechanisms that could have explained the higher reactivity of the (4 × 1) with respect to the (2 × 5), *i.e.*, electron

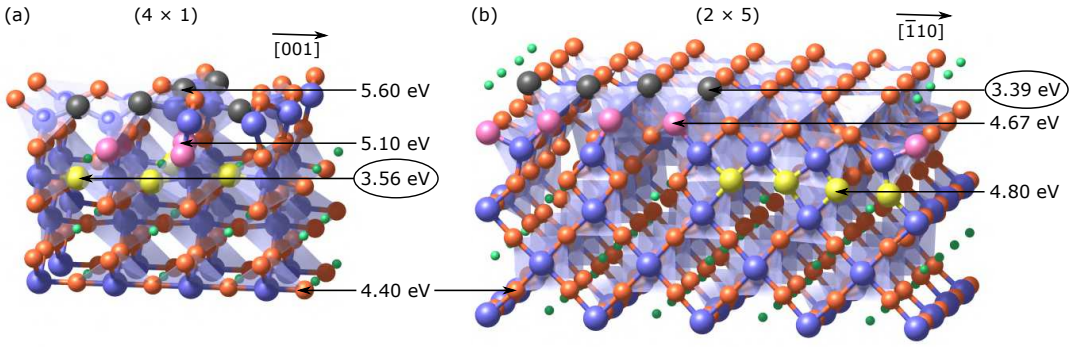

Figure 10.6. Structural models for the (a) $(n \times 1)$ and (b) $(2 \times n)$ reconstructions indicating the positions of oxygen vacancies considered in the calculations. Green, red and blue spheres indicate Sr, O and Ti atoms, respectively. The oxygen atoms removed to create the vacancies are represented by black (surface), pink (sub-surface) and yellow (interface) spheres. Separate calculations were conducted for each individual vacancy. The full set of calculated oxygen vacancy formation energies is found in ref. 71. Here the most favorable formation energies for each type of vacancy (surface, sub-surface, interface) is shown. Adapted from ref. 71.

transfer and surface oxygen vacancies. This Section finally addresses the role of surface structure itself, based on first-principles molecular dynamics (FPMD) calculations. A vacancy-free surface and a defective one with a single V_O were considered for each of the two reconstructions. Figure 10.7 displays selected adsorption structures that showed the lowest energy at the end of the FPMD runs, along with the corresponding energy gains (bottom).

In absence of vacancies [Fig. 10.7(a, b)], O_2 dissociative adsorption/incorporation is considerably more favorable in the (4×1) structure. On the vacancy-free (4×1) surface [Fig. 10.7(a)], O_2 easily dissociates and incorporates at both the six-member and the ten-member rings of TiO_4 tetrahedra (energy gains of 3.17 eV and 2.94 eV, respectively). The Ti atoms that assist the reaction temporarily increase their coordination from four-fold to five-fold to host the additional oxygen. On the contrary, O_2 does not dissociate on the vacancy-free (2×5) surface [Fig. 10.7(b)], remaining instead anchored on top of the Sr rows.

If one V_O is introduced in the (4×1) surface (not shown), O_2 is split and incorporated in a similar fashion as when vacancies are not present. However, the energy gain is smaller (1.8 eV) because of the cost associated to the formation of the oxygen vacancy (see Fig. 10.6). When V_Os are introduced in the (2×5) structure [Fig. 10.7(c)], they become active centers for O_2 dissociation: one O fills the V_O site, whereas the second one hops into a nearby bridge position between two surface Ti atoms. These surface Ti atoms temporarily increase their coordination from six- to seven-fold. The overall energy gain for the process is much smaller than for incorporating O_2 in the (4×1), even when oxygen vacancies are considered (0.08 eV vs. 1.8 eV energy gains, respectively). The larger energy gains for incorporating oxygen for the (4×1) than for the (2×5), both

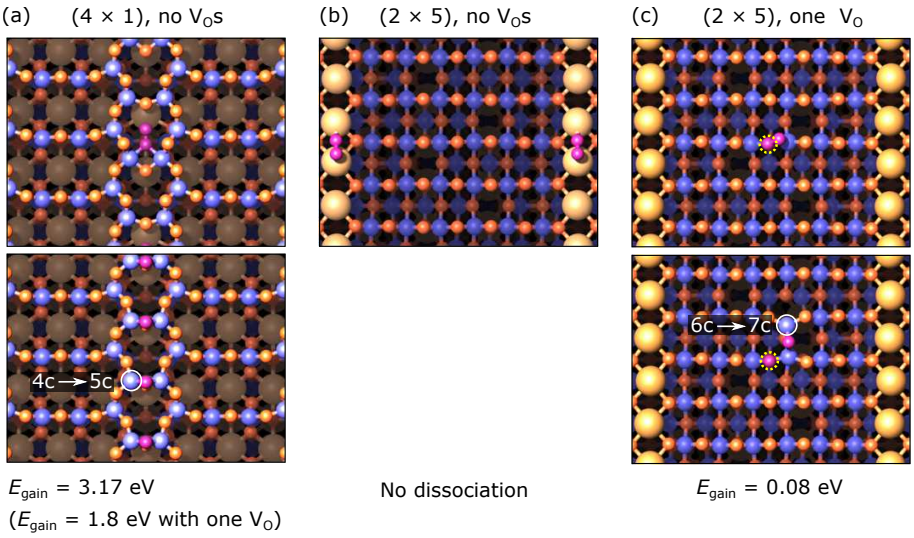

Figure 10.7. O_2 adsorption structures calculated by FPMD-DFT. Lowest-energy structural models for adsorption and dissociation of one O_2 molecule on the $(n \times 1)$ surface without any surface vacancy (a), and on the $(2 \times n)$ with one oxygen vacancy (c). Oxygen molecules do not dissociate on the $(2 \times n)$ without any oxygen vacancy (b). Adapted from ref. 71.

in absence and in presence of oxygen vacancies, are consistent with the larger reactivity of the (4×1) witnessed by LEIS and SIMS (Section 10.2.2).

The considerations above allow us to understand the mechanism that causes the large different energy gains for incorporating oxygen on the (4×1) and on the (2×5). In a nutshell, it boils down to the coordination and arrangement of the surface Ti atoms participating to the reaction. Ti atoms temporarily increase their coordination to host the to-be-incorporated oxygen: The coordination increases from four- to five-fold for the (4×1), and from six- to seven-fold for the (2×5). The easier it is to increase the coordination of the surface Ti atoms, the easier the incorporation. The (2×5) incorporates little oxygen because the surface TiO_6 units are rigid and possess the highest stable coordination observed for Ti: It is not favorable for them to further increase their coordination to seven-fold. On the other hand, the TiO_4 polyhedra of the (4×1) are undercoordinated and flexible. They are more likely to distort and increase their coordination to five-fold and promote oxygen incorporation. These different degrees of structural flexibility are well seen in Fig. 10.8, showing the time evolution of the average O–Ti–O angle for TiO_4 and TiO_6 polyhedra: Larger oscillations are seen for the TiO_4 units.

10.2.4 Summary and discussion

The results discussed here for Nb-doped $SrTiO_3(110)$ single-crystalline and atomically controlled surfaces showcase the power of bridging surface science with macroscopic

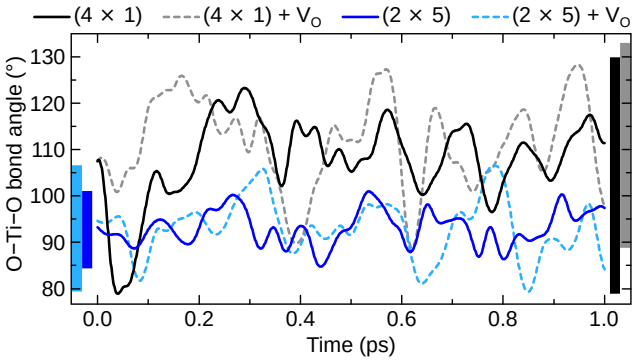

Figure 10.8. Dynamic reorganization of TiO_4 and TiO_6 polyhedra. Time evolution of the average O–Ti–O angle in the (4 × 1) and (2 × 5) surfaces with and without oxygen vacancy. Trajectories are shown during the first 1.0 ps, but qualitatively similar results are obtained for the whole time range considered in the calculation (10 ps). Vertical bars indicate the maximum amplitude of the oscillations during the whole simulation period. Adapted from ref. 71.

kinetic measurements of reaction rates. With this approach, one can independently assess the factors that are commonly considered most relevant for oxygen incorporation, such as (i) the availability and mobility of surface V_Os (the more V_Os, the easier the incorporation);[99,351–354] (ii) the electronic effects that facilitate electron transfer;[355–358] and (iii) step density.[376]

Following these commonly accepted guidelines, one would expect a higher reactivity for the (2 × 5) structure compared to the (4 × 1). Indeed, the DFT results suggest that the (2 × 5) should accomodate a larger concentration of oxygen vacancies at the surface compared to (4 × 1) (Fig. 10.6), while its smaller work function measured by XPS should cause easier electron transfer to the incoming oxygen molecules (Fig. 10.5). Moreover, the STM images in Fig. 10.3 reveal slightly higher step density on the (2 × 5). The data in Section 10.2.2 come then with surprise: They show that (2 × 5) is *less* reactive than the (4 × 1). One can conclude that none of the traditionally considered models can explain the different reactivities of the (4 × 1)- and (2 × 5)-reconstructed surfaces on $SrTiO_3$(110). The computational studies presented here reveal the true determining factor: The details of the atomic structure itself. The enhanced reactivity of the (4 × 1) toward O_2 dissociative adsorption and incorporation is a result of the increased degree of structural and chemical flexibility of its under-coordinated surface TiO_4 units as compared to the almost fully coordinated and rigid TiO_5 and TiO_6 units in the (2 × 5). The rigid TiO_6 polyhedra in the (2 × 5) surface cannot accommodate more oxygen unless surface V_Os assist the reaction. Thus, two parallel oxygen exchange mechanisms are likely present on the $SrTiO_3$(110) surfaces: A structurally mediated mechanism, dominating the exchange rate on the (4 × 1) surface, and a vacancy-mediated one, enabling exchange also on the (2 × 5) surface.

10.3 ^{18}O exchange on undoped $SrTiO_3$(110)

This Section applies the methodology developed for n-doped $SrTiO_3$(110) to the nominally undoped counterpart, focusing once again on the (4 × 1) and (2 × 5) surface reconstructions (Fig. 6.9 in Chapter 6 has shown that these are also observed in the undoped samples). Differently from the donor-doped case, bulk oxygen vacancies are present in the undoped samples at the employed reaction conditions. Hence, the oxygen incorporated at the surface can find a diffusion path in the bulk, and this allows to extend the investigations beyond the topmost surface layer.

Section 10.3.1 shows that the undoped samples qualitatively reproduce the results obtained on the doped ones: The (4 × 1) reconstruction is more reactive than the (2 × 5), only the difference is more marked now. The Section also addresses how the diffusion profiles evolve as a function of the equilibration temperature. The diffusion profiles obtained on the (4 × 1) show a peculiar 'box' shape that is consistent with a p–n–p^+ transition in the first few nanometers, and which becomes more pronounced as the temperature increases. On the other hand, the diffusion profiles obtained on the (2 × 5) structure show no change with the temperature: This reconstruction truly blocks any incorporation of oxygen. Finally, Section 10.3.3 compares the results obtained within this work to the literature: the very clean and stable surfaces used in this work yield up to three orders of magnitude higher incorporation rates than those found in the literature.

10.3.1 $^{18}O_2$ exchange experiments

(4 × 1)- and (2 × 5)-terminated $SrTiO_3$(110) surfaces were prepared and subjected to $^{18}O_2$ following the approach outlined in Section 10.1.2. The exchange experiments were always performed for 4 h, at an O_2 pressure of 0.1 mbar, and substrate temperatures varying between 450 °C and 600 °C [because not stable at higher temperatures, the (2 × 5) surface was only annealed up to 500 °C].

Like before, the stability of the surface reconstructions was tested under reaction conditions prior the exchange. This is no easy task for undoped samples: The oxidizing treatments make the electrical conductivity of the samples decrease to the point where STM and LEED are not possible. Thus, the test partly relied on results obtained on Nb-doped samples. The stability of the (4 × 1) and (2 × 5) reconstructions on a Nb-doped $SrTiO_3$ sample was tested, both by LEED and STM, as shown previously (in this case, 5 h at 500 °C and 0.1 mbar O_2). The same treatment was then performed on the undoped samples, followed by 15 h at 500 °C in UHV to achieve sufficient conductivity for a high-

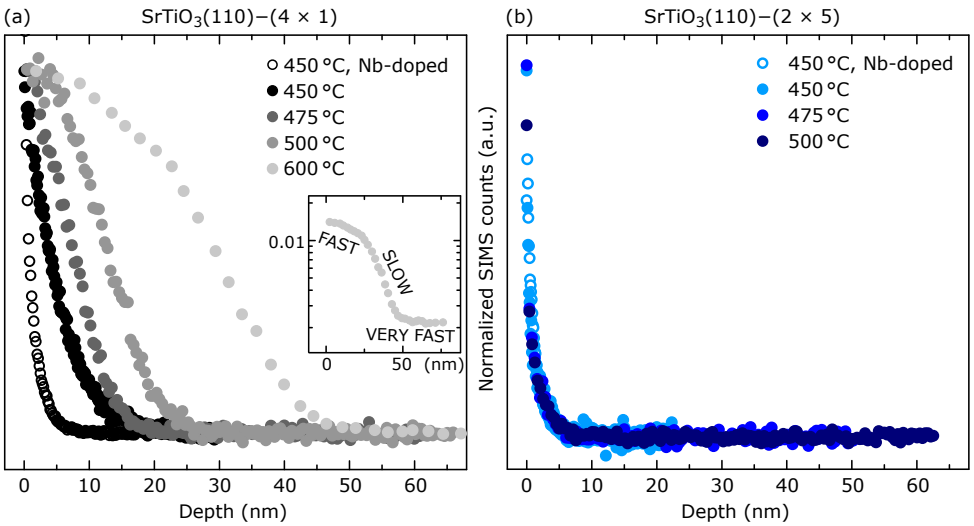

Figure 10.9. SIMS profiles relative to exchange experiments performed at different temperatures on undoped $SrTiO_3(110)$ samples with (4×1) (a) and (2×5) (b) terminations. The profiles in (a) are normalized to the average of the first two/three points in the respective spectra. The inset reports the 600 °C spectrum in logarithmic scale. The profiles in (b) are normalized to the respective integral signals.

quality LEED pattern (note that even after this reduction treatment the samples were not conductive enough for STM). Subsequent tests revealed that the STM appearance of the surface is not affected by the reducing treatment only.

Figure 10.9 compares the measured isotope depth profiles. The (4×1) termination shows considerably higher oxygen exchange than the (2×5), consistently with the results obtained on donor-doped samples. All (2×5) profiles fall on top of each other, always showing a very sharp near-surface drop of the ^{18}O concentration towards the natural ^{18}O abundance. In fact, the (2×5) profiles are so short that they are in the range of the method-related broadening of step profiles (from isotope mixing), and match perfectly the ones measured on doped samples (hollow circles).

On the other hand, the (4×1) profiles change their shape and extend more and more below the surface as the temperature increases. At 450 °C, the (4×1) profile (full black circles) is shallow and rapidly decaying towards the natural ^{18}O abundance. However, it extends more into the bulk as compared to the corresponding profile taken on a doped sample (open circles), meaning that more oxygen is incorporated in the undoped sample. Above 475 °C, an unusual profile shape becomes apparent, which is best visualized in logarithmic scale. The inset of Fig. 10.9(a) replots the 600 °C profile, for which the effect is strongest, in logarithmic scale: The profile slope changes twice, producing a sort of 'box' shape. The origin of this peculiar shape is discussed in Section 10.3.2.

The work in ref. 377 details the methods used to quantitatively determine tracer surface exchange coefficients $k^\star$ and, where possible, tracer diffusion coefficients $D^\star$. The $k^\star$ values are reported in Table 10.1 ($k^\star$ values in the different regions of the box shape

Table 10.1. $k^\star$ values derived from isotope exchange profiles measured on undoped $SrTiO_3(110)$, unless otherwise specified.

Temp. (°C)	**Surf. struct.**	$k^\star$ (cm/s)	$k^\star_{(4\times1)}/k^\star_{(2\times5)}$
450 (Nb-doped)[71]	(4×1)	$1.4\text{–}1.8\times10^{-12}$	3.1 ± 0.6
	(2×5)	$4.5\text{–}6.0\times10^{-13}$	
450	(4×1)	$3.7\text{–}5.6\times10^{-13}$	≈10
	(2×5)	5.7×10^{-14}	
475	(4×1)	$1.3\text{–}1.8\times10^{-12}$	≈10
	(2×5)	1.27×10^{-13}	
500	(4×1)	$4.8\text{–}5.3\times10^{-12}$	≈20
	(2×5)	2.17×10^{-13}	
600	(4×1)	1.26×10^{-10}	

were derived by using finite elements simulation of the depth profiles using diffusion coefficients varying with depth). As expected, the (4×1) shows larger value for $k^\star$ as compared to the (2×5), similarly to what was found on $Nb:SrTiO_3(110)$ samples. However, now the difference is more dramatic: Up to about an order of magnitude, instead of three-fold (cf. the values in the rightmost column of Table 10.1). Once again, the difference between the two reconstructions are assigned to the higher degree of flexibility of the coordination polyhedra of the (4×1). Oxygen is hardly incorporated at the very stiff (2×5) surface, and the situation is not improved by increasing the temperature, as seen by the perfectly overlapped (2×5) profiles in Fig. 10.9(b): The true limiting step is the surface reconstruction (the slight increase in the $k^\star$ values as a function of the temperature is likely linked to an increasing equilibrium concentration of oxygen vacancies at the surface). On the other hand, the diffusion within the bulk of the (4×1)-reconstructed sample is aided by higher temperatures that introduce more bulk oxygen vacancies. These offer a diffusion path into the bulk for the oxygen ions that have made it through the surface.

What if the exchange conditions are not dry?

At the beginning of this Chapter the importance of humidity for the oxygen incorporation rates was mentioned.[368] While the matter has not been investigated systematically within this work, indications exist that the oxygen exchange is greatly assisted by water. An oxygen exchange experiment was once realized on samples that had been prepared

as usual, with the only and crucial difference that the gas-line feeding the ^{18}O gas to the chamber remained unused for several months, and was not baked prior the experiments. SIMS revealed a two-fold increase of incorporated oxygen. It is likely that the humidity present in the gas line had assisted the reaction in the chamber. On another occasion, the samples were prepared in the usual setup to exhibit the usual reconstructions, but taken out to air prior the ^{18}O exchange, which was conducted in another chamber with poor vacuum conditions. The incorporated oxygen appeared, again, higher. The likely mechanism is that isotopically labeled water molecules adsorb and dissociate in correspondence to surface oxygen vacancies.

10.3.2 Diffusion characteristics

This Section aims to rationalize the unusual box shape of the high-temperature exchange diffusion profiles of the (4×1)-terminated samples [Fig. 10.9(a)]. Generally, the slopes and/or shapes of the exchange diffusion profiles reflect the diffusion properties of the tracer ions, with smaller slopes standing for faster diffusion coefficients. The correlation between slopes of diffusion profiles and diffusion coefficients can be intuitively understood by considering the distribution of incorporated ^{18}O atoms in 'slow' and 'fast' diffusion regimes: When diffusion is slow, ^{18}O atoms diffusing from the surface to the bulk are incorporated in a thin layer close to the surface. Instead, fast diffusion will cause a similar amount of ^{18}O atoms to be distributed over a longer distance. In turn, this will result in a lower ^{18}O fraction measured and a faster decay with depth, *i.e.*, smaller slopes in the diffusion profiles.

What ultimately determines the diffusion properties of a given material (and, as a consequence, the shape of the diffusion profiles) is its bulk point defect chemistry. In the most intuitive case, fast diffusion coefficients are induced by a high density of oxygen vacancies (in the dilute limit where each vacancy is treated independently, the diffusion coefficient $D^{\star}$=[V_{O^-}]D_{VO}, where [V_{O^-}] is the concentration of oxygen vacancies and D_{VO} is the diffusion coefficient of a single vacancy). Under thermodynamic equilibrium, the concentration of oxygen vacancies and other bulk point defects like cation vacancies or interstitials is uniquely determined by the oxygen chemical potential, and is summarized in the so-called Brouwer diagrams. Oxygen vacancies diffuse very fast and manage to reach equilibrium even at the moderate temperatures used during the experiments presented here. Cations, on the other hand, are much slower (*i.e.*, there is a much larger barrier for diffusion than for V_Os), and such that thermodynamic equilibrium may not be reached. Local excesses of cations that do not get equilibrated with the bulk can then cause the formation of space charge layers, much like in a p–n junction, where a

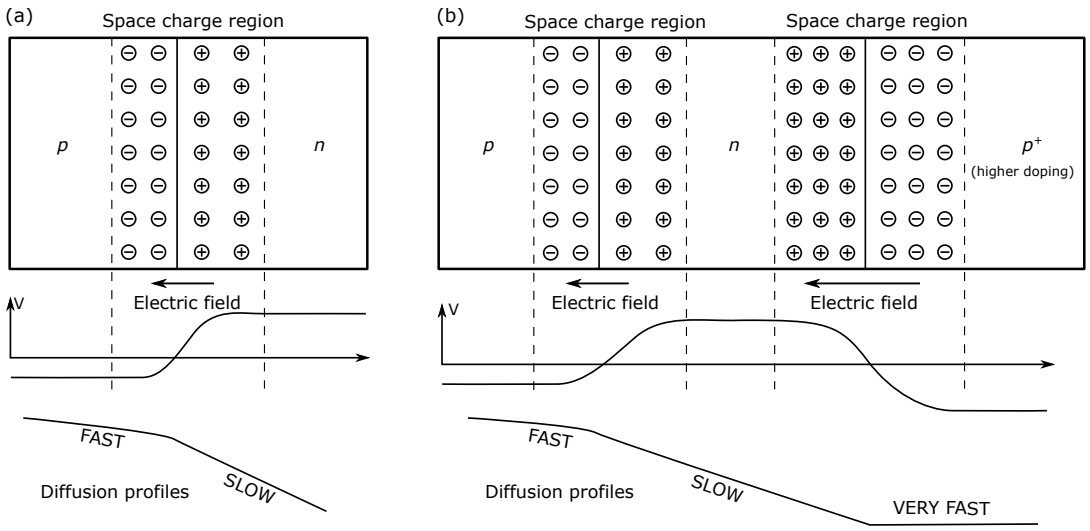

Figure 10.10. p–n junctions and shape of exchange-diffusion profiles. (a) Sketch of a p-n junction. (b) Sketch of a p–n–p^+ junction.

space charge layer arises by coupling two materials with differently charged majority carriers [see the sketch in Fig. 10.10(a)]. In fact, due to the very small extrinsic doping concentration in nominally undoped $SrTiO_3$ (*e.g.*, Fe_{Ti} and Al_{Ti}), even slight amounts of cationic or anionic defects may cause a shift in the defect regime (p vs. n). The diffusing tracer oxygen ions will be affected by the electric field generated by space charge layers, and this will manifest as a change of slope in the diffusion profiles as sketched at the bottom of Fig. 10.10(a). One can understand the box shape of the profiles with the same kind of reasonings. The 'box' means that the diffusion into the material is initially fast, then slow, then fast(er) again [see the inset of Fig. 10.9(a)]. This is consistent with the presence of a p–n–p^+ region, as shown in the sketch of Fig. 10.10(b).

The ToF-SIMS data displayed in Fig. 10.11 support this interpretation. They report peak shifts vs. depth of $^{48}Ti^+$ and $^{86}Sr^+$ ions during depth profiling (measuring positive ions) on the same (4×1)-reconstructed sample, which was exchanged for 4 h at 600 ° and 0.1 mbar O_2 [Fig. 10.9(a)]. The peaks suddenly shift to higher apparent mass at 17 nm and 38 nm depth. In ToF detection, an apparent mass increase is equivalent to a longer flight time for the ions before detection, which may occur as a result of (negative) charging of the sample. Such charging could be consistent with the presence of insulating transition regions in a p–n–p^+ junction. In fact, the measured depths of increased sample charging at 17 nm and 38 nm fit very well to the transitions between fast and slow diffusing zones in the isotope depth profiles measured on the same sample [inset of Fig. 10.9(a)].

The exact origin of the differently doped regions close to the surface is unclear at this stage. Oxygen defects are mobile, and could not create such a complex structure stable at high temperatures over many hours. Instead, it is more likely that this is induced by small cationic defects, possibly introduced during the UHV sample treatment. However,

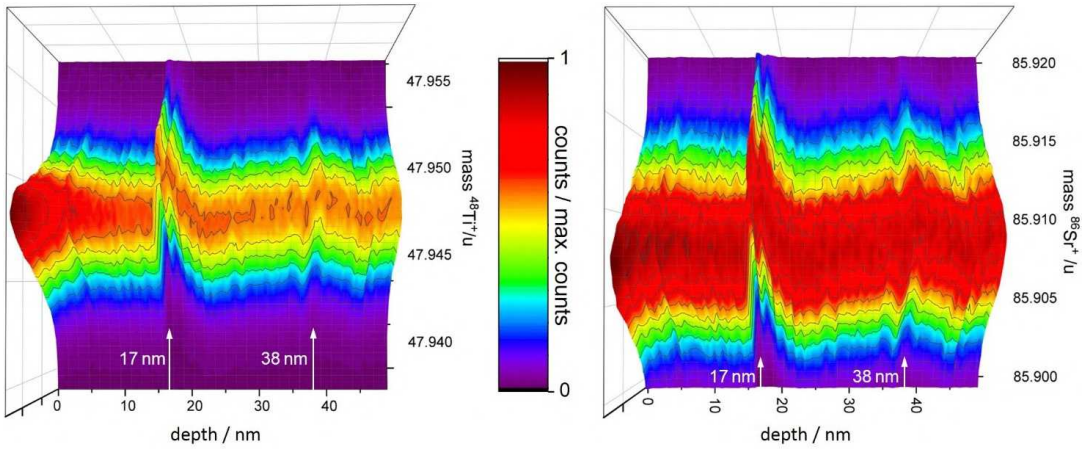

Figure 10.11. Charging effects in UHV-prepared undoped $SrTiO_3$(110) samples. Peak positions as a function of depth for $^{48}Ti^+$ and $^{86}Sr^+$ ions during depth profiling on the same (4 × 1)-reconstructed sample exchanged at 600 °C and 0.1 mbar O_2 for 4 h. The peaks suddenly shift to higher apparent mass at 17 nm and 38 nm depth. This is consistent with the presence of electronically insulating zones at these positions.

it is hard to pinpoint the exact nature of the responsible donor and acceptor defects. It is likely that acceptor dopants are given by metal vacancies. The nature of the donors is unclear: interstitial ions or Ti-antisite defects that could act as donors are usually energetically unfavorable in perovskite oxides.

10.3.3 Comparison with literature data

The investigations presented here have been performed at relatively low diffusion temperatures compared to the literature. To allow comparison, the available literature data for undoped $SrTiO_3$(100)[378] have been extrapolated to the temperatures employed in this work. Data obtained at different pressures were compared by exploiting the known pressure dependence of $k^\star$ [$k^\star(p)$=$k^\star(p_0) \times (p/p_0)^{0.31\pm0.03}$].[379] It was found that the absolute value of $k^\star$ is higher for both the (4 × 1) and the (2 × 5) reconstructions compared with literature. In particular, $k^\star$ for the (4 × 1) samples is about three orders of magnitude higher than literature values. The higher value of $k^\star$ seen on the samples used within this work is ascribed to their very clean and well-defined surfaces. The surface reconstructions are stable at the tested conditions and they are not 'deactivated' as a result of formation of secondary phases, *e.g.*, SrO, contrary to other studies. Another factor possibly playing a role is the crystal orientation, (100) vs. (110).

10.3.4 Conclusions

The studies presented in this Section, regarding the incorporation of oxygen at well-defined surfaces of undoped $SrTiO_3$(110), reinforce the message of the donor-doped counterpart study of Section 10.2: The details of the surface reconstructions are crucial to the amount of oxygen incorporated into the bulk. The (2×5) stops almost all oxygen from being incorporated, regardless of the experimental conditions. The (4×1) incorporates more oxygen (as already seen in Section 10.2, thanks to the flexibility of its surface coordination polyhedra), and increasingly higher amounts with higher temperatures. This is because, differently from the doped case, oxygen vacancies are present in the bulk (and they become more with higher temperatures), and they offer a diffusion path for the oxygen ions that make it through the surface. This makes the difference between the exchange rates of the (2×5) and of the (4×1) more pronounced than for the doped system, now at least one order of magnitude.

Using highly controlled and stable surface reconstructions is overall beneficial: The exchange rates of the surfaces used within this work are three orders of magnitude higher than those extrapolated from the literature. However, this also comes with side effects: The UHV preparation of the surfaces seems to induce local cation enrichments in the subsurface region, which affect the diffusion of tracer oxygen ions in a non-trivial manner. Specifically, a behavior consistent with a p–n–p^+ dopng profile is observed. One should pay attention to such effects when dealing with atomically controlled surface terminations.

10.4 ^{18}O exchange on $La_{0.8}Sr_{0.2}MnO_3$(110)

This Section closes the investigations on the incorporation of oxygen at model perovskite oxide surfaces. The approach is the same as the one applied in the previous Sections to $SrTiO_3$(110) single crystals, but the focus is now LSMO, the cathode material used in applications. The surfaces of LSMO were modelled by using 70 nm-thick $La_{0.8}Sr_{0.2}MnO_3$(110) single-crystalline films that were grown and characterized as described in Chapters 8 and 9. Once again, the results found underscore the importance of the atomic-scale details of the surface to the incorporation of oxygen: At otherwise identical parameters, the reactivity towards oxygen incorporation of two LSMO(110) surface structures with different properties is markedly different.

It is important to recall that the surface of LSMO(110) exhibits a variety of polarity-compensating, composition-related surface reconstructions, some of which, summarized in Fig. 8.2 in Chapter 8, are stable at realistic conditions for SOFCs ($\approx 10^{-1}$ mbar O_2). The

(1 × 1) structure [Fig. 8.2(a)] stands out among these as the most understood: Section 8.3 has discussed the DFT model proposed for this structure. It essentially consists of a single AO_x layer lying on the otherwise unmodified bulk-truncated LSMO system. The other high-pressure reconstructions of LSMO(110) have not been characterized to this level of detail. It was argued before that they consist of a Mn-rich layer lying above a (more or less relaxed) bulk-truncated LSMO(110). For this study, one of these Mn-rich reconstructions, namely the fishbone [see Fig. 8.2(c)], was compared with the (1 × 1) structure. Like for the oxygen exchange studies performed on $SrTiO_3$(110), prior to the exchange experiments, the stability of the reconstructions of interest was successfully tested. Moreover, like for $SrTiO_3$(110), half samples were realized to exclude the influence of extrinsic bulk effects on the results.

10.4.1 $^{18}O_2$ exchange experiments

Figure 10.12 shows the LEIS spectra acquired on pristine and ^{18}O-exchanged monophase samples (solid, and open symbols, respectively), whose surfaces exhibited the (1 × 1) and the fishbone reconstructions (orange, and blue, respectively). After the equilibration step (see Section 10.1.2), the samples were $^{18}O_2$-exchanged for 15 min at 700 °C and 0.3 mbar in the PLD chamber, *i.e.*, under dry conditions. After the exchange, a new, $^{18}O_2$-derived peak appears on both surfaces (highlighted in red). This is considerably more prominent on the fishbone reconstruction, suggesting a higher reactivity of this surface. Figure 10.13(a) shows the SIMS profiles acquired on LSMO(110) half samples prepared and exchanged as the samples analyzed in LEIS. Also in this case, the fishbone reconstruction (blue symbols) appears more reactive than the (1 × 1) (orange), as inferred by the larger area underlying the fishbone profile. However, these conditions appear to be *too favorable* to the system: The profiles do not reach the natural abundance level before the interface with the Nb:$SrTiO_3$(110) substrate (at 70 nm). As discussed in Section 10.2, Nb-doped $SrTiO_3$ lacks bulk oxygen vacancies, and for this reason oxygen cannot be incorporated in its bulk. The interface between LSMO and Nb-doped $SrTiO_3$ acts then as a 'barrier' for the ^{18}O incorporated in the LSMO films, which gets reflected and contributes to the area underlying the profiles. As a result, neither the LEIS data in Fig. 10.12 nor the SIMS data in Fig. 10.13(a) are reliable for quantification.

Reliable data require less favorable conditions for the oxygen incorporation, *e.g.*, slower diffusion. To this end, a lower temperature was used. At the same time, the pressure was also reduced, and such that the oxygen chemical potential was unchanged. The same oxygen chemical potential ensures stability of the reconstructions under investigations, as discussed in Chapter 8. Specifically, the exchange parameters have been

30 min, 570 °C and 1×10^{-3} mbar O_2. The corresponding SIMS profiles are shown in Fig. 10.13(b). It can be seen that the level of natural abundance is reached well before the interface with the Nb-doped substrate. Similarly to the case of undoped $SrTiO_3$ discussed in Section 10.3, 'box'-shaped profiles are obtained (best visible in logarithmic scale in the inset). Once again, one can only speculate about the origin of such unusual shapes. Like before, the fast-slow-fast regimes are possibly consistent with a p–n–p^+ analogue, likely induced by the UHV treatments employed to prepare the surfaces. The LSMO system is naturally p-doped. It is possible that the sputtering treatments, preferential to O and Mn (see Fig. 9.5 in Section 9), create a slight donor doping with respect to the bulk that does not get equilibrated during the annealing at 700 °C. Deposition of Mn on the surface after the sputtering to realize the desired reconstructions might locally replenish the system, and cause a p region to form close to the surface.

10.4.2 Interpreting results

As mentioned before, a DFT model for the fishbone reconstruction is not available. Hence, one cannot address the exact mechanisms of the oxygen incorporation yet. Nonetheless, one can use XPS to test whether the transfer of electrons plays a dominant role for LSMO(110), in analogy to the investigation on $SrTiO_3$(110) discussed in Section 10.2.3. The results are summarized in Fig. 10.14. The measured work function of the fishbone surface is 0.82±0.01 eV larger than the one of the (1×1) surface measured on the same

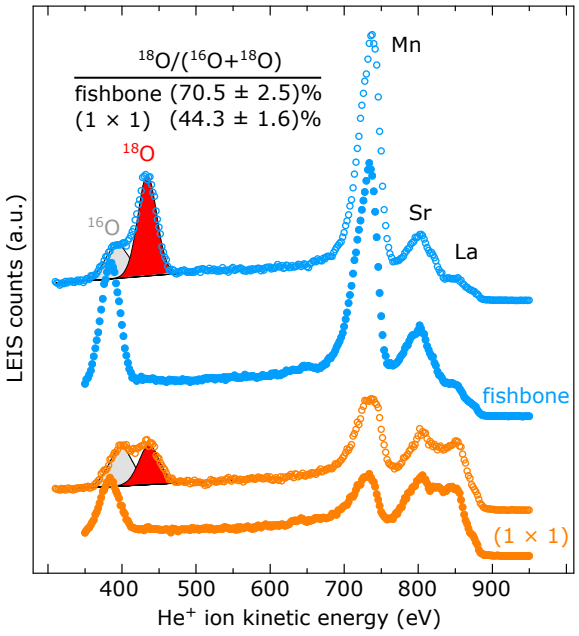

Figure 10.12. LEIS spectra (He^+ with 1000 eV primary energy) measured on pristine (full symbols) and ^{18}O-exchanged (open symbols) LSMO(110) surfaces (15 min at 700 °C and 0.3 mbar O_2). Orange and blue spectra correspond to (1×1)- and fishbone-reconstructed surfaces, respectively.

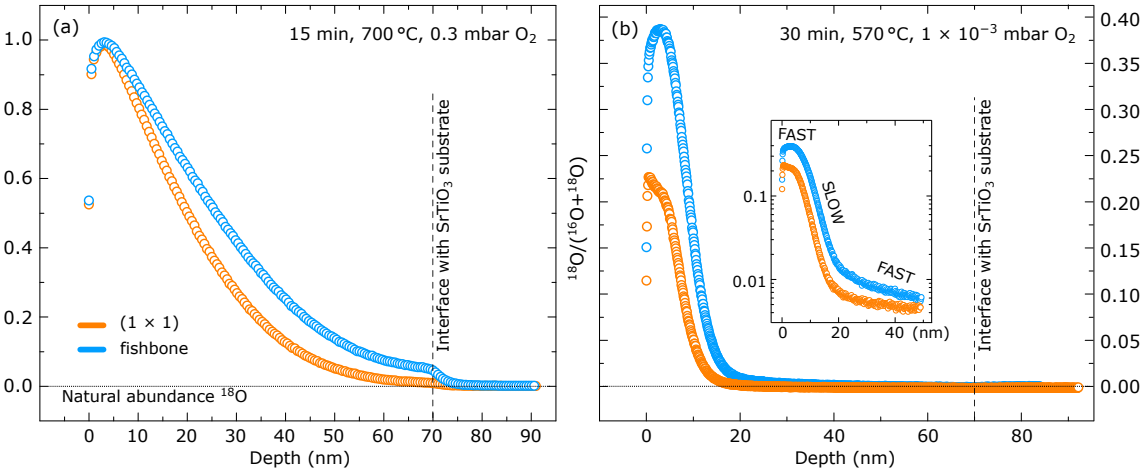

Figure 10.13. SIMS profiles relative to ^{18}O-exchange experiments performed on (1 × 1)- (orange) and fishbone- (blue) reconstructed surfaces. (a) 700 °C, 0.3 mbar O_2, 15 min. (b) 570 °C, 1 × 10^{-3} mbar O_2, 30 min. The inset in panel (b) shows the same spectra as in the main panel in logarithmic scale.

half sample, as shown from the secondary-electron emission spectra in Fig. 10.14(a). The core-level energies of the two zones on the surface half sample are overlapped (not shown), hence one can neglect the influence of surface potential or band bending. The resulting band alignment of the two reconstructions with respect to an O_2 molecule is sketched in Fig. 10.14(b). According to this scenario, one would expect easier electron transfer to O_2 molecules from the (1 × 1) surface than from the fishbone. However, since the (1 × 1) is *less* reactive than the fishbone, one concludes that the ease of electron transfer is *not* the dominant mechanism governing oxygen incorporation, much like for the $SrTiO_3$(110) surfaces. In fact, according to common wisdom, it would work against it. One could expect this behavior to be a more general property of reconstructed perovskite oxide surfaces.

At present, one cannot establish which reconstruction, the (1 × 1) or the fishbone,

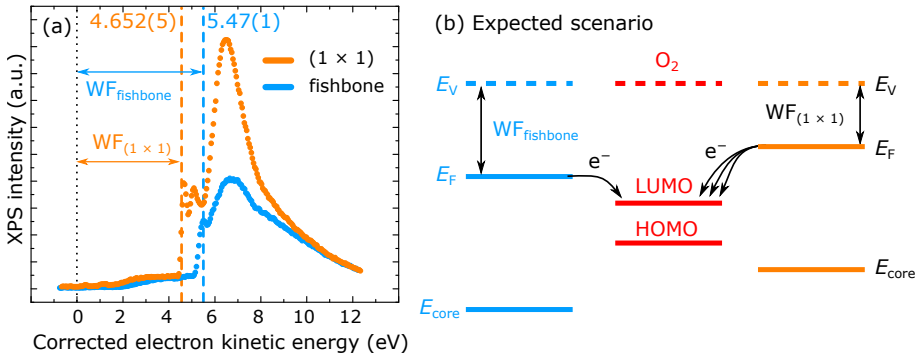

Figure 10.14. Work functions of an LSMO(110) half sample with (1 × 1) and fishbone reconstructions. Spectra acquired in the two regions are represented in orange and blue, respectively. (a) Secondary-electron emission spectra. Work functions are highlighted by vertical dashed lines. (b) Sketch of the expected band alignment of the two surfaces with respect to one O_2 molecule, assuming no band bending. The (1 × 1) should transfer more electrons than the fishbone.

has more surface oxygen vacancies. Hence, one cannot argue whether it is really the atomic arrangement and coordination of the surface atoms that determine higher rates to oxygen incorporation, or rather the amount of surface oxygen vacancies. Nonetheless, it is without doubt that different reconstructions exhibit different reactivities.

It is interesting to observe that the lower reactivity of the (1×1) surface compared to the fishbone is somewhat in agreement with the widely reported observation that AO_x-enriched surfaces cause deactivation towards oxygen incorporation in A-doped manganites. These AO_x-rich surfaces often result from the exsolution of a secondary phase, and are typically associated to ill-defined morphologies. This, however, is not the case for the (1×1) phase investigated here: As argued in Chapter 8, this phase is atomically flat, and it is not driven by cation segregation. It is hence likely that the deactivation mechanism lies in the atomic and electronic details of this surface.

10.5 Conclusions

This Chapter has explored the fundamentals of oxygen incorporation at model perovskite oxide surfaces. Starting from the simpler system, donor-doped $SrTiO_3$, and going through its undoped counterpart and, finally, LSMO, it was shown that the details of the surface reconstructions dominate the reactivity towards oxygen incorporation, at the expense of other, commonly accepted mechanisms such as the number of surface oxygen vacancies or the ease of transferring electrons to the adsorbed oxygen molecules. These investigations were enabled by an approach that combines surface science and *ex-situ* kinetic measurements. Its main merit is the ability to keep all parameters exactly constant except the ones under investigation (in this case, the surface atomic structure). As a result, it allows one to manage the intrinsic complexity of the topic, and to unveil the atomistic mechanisms governing the incorporation of oxygen. While powerful, the surface science approach has shown one main drawback: The needed UHV preparation of the surface structures introduces cation imbalances in the subsurface region that affect the diffusion profiles in a non-trivial way, complicating the analysis. On the bright side, one can imagine to tweak such cation imbalances by means of other UHV treatments or PLD deposition, and thus engineer the performance of ion-conductor materials at will.

11. Self-diffusion of metal oxides and oxygen chemical potential

11.1 Introduction

Surface diffusion is central to film growth: Growth is only allowed in out-of-equilibrium conditions, where the kinetically limited diffusion of the adparticles produces a net mass flow from the deposition source to the sample. The degree to which growth proceeds away from equilibrium, or, in other words, the interplay between thermodynamics and kinetics, determines the growth mode and many of the film properties, including its morphology.

Early works on metals and silicon, summarized in ref. 56, have demonstrated the value of understanding the fundamentals of surface diffusion to optimize film growth. Using STM, these studies have shown the strong dependence of the morphology of a growing film on the diffusivity of adatoms at the surface. They have also demonstrated that surface diffusion not only depends on the substrate temperature, but also on the atomic-scale details of the substrate. This is not surprising, given that surface diffusion is driven by atomic processes. At finite temperatures, single atoms diffuse on the surface by means of thermally activated, random 'hops' from one adsorption site to another, which occur with a probability related to a process-specific energy barrier. The hierarchy of such rates determines the microscopic paths taken by the adatoms, *i.e.*, where, how and when adatoms meet to nucleate an island, to form clusters, and when and if islands merge to produce a continuous film. By complementing the STM analysis with appropriate theoretical modeling, it was possible to gain a deep understanding of the diffusion processes on metal surfaces at the atomic scale, to establish the hierarchy of their rates, and to predict the film evolution as a function of the growth parameters.

The knowledge on self-diffusion on metal-oxide surfaces is not yet as developed as for metals. The main reason is that the presence of oxygen ligands increases the complexity

of diffusion processes notably. The oxygen content of both the substrate and the diffusing adspecies will be affected by the oxygen chemical potential, μ_O. Different oxygen stoichiometries in the substrate will produce new surface reconstructions, characterized by different sites with specific diffusion barriers. Additionally, the composition of the adspecies will be likely dynamically modified by interaction with the substrate. To gain an atomic-scale picture about self-diffusion on metal oxides, all these factors must be isolated, and this is not a trivial task.

This Chapter collects a few case studies that demonstrate the strong dependence of the morphology of metal-oxide single crystalline surfaces on μ_O. It highlights that reducing conditions not only affect the atomic-scale details of the surface (producing different surface reconstructions), but also its mesoscopic morphology: Reducing conditions promote surface flattening, an indication of high surface diffusion. To the best of the author's knowledge, this observation has not been pointed out before. This information could be exploited to optimize the preparation of single-crystalline samples in UHV, and to optimize film growth. It also sets the stage for future systematic studies about the diffusion on metal-oxide surfaces.

11.2 Evidence from a variety of case studies

The selected case studies discussed in the following best illustrate the strong effect of μ_O on the morphology of metal-oxide surfaces.

11.2.1 $In_2O_3(111)$

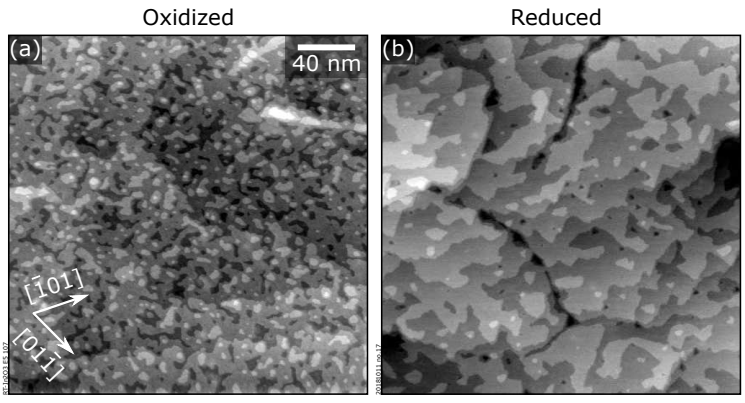

Figure 11.1. Effect of μ_O on surface diffusion on $In_2O_3(111)$. (a, b) 250 × 250 nm^2 STM images of $In_2O_3(111)$ films prepared by sputtering plus annealing at 550 °C, and by sputtering plus annealing in UHV at 550 °C, respectively. Adapted from ref. 67.

As already discussed in detail in Chapter 5, the oxygen chemical potential used dur-

ing the growth of In_2O_3 on YSZ(111) has a strong influence on the diffusivity of indium species: More reducing conditions produce reduced, volatile species that diffuse rapidly on the surface, favoring the close-to-equilibrium, 3D growth of In_2O_3.

A similar effect is also evident when comparing the morphology of the same In_2O_3(111) film after two differently oxidizing UHV treatments (Fig. 11.1). Recall that the surface of In_2O_3(111) can expose two terminations at differently oxidizing annealing conditions: The 'oxidized' termination, obtained by sputtering plus annealing at 550 °C and 7×10^{-6} mbar O_2, and the 'reduced' one, obtained by sputtering plus annealing at 550 °C in UHV (see Chapter 5 for details). Figure 11.1 compares the morphologies of the same film prepared with the two recipes above. The 'oxidized' surface [Fig. 11.1(a)] exhibits small and irregular islands not bigger than a few nanometers. On the other hand, the 'reduced' surface [Fig. 11.1(b)] exposes much bigger terraces. These results are in line with the trends of the morphology of In_2O_3 films grown at different values of μ_O (Chapter 5).

11.2.2 $Fe_2O_3(1\bar{1}02)$

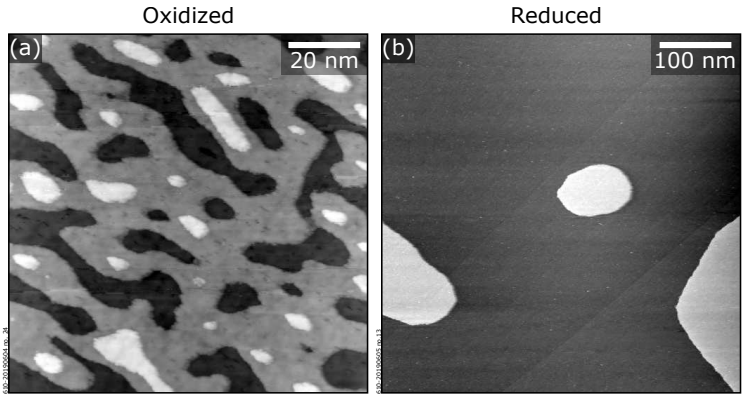

Figure 11.2. Effect of μ_O on surface diffusion on $Fe_2O_3(1\bar{1}02)$. (a, b) 200×200 nm^2 and 500×500 nm^2 STM images of the surface of the same Ti-doped $Fe_2O_3(1\bar{1}02)$ film prepared by sputtering plus annealing for 40 min at 600 °C and 4×10^{-5} mbar O_2, and by subsequent annealing for 40 min at 600 °C in UHV, respectively.

Similarly to the case of In_2O_3(111) discussed above, different annealing conditions produce two distinct surface terminations on $Fe_2O_3(1\bar{1}02)$—the stoichiometric (1×1), obtained at slightly oxidizing conditions, and the reduced (2×1), obtained in UHV (see Chapter 4). Again, similarly to In_2O_3(111), the change in the surface atomic structure produced by annealing at a given μ_O is accompanied by marked changes in the mesoscopic morphology. Figure 11.2 compares the surface morphology of the same 0.8 at.% Ti-doped film (Chapter 4) after annealing for 40 min at 600 °C and 4×10^{-5} mbar O_2, following one Ar^+ sputtering cycle [panel (a)] and after subsequent annealing at same temperature and for the same time in UHV [panel (b)]. The number of exposed layers de-

creases from four to two from the oxidized to the reduced surfaces, and a drastic change is observed in the size of their terraces (note the different image size in the two cases, 200×200 nm^2 vs. 500×500 nm^2 for the oxidized and reduced surfaces, respectively).

11.2.3 LSMO(110)

LSMO(110) offers another example along the lines of those discussed above. As seen in Chapter 8, various surface atomic structures are formed as a function of μ_O. Figure 11.3 shows that the change in the surface atomic structure is accompanied also in this case by a change in the surface morphology. In Fig. 11.3, the surfaces of the same film after different annealing treatments are shown. Figure 11.3(a) shows the result of 11 h annealing at 700 °C at 0.2 mbar O_2, while Fig. 11.3(b) shows the same surface after annealing for only 1 h at the same temperature, but in UHV (see Fig. 9.6 in Chapter 9 for the history of this sample). The number of layers exposed after the reducing treatment decreases significantly, yielding atomically flat terraces of hundreds of nanometers.

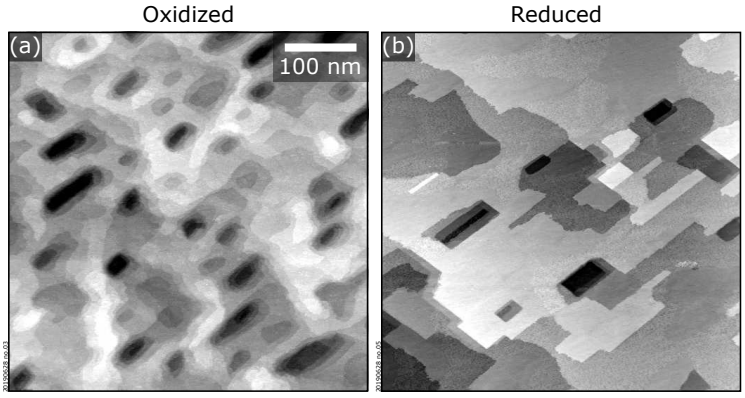

Figure 11.3. Effect of μ_O on surface diffusion on LSMO(110). (a) 500×500 nm^2 STM image of an LSMO(110) film prepared by several cycles of sputtering plus annealing at 700 °C and 0.2 mbar O_2—the last of which lasted for 11 h. (b) 500×500 nm^2 STM image of the same LSMO film after 1 h annealing at 700 °C in UHV.

11.3 Discussion and summary

The cases discussed above show that annealing a given metal-oxide surface at sufficiently reducing conditions triggers the formation of new surface reconstructions, and promotes the flattening of the surface morphology. This is indicative of higher surface diffusivity taking place at reducing conditions. Such behavior has been observed for a multitude of oxide materials, both binary and multicomponent ones, and it is likely to be a general trait of metal-oxide surfaces.

As already argued, the precise atomic mechanisms behind the observed behaviors are hard to pinpoint. A reasonable qualitative explanation is that oxygen is desorbed from the substrate at reducing conditions, causing the formation of reduced species. The correlation between oxygen stoichiometry and volatility can explain the higher diffusivity: Volatile species are associated to weaker binding to the substrate, which promotes surface diffusion.

The observed correlation between μ_O and surface morphology could be used to optimize the preparation of single-crystalline metal-oxide surfaces in UHV. Instead of sputtering plus annealing at the value of μ_O needed to achieve a given reconstruction, one could first sputter plus anneal at reducing conditions—to achieve ideal morphologies—and subsequently anneal at the needed conditions to expose the desired reconstruction.

This information could also be functional to optimize film growth. For kinetically limited types of growth, one could alternate growth at high pressure with annealing at low pressure to improve the film morphology.

Conclusions

This Thesis collects a series of surface science studies performed on a variety of metal oxides grown by PLD. Two parallel themes run through: On the one hand, the aptness of surface science tools (most prominently, STM) to shed light on the mechanisms governing metal-oxide growth by PLD. Through the examples of $In_2O_3(111)$, $SrTiO_3(110)$, and LSMO(110), it was shown how STM can unveil the influence of the PLD parameters on the growth mode and/or on the surface morphology of an oxide film from the measured changes in its composition and surface atomic structure. The few behaviors that the growths of $SrTiO_3(110)$ and LSMO(110) have in common have been highlighted, including nonstoichiometry segregation that causes changes in the surface structures, and surface-dependent sticking. These processes are responsible for the surface roughening observed under non-optimal growth conditions, and are likely shared by a larger number of complex multicomponent oxides. Knowledge brings opportunities: For all cases investigated, the new insights were functional to direct the growth willfully and produce films of the desired properties (*i.e.*, ideal composition, atomically flat surfaces), controlled down to the atomic scale (*i.e.*, exposing a given surface reconstruction).

The other underlying theme of the Thesis is the ability of STM, once a single-crystalline film has been grown, to provide with a model system for fundamental investigations. As it has been repeatedly stated, only with a well-defined and characterized system can the very essence of relevant surface processes be unveiled. This has motivated the studies on Ti-doped $Fe_2O_3(1\bar{1}02)$ and LSMO(110) films: A detailed characterization of their surface structures as a function of the surface composition and the oxygen chemical potential has been complemented by the establishment of surface structural models. In the case of LSMO(110) [but also of its simpler relative, $SrTiO_3(110)$], such knowledge has been exploited to explore the fundamentals of how oxygen incorporation occurs at model perovskite oxide surfaces. These studies have revealed the unexpected and crucial role of the surface atomic structure: The oxygen incorporation rates are mostly determined by the coordination and the arrangement of the surface species.

This Thesis does not hide the challenges intrinsic to combining PLD with surface science, as much as it underlines the benefits of such marriage. The authors believe that

the approach and the results presented here, yielding atomically controlled metal-oxide films with tunable properties, could apply to a larger number of oxide materials, and could be of value for a variety of fundamental and applied lines of research. On a fundamental level, appropriately characterized single-crystalline films can be used as model systems for investigating the atomic-scale mechanisms of relevant surface processes. On a more applied level, the ability to synthesize atomically precise thin films and thin-film heterostructures meets the ever-growing demand for downscaling the dimensions of thin-film devices.

Appendices

A XPS and LEIS settings

XPS settings

Photoelectrons were always detected at normal emission and in constant pass energy mode (50 eV for surveys and 10 eV for detailed spectra). The entrance slit was circular, with 7 mm diameter, while the exit slit was rectangular (20×39 mm^2). The accepted solid angle was regulated via an iris placed in the back focal plane of the electron optics, which was always kept to 7 mm. With these parameters, the x-ray spot on the sample is 1.5 mm in diameter when using a 'medium-magnification' mode. Before acquiring the spectra, the sample position was aligned such that no contributions from the clips and the sample plate were visible. The procedure consisted in fixing the energy of an intense peak of the sample which is not overlapped with any of the plate, and moving along the manipulator axis until the two minima of the signal, corresponding to the edges of the crystal, were identified. The sample position was set at half the distance between the two minima. The same procedure was used for the alignment along the direction orthogonal to the manipulator axis.

LEIS settings

He^+ ions were used for LEIS measurements (1 keV energy, 5×10^{-8} mbar, $\approx$1.5 nA/mm^2, 10–20 consecutive scans). The entrance slit of the hemispherical analyzer was rectangular (7×20 mm^2), while the exit slit was the same as for XPS. The iris was set to 30 mm. The sample alignment was the same as for XPS measurements. Since LEIS induces a (mild) sputtering of the surface, all samples analyzed with LEIS were prepared anew.

B UV laser optical elements: Technical details

In absence of a shutter, the entrance window of the PLD chamber gets covered with PLD deposits over time, causing its transmittivity, hence the available pulse energy density, to decrease accordingly. Major effects have been observed after deposition of TiO_2. In_2O_3, $La_{1-x}Sr_xMnO_3$, $SrTiO_3$, La_2O_3, and MnO deposition do not seem to cause significant changes. To recover the needed transmittivity/pulse energy density on the target, the entrance window was periodically cleaned by following the steps listed below:

- Wrap a napkin around plastic tweezers with rounded tips (Kimtech tissues do not leave residues, and they seem resistant to HNO_3).
- Slightly damp the napkin in concentrated HNO_3 (65 wt.%). Move it circularly on the window for a few minutes (change napkin as soon as it gets fluffy. Probably some 10 min total per spot is needed). Note the solution can dissolve Ni and Fe as well, which compose the brazed connection between the quartz and the stainless steel flange (Kovar). Do not exceed with dampening the napkin, and take care of staying a few millimiters away from the glass/steel brazing.
- Repeat to cover the whole window.
- Dilute the solution residues by repeating the same process with a napkin slightly dampened in ultrapure water. Repeat at least 4 times. Rinse the window under flowing ultrapure water for 5 min. If needed, the cleaning process can be repeated by using also diluted HNO_3, concentrated or diluted HCl, and aqua regia (HCl:HNO_3=3:1).
- To remove H_2O residues, the window can be baked in air (150 °C, max 200 °C, maximum ramp 2 °C/min).
- Before pumping down and baking the system with the freshly cleaned window, check that its transmission is indeed restored by temporarily mounting the window back.

Typical transmittivities of the entrance window after cleaning are between 85% and 90%.

C New μ-metal PLD chamber

The PLD laboratory is located in the center of Vienna: Many tram and underground lines run in front and below the building. The resulting electromagnetic fields are strong, and can deviate electrons produced by some of the lab sources. The RHEED is affected the most: The signal is so unstable that it is hard to detect RHEED oscillations at day time. To overcome this issue and to implement other improvements, Michele Riva has designed a new μ-metal chamber (μ-metal effectively screens magnetic fields), which was manufactured by VAb GmbH. We have replaced the old stainless steel chamber for this one in October 2018. Some of the improvements implemented in the new design are:

- Movable shutter in front of the UV laser exit window. This ensures a constant transmittivity of the exit window (no coating), resulting in more reliable evaluation of the laser fluence.
- Movable shutter in front of the IR laser entrance window. This prevents the window to be coated with deposits, especially during pre-ablation, when the sample is kept in an adjacent chamber.
- Possibility to isolate the entrance window of the UV laser from the main chamber (VAT valve). This allows one to vent a small volume around the entrance window that can then be cleaned from PLD deposits, without the need to vent the main chamber.
- Differential pumping for mass-spectrometer and gas line that allows one to leak the gases composing the atmosphere in the main PLD chamber to it. This allows one to measure the composition and purity of the background gas, up to atmospheric pressure.
- New design of the target carousel and receptacle, for reproducible positioning and alignment.

D Masks to deposit Pt contacts: Dimensional drawings

See Fig. D.

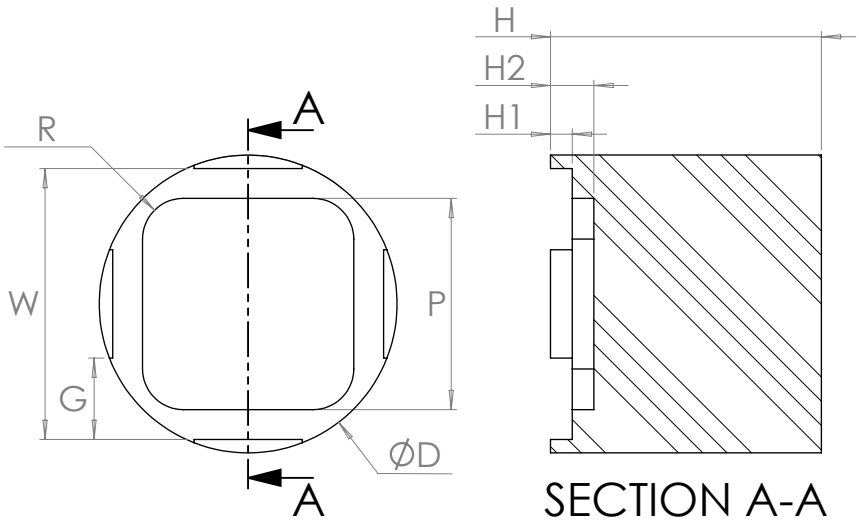

Type	5×5×0.5 large electrodes	5×5×0.5 small electrodes	10×10×1 front	10×10×1 back, window
W	5.0(±0.05)	5.0(±0.05)	10(±0.05)	10(±0.05)
H1	0.4(±0.05)	0.4(±0.05)	0.8(±0.10)	0.8(±0.10)
D	5.5(−0.05)	6.0(±0.05)	12(±0.10)	12(±0.10)
P	3.9(±0.10)	3.9(±0.10)	8.5(±0.20)	8.5(±0.20)
G	1.5(±0.20)	1.5(±0.20)	2.5(±0.10)	2.5(±0.10)
R	0.75	0.75	1.0	1.0
H	5.0(±0.50)	5.0(±0.50)	5.0(±0.50)	5.0(±0.50)
H2	0.8(±0.20)	0.9(±0.20)	1.3(±0.20)	H

Figure D. Dimensional drawings of PEEK masks used to deposit Pt contacts on samples of various size.

E References for Sr and TiO_2 deposition

To prepare a $SrTiO_3$(110) surface to exhibit the desired reconstruction, its near-surface stoichiometry was adjusted by depositing controlled amounts of TiO_2 and SrO, followed by O_2 annealing (30 min, 1000 °C, 7×10^{-6} mbar O_2). TiO_2 was deposited by PLD, from a single-crystalline target, at RT, 2.5 J/cm^2, 7×10^{-6} mbar O_2. SrO was deposited by an effusion cell, also at RT (details in Chapter 2). The amounts to be deposited were chosen based on the surface phase diagram described in Chapter 6, after proper calibration of the Sr and Ti doses. Figure E reports a series of reference experiments that might help to reach the desired reconstruction. Note that variations in the history of the sample or in the fluxes calibrations may cause deviations from the amounts reported here.

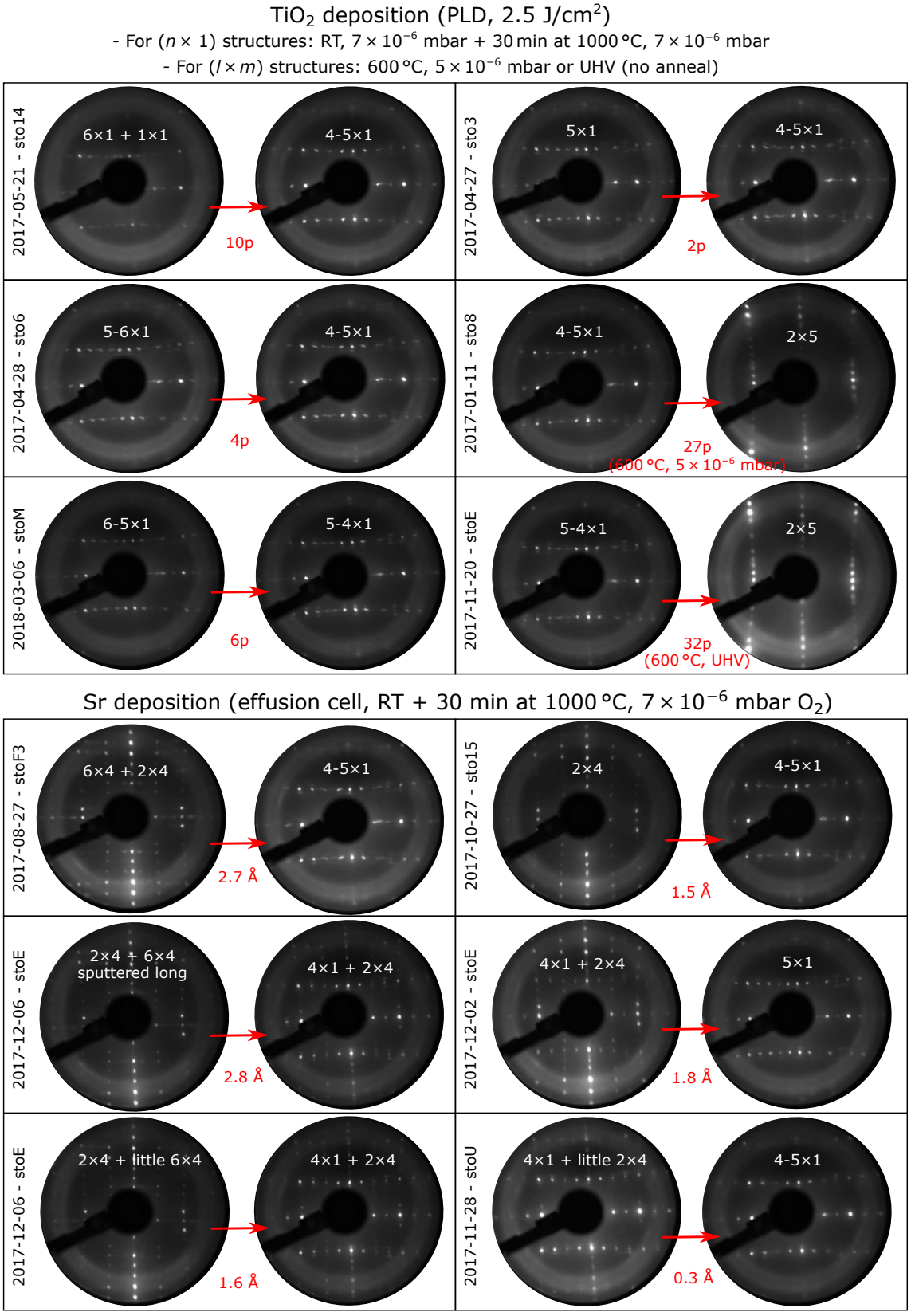

Figure E. Reference experiments (LEED patterns) for Sr and TiO_2 deposition, to adjust the near-surface stoichiometry of $SrTiO_3$(110) samples. TiO_2 amounts are expressed in terms of the number of pulses shot on the TiO_2 target.

F Non-uniform $SrTiO_3$(110) samples

As mentioned in Chapter 2, misalignment of both the Sr evaporation and the sputtering positions can lead to gradients in the near-surface stoichiometry of $SrTiO_3$(110) samples, manifested as different reconstructions at different positions of the sample. As discussed in the Sections below, the extent of the problem was reduced through a careful calibration of the sample positions for both sputtering and Sr evaporation. Residual spatial disuniformities were resolved by depositing controlled amounts of TiO_2 on selected areas of the sample.

Position calibration of the sputtering gun and the Sr evaporator

The optimum sample position for the sputtering was found with a home-made 'Faraday-cup': The current was measured at the manipulator filament while sputtering a stainless steel plate with a 1 mm-diameter hole in the middle. The (grounded) plate was positioned orthogonal to the gun axis. A BNC cable was connected to the filament and ground, and the connection was shielded with aluminum foil. After measuring the dark current, the plate was sputtered with an Ar pressure of 9×10^{-6} mbar, while monitoring the current as a function of the 2D position of the sample manipulator (the x position was fixed to a reasonable value, and movements in y and z followed). The center of the corresponding gaussian-type curve identified the new center position. Refer to the SPECS logbook (25.09.2017) for additional details.

Even after optimal alignment of the sputter gun, the sputtered samples are not uniformly reconstructed: The center is sputtered more than the sides, resulting in the formation of Ti-richer reconstructions at the center of the sample. To solve the issue, the sample was manually rastered into the sputtering beam, following a 5×5 grid of points (separation between points of 0.8 mm both in the vertical and horizontal direction), and keeping the sample at each position for 30 s (for a total sputtering time of 12 min 30 s). Another (more time consuming) approach that was used before thinking about the manual rastering is combining TiO_2 deposition with partial and iterative shading of the sample (see below).

The optimum position for the Sr evaporation was found by depositing 1 nm Sr on a clean Nicrofer® sample plate, and then evaluating XPS intensity ratios of the Ni LMM over Sr 3d peaks. The spectra were acquired in several positions on the plate (1 mm spacing along z and along y, while fixing the distance from the analyzer cone), to realize a grid where the ratios were plot in 2D. The center of the corresponding gaussian-type curve identified the new center position. For additional details, refer to SPECS logbook, 23.01.18.

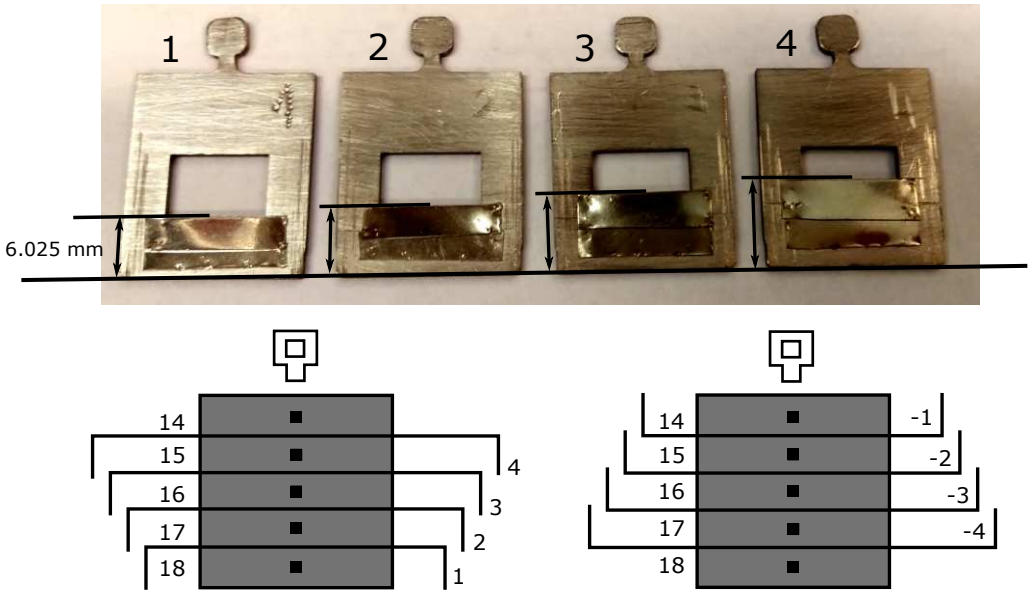

Figure F. (a) Masks to adjust the uniformity of the surface reconstructions on $SrTiO_3$(110) samples. A mask can be placed in front of the sample during TiO_2 deposition, by means of a double decker sample holder, such that only the unshaded parts of the sample will be covered by TiO_2, and change their surface reconstruction accordingly. From mask '1' to mask '4', the masks shade the first bottom-most millimeter of the sample, up to leaving free only the top-most millimeter. By iteratively shading different areas of the sample, the surface can be made uniform. (b) Sketch of the sample, and of the portions that are shaded by each mask. On the left of the sample, the LEED positions (y) are reported.

Making non-uniform samples uniform

Another approach to obtain spatially uniform samples (besides the manual raster sputtering) is the iterative deposition of TiO_2 by PLD on differently shaded parts of the sample. This was achieved by means of the home-made masks depicted in Fig. F. Each mask consists of a Nicrofer® plate with a hole centered with the sample position, and a Nicrofer® foil (0.03 mm thickness) spot-welded on the mask to shade the desired portion of the sample. During deposition, the mask was placed in front of the sample, as allowed by the double-decker geometry of our home-designed PLD holder. The mask labeled as '1' shades the bottom-most mm of the sample, mask '2' the bottom-most 2 mm, and so on. The same concept is used to prepare the 'half sample' for the oxygen exchange experiments of Chapter 10. There, the foil shades half of the sample.

The following example exemplifies the use of the masks: Take a gradient from Ti-rich to more Sr-rich from the bottom part to the top part of the sample. In such a case, the following iterative process is employed: The bottom-most part of the sample (LEED position 18, see Fig. F) is shaded with mask number one, while TiO_2 is deposited on the rest of the sample. In this way, all the sample surface, apart from the bottom-most millimeter, gets Ti-enriched. Next, one millimeter more at the bottom of the sample is shaded by using mask number 2, and more TiO_2 is deposited. Now, only the three top-

most millimeters are covered with TiO_2, and get Ti-enriched. The same procedure is applied until no gradient is seen anymore in LEED. If a gradient is present in the other direction, masks are employed that are complementary to the ones shown in the picture (labeled as -1, -2, -3, -4 at the bottom right of Fig. F). The amounts to be deposited are chosen based on the reference experiments reported above.

Bibliography

[1] U. Diebold, S.-C. Li, and M. Schmid, *Oxide surface science,* Annu. Rev. Phys. Chem. **61**, 129 (2010).

[2] D. G. Schlom, L.-Q. Chen, X. Pan, A. Schmehl, and M. A. Zurbuchen, *A thin film approach to engineering functionality into oxides,* J. Am. Ceram. Soc. **91**, 2429 (2008).

[3] A. S. Bhalla, R. Guo, and R. Roy, *The perovskite structure–a review of its role in ceramic science and technology,* Mater. Res. Innovations **4**, 3 (2000).

[4] M. A. Peña and J. L. G. Fierro, *Chemical structures and performance of perovskite oxides,* Chem. Rev. **101**, 1981 (2001).

[5] D. P. Kumah, J. H. Ngai, and L. Kornblum, *Epitaxial oxides on semiconductors: From fundamentals to new devices,* Adv. Funct. Mater. , 1901597 (2019).

[6] P. Zubko, S. Gariglio, M. Gabay, P. Ghosez, and J.-M. Triscone, *Interface physics in complex oxide heterostructures,* Annu. Rev. Condens. Matter Phys. **2**, 141 (2011).

[7] H. Y. Hwang, Y. Iwasa, M. Kawasaki, B. Keimer, N. Nagaosa, and Y. Tokura, *Emergent phenomena at oxide interfaces,* Nat. Mater. **11**, 103 (2012).

[8] M. Setvín, M. Wagner, M. Schmid, G. S. Parkinson, and U. Diebold, *Surface point defects on bulk oxides: atomically-resolved scanning probe microscopy,* Chem. Soc. Rev. **46**, 1772 (2017).

[9] J. Jupille and G. Thornton, *Defects at oxide surfaces*, Vol. 58 (Springer, 2015).

[10] D. P. Woodruff, *Oxide surfaces* (Elsevier, 2001).

[11] G. S. Parkinson and U. Diebold, *Adsorption on metal oxide surfaces,* in *Surface and Interface Science* (Wiley Online Library) pp. 793–817.

[12] M. Coll, J. Fontcuberta, M. Althammer, M. Bibes, H. Boschker, A. Calleja, G. Cheng, M. Cuoco, R. Dittmann, B. Dkhil, I. El Baggari, M. Fanciulli, I. Fina,

E. Fortunato, C. Frontera, S. Fujita, V. Garcia, S. T. B. Goennenwein, C.-G. Granqvist, J. Grollier, R. Gross, A. Hagfeldt, G. Herranz, K. Hono, E. Houwman, M. Huijben, A. Kalaboukhov, D. J. Keeble, G. Koster, L. F. Kourkoutis, J. Levy, M. Lira-Cantu, J. L. MacManus-Driscoll, J. Mannhart, R. Martins, S. Menzel, T. Mikolajick, M. Napari, M. D. Nguyen, G. Niklasson, C. Paillard, S. Panigrahi, G. Rijnders, F. Sánchez, P. Sanchis, S. Sanna, D. G. Schlom, U. Schroeder, K. M. Shen, A. Siemon, M. Spreitzer, H. Sukegawa, R. Tamayo, J. van den Brink, N. Pryds, and F. Miletto Granozio, *Towards oxide electronics: a roadmap,* Appl. Surf. Sci. **482**, 1 (2019).

[13] H. Boschker and J. Mannhart, *Quantum-matter heterostructures,* Annu. Rev. Condens. Matter Phys. **8**, 145 (2017).

[14] F. Miletto Granozio, G. Koster, and G. Rijnders, *Functional oxide interfaces,* MRS Bull. **38**, 1017 (2013).

[15] A. Ohtomo and H. Y. Hwang, *A high-mobility electron gas at the $LaAlO_3/SrTiO_3$ heterointerface,* Nature **427**, 423 (2004).

[16] R. B. Comes, S. R. Spurgeon, S. M. Heald, D. M. Kepaptsoglou, L. Jones, P. V. Ong, M. E. Bowden, Q. M. Ramasse, P. V. Sushko, and S. A. Chambers, *Interface-induced polarization in $SrTiO_3$-$LaCrO_3$ superlattices,* Adv. Mater. Interfaces **3**, 1500779 (2016).

[17] P. Schütz, D. Di Sante, L. Dudy, J. Gabel, M. Stübinger, M. Kamp, Y. Huang, M. Capone, M.-A. Husanu, V. N. Strocov, G. Sangiovanni, M. Sing, and R. Claessen, *Dimensionality-driven metal-insulator transition in spin-orbit-coupled $SrIrO_3$,* Phys. Rev. Lett. **119**, 256404 (2017).

[18] F. Gunkel, C. Bell, H. Inoue, B. Kim, A. G. Swartz, T. A. Merz, Y. Hikita, S. Harashima, H. K. Sato, M. Minohara, S. Hoffmann-Eifert, R. Dittmann, and H. Y. Hwang, *Defect control of conventional and anomalous electron transport at complex oxide interfaces,* Phys. Rev. X **6**, 031035 (2016).

[19] A. Chikina, F. Lechermann, M.-A. Husanu, M. Caputo, C. Cancellieri, X. Wang, T. Schmitt, M. Radovic, and V. N. Strocov, *Orbital ordering of the mobile and localized electrons at oxygen-deficient $LaAlO_3/SrTiO_3$ interfaces,* ACS Nano **12**, 7927 (2018).

[20] Z. Zhong and P. Hansmann, *Band alignment and charge transfer in complex oxide interfaces,* Phys. Rev. X **7**, 011023 (2017).

[21] S.-C. Lin, C.-T. Kuo, R. B. Comes, J. E. Rault, J.-P. Rueff, S. Nemšák, A. Taleb, J. B. Kortright, J. Meyer-Ilse, E. Gullikson, P. V. Sushko, S. R. Spurgeon, M. Gehlmann, M. E. Bowden, L. Plucinski, S. A. Chambers, and C. S. Fadley, *Interface properties and built-in potential profile of a $LaCrO_3/SrTiO_3$ superlattice determined by standing-wave excited photoemission spectroscopy,* Phys. Rev. B **98**, 165124 (2018).

[22] Z. Huang, A. Ariando, X. R. Wang, A. Rusydi, J. Chen, H. Yang, and T. Venkatesan, *Interface engineering and emergent phenomena in oxide heterostructures,* Adv. Mater. **30**, 1802439 (2018).

[23] F. Hellman, A. Hoffmann, Y. Tserkovnyak, G. S. D. Beach, E. E. Fullerton, C. Leighton, A. H. MacDonald, D. C. Ralph, D. A. Arena, H. A. Dürr, P. Fischer, J. Grollier, J. P. Heremans, T. Jungwirth, A. V. Kimel, B. Koopmans, I. N. Krivorotov, S. J. May, A. K. Petford-Long, J. M. Rondinelli, N. Samarth, I. K. Schuller, A. N. Slavin, M. D. Stiles, O. Tchernyshyov, A. Thiaville, and B. L. Zink, *Interface-induced phenomena in magnetism,* Rev. Mod. Phys. **89**, 025006 (2017).

[24] J. D. Hoffman, B. J. Kirby, J. Kwon, G. Fabbris, D. Meyers, J. W. Freeland, I. Martin, O. G. Heinonen, P. Steadman, H. Zhou, C. M. Schlepütz, M. P. M. Dean, S. G. E. te Velthuis, J.-M. Zuo, and A. Bhattacharya, *Oscillatory noncollinear magnetism induced by interfacial charge transfer in superlattices composed of metallic oxides,* Phys. Rev. X **6**, 041038 (2016).

[25] P. Chen, Z. Huang, C. Li, B. Zhang, N. Bao, P. Yang, X. Yu, S. Zeng, C. Tang, X. Wu, J. Chen, J. Ding, S. J. Pennycook, A. Ariando, T. V. Venkatesan, and G. M. Chow, *Binary controls on interfacial magnetism in manganite heterostructures,* Adv. Funct. Mater. **28**, 1801766 (2018).

[26] F. Motti, G. Vinai, A. Petrov, B. A. Davidson, B. Gobaut, A. Filippetti, G. Rossi, G. Panaccione, and P. Torelli, *Strain-induced magnetization control in an oxide multiferroic heterostructure,* Phys. Rev. B **97**, 094423 (2018).

[27] Y. J. Shin, Y. Kim, S.-J. Kang, H.-H. Nahm, P. Murugavel, J. R. Kim, M. R. Cho, L. Wang, S. M. Yang, J.-G. Yoon, J.-S. Chung, M. Kim, H. Zhou, S. H. Chang, and T. W. Noh, *Interface control of ferroelectricity in an $SrRuO_3/BaTiO_3/SrRuO_3$ capacitor and its critical thickness,* Adv. Mater. **29**, 1602795 (2017).

[28] D. A. Gilbert, A. J. Grutter, P. D. Murray, R. V. Chopdekar, A. M. Kane, A. L. Ionin, M. S. Lee, S. R. Spurgeon, B. J. Kirby, B. B. Maranville, A. T. N'Diaye, A. Mehta, E. Arenholz, K. Liu, Y. Takamura, and J. A. Borchers, *Ionic tuning of cobaltites at the nanoscale,* Phys. Rev. Mater. **2**, 104402 (2018).

[29] T. Fukumura, M. Ohtani, M. Kawasaki, Y. Okimoto, T. Kageyama, T. Koida, T. Hasegawa, Y. Tokura, and H. Koinuma, *Rapid construction of a phase diagram of doped Mott insulators with a composition-spread approach,* Appl. Phys. Lett. **77**, 3426 (2000).

[30] R. Potyrailo, K. Rajan, K. Stoewe, I. Takeuchi, B. Chisholm, and H. Lam, *Combinatorial and high-throughput screening of materials libraries: review of state of the art,* ACS Comb. Sci. **13**, 579 (2011).

[31] M. Murakami, K.-S. Chang, M. A. Aronova, C.-L. Lin, M. H. Yu, J. H. Simpers, M. Wuttig, and I. Takeuchi, *Tunable multiferroic properties in nanocomposite $PbTiO_3$–$CoFe_2O_4$ epitaxial thin films,* Appl. Phys. Lett. **87**, 112901 (2005).

[32] K.-S. Chang, M. Aronova, O. Famodu, I. Takeuchi, S. E. Lofland, J. Hattrick-Simpers, and H. Chang, *Multimode quantitative scanning microwave microscopy of in situ grown epitaxial $Ba_{1-x}Sr_xTiO_3$ composition spreads,* Appl. Phys. Lett. **79**, 4411 (2001).

[33] S. Fujino, M. Murakami, V. Anbusathaiah, S.-H. Lim, V. Nagarajan, C. J. Fennie, M. Wuttig, L. Salamanca-Riba, and I. Takeuchi, *Combinatorial discovery of a lead-free morphotropic phase boundary in a thin-film piezoelectric perovskite,* Appl. Phys. Lett. **92**, 202904 (2008).

[34] A. Ojeda-G-P, M. Döbeli, and T. Lippert, *Influence of plume properties on thin film composition in pulsed laser deposition,* Adv. Mater. Interfaces **5**, 1701062 (2018).

[35] B. Gobaut, P. Orgiani, A. Sambri, E. di Gennaro, C. Aruta, F. Borgatti, V. Lollobrigida, D. Ceolin, J.-P. Rueff, R. Ciancio, C. Bigi, P. K. Das, J. Fujii, D. Krizmancic, P. Torelli, I. Vobornik, G. Rossi, F. M. Granozio, U. S. diUccio, and G. Panaccione, *Role of oxygen deposition pressure in the formation of Ti defect states in TiO_2(001) anatase thin films,* ACS Appl. Mater. Interfaces **9**, 23099 (2017).

[36] T. Ohnishi, H. Koinuma, and M. Lippmaa, *Pulsed laser deposition of oxide thin films,* Appl. Surf. Sci. **252**, 2466 (2006).

[37] T. Ohnishi, K. Shibuya, T. Yamamoto, and M. Lippmaa, *Defects and transport in complex oxide thin films,* J. Appl. Phys. **103**, 103703 (2008).

[38] C. M. Brooks, L. F. Kourkoutis, T. Heeg, J. Schubert, D. A. Muller, and D. G. Schlom, *Growth of homoepitaxial $SrTiO_3$ thin films by molecular-beam epitaxy,* Appl. Phys. Lett. **94**, 162905 (2009).

[39] C. Xu, H. Du, A. J. H. van der Torren, J. Aarts, C.-L. Jia, and R. Dittmann, *Formation mechanism of Ruddlesden-Popper-type antiphase boundaries during the kinetically limited growth of Sr rich $SrTiO_3$ thin films,* Sci. Rep. **6**, 38296 (2016).

[40] S. Wicklein, A. Sambri, S. Amoruso, X. Wang, R. Bruzzese, A. Koehl, and R. Dittmann, *Pulsed laser ablation of complex oxides: The role of congruent ablation and preferential scattering for the film stoichiometry,* Appl. Phys. Lett. **101**, 131601 (2012).

[41] J. Chen, M. Döbeli, D. Stender, K. Conder, A. Wokaun, C. W. Schneider, and T. Lippert, *Plasma interactions determine the composition in pulsed laser deposited thin films,* Appl. Phys. Lett. **105**, 114104 (2014).

[42] A. Simon and Z. Kantor, *New challenges in rutherford backscattering spectrometric (RBS) analysis of nanostructured thin films,* in *Nanotechnology*, Vol. 5118 (International Society for Optics and Photonics, 2003) p. 179.

[43] S. M. Mukhopadhyay, *Sample preparation for microscopic and spectroscopic characterization of solid surfaces and films,* in *Sample preparation techniques in analytical chemistry* (Wiley Online Library, 2003) p. 377.

[44] T. Denneulin, W. Maeng, C.-B. Eom, and M. Hÿtch, *Lattice reorientation in tetragonal PMN-PT thin film induced by focused ion beam preparation for transmission electron microscopy,* J. Appl. Phys. **121**, 055302 (2017).

[45] G. Koster, *Reflection high-energy electron diffraction (RHEED) for in situ characterization of thin film growth,* in *In situ characterization of thin film growth* (Elsevier, 2011) p. 3.

[46] A. Rijnders and D. Blank, *Growth kinetics during PLD,* in *Pulsed Laser Deposition of Thin Films: Applications-led Growth of Functional Materials* (Wiley, 2007) p. 177.

[47] A. P. Kajdos and S. Stemmer, *Surface reconstructions in molecular beam epitaxy of $SrTiO_3$,* Appl. Phys. Lett. **105**, 191901 (2014).

[48] J. Feng, F. Yang, Z. Wang, Y. Yang, L. Gu, J. Zhang, and J. Guo, *Growth of $SrTiO_3$(110) film by oxide molecular beam epitaxy with feedback control,* AIP Adv. **2**, 041407 (2012).

[49] S. Amoruso, B. Toftmann, and J. Schou, *Thermalization of a UV laser ablation plume in a background gas: From a directed to a diffusionlike flow,* Phys. Rev. E **69**, 056403 (2004).

[50] M. Esposito, M. Bator, M. Döbeli, T. Lippert, C. W. Schneider, and A. Wokaun, *Negative ions: The overlooked species in thin film growth by pulsed laser deposition,* Appl. Phys. Lett. **99**, 191501 (2011).

[51] J. Chen, J. G. Lunney, T. Lippert, A. Ojeda-G-P, D. Stender, C. W. Schneider, and A. Wokaun, *Langmuir probe measurements and mass spectrometry of plasma plumes generated by laser ablation of $La_{0.4}Ca_{0.6}MnO_3$,* J. Appl. Phys. **116**, 073303 (2014).

[52] S. Amoruso, C. Aruta, R. Bruzzese, D. Maccariello, L. Maritato, F. M. Granozio, P. Orgiani, U. Scotti di Uccio, and X. Wang, *Optimization of $La_{0.7}Ba_{0.3}MnO_{3-\delta}$ complex oxide laser ablation conditions by plume imaging and optical emission spectroscopy,* J. Appl. Phys. **108**, 043302 (2010).

[53] R. A. Al-Wazzan, C. L. S. Lewis, and T. Morrow, *A technique for mapping three-dimensional number densities of species in laser produced plumes,* Rev. Sci. Instrum. **67**, 85 (1996).

[54] K. Orsel, R. Groenen, H. M. J. Bastiaens, G. Koster, G. Rijnders, and K.-J. Boller, *Spatial and temporal mapping of Al and AlO during oxidation in pulsed laser ablation of $LaAlO_3$,* J. Instrum. **8**, C10021 (2013).

[55] K. Orsel, R. Groenen, B. Bastiaens, G. Koster, G. Rijnders, and K.-J. Boller, *Influence of the oxidation state of $SrTiO_3$ plasmas for stoichiometric growth of pulsed laser deposition films identified by laser induced fluorescence,* APL Mater. **3**, 106103 (2015).

[56] G. Franceschi, M. Riva, M. Schmid, and U. Diebold, *Scanning probe microscopy,* in *The world scientific materials science handbook of thin film deposition by molecular beam epitaxy: With applications to different metals, material compounds and groups (In 4 Volumes)* (2020).

[57] T. Koida and M. Kondo, *High electron mobility of indium oxide grown on yttria-stabilized zirconia,* J. Appl. Phys. **99**, 123703 (2006).

[58] M. Koubaa, A. M. Haghiri-Gosnet, R. Desfeux, P. Lecoeur, W. Prellier, and B. Mercey, *Crystallinity, surface morphology, and magnetic properties of $La_{0.7}Sr_{0.3}MnO_3$ thin films: an approach based on the laser ablation plume range models,* J. Appl. Phys. **93**, 5227 (2003).

[59] C. Wang, B. L. Cheng, S. Wang, H. B. Lu, Y. L. Zhou, Z. H. Chen, and G. Z. Yang, *Effects of oxygen pressure on lattice parameter, orientation, surface morphology and*

deposition rate of $(Ba_{0.02}Sr_{0.98})TiO_3$ thin films grown on MgO substrate by pulsed laser deposition, Thin Solid Films **485**, 82 (2005).

[60] E. Tarsa, E. Hachfeld, F. Quinlan, J. Speck, and M. Eddy, *Growth-related stress and surface morphology in homoepitaxial $SrTiO_3$ films,* Appl. Phys. Lett. **68**, 490 (1996).

[61] T. Ohsawa, K. Iwaya, R. Shimizu, T. Hashizume, and T. Hitosugi, *Thickness-dependent local surface electronic structures of homoepitaxial $SrTiO_3$ thin films,* J. Appl. Phys. **108**, 073710 (2010).

[62] R. Shimizu, K. Iwaya, T. Ohsawa, S. Shiraki, T. Hasegawa, T. Hashizume, and T. Hitosugi, *Atomic-scale visualization of initial growth of homoepitaxial $SrTiO_3$ thin film on an atomically ordered substrate,* ACS Nano **5**, 7967 (2011).

[63] R. Shimizu, T. Ohsawa, K. Iwaya, S. Shiraki, and T. Hitosugi, *Epitaxial growth process of $La_{0.7}Ca_{0.3}MnO_3$ thin films on $SrTiO_3(001)$: thickness-dependent inhomogeneity caused by excess Ti atoms,* Cryst. Growth Des. **14**, 1555 (2014).

[64] A. Tselev, R. K. Vasudevan, A. G. Gianfrancesco, L. Qiao, P. Ganesh, T. L. Meyer, H. N. Lee, M. D. Biegalski, A. P. Baddorf, and S. V. Kalinin, *Surface control of epitaxial manganite films via oxygen pressure,* ACS Nano **9**, 4316 (2015).

[65] G. Franceschi, M. Schmid, U. Diebold, and M. Riva, *Movable holder for a quartz crystal microbalance for exact growth rates in pulsed laser deposition,* Rev. Sci. Instrum. **91**, 065003 (2020).

[66] G. Franceschi, F. Kraushofer, M. Meier, G. Parkinson, M. Schmid, U. Diebold, and M. Riva, *A model system for photocatalysis: Ti-doped $Fe_2O_3(1\bar{1}02)$ single-crystalline films,* Chem. Mater. **32**, 3753 (2020).

[67] G. Franceschi, M. Wagner, J. Hofinger, T. Krajňák, M. Schmid, U. Diebold, and M. Riva, *Growth of $In_2O_3(111)$ thin films with optimized surfaces,* Phys. Rev. Mater. **3**, 103403 (2019).

[68] M. Riva, G. Franceschi, M. Schmid, and U. Diebold, *Epitaxial growth of complex oxide films: Role of surface reconstructions,* Phys. Rev. Research **1**, 033059 (2019).

[69] M. Riva, G. Franceschi, Q. Lu, M. Schmid, B. Yildiz, and U. Diebold, *Pushing the detection of cation nonstoichiometry to the limit,* Phys. Rev. Mater. **3**, 043802 (2019).

[70] G. Franceschi, M. Schmid, U. Diebold, and M. Riva, *Atomically resolved surface phases of $La_{0.8}Sr_{0.2}MnO_3(110)$ thin films,* J. Mater. Chem. A (2020), 10.1039/D0TA07032G, *accepted*.

[71] M. Riva, M. Kubicek, X. Hao, G. Franceschi, S. Gerhold, M. Schmid, H. Hutter, J. Fleig, C. Franchini, B. Yildiz, and U. Diebold, *Influence of surface atomic structure demonstrated on oxygen incorporation mechanism at a model perovskite oxide,* Nat. Commun. **9**, 3710 (2018).

[72] R. Eason, *Pulsed laser deposition of thin films: applications-led growth of functional materials* (John Wiley & Sons, 2007).

[73] A. Ojeda-G-P, C. W. Schneider, M. Döbeli, T. Lippert, and A. Wokaun, *The importance of pressure and mass ratios when depositing multi-element oxide thin films by pulsed laser deposition,* Appl. Surf. Sci. **389**, 126 (2016).

[74] P. Orgiani, R. Ciancio, A. Galdi, S. Amoruso, and L. Maritato, *Physical properties of $La_{0.7}Ba_{0.3}MnO_{3-\delta}$ complex oxide thin films grown by pulsed laser deposition technique,* Appl. Phys. Lett. **96**, 032501 (2010).

[75] C. A. Schneider, W. S. Rasband, and K. W. Eliceiri, *NIH Image to ImageJ: 25 years of image analysis,* Nat. Methods **9**, 671 (2012).

[76] S. Gerhold, M. Riva, B. Yildiz, M. Schmid, and U. Diebold, *Adjusting island density and morphology of the $SrTiO_3$(110)-(4× 1) surface: Pulsed laser deposition combined with scanning tunneling microscopy,* Surf. Sci. **651**, 76 (2016).

[77] H. Schraknepper, C. Bäumer, F. Gunkel, R. Dittmann, and R. A. De Souza, *Pulsed laser deposition of $SrRuO_3$ thin-films: The role of the pulse repetition rate,* APL Mater. **4**, 126109 (2016).

[78] M. M. Urtasun, *Perovskite thin films deposoited by pulsed reactive crossed beam laser ablation as model systems for electrochemical applications*, Ph.D. thesis, Universität Zürich (2005).

[79] B. Dam, J. H. Rector, J. Johansson, J. Huijbregtse, and D. G. De Groot, *Mechanism of incongruent ablation of $SrTiO_3$,* J. Appl. Phys. **83**, 3386 (1998).

[80] J. Hofinger, *Pulsed-laser growth of In_2O_3 thin films on YSZ(111) substrates*, Master's thesis, TU Wien (2018).

[81] V. M. Mecea, *Is quartz crystal microbalance really a mass sensor?* Sens. Actuators, A **128**, 270 (2006).

[82] G. Sauerbrey, *The use of quarts oscillators for weighing thin layers and for microweighing,* Z. Phys. **155**, 206 (1959).

[83] C. S. Lu and O. Lewis, *Investigation of film thickness determination by oscillating quartz resonators with large mass load,* J. Appl. Phys. **43**, 4385 (1972).

[84] G. Hayderer, M. Schmid, P. Varga, H. P. Winter, and F. Aumayr, *A highly sensitive quartz-crystal microbalance for sputtering investigations in slow ion–surface collisions,* Rev. Sci. Instrum. **70**, 3696 (1999).

[85] J. Zuo, *Deposition of Ag nanostructures on TiO_2 thin films by RF magnetron sputtering,* Appl. Surf. Sci. **256**, 7096 (2010).

[86] K. Pradhan and P. F. Lyman, *Study of atomic layer deposition of ZnO on a polar oxide substrate by in situ quartz crystal microbalance,* ECS Trans. **41**, 247 (2011).

[87] L. Bouzidi, S. S. Narine, K. G. Stefanov, and A. J. Slavin, *High-stability quartz-crystal microbalance for investigations in surface science,* Rev. Sci. Instrum. **74**, 3039 (2003).

[88] M. F. Danışman and B. Özkan, *Simultaneous detection of surface coverage and structure of krypton films on gold by helium atom diffraction and quartz crystal microbalance techniques,* Rev. Sci. Instrum. **82**, 115104 (2011).

[89] J. A. Greer, M. D. Tabat, and C. Lu, *Future trends for large-area pulsed laser deposition,* Nucl. Instrum. Methods Phys. Res. B **121**, 357 (1997).

[90] E. Benes, *Improved quartz crystal microbalance technique,* J. Appl. Phys. **56**, 608 (1984).

[91] E. P. EerNisse, *Simultaneous thin-film stress and mass-change measurements using quartz resonators,* J. Appl. Phys. **43**, 1330 (1972).

[92] E. Benes, M. Schmid, and V. Kravchenko, *Vibration modes of mass-loaded planoconvex quartz crystal resonators,* J. Acoust. Soc. Am. **90**, 700 (1991).

[93] E. Benes, M. Schmid, and G. Thorn, *Progress in monitoring thin film thickness by use of quartz crystals,* Thin Solid Films **174**, 307 (1989).

[94] G. Ketteler, W. Weiss, W. Ranke, and R. Schlögl, *Bulk and surface phases of iron oxides in an oxygen and water atmosphere at low pressure,* Phys. Chem. Chem. Phys. **3**, 1114 (2001).

[95] A. P. Grosvenor, B. A. Kobe, M. C. Biesinger, and N. S. McIntyre, *Investigation of multiplet splitting of Fe 2p XPS spectra and bonding in iron compounds,* Surf. Interface Anal. **36**, 1564 (2004).

[96] F. Kraushofer, Z. Jakub, M. Bichler, J. Hulva, P. Drmota, M. Weinold, M. Schmid, M. Setvin, U. Diebold, P. Blaha, and G. S. Parkinson, *Atomic-scale structure of the hematite α-$Fe_2O_3(1\bar{1}02)$"R-Cut" surface,* J. Phys. Chem. C. **122**, 1657 (2018).

[97] H. Thanner, P. W. Krempl, W. Wallnöfer, and P. M. Worsch, *$GaPO_4$ high temperature crystal microbalance with zero temperature coefficient,* Vacuum **67**, 687 (2002).

[98] D. Kriegner, E. Wintersberger, and J. Stangl, *Xrayutilities: A versatile tool for reciprocal space conversion of scattering data recorded with linear and area detectors,* J. Appl. Crystallogr. **46**, 1162 (2013).

[99] U. Diebold, *The surface science of titanium dioxide,* Surf. Sci. Rep. **48**, 53 (2003).

[100] J.-G. Li, T. Ishigaki, and X. Sun, *Anatase, brookite, and rutile nanocrystals via redox reactions under mild hydrothermal conditions: phase-selective synthesis and physicochemical properties,* J. Phys. Chem. C **111**, 4969 (2007).

[101] M. Xu, Y. Gao, E. M. Moreno, M. Kunst, M. Muhler, Y. Wang, H. Idriss, and C. Wöll, *Photocatalytic activity of bulk TiO_2 anatase and rutile single crystals using infrared absorption spectroscopy,* Phys. Rev. Lett. **106**, 138302 (2011).

[102] A. L. Linsebigler, G. Lu, and J. T. Yates Jr, *Photocatalysis on TiO_2 surfaces: principles, mechanisms, and selected results,* Chem. Rev. **95**, 735 (1995).

[103] J. Yu, C. Y. Jimmy, M. K.-P. Leung, W. Ho, B. Cheng, X. Zhao, and J. Zhao, *Effects of acidic and basic hydrolysis catalysts on the photocatalytic activity and microstructures of bimodal mesoporous titania,* J. Catal. **217**, 69 (2003).

[104] Y. Wang, H. Sun, S. Tan, H. Feng, Z. Cheng, J. Zhao, A. Zhao, B. Wang, Y. Luo, J. Yang, and J. G. Hou, *Role of point defects on the reactivity of reconstructed anatase titanium dioxide (001) surface,* Nat. Commun. **4**, 1 (2013).

[105] M. Lazzeri, A. Vittadini, and A. Selloni, *Structure and energetics of stoichiometric TiO_2 anatase surfaces,* Phys. Rev. B **63**, 155409 (2001).

[106] M. Radović, M. Salluzzo, Z. Ristić, R. Di Capua, N. Lampis, R. Vaglio, and F. M. Granozio, *In situ investigation of the early stage of TiO_2 epitaxy on (001) $SrTiO_3$,* J. Chem. Phys. **135**, 034705 (2011).

[107] Y. Du, D. J. Kim, T. C. Kaspar, S. E. Chamberlin, I. Lyubinetsky, and S. A. Chambers, *In-situ imaging of the nucleation and growth of epitaxial anatase $TiO_2(001)$ films on $SrTiO_3(001)$,* Surf. Sci. **606**, 1443 (2012).

[108] G. S. Herman, Y. Gao, T. T. Tran, and J. Osterwalder, *X-ray photoelectron diffraction study of an anatase thin film: TiO_2(001)*, Surf. Sci. **447**, 201 (2000).

[109] G. S. Herman and Y. Gao, *Growth of epitaxial anatase (001) and (101) films*, Thin Solid Films **397**, 157 (2001).

[110] M. Murakami, Y. Matsumoto, K. Nakajima, T. Makino, Y. Segawa, T. Chikyow, P. Ahmet, M. Kawasaki, and H. Koinuma, *Anatase TiO_2 thin films grown on lattice-matched $LaAlO_3$ substrate by laser molecular-beam epitaxy*, Appl. Phys. Lett. **78**, 2664 (2001).

[111] X.-Q. Gong, A. Selloni, and A. Vittadini, *Density functional theory study of formic acid adsorption on anatase TiO_2(001): geometries, energetics, and effects of coverage, hydration, and reconstruction*, J. Phys. Chem. B **110**, 2804 (2006).

[112] M. Lazzeri and A. Selloni, *Stress-driven reconstruction of an oxide surface: the anatase TiO_2(001)-(1×4) surface*, Phys. Rev. Lett. **87**, 266105 (2001).

[113] F. De Angelis, C. Di Valentin, S. Fantacci, A. Vittadini, and A. Selloni, *Theoretical studies on anatase and less common TiO_2 phases: bulk, surfaces, and nanomaterials*, Chem. Rev. **114**, 9708 (2014).

[114] S. Selcuk and A. Selloni, *Facet-dependent trapping and dynamics of excess electrons at anatase TiO_2 surfaces and aqueous interfaces*, Nat. Mater. **15**, 1107 (2016).

[115] J. Balajka, J. Pavelec, M. Komora, M. Schmid, and U. Diebold, *Apparatus for dosing liquid water in ultrahigh vacuum*, Rev. Sci. Instrum. **89**, 083906 (2018).

[116] T. Ohsawa, Y. Yamamoto, M. Sumiya, Y. Matsumoto, and H. Koinuma, *Combinatorial scanning tunneling microscopy study of Cr deposited on anatase TiO_2(001) surface*, Langmuir **20**, 3018 (2004).

[117] A. Lotnyk, S. Senz, and D. Hesse, *Epitaxial growth of TiO_2 thin films on $SrTiO_3$, $LaAlO_3$ and yttria-stabilized zirconia substrates by electron beam evaporation*, Thin Solid Films **515**, 3439 (2007).

[118] S. A. Chambers, T. C. Droubay, C. Capan, and G. Y. Sun, *Unintentional F doping of $SrTiO_3$(001) etched in HF acid-structure and electronic properties*, Surf. Sci. **606**, 554 (2012).

[119] J. G. Connell, B. J. Isaac, G. B. Ekanayake, D. R. Strachan, and S. S. A. Seo, *Preparation of atomically flat $SrTiO_3$ surfaces using a deionized-water leaching and thermal annealing procedure*, Appl. Phys. Lett. **101**, 251607 (2012).

[120] G. Koster, B. L. Kropman, G. J. H. M. Rijnders, D. H. A. Blank, and H. Rogalla, *Quasi-ideal strontium titanate crystal surfaces through formation of strontium hydroxide,* Appl. Phys. Lett. **73**, 2920 (1998).

[121] T. Kubo and H. Nozoye, *Surface structure of $SrTiO_3(100)$,* Surf. Sci. **542**, 177 (2003).

[122] D. T. Newell, A. Harrison, F. Silly, and M. R. Castell, *$SrTiO_3(001)$-$(\sqrt{5}\times\sqrt{5})$-$R26.6°$ reconstruction: A surface resulting from phase separation in a reducing environment,* Phys. Rev. B **75**, 205429 (2007).

[123] T. Ohsawa, I. V. Lyubinetsky, M. A. Henderson, and S. A. Chambers, *Hole-mediated photodecomposition of trimethyl acetate on a $TiO_2(001)$ anatase epitaxial thin film surface,* J. Phys. Chem. C **112**, 20050 (2008).

[124] W. J. I. DeBenedetti, E. S. Skibinski, D. Jing, A. Song, and M. A. Hines, *Atomic-scale understanding of catalyst activation: Carboxylic acid solutions, but not the acid itself, increase the reactivity of anatase (001) faceted nanocatalysts,* J. Phys. Chem. C **122**, 4307 (2018).

[125] W. Weiss and W. Ranke, *Surface chemistry and catalysis on well-defined epitaxial iron-oxide layers,* Progr. Surf. Sci. **70**, 1 (2002).

[126] P. L. S. G. Poizot, S. Laruelle, S. Grugeon, L. Dupont, and J. M. Tarascon, *Nano-sized transition-metal oxides as negative-electrode materials for lithium-ion batteries,* Nature **407**, 496 (2000).

[127] P. Tartaj and J. M. Amarilla, *Iron oxide porous nanorods with different textural properties and surface composition: Preparation, characterization and electrochemical lithium storage capabilities,* J. Power Sources **196**, 2164 (2011).

[128] J. Chen, L. Xu, W. Li, and X. Gou, *α-Fe_2O_3 nanotubes in gas sensor and lithium-ion battery applications,* Adv. Mater. **17**, 582 (2005).

[129] O. Shekhah, W. Ranke, and R. Schlögl, *Styrene synthesis: in situ characterization and reactivity studies of unpromoted and potassium-promoted iron oxide model catalysts,* J. Catal. **225**, 56 (2004).

[130] Z. Wei, R. Xing, X. Zhang, S. Liu, H. Yu, and P. Li, *Facile template-free fabrication of hollow nestlike α-Fe_2O_3 nanostructures for water treatment,* ACS Appl. Mater. Interfaces **5**, 598 (2013).

[131] M. Vargas, K. Kashefi, E. L. Blunt-Harris, and D. R. Lovley, *Microbiological evidence for Fe(III) reduction on early Earth,* Nature **395**, 65 (1998).

[132] K. M. H. Young, B. M. Klahr, O. Zandi, and T. W. Hamann, *Photocatalytic water oxidation with hematite electrodes,* Catal. Sci. Technol. **3**, 1660 (2013).

[133] A. Fujishima and K. Honda, *Electrochemical photolysis of water at a semiconductor electrode,* Nature **238**, 37 (1972).

[134] J. Li and N. Wu, *Semiconductor-based photocatalysts and photoelectrochemical cells for solar fuel generation: a review,* Catal. Sci. Technol. **5**, 1360 (2015).

[135] A. Valdes, Z.-W. Qu, G.-J. Kroes, J. Rossmeisl, and J. K. Nørskov, *Oxidation and photo-oxidation of water on TiO_2 surface,* J. Phys. Chem. C **112**, 9872 (2008).

[136] A. G. Tamirat, J. Rick, A. A. Dubale, W.-N. Su, and B.-J. Hwang, *Using hematite for photoelectrochemical water splitting: a review of current progress and challenges,* Nanoscale Horiz. **1**, 243 (2016).

[137] C. Kronawitter, I. Zegkinoglou, S.-H. Shen, P. Liao, I. Cho, O. Zandi, Y.-S. Liu, K. Lashgari, G. Westin, J.-H. Guo, F. Himpsel, E. Carter, X. Zheng, T. Hamann, B. Koel, S. Mao, and L. Vayssieres, *Titanium incorporation into hematite photoelectrodes: theoretical considerations and experimental observations,* Energy Environ. Sci. **7**, 3100 (2014).

[138] H. Magnan, D. Stanescu, M. Rioult, E. Fonda, and A. Barbier, *Enhanced photoanode properties of epitaxial Ti doped α-Fe_2O_3(0001) thin films,* Appl. Phys. Lett. **101**, 133908 (2012).

[139] J. A. Glasscock, P. R. Barnes, I. C. Plumb, and N. Savvides, *Enhancement of photoelectrochemical hydrogen production from hematite thin films by the introduction of Ti and Si,* J. Phys. Chem. C **111**, 16477 (2007).

[140] C. Miao, T. Shi, G. Xu, S. Ji, and C. Ye, *Photocurrent enhancement for Ti-doped Fe_2O_3 thin film photoanodes by an in situ solid-state reaction method,* ACS Appl. Mater. Interfaces **5**, 1310 (2013).

[141] J. Deng, J. Zhong, A. Pu, D. Zhang, M. Li, X. Sun, and S.-T. Lee, *Ti-doped hematite nanostructures for solar water splitting with high efficiency,* J. Appl. Phys. **112**, 084312 (2012).

[142] G. S. Parkinson, *Iron oxide surfaces,* Surf. Sci. Rep. **71**, 272 (2016).

[143] N. Yatom, O. Neufeld, and M. Caspary Toroker, *Toward settling the debate on the role of Fe_2O_3 surface states for water splitting,* J. Phys. Chem. C **119**, 24789 (2015).

[144] M. Rioult, H. Magnan, D. Stanescu, and A. Barbier, *Single crystalline hematite films for solar water splitting: Ti-doping and thickness effects,* J. Phys. Chem. C **118**, 3007 (2014).

[145] T. Droubay, K. M. Rosso, S. M. Heald, D. E. Mccready, C. M. Wang, and S. A. Chambers, *Structure, magnetism, and conductivity in epitaxial Ti-doped α-Fe_2O_3 hematite: Experiment and density functional theory calculations,* Phys. Rev. B **75**, 104412 (2007).

[146] H. Kuhlenbeck, S. Shaikhutdinov, and H.-J. Freund, *Well-ordered transition metal oxide layers in model catalysis-a series of case studies,* Chem. Rev. **113**, 3986 (2013).

[147] M. A. Henderson, *Insights into the (1×1)-to-(2×1) phase transition of the α-Fe_2O_3(012) surface using EELS, LEED and water TPD,* Surf. Sci. **515**, 253 (2002).

[148] F. Kraushofer, T. Kisslinger, G. Franceschi, U. Diebold, H. Lutz, G. Parkinson, and M. Riva, *A revised model for the (2 × 1) termination of α-$Fe_2O_3(1\bar{1}02)$,* (2020), *in preparation.*

[149] G. Kresse and J. Hafner, *Ab initio molecular dynamics for open-shell transition metals,* Phys. Rev. B **48**, 13115 (1993).

[150] G. Kresse and J. Furthmüller, *Efficiency of ab-initio total energy calculations for metals and semiconductors using a plane-wave basis set,* Comput. Mater. Sci. **6**, 15 (1996).

[151] P. E. Blöchl, *Projector augmented-wave method,* Phys. Rev. B **50**, 17953 (1994).

[152] G. Kresse and D. Joubert, *From ultrasoft pseudopotentials to the projector augmented-wave method,* Phys. Rev. B **59**, 1758 (1999).

[153] J. P. Perdew, K. Burke, and M. Ernzerhof, *Generalized gradient approximation made simple,* Phys. Rev. Lett. **77**, 3865 (1996).

[154] R. Ovcharenko, E. Voloshina, and J. Sauer, *Water adsorption and O-defect formation on Fe_2O_3(0001) surfaces,* Phys. Chem. Chem. Phys. **18**, 25560 (2016).

[155] V. I. Anisimov, J. Zaanen, and O. K. Andersen, *Band theory and Mott insulators: Hubbard U instead of Stoner I,* Phys. Rev. B **44**, 943 (1991).

[156] G. Rollmann, A. Rohrbach, P. Entel, and J. Hafner, *First-principles calculation of the structure and magnetic phases of hematite,* Phys. Rev. B **69**, 165107 (2004).

[157] P. Liao, J. A. Keith, and E. A. Carter, *Water oxidation on pure and doped hematite (0001) surfaces: Prediction of Co and Ni as effective dopants for electrocatalysis,* J. Am. Chem. Soc. **134**, 13296 (2012).

[158] A. E. Bocquet, T. Mizokawa, K. Morikawa, A. Fujimori, S. R. Barman, K. Maiti, D. D. Sarma, Y. Tokura, and M. Onoda, *Electronic structure of early 3d-transition-metal oxides by analysis of the 2p core-level photoemission spectra,* Phys. Rev. B **53**, 1161 (1996).

[159] C. J. Calzado, N. C. Hernández, and J. F. Sanz, *Effect of on-site coulomb repulsion term U on the band-gap states of the reduced rutile (110) TiO_2 surface,* Phys. Rev. B **77**, 045118 (2008).

[160] K. Reuter and M. Scheffler, *Composition, structure, and stability of RuO_2(110) as a function of oxygen pressure,* Phys. Rev. B **65**, 035406 (2001), S, H from webbook.nist.gov, JANAF Thermochemical Tables 1998.

[161] A. C. S. Sabioni, A.-M. Huntz, A. M. J. M. Daniel, and W. A. A. Macedo, *Measurement of iron self-diffusion in hematite single crystals by secondary ion-mass spectrometry (SIMS) and comparison with cation self-diffusion in corundum-structure oxides,* Philos. Mag. **85**, 3643 (2005).

[162] S. Hallström, L. Höglund, and J. Ågren, *Modeling of iron diffusion in the iron oxides magnetite and hematite with variable stoichiometry,* Acta Mater. **59**, 53 (2011).

[163] A. Atkinson and R. I. Taylor, *Diffusion of ^{55}Fe in Fe_2O_3 single crystals,* J. Phys. Chem. Solids **46**, 469 (1985).

[164] M. Reticcioli, M. Setvin, M. Schmid, U. Diebold, and C. Franchini, *Formation and dynamics of small polarons on the rutile TiO_2(110) surface,* Phys. Rev. B **98**, 045306 (2018).

[165] T. R. Durrant, S. T. Murphy, M. B. Watkins, and A. L. Shluger, *Relation between image charge and potential alignment corrections for charged defects in periodic boundary conditions,* J. Chem. Phys. **149**, 024103 (2018).

[166] Z. Novotny, N. Mulakaluri, Z. Edes, M. Schmid, R. Pentcheva, U. Diebold, and G. S. Parkinson, *Probing the surface phase diagram of Fe_3O_4(001) towards the Fe-rich limit: Evidence for progressive reduction of the surface,* Phys. Rev. B **87**, 195410 (2013).

[167] Z. Jakub, F. Kraushofer, M. Bichler, J. Balajka, J. Hulva, J. Pavelec, I. Sokolovič, M. Müllner, M. Setvin, M. Schmid, U. Diebold, P. Blaha, and G. S. Parkinson, *Partially dissociated water dimers at the water–hematite interface,* ACS Energy Lett. **4**, 390 (2019).

[168] M. E. McBriarty, J. E. Stubbs, P. J. Eng, and K. M. Rosso, *Potential-specific structure at the hematite–electrolyte interface,* Adv. Funct. Mater. **28**, 1705618 (2018).

[169] Y. Pan, C. Zhang, Z. Liu, C. Chen, and Y. Li, *Structural regulation with atomic-level precision: From single-atomic site to diatomic and atomic interface catalysis,* Matter **2**, 78 (2020).

[170] Z. Jakub, J. Hulva, M. Meier, R. Bliem, F. Kraushofer, M. Setvin, M. Schmid, U. Diebold, C. Franchini, and G. S. Parkinson, *Local structure and coordination define adsorption in a model Ir_1/Fe_3O_4 single-atom catalyst,* Ang. Chem. **131**, 14099 (2019).

[171] J. Engel and H. L. Tuller, *The electrical conductivity of thin film donor doped hematite: from insulator to semiconductor by defect modulation,* Phys. Chem. Chem. Phys. **16**, 11374 (2014).

[172] A. Walsh and C. R. A. Catlow, *Structure, stability and work functions of the low index surfaces of pure indium oxide and Sn-doped indium oxide (ITO) from density functional theory,* J. Mater. Chem. **20**, 10438 (2010).

[173] P. D. C. King, T. D. Veal, F. Fuchs, C. Y. Wang, D. J. Payne, A. Bourlange, H. Zhang, G. R. Bell, V. Cimalla, O. Ambacher, R. G. Egdell, F. Bechstedt, and C. F. McConville, *Band gap, electronic structure, and surface electron accumulation of cubic and rhombohedral In_2O_3,* Phys. Rev. B **79**, 205211 (2009).

[174] P. D. C. King and T. D. Veal, *Conductivity in transparent oxide semiconductors,* J. Phys.: Condens. Matter **23**, 334214 (2011).

[175] H. Hosono and D. C. Paine, *Handbook of Transparent Conductors* (Springer Science & Business Media, 2010).

[176] R. G. Egdell, *Dopant and defect induced electronic states at In_2O_3 surfaces,* in *Defects at Oxide Surfaces* (Springer, 2015) p. 351.

[177] C. G. Granqvist and A. Hultåker, *Transparent and conducting ITO films: New developments and applications,* Thin solid films **411**, 1 (2002).

[178] Q. Liu, Y. Liu, F. Wu, X. Cao, Z. Li, M. Alharbi, A. N. Abbas, M. R. Amer, and C. Zhou, *Highly sensitive and wearable In_2O_3 nanoribbon transistor biosensors with integrated on-chip gate for glucose monitoring in body fluids,* ACS nano **12**, 1170 (2018).

[179] M. Suchea, N. Katsarakis, S. Christoulakis, S. Nikolopoulou, and G. Kiriakidis, *Low temperature indium oxide gas sensors,* Sens. Actuators, B **118**, 135 (2006).

[180] P. D. C. King, T. D. Veal, D. J. Payne, A. Bourlange, R. G. Egdell, and C. F. McConville, *Surface electron accumulation and the charge neutrality level in In_2O_3,* Phys. Rev. Lett. **101**, 116808 (2008).

[181] L. B. Hoch, T. E. Wood, P. G. O'Brien, K. Liao, L. M. Reyes, C. A. Mims, and G. A. Ozin, *The rational design of a single-component photocatalyst for gas-phase CO_2 reduction using both UV and visible light,* Adv. Sci. **1**, 1400013 (2014).

[182] K. K. Ghuman, T. E. Wood, L. B. Hoch, C. A. Mims, G. A. Ozin, and C. V. Singh, *Illuminating CO_2 reduction on frustrated lewis pair surfaces: Investigating the role of surface hydroxides and oxygen vacancies on nanocrystalline $(In_2O_3)_x(OH)_y$,* Phys. Chem. Chem. Phys. **17**, 14623 (2015).

[183] O. Martin, A. J. Martín, C. Mondelli, S. Mitchell, T. F. Segawa, R. Hauert, C. Drouilly, D. Curulla-Ferré, and J. Pérez-Ramírez, *Indium oxide as a superior catalyst for methanol synthesis by CO_2 hydrogenation,* Angew. Chem., Int. Ed. **55**, 6261 (2016).

[184] M. S. Frei, C. Mondelli, R. García-Muelas, K. S. Kley, B. Puértolas, N. López, O. V. Safonova, J. A. Stewart, D. C. Ferré, and J. Pérez-Ramírez, *Atomic-scale engineering of indium oxide promotion by palladium for methanol production via CO_2 hydrogenation,* Nat. Commun. **10**, 3377 (2019).

[185] D. Albani, M. Capdevila-Cortada, G. Vilé, S. Mitchell, O. Martin, N. López, and J. Pérez-Ramírez, *Semihydrogenation of acetylene on indium oxide: Proposed single-ensemble catalysis,* Angew. Chem., Int. Ed. **56**, 10755 (2017).

[186] M. Wagner, S. Seiler, B. Meyer, L. A. Boatner, M. Schmid, and U. Diebold, *Reducing the $In_2O_3(111)$ surface results in ordered indium adatoms,* Adv. Mater. Interfaces **1**, 1400289 (2014).

[187] T. Berthold, S. Katzer, J. Rombach, S. Krischok, O. Bierwagen, and M. Himmerlich, *Towards understanding the cross-sensitivity of In_2O_3 based ozone sensors: Effects of*

O_3, O_2 and H_2O adsorption at In_2O_3(111) surfaces, Phys. Status Solidi B **255**, 1700324 (2018).

[188] M. Wagner, P. Lackner, S. Seiler, A. Brunsch, R. Bliem, S. Gerhold, Z. Wang, J. Osieck, K. Schulte, L. A. Boatner, M. Schmid, B. Meyer, and U. Diebold, *Resolving the structure of a well-ordered hydroxyl overlayer on In_2O_3(111): Nanomanipulation and theory,* ACS Nano **11**, 11531 (2017).

[189] M. Wagner, J. Hofinger, M. Setvín, L. A. Boatner, M. Schmid, and U. Diebold, *Prototypical organic-oxide interface: Intramolecular resolution of sexiphenyl on In_2O_3(111),* ACS Appl. Mater. Interfaces **10**, 14175 (2018).

[190] D. R. Hagleitner, M. Menhart, P. Jacobson, S. Blomberg, K. Schulte, E. Lundgren, M. Kubicek, J. Fleig, F. Kubel, C. Puls, A. Limbeck, H. Hutter, L. A. Boatner, M. Schmid, and U. Diebold, *Bulk and surface characterization of In_2O_3(001) single crystals,* Phys. Rev. B **85**, 115441 (2012).

[191] L. He, T. E. Wood, B. Wu, Y. Dong, L. B. Hoch, L. M. Reyes, D. Wang, C. Kübel, C. Qian, J. Jia, K. Liao, P. G. O'Brien, A. Sandhel, J. Y. Y. Loh, N. P. Szymanski, Paul Kherani, T. C. Sum, C. A. Mims, and G. A. Ozin, *Spatial separation of charge carriers in $In_2O_{3-x}(OH)_y$ nanocrystal superstructures for enhanced gas-phase photocatalytic activity,* ACS Nano **10**, 5578 (2016).

[192] K. K. Ghuman, L. B. Hoch, P. Szymanski, J. Y. Loh, N. P. Kherani, M. A. El-Sayed, G. A. Ozin, and C. V. Singh, *Photoexcited surface frustrated lewis pairs for heterogeneous photocatalytic CO_2 reduction,* J. Am. Chem. Soc. **138**, 1206 (2016).

[193] L. B. Hoch, P. Szymanski, K. K. Ghuman, L. He, K. Liao, Q. Qiao, L. M. Reyes, Y. Zhu, M. A. El-Sayed, C. V. Singh, and G. A. Ozin, *Carrier dynamics and the role of surface defects: Designing a photocatalyst for gas-phase CO_2 reduction,* Proc. Nat. Acad. Sci. **113**, E8011 (2016).

[194] J. Ye, C. Liu, D. Mei, and Q. Ge, *Active oxygen vacancy site for methanol synthesis from CO_2 hydrogenation on In_2O_3(110): A DFT study,* ACS Catalysis **3**, 1296 (2013).

[195] J. Pavelec, J. Hulva, D. Halwidl, R. Bliem, O. Gamba, Z. Jakub, F. Brunbauer, M. Schmid, U. Diebold, and G. S. Parkinson, *A multi-technique study of CO_2 adsorption on Fe_3O_4 magnetite,* J. Chem. Phys. **146**, 014701 (2017).

[196] E. H. Morales, Y. He, M. Vinnichenko, B. Delley, and U. Diebold, *Surface structure of Sn-doped In_2O_3(111) thin films by STM,* New J. Phys. **10**, 125030 (2008).

[197] H. Ohta, M. Orita, M. Hirano, and H. Hosono, *Surface morphology and crystal quality of low resistive indium tin oxide grown on yittria-stabilized zirconia,* J. Appl. Phys. **91**, 3547 (2002).

[198] K. H. L. Zhang, V. K. Lazarov, H. H.-C. Lai, and R. G. Egdell, *Influence of temperature on the epitaxial growth of In_2O_3 thin films on Y-ZrO_2(111),* J. Cryst. Growth **318**, 345 (2011).

[199] H. Kim, a. C. M. Gilmore, A. Pique, J. S. Horwitz, H. Mattoussi, H. Murata, Z. H. Kafafi, and D. Chrisey, *Electrical, optical, and structural properties of indium-tin-oxide thin films for organic light-emitting devices,* J. Appl. Phys. **86**, 6451 (1999).

[200] S. Lany and A. Zunger, *Dopability, intrinsic conductivity, and nonstoichiometry of transparent conducting oxides,* Phys. Rev. Lett. **98**, 045501 (2007).

[201] T. Tomita, K. Yamashita, Y. Hayafuji, and H. Adachi, *The origin of n-type conductivity in undoped In_2O_3,* Appl. Phys. Lett. **87**, 051911 (2005).

[202] P. Vogt and O. Bierwagen, *The competing oxide and sub-oxide formation in metal-oxide molecular beam epitaxy,* Appl. Phys. Lett. **106**, 081910 (2015).

[203] N. Nicoloso, A. Löbert, and B. Leibold, *Optical absorption studies of tetragonal and cubic thin-film yttria-stabilized zirconia,* Sens. Actuators, B **8**, 253 (1992).

[204] M. W. Chase, Jr., C. A. Davies, J. R. Downey, Jr., D. J. Frurip, R. A. McDonald, and A. N. Syverud, *NIST-JANAF thermochemical tables,* National Institute of Standards and Technology, Gaithersburg, MD (1998).

[205] Z. Wang, M. Saito, K. P. McKenna, L. Gu, S. Tsukimoto, A. L. Shluger, and Y. Ikuhara, *Atom-resolved imaging of ordered defect superstructures at individual grain boundaries,* Nature **479**, 380 (2011).

[206] J. Fleig, *Solid oxide fuel cell cathodes: Polarization mechanisms and modeling of the electrochemical performance,* Annu. Rev. Mater. Res. **33**, 361 (2003).

[207] J. Schou, *Physical aspects of the pulsed laser deposition technique: The stoichiometric transfer of material from target to film,* Appl. Surf. Sci. **255**, 5191 (2009).

[208] M. Schmid, C. Lenauer, A. Buchsbaum, F. Wimmer, G. Rauchbauer, P. Scheiber, G. Betz, and P. Varga, *High island densities in pulsed laser deposition: Causes and implications,* Phys. Rev. Lett. **103**, 076101 (2009).

[209] P. Erhart, A. Klein, R. G. Egdell, and K. Albe, *Band structure of indium oxide: Indirect versus direct band gap,* Phys. Rev. B **75**, 153205 (2007).

[210] Y. Gassenbauer, R. Schafranek, A. Klein, S. Zafeiratos, M. Hävecker, A. Knop-Gericke, and R. Schlögl, *Surface states, surface potentials, and segregation at surfaces of tin-doped In_2O_3,* Phys. Rev. B **73**, 245312 (2006).

[211] J. H. W. De Wit, G. Van Unen, and M. Lahey, *Electron concentration and mobility in In_2O_3,* J. Phys. Chem. Solids **38**, 819 (1977).

[212] G. Moretti, *Auger parameter and Wagner plot in the characterization of chemical states by X-ray photoelectron spectroscopy: a review,* J. Electron Spectrosc. Relat. Phenom. **95**, 95 (1998).

[213] C. D. Wagner and A. Joshi, *The Auger parameter, its utility and advantages: a review,* J. Electron Spectrosc. Relat. Phenom. **47**, 283 (1988).

[214] P. Vogt and O. Bierwagen, *Comparison of the growth kinetics of In_2O_3 and Ga_2O_3 and their suboxide desorption during plasma-assisted molecular beam epitaxy,* Appl. Phys. Lett. **109**, 062103 (2016).

[215] K. Oura, V. G. Lifshits, A. A. Saranin, A. V. Zotov, and M. Katayama, *Surface science: An introduction,* (Springer Science & Business Media, 2013) Chap. 13, p. 327.

[216] H. Chen, M. Blatnik, F. Mirabella, G. Franceschi, M. Riva, M. Schmid, J. Cechal, M. Bernd, U. Diebold, and M. Wagner, *From UHV to ambient conditions: Water on In_2O_3,* (2020), *in preparation.*

[217] G. O. Larrazábal, A. J. Martín, S. Mitchell, R. Hauert, and J. Pérez-Ramírez, *Enhanced reduction of CO_2 to CO over Cu–In electrocatalysts: catalyst evolution is the key,* ACS Catalysis **6**, 6265 (2016).

[218] E. Breckenfeld, R. Wilson, J. Karthik, A. R. Damodaran, D. G. Cahill, and L. W. Martin, *Effect of growth induced (non)stoichiometry on the structure, dielectric response, and thermal conductivity of $SrTiO_3$ thin films,* Chem. Mater. **24**, 331 (2012).

[219] T. Ohnishi, M. Lippmaa, T. Yamamoto, S. Meguro, and H. Koinuma, *Improved stoichiometry and misfit control in perovskite thin film formation at a critical fluence by pulsed laser deposition,* Appl. Phys. Lett. **87**, 241919 (2005).

[220] F. Yang, Q. Zhang, Z. Yang, J. Gu, Y. Liang, W. Li, W. Wang, K. Jin, L. Gu, and J. Guo, *Room-temperature ferroelectricity of $SrTiO_3$ films modulated by cation concentration,* Appl. Phys. Lett. **107**, 082904 (2015).

[221] Y. S. Kim, D. J. Kim, T. H. Kim, T. W. Noh, J. S. Choi, B. H. Park, and J.-G. Yoon, *Observation of room-temperature ferroelectricity in tetragonal strontium titanate thin films on $SrTiO_3(001)$ substrates,* Appl. Phys. Lett. **91**, 042908 (2007).

[222] A. Biswas, M. Talha, A. Kashir, and Y. H. Jeong, *A thin film perspective on quantum functional oxides,* Curr. Appl. Phys. **19**, 207 (2019).

[223] S. Förster and W. Widdra, *Growth, structure, and thermal stability of epitaxial $BaTiO_3$ films on Pt(111),* Surf. Sci. **604**, 2163 (2010).

[224] A. M. Kolpak, D. Li, R. Shao, A. M. Rappe, and D. A. Bonnell, *Evolution of the structure and thermodynamic stability of the $BaTiO_3(001)$ surface,* Phys. Rev. Lett. **101**, 036102 (2008).

[225] B. Stöger, M. Hieckel, F. Mittendorfer, Z. Wang, M. Schmid, G. S. Parkinson, D. Fobes, J. Peng, J. E. Ortmann, A. Limbeck, Z. Mao, J. Redinger, and U. Diebold, *Point defects at cleaved $Sr_{n+1}Ru_nO_{3n+1}(001)$ surfaces,* Phys. Rev. B **90**, 165438 (2014).

[226] D. Halwidl, W. Mayr-Schmölzer, D. Fobes, J. Peng, Z. Mao, M. Schmid, F. Mittendorfer, J. Redinger, and U. Diebold, *Ordered hydroxyls on $Ca_3Ru_2O_7(001)$,* Nat. Commun. **8**, 23 (2017).

[227] I. Sokolović, M. Schmid, U. Diebold, and M. Setvin, *Incipient ferroelectricity: A route towards bulk-terminated $SrTiO_3$,* Phys. Rev. Mater. **3**, 034407 (2019).

[228] T. K. Andersen, S. Wang, M. R. Castell, D. D. Fong, and L. D. Marks, *Single-layer TiO_x reconstructions on $SrTiO_3(111)$: $(\sqrt{7}\times\sqrt{7})R19.1°$, $(\sqrt{13}\times\sqrt{13})R13.9°$, and related structures,* Surf. Sci. **675**, 36 (2018).

[229] M. Setvin, M. Reticcioli, F. Poelzleitner, J. Hulva, M. Schmid, L. A. Boatner, C. Franchini, and U. Diebold, *Polarity compensation mechanisms on the perovskite surface $KTaO_3(001)$,* Science **359**, 572 (2018).

[230] J. A. Enterkin, A. K. Subramanian, B. C. Russell, M. R. Castell, K. R. Poeppelmeier, and L. D. Marks, *A homologous series of structures on the surface of $SrTiO_3(110)$,* Nat. Mater. **9**, 245 (2010).

[231] D. Kienzle, P. Koirala, and L. D. Marks, *Lanthanum aluminate(110) 3×1 surface reconstruction,* Surf. Sci. **633**, 60 (2015).

[232] A. Spinelli, M. A. Torija, C. Liu, C. Jan, and C. Leighton, *Electronic transport in doped $SrTiO_3$: Conduction mechanisms and potential applications,* Phys. Rev. B **81**, 155110 (2010).

[233] K. S. Takahashi, M. Gabay, D. Jaccard, K. Shibuya, T. Ohnishi, M. Lippmaa, and J. M. Triscone, *Local switching of two-dimensional superconductivity using the ferroelectric field effect,* Nature **441**, 195 (2006).

[234] K. Shibuya, T. Ohnishi, T. Uozumi, T. Sato, M. Lippmaa, M. Kawasaki, K. Nakajima, T. Chikyow, and H. Koinuma, *Field-effect modulation of the transport properties of nondoped $SrTiO_3$,* Appl. Phys. Lett. **88**, 212116 (2006).

[235] Z. Wang, Z. Zhong, X. Hao, S. Gerhold, B. Stöger, M. Schmid, J. Sánchez-Barriga, A. Varykhalov, C. Franchini, K. Held, and U. Diebold, *Anisotropic two-dimensional electron gas at $SrTiO_3(110)$,* Proc. Natl. Acad. Sci. U. S. A. **111**, 3933 (2014).

[236] L. Dudy, M. Sing, P. Scheiderer, J. D. Denlinger, P. Schütz, J. Gabel, M. Buchwald, C. Schlueter, T.-L. Lee, and R. Claessen, *In situ control of separate electronic phases on $SrTiO_3$ surfaces by oxygen dosing,* Adv. Mater. **28**, 7443 (2016).

[237] I. Sokolović, G. Franceschi, J. Xu, Z. Wang, J. Pavelec, M. Riva, M. Schmid, U. Diebold, and M. Setvin, *Does a pristine, unreconstructed $SrTiO_3(001)$ exist?* (2020), *in preparation.*

[238] S. Gerhold, Z. Wang, M. Schmid, and U. Diebold, *Stoichiometry-driven switching between surface reconstructions on $SrTiO_3(001)$,* Surf. Sci. **621**, L1 (2014).

[239] P. W. Tasker, *The stability of ionic crystal surfaces,* J. Phys. C: Solid State Phys. **12**, 4977 (1979).

[240] C. Noguera and J. Goniakowski, *Polarity in oxide nano-objects,* Chem. Rev. **113**, 4073 (2013).

[241] Z. Wang, X. Hao, S. Gerhold, M. Schmid, C. Franchini, and U. Diebold, *Vacancy clusters at domain boundaries and band bending at the $SrTiO_3(110)$ surface,* Phys. Rev. B **90**, 035436 (2014).

[242] Z. Wang, A. Loon, A. Subramanian, S. Gerhold, E. McDermott, J. A. Enterkin, M. Hieckel, B. C. Russell, R. J. Green, A. Moewes, J. Guo, P. Blaha, M. R. Castell,

U. Diebold, and L. D. Marks, *Transition from reconstruction toward thin film on the (110) surface of strontium titanate,* Nano Lett. **16**, 2407 (2016).

[243] Z. Wang, F. Li, S. Meng, J. Zhang, E. W. Plummer, U. Diebold, and J. Guo, *Strain-induced defect superstructure on the $SrTiO_3$(110) surface,* Phys. Rev. Lett. **111**, 056101 (2013).

[244] Z. Wang, F. Yang, Z. Zhang, Y. Tang, J. Feng, K. Wu, Q. Guo, and J. Guo, *Evolution of the surface structures on $SrTiO_3$(110) tuned by Ti or Sr concentration,* Phys. Rev. B **83**, 155453 (2011).

[245] Z. Wang, J. Feng, Y. Yang, Y. Yao, L. Gu, F. Yang, Q. Guo, and J. Guo, *Cation stoichiometry optimization of $SrTiO_3$(110) thin films with atomic precision in homogeneous molecular beam epitaxy,* Appl. Phys. Lett. **100**, 051602 (2012).

[246] S. V. Levchenko and A. M. Rappe, *Influence of ferroelectric polarization on the equilibrium stoichiometry of lithium niobate* (0001) *surfaces,* Phys. Rev. Lett. **100**, 256101 (2008).

[247] W. A. Saidi, J. M. P. Martirez, and A. M. Rappe, *Strong reciprocal interaction between polarization and surface stoichiometry in oxide ferroelectrics,* Nano Lett. **14**, 6711 (2014).

[248] S. Cook and L. D. Marks, Ab Initio *predictions of double-layer TiO_2-terminated $SrTiO_3$(001) surface reconstructions,* J. Phys. Chem. C **122**, 21991 (2018).

[249] F. Yang, Y. Liang, L.-X. Liu, Q. Zhu, W.-H. Wang, X.-T. Zhu, and J.-D. Guo, *Controlled growth of complex polar oxide films with atomically precise molecular beam epitaxy,* Front. Phys. **13**, 136802 (2018).

[250] B. C. Russell and M. R. Castell, *Surface of sputtered and annealed polar $SrTiO_3$(111): TiO_x-rich ($n \times n$) reconstructions,* J. Phys. Chem. C **112**, 6538 (2008).

[251] F. Li, Z. Wang, S. Meng, Y. Sun, J. Yang, Q. Guo, and J. Guo, *Reversible transition between thermodynamically stable phases with low density of oxygen vacancies on the $SrTiO_3$(110) surface,* Phys. Rev. Lett. **107**, 036103 (2011).

[252] G. Z. Liu, Q. Y. Lei, and X. X. Xi, *Stoichiometry of $SrTiO_3$ films grown by pulsed laser deposition,* Appl. Phys. Lett. **100**, 202902 (2012).

[253] Z. Wang, *Epitaxial Growth and Investigation of the Surface Properties of $SrTiO_3$ Thin Films*, Ph.D. thesis, Institute of Physics, Chinese Academy of Sciences, Beijing, China (2011).

[254] W. Gao, M. Yao, and X. Yao, *Achieving ultrahigh breakdown strength and energy storage performance through periodic interface modification in $SrTiO_3$ thin film,* ACS Appl. Mater. Interfaces **10**, 28745 (2018).

[255] S. W. Zeng, X. M. Yin, T. S. Herng, K. Han, Z. Huang, L. C. Zhang, C. J. Li, W. X. Zhou, D. Y. Wan, P. Yang, J. Ding, A. T. S. Wee, J. M. D. Coey, T. Venkatesan, A. Rusydi, and A. Ariando, *Oxygen electromigration and energy band reconstruction induced by electrolyte field effect at oxide interfaces,* Phys. Rev. Lett. **121**, 146802 (2018).

[256] D. A. Freedman, D. Roundy, and T. A. Arias, *Elastic effects of vacancies in strontium titanate: Short- and long-range strain fields, elastic dipole tensors, and chemical strain,* Phys. Rev. B **80**, 064108 (2009).

[257] D. Fuchs, M. Adam, P. Schweiss, S. Gerhold, S. Schuppler, R. Schneider, and B. Obst, *Structural properties of slightly off-stoichiometric homoepitaxial $SrTi_xO_{3-\delta}$ thin films,* J. Appl. Phys. **88**, 1844 (2000).

[258] A. I. Benediktovich, I. D. Feranchuk, and A. Ulyanenkov, *X-ray dynamical diffraction from partly relaxed epitaxial structures,* Phys. Rev. B **80**, 235315 (2009).

[259] M. Birkholtz, *Thin Film Analysis by X-Ray Scattering* (Wiley-VCH Verlag GmbH, 2005).

[260] C. J. Powell and A. Jablonski, *NIST Electron Inelastic-Mean-Free-Path Database - Version 1.2* (National Institute of Standards and Technology, Gaithersburg, MD, 2010).

[261] W. Smekal, W. S. M. Werner, and C. J. Powell, *Simulation of electron spectra for surface analysis (SESSA): A novel software tool for quantitative Auger-electron spectroscopy and X-ray photoelectron spectroscopy,* Surf. Interface Anal. **37**, 1059 (2005).

[262] M. Choi, F. Oba, and I. Tanaka, *Role of Ti antisitelike defects in $SrTiO_3$,* Phys. Rev. Lett. **103**, 185502 (2009).

[263] J. H. Lee, G. Luo, I. C. Tung, S. H. Chang, Z. Luo, M. Malshe, M. Gadre, A. Bhattacharya, S. M. Nakhmanson, J. A. Eastman, H. Hong, J. Jellinek, D. Morgan, D. D. Fong, and J. W. Freeland, *Dynamic layer rearrangement during growth of layered oxide films by molecular beam epitaxy,* Nat. Mater. **13**, 879 (2014).

[264] T. Shi, Y. Chen, and X. Guo, *Defect chemistry of alkaline earth metal (Sr/Ba) titanates,* Prog. Mater. Sci. **80**, 77 (2016).

[265] S. M. Alay-e Abbas, S. Nazir, S. Cottenier, and A. Shaukat, *Evaluation of thermodynamics, formation energetics and electronic properties of vacancy defects in $CaZrO_3$*, Sci. Rep. **7**, 8439 (2017).

[266] F. H. Taylor, J. Buckeridge, and C. R. A. Catlow, *Defects and oxide ion migration in the solid oxide fuel cell cathode material $LaFeO_3$*, Chem. Mater. **28**, 8210 (2016).

[267] Y.-L. Lee and D. Morgan, *Ab initio and empirical defect modeling of $LaMnO_{3\pm\delta}$ for solid oxide fuel cell cathodes*, Phys. Chem. Chem. Phys. **14**, 290 (2012).

[268] Z. Li, B. Liu, J. M. Wang, L. C. Sun, J. Y. Wang, Y. C. Zhou, and Z. J. Hu, *First-principles study of point defects in stoichiometric and non-stoichiometric $Y_4Al_2O_9$*, J. Mater. Sci. Technol. **29**, 1161 (2013).

[269] C. Sun, R. Hui, and J. Roller, *Cathode materials for solid oxide fuel cells: a review*, J. Solid State Electrochem. **14**, 1125 (2010).

[270] Jiang and S. Ping, *Development of lanthanum strontium manganite perovskite cathode materials of solid oxide fuel cells: a review*, J. Mater. Sci. **43**, 6799 (2008).

[271] J. Hwang, R. R. Rao, L. Giordano, Y. Katayama, Y. Yu, and Y. Shao-Horn, *Perovskites in catalysis and electrocatalysis*, Science **358**, 751 (2017).

[272] Y. Wang, H. Arandiyan, H. A. Tahini, J. Scott, X. Tan, H. Dai, J. D. Gale, A. L. Rohl, S. C. Smith, and R. Amal, *The controlled disassembly of mesostructured perovskites as an avenue to fabricating high performance nanohybrid catalysts*, Nat. Commun. **8**, 15553 (2017).

[273] C. H. Kim, G. Qi, K. Dahlberg, and W. Li, *Strontium-doped perovskites rival platinum catalysts for treating NO_x in simulated diesel exhaust*, Science **327**, 1624 (2010).

[274] S. Ponce, M. A. Peña, and J. L. G. Fierro, *Surface properties and catalytic performance in methane combustion of Sr-substituted lanthanum manganites*, Appl. Catal. B **24**, 193 (2000).

[275] S. Majumdar and S. van Dijken, *Pulsed laser deposition of $La_{1-x}Sr_xMnO_3$: thin-film properties and spintronic applications*, J. Phys. D: Appl. Phys. **47**, 034010 (2013).

[276] J.-H. Park, E. Vescovo, H.-J. Kim, C. Kwon, R. Ramesh, and T. Venkatesan, *Direct evidence for a half-metallic ferromagnet*, Nature **392**, 794 (1998).

[277] Y. Tokura, *Critical features of colossal magnetoresistive manganites,* Rep. Prog. Phys. **69**, 797 (2006).

[278] J. Huang, H. Wang, X. Sun, X. Zhang, and H. Wang, *Multifunctional $La_{0.67}Sr_{0.33}MnO_3$ (LSMO) thin films integrated on mica substrates toward flexible spintronics and electronics,* ACS Appl. Mater. Interfaces **10**, 42698 (2018).

[279] A. M. Haghiri-Gosnet, T. Arnal, R. Soulimane, M. Koubaa, and J. P. Renard, *Spintronics: perspectives for the half-metallic oxides,* Phys. Status Solidi A **201**, 1392 (2004).

[280] J. Junquera and P. Ghosez, *Critical thickness for ferroelectricity in perovskite ultrathin films,* Nature **422**, 506 (2003).

[281] Z. Liao and J. Zhang, *Metal-to-insulator transition in ultrathin manganite heterostructures,* Appl. Sci. **9**, 144 (2019).

[282] J. Hemberger, A. Krimmel, T. Kurz, H.-A. Krug von Nidda, V. Y. Ivanov, A. A. Mukhin, A. M. Balbashov, and A. Loidl, *Structural, magnetic, and electrical properties of single-crystalline $La_{1-x}Sr_xMnO_3$ (0.4<x<0.85),* Phys. Rev. B **66**, 094410 (2002).

[283] D. G. Schlom, *Perspective: Oxide molecular-beam epitaxy rocks!* APL Mater. **3**, 062403 (2015).

[284] J. Chen, H. Arandiyan, X. Gao, and J. Li, *Recent advances in catalysts for methane combustion,* Catal. Surv. Asia **19**, 140 (2015).

[285] B.-C. Huang, P. Yu, Y. H. Chu, C.-S. Chang, R. Ramesh, R. E. Dunin-Borkowski, P. Ebert, and Y.-P. Chiu, *Atomically resolved electronic states and correlated magnetic order at termination engineered complex oxide heterointerfaces,* ACS Nano **12**, 1089 (2018).

[286] M. P. de Jong, I. Bergenti, V. Dediu, M. Fahlman, M. Marsi, and C. Taliani, *Evidence for Mn^{2+} ions at surfaces of $La_{0.7}Sr_{0.3}MnO_3$ thin films,* Phys. Rev. B **71**, 014434 (2005).

[287] J. Krempaskỳ, V. Strocov, P. Blaha, L. Patthey, M. Radović, M. Falub, M. Shi, and K. Hricovini, *Bulk vs. surface effects in ARPES experiment from $La_{2/3}Sr_{1/3}MnO_3$ thin films,* J. Electron Spectrosc. Relat. Phenom. **181**, 63 (2010).

[288] E. Annese, T. J. A. Mori, P. Schio, B. R. Salles, and J. C. Cezar, *Influence of the growth parameters on the electronic and magnetic properties of $La_{0.67}Sr_{0.33}MnO_3$ epitaxial thin films,* Appl. Surf. Sci. **437**, 281 (2018).

[289] R. Bachelet, D. Pesquera, G. Herranz, F. Sánchez, and J. Fontcuberta, *Persistent two-dimensional growth of (110) manganite films,* Appl. Phys. Lett. **97**, 121904 (2010).

[290] H. M. Rønnow, C. Renner, G. Aeppli, T. Kimura, and Y. Tokura, *Polarons and confinement of electronic motion to two dimensions in a layered manganite,* Nature **440**, 1025 (2006).

[291] T. Becker, C. Streng, Y. Luo, V. Moshnyaga, B. Damaschke, N. Shannon, and K. Samwer, *Intrinsic inhomogeneities in manganite thin films investigated with scanning tunneling spectroscopy,* Phys. Rev. Lett. **89**, 237203 (2002).

[292] P. Perna, C. Rodrigo, E. Jiménez, F. J. Teran, N. Mikuszeit, L. Méchin, J. Camarero, and R. Miranda, *Tailoring magnetic anisotropy in epitaxial half metallic $La_{0.7}Sr_{0.3}MnO_3$ thin films,* J. Appl. Phys. **110**, 013919 (2011).

[293] H. Guo, D. Sun, W. Wang, Z. Gai, I. Kravchenko, J. Shao, L. Jiang, T. Z. Ward, P. C. Snijders, and L. Yin, *Growth diagram of $La_{0.7}Sr_{0.3}MnO_3$ thin films using pulsed laser deposition,* J. Appl. Phys. **113**, 234301 (2013).

[294] A. Rana, K. Bogle, O. Game, S. Patil, N. Valanoor, and S. Ogale, *Nanoscale modulation of electronic states across unit cell steps on the surface of an epitaxial colossal magnetoresistance manganite film,* Appl. Phys. Lett. **96**, 263108 (2010).

[295] T. T. Fister, D. D. Fong, J. A. Eastman, P. M. Baldo, M. J. Highland, P. H. Fuoss, K. R. Balasubramaniam, J. C. Meador, and P. A. Salvador, *In situ characterization of strontium surface segregation in epitaxial $La_{0.7}Sr_{0.3}MnO_3$ thin films as a function of oxygen partial pressure,* Appl. Phys. Lett. **93**, 151904 (2008).

[296] H. Jalili, Y. Chen, and B. Yildiz, *Structural, chemical, and electronic state on $La_{0.7}Sr_{0.3}MnO_3$ dense thin-film surfaces at high temperature: Surface segregation,* ECS Trans. **28**, 235 (2010).

[297] H. Dulli, P. A. Dowben, S.-H. Liou, and E. W. Plummer, *Surface segregation and restructuring of colossal-magnetoresistant manganese perovskites $La_{0.65}Sr_{0.35}MnO_3$,* Phys. Rev. B **62**, R14629 (2000).

[298] M. G. Harwood, *The crystal structure of lanthanum-strontium manganites,* Proc. Phys. Soc., London, Sect. B **68**, 586 (1955).

[299] L. Rørmark, K. Wiik, S. Stølen, and T. Grande, *Oxygen stoichiometry and structural properties of $La_{1-x}A_xMnO_{3\pm\delta}$ (A=Ca or Sr and $0 \leq x \leq 1$),* J. Mater. Chem. **12**, 1058 (2002).

[300] J. He, M. X. Chen, X. Q. Chen, and C. Franchini, *Structural transitions and transport-half-metallic ferromagnetism in $LaMnO_3$ at elevated pressure,* Phys. Rev. B **85**, 195135 (2012).

[301] *Vapor pressure calculator, utility by m. schmid (iap/tu wien surface physics group), vienna,* (2018).

[302] *LEEDpat, Version 4.2, utility by K.E. Hermann (FHI) and M.A. Van Hove (HKBU), Berlin / Hong Kong,* (2014).

[303] M. A. Stranick, *Mn_2O_3 by XPS,* Surf. Sci. Spectra **6**, 39 (1999).

[304] M. A. Stranick, *MnO_2 by XPS,* Surf. Sci. Spectra **6**, 31 (1999).

[305] M. C. Militello and S. W. Gaarenstroom, *Manganese dioxide (MnO_2) by XPS,* Surf. Sci. Spectra **8**, 200 (2001).

[306] J. J. Rosso and M. F. Hochella Jr, *Natural iron and manganese oxide samples by XPS,* Surf. Sci. Spectra **4**, 253 (1996).

[307] M. Oku and K. Hirokawa, *X-ray photoelectron spectroscopy of Co_3O_4, Fe_3O_4, Mn_3O_4, and related compounds,* J. Electron. Spectrosc. Relat. Phenomena **8**, 475 (1976).

[308] J. S. Foord, R. B. Jackman, and G. C. Allen, *An X-ray photoelectron spectroscopic investigation of the oxidation of manganese,* Philos. Mag. A **49**, 657 (1984).

[309] L. Z. Zhao and V. Young, *XPS studies of carbon supported films formed by the resistive deposition of manganese,* J. Electron Spectrosc. Relat. Phenom. **34**, 45 (1984).

[310] A. J. Nelson, J. G. Reynolds, and J. W. Roos, *Core-level satellites and outer core-level multiplet splitting in Mn model compounds,* J. Vac. Sci. Technol. **18**, 1072 (2000).

[311] V. Di Castro and G. Polzonetti, *XPS study of MnO oxidation,* J. Electron Spectrosc. Relat. Phenom. **48**, 117 (1989).

[312] G. K. Wertheim, S. Hüfner, and H. J. Guggenheim, *Systematics of core-electron exchange splitting in $3d$-group transition-metal compounds,* Phys. Rev. B **7**, 556 (1973).

[313] M. C. Biesinger, B. P. Payne, A. P. Grosvenor, L. W. Lau, A. R. Gerson, and R. S. C. Smart, *Resolving surface chemical states in XPS analysis of first row transition metals, oxides and hydroxides: Cr, Mn, Fe, Co and Ni,* Appl. Surf. Sci. **257**, 2717 (2011).

[314] B. R. Strohmeier and D. M. Hercules, *Surface spectroscopic characterization of manganese/aluminum oxide catalysts,* J. Phys. Chem. **88**, 4922 (1984).

[315] P. Lackner, Z. Zou, S. Mayr, U. Diebold, and M. Schmid, *Using photoelectron spectroscopy to observe oxygen spillover to zirconia,* Phys. Chem. Chem. Phys. **21**, 17613 (2019).

[316] J. A. D. Matthew and S. Parker, *Correlations between the Auger parameters of oxygen and metal atoms in oxygen-containing compounds,* J. Electron Spectrosc. Relat. Phenom. **85**, 175 (1997).

[317] F. Hess and B. Yildiz, *Polar or not polar? The interplay between reconstruction, Sr enrichment, and reduction at the $La_{0.75}Sr_{0.25}MnO_3$ (001) surface,* Phys. Rev. Materials **4**, 015801 (2020).

[318] T. K. Andersen, D. D. Fong, and L. D. Marks, *Pauling's rules for oxide surfaces,* Surf. Sci. Rep. **73**, 213 (2018).

[319] N. Doudin, D. Kuhness, M. Blatnik, F. Netzer, and S. Surnev, *Phase behaviour of 2D $MnWO_x$ and $FeWO_x$ ternary oxide layers on Pd(100),* J. Phys.: Condens. Matter **29**, 234004 (2017).

[320] A. T. Kozakov, A. G. Kochur, K. A. Googlev, A. V. Nikolskii, V. I. Torgashev, V. G. Trotsenko, and A. A. Bush, *Valence state of manganese and iron ions in $La_{1-x}A_xMnO_3$ (A=Ca, Sr) and $Bi_{1-x}Sr_xFeO_3$ systems from Mn 2p, Mn 3s, Fe 2p and Fe 3s X-ray photoelectron spectra. effect of delocalization on Fe 3s spectra splitting,* J. Alloys Compd. **647**, 947 (2015).

[321] M. Abbate, F. M. de Groot, J. C. Fuggle, A. Fujimori, O. Strebel, F. Lopez, M. Domke, G. Kaindl, G. A. Sawatzky, M. Takano, Y. Takeda, H. Eisaki, and S. Uchida, *Controlled-valence properties of $La_{1-x}Sr_xFeO_3$ and $La_{1-x}Sr_xMnO_3$ studied by soft-X-ray absorption spectroscopy,* Phys. Rev. B **46**, 4511 (1992).

[322] T. Saitoh, A. E. Bocquet, T. Mizokawa, H. Namatame, A. Fujimori, M. Abbate, Y. Takeda, and M. Takano, *Electronic structure of $La_{1-x}Sr_xMnO_3$ studied by photoemission and X-ray-absorption spectroscopy,* Phys. Rev. B **51**, 13942 (1995).

[323] E. Beyreuther, S. Grafström, L. M. Eng, C. Thiele, and K. Dörr, *XPS investigation of Mn valence in lanthanum manganite thin films under variation of oxygen content,* Phys. Rev. B **73**, 155425 (2006).

[324] K. A. Stoerzinger, M. Risch, J. Suntivich, W. Lü, J. Zhou, M. D. Biegalski, H. M. Christen, Ariando, T. Venkatesan, and Y. Shao-Horn, *Oxygen electrocatalysis on (001)-oriented manganese perovskite films: Mn valency and charge transfer at the nanoscale,* Energy Environ. Sci. **6**, 1582 (2013).

[325] D. S. Mebane, Y. Liu, and M. Liu, *Refinement of the bulk defect model for $La_xSr_{1-x}MnO_{3\pm\delta}$*, Solid State Ionics **178**, 1950 (2008).

[326] B. C. Russell and M. R. Castell, *Reconstructions on the polar $SrTiO_3(110)$ surface: Analysis using STM, LEED, and AES*, Phys. Rev. B **77**, 245414 (2008).

[327] Z. Cai, M. Kubicek, J. Fleig, and B. Yildiz, *Chemical heterogeneities on $La_{0.6}Sr_{0.4}CoO_{3-\delta}$ thin films–correlations to cathode surface activity and stability*, Chem. Mater. **24**, 1116 (2012).

[328] W. Lee, J. W. Han, Y. Chen, Z. Cai, and B. Yildiz, *Cation size mismatch and charge interactions drive dopant segregation at the surfaces of manganite perovskites*, J. Am. Chem. Soc. **135**, 7909 (2013).

[329] M. Niania, R. Podor, T. B. Britton, C. Li, S. J. Cooper, N. Svetkov, S. Skinner, and J. Kilner, *In situ study of strontium segregation in $La_{0.6}Sr_{0.4}Co_{0.2}Fe_{0.8}O_{3-\delta}$ in ambient atmospheres using high-temperature environmental scanning electron microscopy*, J. Mater. Chem. A **6**, 14120 (2018).

[330] M. Kubicek, G. M. Rupp, S. Huber, A. Penn, A. K. Opitz, J. Bernardi, M. Stöger-Pollach, H. Hutter, and J. Fleig, *Cation diffusion in $La_{0.6}Sr_{0.4}CoO_{3-\delta}$ below $800°C$ and its relevance for Sr segregation*, Phys. Chem. Chem. Phys. **16**, 2715 (2014).

[331] J. Druce, H. Téllez, M. Burriel, M. D. Sharp, L. J. Fawcett, S. N. Cook, D. S. McPhail, T. Ishihara, H. H. Brongersma, and J. A. Kilner, *Surface termination and subsurface restructuring of perovskite-based solid oxide electrode materials*, En. Environ. Sci. **7**, 3593 (2014).

[332] Y. Chen, H. Téllez, M. Burriel, F. Yang, N. Tsvetkov, Z. Cai, D. W. McComb, J. A. Kilner, and B. Yildiz, *Segregated chemistry and structure on (001) and (100) surfaces of $(La_{1-x}Sr_x)_2CoO_4$ override the crystal anisotropy in oxygen exchange kinetics*, Chem. Mater. **27**, 5436 (2015).

[333] H. Téllez, J. Druce, Y.-W. Ju, J. Kilner, and T. Ishihara, *Surface chemistry evolution in $LnBaCo_2O_{5+\delta}$ double perovskites for oxygen electrodes*, Int. J. Hydrogen Energy **39**, 20856 (2014).

[334] Y. Chen, W. Jung, Z. Cai, J. J. Kim, H. L. Tuller, and B. Yildiz, *Impact of Sr segregation on the electronic structure and oxygen reduction activity of $SrTi_{1-x}Fe_xO_3$ surfaces*, En. Environ. Sci. **5**, 7979 (2012).

[335] G. Kresse and J. Hafner, *Ab initio molecular dynamics for liquid metals*, Phys. Rev. B **47**, 558 (1993).

[336] G. Kresse and J. Furthmüller, *Efficient iterative schemes for ab initio total-energy calculations using a plane-wave basis set,* Phys. Rev. B **54**, 11169 (1996).

[337] S. Dudarev and G. Botton, *Electron-energy-loss spectra and the structural stability of nickel oxide: An LSDA+U study,* Phys. Rev. B **57**, 1505 (1998).

[338] J. Tersoff and D. R. Hamann, *Theory of the scanning tunneling microscope,* in *Scanning Tunneling Microscopy* (Springer, 1985) p. 59.

[339] F. Huber and F. J. Giessibl, *Low noise current preamplifier for qPlus sensor deflection signal detection in atomic force microscopy at room and low temperatures,* Rev. Sci. Instrum. **88**, 073702 (2017).

[340] F. J. Giessibl, *The qplus sensor, a powerful core for the atomic force microscope,* Rev. Sci. Instrum. **90**, 011101 (2019).

[341] V. Blum and K. Heinz, *Fast LEED intensity calculations for surface crystallography using Tensor LEED,* Comput. Phys. Commun. **134**, 392 (2001).

[342] B. Stöger, M. Hieckel, F. Mittendorfer, Z. Wang, D. Fobes, J. Peng, Z. Mao, M. Schmid, J. Redinger, and U. Diebold, *High chemical activity of a perovskite surface: reaction of CO with $Sr_3Ru_2O_7$,* Phys. Rev. Lett. **113**, 116101 (2014).

[343] W. Mayr-Schmölzer, D. Halwidl, F. Mittendorfer, M. Schmid, U. Diebold, and J. Redinger, *Adsorption of CO on the $Ca_3Ru_2O_7(001)$ surface,* Surf. Sci. **680**, 18 (2019).

[344] G. Franceschi, M. Schmid, U. Diebold, and M. Riva, *2d surface phase diagram of a multicomponent perovskite oxide: $La_{0.8}Sr_{0.2}MnO_3(110)$,* (2020), submitted.

[345] J. X. Ma, X. F. Liu, T. Lin, G. Y. Gao, J. P. Zhang, W. B. Wu, X. G. Li, and J. Shi, *Interface ferromagnetism in (110)-oriented $La_{0.7}Sr_{0.3}MnO_3/SrTiO_3$ ultrathin superlattices,* Phys. Rev. B **79**, 174424 (2009).

[346] M. Huijben, L. W. Martin, Y.-H. Chu, M. B. Holcomb, P. Yu, G. Rijnders, D. H. A. Blank, and R. Ramesh, *Critical thickness and orbital ordering in ultrathin $La_{0.7}Sr_{0.3}MnO_3$ films,* Phys. Rev. B **78**, 094413 (2008).

[347] N. Mahato, A. Banerjee, A. Gupta, S. Omar, and K. Balani, *Progress in material selection for solid oxide fuel cell technology: A review,* Prog. Mater. Sci. **72**, 141 (2015).

[348] E. D. Wachsman and K. T. Lee, *Lowering the temperature of solid oxide fuel cells,* Science **334**, 935 (2011).

[349] R. M. Ormerod, *Solid oxide fuel cells,* Chem. Soc. Rev. **32**, 17 (2003).

[350] M. S. Dresselhaus and I. L. Thomas, *Alternative energy technologies,* Nature **414**, 332 (2001).

[351] M. M. Kuklja, E. A. Kotomin, R. Merkle, Y. A. Mastrikov, and J. Maier, *Combined theoretical and experimental analysis of processes determining cathode performance in solid oxide fuel cells,* Phys. Chem. Chem. Phys. **15**, 5443 (2013).

[352] O. Bikondoa, C. L. Pang, R. Ithnin, C. A. Muryn, H. Onishi, and G. Thornton, *Direct visualization of defect-mediated dissociation of water on TiO_2(110),* Nat. Mater. **5**, 189 (2006).

[353] R. Schaub, P. Thostrup, N. Lopez, E. Lægsgaard, I. Stensgaard, J. K. Nørskov, and F. Besenbacher, *Oxygen vacancies as active sites for water dissociation on rutile TiO_2(110),* Phys. Rev. Lett. **87**, 266104 (2001).

[354] P. Scheiber, A. Riss, M. Schmid, P. Varga, and U. Diebold, *Observation and destruction of an elusive adsorbate with STM: O_2/TiO_2(110),* Phys. Rev. Lett. **105**, 216101 (2010).

[355] N. A. Deskins, R. Rousseau, and M. Dupuis, *Defining the role of excess electrons in the surface chemistry of TiO_2,* J. Phys. Chem. C **114**, 5891 (2010).

[356] M. T. Greiner, M. G. Helander, W.-M. Tang, Z.-B. Wang, J. Qiu, and Z.-H. Lu, *Universal energy-level alignment of molecules on metal oxides,* Nat. Mater. **11**, 76 (2012).

[357] M. T. Greiner, L. Chai, M. G. Helander, W.-M. Tang, and Z.-H. Lu, *Transition metal oxide work functions: the influence of cation oxidation state and oxygen vacancies,* Adv. Funct. Mater. **22**, 4557 (2012).

[358] Y. Chen, Z. Cai, Y. Kuru, W. Ma, H. L. Tuller, and B. Yildiz, *Electronic activation of cathode superlattices at elevated temperatures–source of markedly accelerated oxygen reduction kinetics,* Adv. En. Mater. **3**, 1221 (2013).

[359] R. Merkle and J. Maier, *Oxygen incorporation into Fe-doped $SrTiO_3$: Mechanistic interpretation of the surface reaction,* Phys. Chem. Chem. Phys. **4**, 4140 (2002).

[360] Y.-L. Lee, J. Kleis, J. Rossmeisl, Y. Shao-Horn, and D. Morgan, *Prediction of solid oxide fuel cell cathode activity with first-principles descriptors,* En. Environ. Sci. **4**, 3966 (2011).

[361] M. Burriel, J. Pena-Martinez, R. J. Chater, S. Fearn, A. V. Berenov, S. J. Skinner, and J. A. Kilner, *Anisotropic oxygen ion diffusion in layered $PrBaCo_2O_{5+\delta}$*, Chem. Mater. **24**, 613 (2012).

[362] L. Yan, K. Balasubramaniam, S. Wang, H. Du, and P. A. Salvador, *Effects of crystallographic orientation on the oxygen exchange rate of $La_{0.7}Sr_{0.3}MnO_3$ thin films,* Solid State Ionics **194**, 9 (2011).

[363] M. Burriel, H. Téllez, R. J. Chater, R. Castaing, P. Veber, M. Zaghrioui, T. Ishihara, J. A. Kilner, and J.-M. Bassat, *Influence of crystal orientation and annealing on the oxygen diffusion and surface exchange of $La_2NiO_{4+\delta}$*, J. Phys. Chem. C **120**, 17927 (2016).

[364] S. H. Chang, N. Danilovic, K.-C. Chang, R. Subbaraman, A. P. Paulikas, D. D. Fong, M. J. Highland, P. M. Baldo, V. R. Stamenkovic, J. W. Freeland, J. A. Eastman, and N. M. Markovic, *Functional links between stability and reactivity of strontium ruthenate single crystals during oxygen evolution,* Nat. Commun. **5**, 4191 (2014).

[365] K. Kerman, C. Ko, and S. Ramanathan, *Orientation dependent oxygen exchange kinetics on single crystal $SrTiO_3$ surfaces,* Phys. Chem. Chem. Phys. **14**, 11953 (2012).

[366] R. A. De Souza and M. Martin, *Probing diffusion kinetics with secondary ion mass spectrometry,* MRS bulletin **34**, 907 (2009).

[367] E. Navickas, T. M. Huber, Y. Chen, W. Hetaba, G. Holzlechner, G. Rupp, M. Stöger-Pollach, G. Friedbacher, H. Hutter, B. Yildiz, and J. Fleig, *Fast oxygen exchange and diffusion kinetics of grain boundaries in Sr-doped $LaMnO_3$ thin films,* Phys. Chem. Chem. Phys. **17**, 7659 (2015).

[368] A. Staykov, S. Fukumori, K. Yoshizawa, K. Sato, T. Ishihara, and J. Kilner, *Interaction of SrO-terminated $SrTiO_3$ surface with oxygen, carbon dioxide, and water,* J. Mater. Chem. A **6**, 22662 (2018).

[369] T. Ohsawa, R. Shimizu, K. Iwaya, S. Shiraki, and T. Hitosugi, *Negligible Sr segregation on $SrTiO_3(001)$-$(\sqrt{13}\times\sqrt{13})$-R33.7° reconstructed surfaces,* Appl. Phys. Lett. **108**, 161603 (2016).

[370] M. G. Helander, M. T. Greiner, Z. B. Wang, and Z. H. Lu, *Pitfalls in measuring work function using photoelectron spectroscopy,* Appl. Surf. Sci. **256**, 2602 (2010).

[371] M. Kubicek, G. Holzlechner, A. K. Opitz, S. Larisegger, H. Hutter, and J. Fleig, *A novel ToF-SIMS operation mode for sub 100 nm lateral resolution: Application and performance,* Appl. Surf. Sci. **289**, 407 (2014).

[372] G. Holzlechner, M. Kubicek, H. Hutter, and J. Fleig, *A novel ToF-SIMS operation mode for improved accuracy and lateral resolution of oxygen isotope measurements on oxides,* J. Analyt. Atom. Spectrom. **28**, 1080 (2013).

[373] I. Denk, W. Münch, and J. Maier, *Partial conductivities in $SrTiO_3$: bulk polarization experiments, oxygen concentration cell measurements, and defect-chemical modeling,* J. Amer. Ceram. Soc. **78**, 3265 (1995).

[374] R. Meyer, A. F. Zurhelle, R. A. De Souza, R. Waser, and F. Gunkel, *Dynamics of the metal-insulator transition of donor-doped $SrTiO_3$,* Phys. Rev. B **94**, 115408 (2016).

[375] S. Saraf, M. Markovich, and A. Rothschild, *Defect chemistry of pn junctions in complex oxides,* Phys. Rev. B **82**, 245208 (2010).

[376] X.-Q. Gong, A. Selloni, M. Batzill, and U. Diebold, *Steps on anatase $TiO_2(101)$,* Nat. Mater. **5**, 665 (2006).

[377] M. Kubicek, M. Riva, G. Franceschi, H. Hutter, M. Schmid, U. Diebold, and J. Fleig, *Isolating intrinsic effects governing oxygen incorporation at model perovskite surfaces, in preparation.*

[378] R. A. De Souza, V. Metlenko, D. Park, and T. E. Weirich, *Behavior of oxygen vacancies in single-crystal $SrTiO_3$: Equilibrium distribution and diffusion kinetics,* Phys. Rev. B **85**, 174109 (2012).

[379] M. Leonhardt, R. A. De Souza, J. Claus, and J. Maier, *Surface kinetics of oxygen incorporation into $SrTiO_3$,* J. Electrochem. Soc. **149**, J19 (2002).

List of publications

In preparation

- G. Franceschi, M. Schmid, R. Heller, M. Stoeger-Pollach, U. Diebold, and M. Riva, "A surface approach towards achieving flat and stoichiometric perovskite-oxide films" (2020)
- M. Kubicek, M. Riva, G. Franceschi, H. Hutter, M. Schmid, U. Diebold, and J. Fleig, "Oxygen exchange studied on controlled strontium titanate surfaces" (2020)
- G. Franceschi, M. Reticcioli, T. Kißlinger, M. Setvin, M. Schmid, C. Franchini, L. Hammer, U. Diebold, and M. Riva, "AO_x-terminated surface reconstructions of $La_{0.8}Sr_{0.2}MnO_3(110)$" (2020)
- H. Chen, M. Blatnik, F. Mirabella, G. Franceschi, M. Riva, B. Meyer, U. Diebold, and M. Wagner "From UHV to ambient conditions: Water on $In_2O_3(111)$" (2020)
- I. Sokolović, G. Franceschi, J. Xu, Z. Wang, J. Pavelec, M. Riva, M. Schmid, U. Diebold, and M. Setvin "Does a pristine, unreconstructed $SrTiO_3(001)$ exist?" (2020)

Submitted

- G. Franceschi, M. Schmid, U. Diebold, and M. Riva, "2D surface phase diagram of a multicomponent perovskite oxide: $La_{0.8}Sr_{0.2}MnO_3(110)$" (2020)

Accepted/Published

- G. Franceschi, M. Schmid, U. Diebold, and M. Riva, "Atomically resolved surface phases of $La_{0.8}Sr_{0.2}MnO_3(110)$ thin films", J. Mater. Chem. A (2020), *in press*
- G. Franceschi, M. Riva, M. Schmid, and U. Diebold, "Scanning Probe Microscopy", in *The World Scientific Materials Science Handbook of Thin Film Deposition by Molecular Beam Epitaxy: With Applications to Different Metals, Material Compounds and Groups (In 4 Volumes)*, edited by S. Chambers, World Scientific Publishing (2021), *in press*

- G. Franceschi, M. Schmid, U. Diebold, and M. Riva, "Movable holder for a quartz crystal microbalance for exact growth rates in pulsed laser deposition", Rev. Sci. Instr. **91**, 065003 (2020)

- G. Franceschi, F. Kraushofer, M. Meier, G. Parkinson, M. Schmid, U. Diebold, and M. Riva, "A model system for photocatalysis: Ti-doped single-crystalline $Fe_2O_3(1\bar{1}02)$ films", Chem. Mater. **32**, 3753 (2020)

- G. Franceschi, M. Wagner, J. Höfinger, T. Krajňák, M. Schmid, U. Diebold, and M. Riva, "Growth of $In_2O_3(111)$ thin films with optimized surfaces", Phys. Rev. Mater. **3**, 103403 (2019)

- M. Riva, G. Franceschi, M. Schmid, and U. Diebold, "Epitaxial growth of complex oxide films: Role of surface reconstructions", Phys. Rev. Res. **1**, 033059 (2019)

- M. Riva, G. Franceschi, Q. Lu, M. Schmid, B. Yildiz, and U. Diebold, "Pushing the detection of cation nonstoichiometry to the limit", Phys. Rev. Mater. **3**, 043802 (2019)

- M. Riva, M. Kubicek, X. Hao, G. Franceschi, S. Gerhold, M. Schmid, H. Hutter, J. Fleig, C. Franchini, B. Yildiz, and U. Diebold, "Influence of surface atomic structure demonstrated on oxygen incorporation mechanism at a model perovskite oxide", Nat. Comm. **9**, 3710 (2018)

As of September 2020

Acknowledgments

I am forever indebted to many people for making my Ph.D. an experience I will treasure. I would like to thank them here.

First, Ulli. Thank you for giving me the opportunity to carry out my Ph.D. in your outstanding group—I am spoiled forever now. Thank you for the trust, the challenges, the opportunities, the advices, and for managing everything so well. I appreciated every discussion we had in front of the STM, your always volcanic ideas, and your unfailing enthusiasm for fresh data. You truly inspire me. Thank you also for the careful reading of this (long) Thesis, for your valuable inputs, and for letting me participate to skiing conferences. I must then thank Michael, the most brilliant, technically skilled, and sharp-eyed physicist I know. I have learnt so much in each and every scientific discussion together, and always appreciated your outstanding review processes (and always was relieved when passing). My Ph.D. could not have been possible without financial support: I would also like to express my gratitude to the Austrian Science Fund (FWF) projects F45-07 (FOXSI) and Z-250 (Wittgensteinpreis), and to the TU-D doctoral college.

An essential reason for these years to have been this enjoyable has been you guys of Ulli's group. I am thankful for all the scientific (but not only) discussions in the coffee room, and for the many enjoyable lunch and coffee breaks. Thank you Peter for never stopping believing in my German (and for your dark humor). Thanks to all the amazing Czech guys whom I had the pleasure to meet: Jiři, with the most contagious and lifting laugh in the world, and never tired of trying to convince me (not only me...) to drink. Honza and his few, but always good, words. Zdenek, funny, brilliant, and with the kindest soul. Thank you Florian for the fun times together. Thanks also to the IWOX2020 gang (Francesca, Matthias Me. and Michele Re.) for the good times together while mocking cutematthiasmeier. Matthias, thank you for our always interesting chats, and for making me laugh so much. Thank you Fra for the support during my tough decision-making quarantine months. And thank you also to David, Jan, Igor, Gareth, Daniel, Manuel, Martin, Patricio, Jonaš, Erik, and to all the other group members for always being there to share a laugh or a work-related issue. Special thanks to Sebastian, Jakob, Rosi and Nora for their help in the lab, and to Florian, Igor, Michele Re. and Jesus

for making our shared projects enjoyable and fruitful.

Then thanks to whom was not with me everyday physically, but was cheering from the distance—my parents and my monsters. Your unconditional support gives me all the strength I need to pursue my dreams. Thanks to you Mom, for showing me how to be strong in face of all that happens, and to appreciate the little beautiful things that surround us everyday (and to submerge me with food, even from the distance—never stop this please). Thanks to you Daddy, for you taught me how to be determined and let my voice be heard. Thanks to Nicus: You set an example of perseverance and humbleness, and with your weird sense of humor you remind me not to take things too seriously. And then to my sweet, kick-ass, doctor-to-be Lottolina: Thank you for the countless visits to Vienna, and for teaching me everyday to be myself and do what I love, whatever the challenges and whatever people think. I love you tantissimo, you inspire me everyday, and you are always in my thoughts.

Thanks to the swaggers (Ste, Massi, Fabri, Ale, Giulio, Giulia, Petra, Jack) for welcoming me in your traditions and holidays, and for the best laughs together. A special thank you to my fellow travelers (Michi, Fabri, Massi, Giorgio) for our crazy backpacking trips. I am thrilled for our next adventures.

Finally, the biggest thank you is for you, Michele, my favorite weirdo. Unexpected and overwhelming, you flipped my life over. Thank you for sometimes landing me your nice brain and what's inside it, and for pushing me to the limits when I wouldn't. Thank you for patiently and selflessly teaching me everything you know, for your exceptional mentoring and guidance, and for always gifting me (and everybody in the group) with prompt help, advices, and fruitful discussions. Your passion for science and work ethics are inspiring. A million thank you for planning, discussing, not understanding and then understanding our results together, for running to the lab each time I texted you I had a nice STM tip, and for the careful reading of this Thesis. Without a shadow of a doubt, none of this work would have been possible without you. But also thank you for making these years so special—joyful, adventurous, intense, and filled with the most delicious food, lots of spanzing, many ass falls on the snowboard (totally worth it), awkward dance moves, and so much more.

Thanks to everybody who has been besides me, and to the ones who will stay for the next adventure.

Giada